STRUCTURAL STUDY OF METAL NANOSTRUCTURE ON SEMICONDUCTOR SURFACE AND THEIR MULTIFUNCTIONAL APPLICATIONS

by

Abhijit Roy

(Enrolment No.-PHYS05201504002)

Saha Institute of Nuclear Physics, Kolkata

A thesis submitted to the

Board of Studies in Physical Sciences

In partial fulfillment of requirements

for the degree of

DOCTOR OF PHILOSOPHY

of

HOMI BHABHA NATIONAL INSTITUTE

January, 2020

Homi Bhabha National Institute

Recommendations of the Viva Voce Board

As members of the Viva Voce Board, we certify that we have read the dissertation prepared by Abhijit Roy entitled STRUCTURAL STUDY OF METAL NANOSTRUCTURE ON SEMICONDUCTOR SURFACE AND THEIR MULTIFUNCTIONAL APPLICATIONS and recommend that it may be accepted as fulfilling the thesis requirement for the award of Degree of Doctor of Philosophy.

Chairman - Prof. Satyaranjan Bhattacharyya	SBhattacharyya	**Date:** 09.09.2020
Guide/Convener - Dr. Biswarup Satpati	Biswarup Satpati	**Date:** 09/09/2020
Co-guide - NA		**Date:**
Examiner - Prof. Dipak Kumar Goswami	DKGoswami	**Date:** 09/09/2020
Member 1 - Prof. Tapas Kumar Chini	Tapas Kumar Chini	**Date:** 09/09/2020
Member 2 - Prof. Dulal Senapati		**Date:** 09.09.2020.
Member 3 - Dr. Prasanta Karmakar	Prasanta Karmakar	**Date:** 09-09-2020

Final approval and acceptance of this thesis is contingent upon the candidate's submission of the final copies of the thesis to HBNI.

I/We hereby certify that I/we have read this thesis prepared under my/our direction and recommend that it may be accepted as fulfilling the thesis requirement.

Date: 09.09.2020
Place: Kolkata

Biswarup Satpati

Co-guide (if any) **Guide**

STATEMENT BY AUTHOR

This dissertation has been submitted in partial fulfillment of requirements for the doctoral degree at Homi Bhabha National Institute (HBNI) and is deposited in the Library to be made available to borrowers under rules of the HBNI.

Brief quotations from this dissertation are allowable without special permission, provided that accurate acknowledgement of source is made. Requests for permission for extended quotation from or reproduction of this manuscript in whole or in part may be granted by the Competent Authority of HBNI when in his or her judgment the proposed use of the material is in the interests of scholarship. In all other instances, however, permission must be obtained from the author.

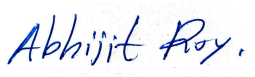

Abhijit Roy

DECLARATION

I, hereby declare that the investigation presented in the thesis has been carried out by me. The work is original and has not been submitted earlier as a whole or in part for a degree / diploma at this or any other Institution / University.

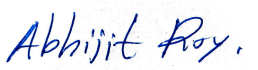

Abhijit Roy

List of Publications

Publications related to this thesis

Publications in peer reviewed Journals:

1. *Annealing Induced Morphology of Silver Nanoparticles on Pyramidal Silicon Surface and Their Application to Surface-Enhanced Raman Scattering.*
   A. **Roy**, A. Maiti, T. K. Chini and B. Satpati, *ACS. Appl. Mat. Interfaces* **9**, 34405-34415 (2017).

2. *Electroless Deposition of Pd Nanostructures for Multifunctional Applications as Surface-Enhanced Raman Scattering Substrates and Electrochemical Nonenzymatic Sensors.*
   A. **Roy**, S. S. Singha, S.Majumder, A. Singha, S. Banerjee and B. Satpati, *ACS. Appl. Nano. Mater.* **2**, 2503-2514(2019).

3. *Metal Nanoparticle-Decorated Silicon Nanowire Arrays on Silicon Substrate and their Applications.*
   A. **Roy** and B. Satpati, *Microsc. Microanal.*, 1-9 (2019).

4. *A simple method of growing endotaxial silver nanostructures on silicon for applications in surface enhanced Raman scattering (SERS).*
   A. **Roy**, T. K. Chini and B. Satpati, *Appl. Surf. Sci.*, **501**, 144225 (2020).

In conference proceeding:

1. *Facile Synthesis of Silicon Nanowire-Nanopillar Superhydrophobic Structures.*
   A. **Roy** and B. Satpati, *AIP Conf. Proc.* **1942**, 080061 (2018).

2. *Effect of Annealing on Gold Thin Film on Silicon Surfaces Deposited by Electroless Deposition.*

A. **Roy** and B. Satpati, *AIP Conf. Proc.* **2115**, 030298 (2019).

Abhijit Roy

Abhijit Roy

To my "Family and Teachers"

Acknowledgements

The research work included in this thesis owes its existence to the patience, assistance and support of many special individuals. Firstly, I would like to acknowledge my Ph.D thesis supervisor Dr. Biswarup Satpati. No proper word can be used to describe my respect for him. He introduced me with the world of transmission electron microscopy, plasmonics and nanotechnology. He has made me an independent researcher by giving constant encouragement along with proper guidance without which the dream of completing my Ph.D would not have been possible. Really thank you very much Sir for your constant involvement with me and my research work.

I gratefully acknowledge Prof. Tapas Kumar Chini, for his help in cathodoluminescence spectroscopy and in FDTD simulation. He also gave me constant encouragement about my work and was ready to help always. I would like to thank all the other faculties and staff of our division for their help and guidance during my Ph.D work.

I would like to thank the rest of my HBNI doctoral committee members, Prof. Satyaranjan Bhattacharyya, Prof. Dulal Senapati and Dr. Prasanta Karmakar for the yearly progress review and for proper suggestions. I would like to acknowledge former director of SINP, Prof. Ajit Kumar Mohanty and present director, Prof. Gautam Bhattacharyya for giving the opportunity to work in this premier institute and also for making the best facility available. I would like to thank department of atomic energy (DAE), Government of India, for the financial assistance.

I thankfully acknowledge our collaborators Prof. Sangam Banerjee, Prof. Achintya

Singha, Dr. Shib Shankar Singha and Dr. Sumit Majumder for helping me with my thesis work. I would like to thank our lab seniors Dr. Tanmoy Ghosh and Dr. Tapas Ghosh for sharing their research knowledge and experience during the early days of my doctoral work. I also thank my labmate Gourab for being a constant part of this long journey. I always enjoyed the time we had on and off our research work. I also would like to thanks my current labmates, friends of Post M.Sc and juniors of our division.

I cannot express the gratitude with words for the support I got from my best friend, my better half Debopriya. Thank you for all the love, support and constant encouragement without which the journey would have been much harder. I am very much thankful to my family, especially my parents whose contributions is beyond words. Thank you Baba and Ma for all the support I need. I would like to thank my sister, brother-in-law and their son (Duggu) for the constant encouragement.

Lastly, I really express my sincere apologies to everyone of those for my inability to acknowledge individually who have contributed in my Ph.D thesis work.

SINP, Kolkata

February, 2020 Abhijit Roy

Contents

Summary xiii

Synopsis xv

List of Figures xxvi

List of Tables xxxviii

Nomenclature xxxix

1 General Introduction 1
- 1.1 Introduction . . . 2
  - 1.1.1 Metallic Nanoparticles . . . 3
  - 1.1.2 Galvanic Displacement Reaction . . . 4
  - 1.1.3 Metal-Assisted Chemical Etching . . . 5
  - 1.1.4 SPR Driven Properties of Nanomaterials . . . 6
  - 1.1.5 LSPR . . . 8
  - 1.1.6 Surface-Enhanced Raman Scattering . . . 8
  - 1.1.7 Substrate Supported Nanoparticles . . . 11
  - 1.1.8 Advantages of 3D Substrate . . . 11
  - 1.1.9 Advantages of Ag and Pd nanoparticles . . . 12
  - 1.1.10 Recent Progress on Ag Deposited SERS Substrates . . . 14
  - 1.1.11 Recent Progress on 3D Si SERS Substrate . . . 15
  - 1.1.12 Epitaxy and Endotaxy . . . 16
  - 1.1.13 Annealing Induced Structural Variations of Nanoparticles . . . 18
  - 1.1.14 Finite-Difference Time-Domain Simulation . . . 20
- 1.2 Outline of The Thesis . . . 23

2 Experimental methods 25
- 2.1 Introduction . . . 26
- 2.2 Synthesis of Different Metal Nanostructures on Semiconductor Substrates . . . 26
  - 2.2.1 Synthesis of Ag on Planar Si and Formation of Endotaxial Ag 26

2.2.2 Ag Deposition on Pyramdial Si and Formation of Coupled Ag Nanostructure . . . 27
2.2.3 Production of Si-Nanowire on Pyramidal Si and GDR of Ag 28
2.2.4 Electroless Deposition Process of Pd . . . 29
2.3 Characterization and Application Techniques . . . 30
2.3.1 Transmission Electron Microscopy (TEM) . . . 30
2.3.2 Different Components of TEM . . . 34
2.3.3 Projection System . . . 41
2.3.4 Vacuum System . . . 42
2.3.5 TEM Imaging and Diffraction . . . 45
2.3.6 Bright-Field and Dark-Field Operation . . . 48
2.3.7 Scanning Transmission Electron Microscope . . . 49
2.3.8 Phase Contrast Microscopy . . . 50
2.3.9 Moiré Pattern . . . 54
2.3.10 Energy-Dispersive X-ray . . . 54
2.3.11 TEM Cross-Sectional Sample Preparation . . . 56
2.3.12 TEM Characterization . . . 59
2.3.13 Scanning Electron Microscope . . . 59
2.3.14 Raman Spectroscopy . . . 63
2.3.15 Electrochemical Workstation . . . 65
2.3.16 FDTD Simulation Set Up for Different Structures . . . 66

3 Galvanic displacement reaction 69
3.1 Introduction . . . 70
3.2 Electrodeposition Process . . . 71
3.2.1 Autocalytic and Substrate Catalytic Process . . . 71
3.2.2 Galvanic Displacement Process . . . 71
3.3 Si . . . 72
3.4 Galvanic Displacement on Ge Substrate . . . 75
3.5 Displacement of Noble Metals . . . 76
3.5.1 Displacement of Pt group metals . . . 78
3.5.2 Effect of Surfactants . . . 78
3.6 Metal Assisted Chemical Etching . . . 79

4 Structural Study of Nanoparticles Deposited on Semiconductor Substrates by Electroless Method 83
4.1 Introduction . . . 84
4.2 Structural Evolution of Ag Deposited on Planar Si . . . 85
4.2.1 Morphology: SEM Analysis . . . 85
4.2.2 Study of Crystallinity: XRD analysis . . . 86
4.2.3 Structural Study: TEM Analysis . . . 88
4.2.4 HRTEM Analysis of Endotaxial Particles . . . 92

4.3 Effect of Annealing on Gold Thin Film on Silicon Surfaces Deposited by Electroless Deposition . . . 99
4.3.1 TEM Analysis . . . 99
4.4 Structural Study of Ag Deposited on Pyramidal Si and Their Evolution Due to RTA . . . 102
4.4.1 Morphology Analysis: SEM Observations . . . 102
4.4.2 Analysis of Crystalline Structure: TEM Observation . . . 108
4.5 Morphology of Si Nanowire Produced on Planar and Pyramidal Si . 112
4.5.1 FESEM and TEM Study . . . 112
4.6 Pd Nanoparticles on Semiconductor Substrates . . . 121
4.6.1 Morphology: SEM Analysis . . . 121
4.6.2 TEM Analysis . . . 123
4.6.3 Crystal Structure Analysis . . . 125
4.7 Conclusions . . . 128

5 SERS Application and Near-Field Study Using FDTD Simulation and Cathodoluminescence Spectroscopy 130
5.1 Introduction . . . 131
5.1.1 EM Enhancement . . . 132
5.1.2 Chemical Enhancement . . . 133
5.2 SERS Measurement of Ag Deposited on Planar Si . . . 134
5.2.1 Optical Property: UV-Vis Spectroscopy . . . 136
5.2.2 FDTD Simulation . . . 137
5.3 SERS Activity of Ag Deposited on Pyramidal Si . . . 140
5.3.1 Cathodoluminescence Measurements . . . 145
5.3.2 UV-Visible Spectroscopy . . . 146
5.3.3 Near Field Intensity Distribution: FDTD Simulation . . . 147
5.4 SERS Study of Ag Deposited on P-Si/Si-NW Substrate . . . 149
5.4.1 FDTD Simulation of Ag deposited on Si-Nanowire . . . 151
5.5 SERS Activity Measurement of Pd Nanoparticles Deposited on Semiconductor Substrate . . . 153
5.5.1 FDTD Simulation Study . . . 160
5.6 Conclusions . . . 162

6 Electrochemical Detection of Glucose and AA Using Pd Nanoparticle Deposited on Semiconductor Substrate 164
6.1 Introduction . . . 165
6.2 Electrochemical Cyclic Voltammetry Study . . . 168
6.2.1 Glucose and Ascorbic Acid Sensing Study . . . 168
6.2.2 Interference Study . . . 174
6.3 Conclusions . . . 174

7 Summary **178**

List of Figures

1 *(a) Low magnification bright-field XTEM image of S1 and S2, (b) STEM-HAADF image of O_2 annealed substrate and the EDX spectrum showing presence of Ag and Si (inset), (c) EDX elemental map from the rectangular region in (b), (d) Enlarged view of S1 showing the formation of buried Ag nanoparticle, (e)Low magnification bright-field XTEM image of S1 and S2, (b) STEM-HAADF image of N_2 annealed substrate showing formation of only spherical Ag particle* xviii

2 *(a) SE image of N_2 annealed sample showing the particle size variation from bottom to top of the pyramid (b) BSE images showing the atomic contrast between Si and Ag (c) bright-field XTEM image of N_2 annealed sample showing formation of only spherical particle on Si. (d) SE image of O_2 annealed sample showing the particle size variation from bottom to top of the pyramid and also formation of triangular Ag underneath of spherical Ag (e) BSE images confirming that the triangular particles are Ag (f) bright-field XTEM image of O_2 annealed sample (g) SERS spectra at day 1 using 10^{-6} M R6G for all the three samples (h) SERS spectra at day 28.* xx

3 *(a) Bright-field XTEM image of Si nanowire on planar Si produced by MACE process (b) HRTEM image of sidewall of a Si nanowire showing formation of amorphous sidewall (c) HRTEM image of Ag-Si interface. (d) bright-field XTEM image of Si nanowire on pyramidal Si (e) HRTEM image showing presence of Ag nanoparticles at the bottom of the nanowires (f) HRTEM image of a single Si nanowire showing formation of zig-zag sidewalls.* xxi

4 *(a), (b) and (c) shows formation of Pd on Ge for* 10, 20 *and* 60 *minutes respectively, (d), (e) and (f) shows formation of Pd on Si for* 10, 20 *and* 60 *minutes respectively and (g), (h) and (i) shows formation of Pd on pyramidal Si for* 10, 20 *and* 60 *minutes respectively.* xxiii

1.1 *The Lycurgus Cup placed in British Museum, London. Made in Rome probably in 4th century AD (a) Shows green color when lightened externally (b) shows red color when lightened internally. The Au and Ag nanoparticles embedded in the glass are responsible for such dichroic effect. (c) Strained glass window in Chartres cathedral. The different colors are due to the presence of metal oxide nanoparticles. Source: internet.* 7

1.2 *Farady's Au colloid. (a) Farday's Au colloid solution stored in Royal Institution of Great Britain (b) High resolution TEM data of Au colloid. Source: Thomas, J. M., Midgeley, P. A. Chemical Communication (2004)* 8

1.3 *Different growth mechanisms (a) F-M growth (b) V-W growth (c) S-K growth and (d) Endotaxial growth* 17

1.4 *Thermal diffusion of nanoparticles* 19

1.5 *Components of different electric and magnetic field vectors within Yee's grid.* 21

2.1 *(a) Schematic of GDR. (b) Schematic of MACE process.* 29

2.2 *Schematic representation of generation of various signals due to interaction of highly energetic electrons with a thin specimen.* 32

2.3 *300 keV FEI TECNAI G20 Twin Microscope facility at SINP, Kolkata.* 34

2.4 *Schematic representation of (a) magnetic lens and (b) path of and electron in a magnetic field.* 39

2.5 *Schematic diagram of TEM vacuum system.* 43

2.6 *Two most basic TEM operation (a) image mode (b) diffraction mode.* 46

2.7 *(a) Representation of scattering from two atomic planes where* W_1 *and* W_D *are the incident and diffracted waves respectively. (b) incident wave vector is* k_1*, diffracted wave vector is* k_d *and* K *is the difference vector.* 47

2.8 *Ray diagram of bright and dark-field mode of operation using objective lens and objective aperture (a) BF mode of operation using direct beam. (b) off-axis DF mode of operation using an off-axis beam. (c) CDF mode where the incident beam is tilted to make the scattered beam travel along the optic axis.* 49
2.9 *Schematic representation of (a) diffraction of wave through a crystal (b) realationship between spherical wavefront radius r, position vector of the i-th atom r_i and the point P at which the intensity is to be calculated.* 51
2.10 *Schematic representation of EDX signal generation processing unit .* 55
2.11 *Schematic of TEM cross-section sample preparation process.* 56
2.12 *Photograph of Gatan CL-SEM installed at SINP, Kolkata* 60
2.13 *Detailed schematic diagram of the CL-SEM system* 61
2.14 *(a) Labram HR 800 installed at SINP, Kolkata (b) Schematic of different unit and working process of a Raman spectrometer.* 63
2.15 *(a) Schematic of three electrode configuration of a electrochemical workstation (b) Photograph of a three electrode system in working condition.* 64
2.16 *Structural geometry used for FDTD simulation.* 66

3.1 *Schematic of (a) Electrocatalytic process (b) Electroless process* . . . 70
3.2 *(a) and (b) Potential-pH diagram for $Si - F - H_2O$ system for different concentration of F^- ion. Image: ref 111* 73
3.3 *Schematic of H-terminated Si dissolution in (a) water (b) in HF.* . . . 74
3.4 *Galvanic displacement process on (a) Si substrate and (b)Ge substrate.* 75
3.5 *Different steps of metal-assisted chemical etching process for an isolated metal nanoparticle. (a) Reduction of H_2O_2 at the meta particle surface and insertion of hole into the Si surface (b) oxidation of Si surface and subsequent dissolution leads the metal particle to penetrate inside the substrate (c) diffusion of holes towards the Si surface and subsequent oxidation of Si leads to formation of porous Si.* . . . 79
3.6 *(a) Schematic of reduction potential for the two MACE half reaction process vs V_{SHE} (b) and (c) Au-Si interface band diagram for n-type and p-type Si substrate respectively.* 81

4.1 *SE image of (a) Ag deposited on Si (*100*) by galvanic displacement method for* 1 *minute, (b) Bird's eye view of (a), (c) Histogram of particle size distribution, (d) Ag deposition on Si for* 3 *minutes, (e) magnified view of (d) showing a spaghetti-like structure, (f) Bird's eye view of (d) showing a flat top morphology of Ag nanoparticles.* . 85

4.2 *(a) XRD peaks of cubic Ag according to JCPDS data. (b) XRD pattern of Ag deposited on Si for* 1 *minute and* 3 *minutes, respectively. (c) XRD pattern of Ag deposited on Si for* 3 *minutes and annealed at* N_2 *and* O_2 *atmosphere, respectively. (d) Ag deposited for* 1 *minute and annealed at* O_2 *atmosphere for planar Si and P-Si, respectively (e) GIXRD pattern of blank Si* 86

4.3 *(a) Low magnification BF XTEM image showing Ag deposition on Si for* 1 *minute, (b) STEM-HAADF image (c) STEM-HAADF image from the area marked by the rectangular portion in (b) and corresponding EDX maps (Ag-L map, Si-K map and composite map), (d) HRTEM image of the interface between Ag and Si. (e) and (f) FFT pattern and inverse FFT image from the region marked by red square in (d), respectively, (g) High magnification image of (a) showing almost identical height of the nanoparticles, (h) Low magnification bright-field image of* 3 *minutes Ag deposition on Si showing the formation of quasi-continuous layer, (i) High magnification image of (h).* 89

4.4 *(a) Low magnification BF XTEM image of* $S1$ *and* $S2$*, (b) STEM-HAADF image of* $S1$*, (c) EDX elemental map from the rectangular region in (b), (d) Enlarged view of* $S1$ *showing the formation of buried Ag nanoparticle, (e) EDX spectrum from region* 1 *in (b).* . . 90

4.5 *(a) Bright-field XTEM image of 1minute Ag deposition on Si (100) showing formation of direct contact points between Ag and Si, (b) Enlarged view from the region bounded by yellow rectangle in (a).* . 92

4.6 *(a) HRTEM image of an endotaxial particle for sample* $S1$*, (b) and (c) are FFT patterns from the region 1 and 2 in (a), respectively showing epitaxial relationship between Ag and Si on both facets, (d) and (e) IFFT image of (c) and (b), respectively showing orientation of Si (1 1 1) and Ag (1 1 1) plane along the facets.* 93

4.7 *(a) HRTEM image of an endotaxial Ag particle in Si which is taken as reference to analyze the structure, (b) Simulated diffraction pattern of Si and Ag along 110 zone axis, (c) rotated diffraction pattern (*57 *clockwise) to obtain similar FFT pattern showed in Figure 4(b). (d) Reformation of endotaxial particle of (a) showing the facet directions, the [110] view of Ag and Si is also shown.* 94

4.8 *(a) STEM-HAADF image of S*1 *and S*2*, (b) EDX elemental mapping from region bounded by the orange rectangle in (a), (c) XTEM image of S*2*, (d) XTEM image of Ag deposited for* 3 *minute and* N_2 *annealed (S*3*).* 96

4.9 *(a) STEM-HAADF image of S*1 *and S*2*, (b) EDX elemental mapping from region bounded by the orange rectangle in (a), XTEM image of S*2*, (d) XTEM image of Ag deposited for* 3 *minute and* N_2 *annealed (S*3*).* 97

4.10 *(a) SE image of Ag deposited for* 1 *minute on P-Si substrate, (b) XSEM view of (a). (c) BF XTEM image of* O_2 *annealed Ag on P-Si showing the formation of the triangular particle in addition to spherical Ag. (d) STEM-HAADF image of (c) showing the position of Ag triangle on the substrate, (e) BF XTEM image of* N_2 *annealed Ag on P-Si showing the formation of only spherical particle.* 98

4.11 *(a) BF TEM image of Au deposited on Si for* 15 *minutes by GDR. (b) Magnified image of (a). (c) HRTEM image of Au film showing formation of various defects at the middle and top portion of the film. (d) and (e) HRTEM image and FFT pattern from the region bounded by red rectangle in (c) showing formation of Au (111) plane. (f) STEM-HAADF image. (g) EDX spectra from the region bounded by yellow rectangle in (f) confirming presence of Si and Au* 100

4.12 *(a) BF TEM image of RTA annealed Au nanoparticles showing formation of isolated spherical Au nanoparticles with endotaxial particles. (b) HRTEM image of a single Au particle showing formation of Moïre fringes. (c) FFT pattern from the interface indicating an epitaxial relationship between Au and Si. (d) STEM-HAADF image showing Au nanoparticles with higher contrast. (e) EDX line profile taken along the line shown in (d) Confirming the endotaxial particle is made of Au. (f) BF TEM image of normal annealed Au thin film on Si at ambient atmosphere. Formation of endotaxial Au on Si is observed in this case also.* 101

4.13 *(a) SE images of micropyramids on Si, (b) histogram of base length distribution, (c) XSEM view, and (d) histogram of height distribution.* 102

4.14 *Plane view SE image of Ag deposited on Si pyramids for different reaction times: (a)* 10*, (b)* 30*, (c)* 60*, and (d)* 90 *s; (e) magnified view of (d) showing dendritic Ag nanostructure formation on top of the pyramid, and (f) XSEM view of (d) showing the presence of dendritic structure at the top in most of the pyramids.* 103

4.15 *Ag nanoparticles deposited by galvanic displacement method on Si (*100*) substrate for reaction time of (a)* 60 *and (b)* 180 *s.* 104

4.16 *XSEM images: (a) SE image of S*2 *sample showing the particle size variation from bottom to the top of the pyramid, (b and c) corresponding BSE images showing the atomic contrast between Si and Ag, (d) SE image of S*3 *sample showing the formation of spherical-shaped particles along with the triangular one, (e and f) corresponding BSE images confirm that the triangles are also made of Ag.* . . 105

4.17 *(a)-(b) Top-view SEM image of S2, (c)-(d) Top view SEM image of S3 showing that the triangles are at the bottom of spheres and Si etch pit formation (shown by red arrow) during annealing at* O_2 *atmosphere, respectively* 106

4.18 *(a) [100] XTEM image of S3 showing the separation between triangular and spherical particle, (b) corresponding HRTEM image, (c) HRTEM image from another pair of triangular and spherical particle clearly showing a thin layer of SiO_X covering triangular particle. (d) TEM tomography data showing such separation with different projections [−68, −34, 0, +36 and +62], (e) STEM-HAADF image, (f) EDX spectra from three different points shown in (e) clearly showing the presence of Si upto the surface (electron beam of spot size 2 nm), (g) STEM-HAADF image, (h) Magnified STEM-HAADF image and EDX elemental maps from a region marked in (g) showing the presence of Si and O upto the surface region.* 107

4.19 *(a) Low-magnification BF XTEM image of S1, (b) STEM-HAADF image, (c) EDX spectrum from region 1 is shown in (b), (d) elemental map from region 2 using Si–K and Ag–L energy, (e) histogram of particle size distribution, and (f) HRTEM image at the interface. (Inset) Fourier-filtered image of the red-dotted region of the interface showing crystallographic relation between Si (111) and Ag (111) planes.* 109

4.20 *(a) BF XTEM image of S2 showing formation of only spherical particle on Si due toN_2 annealing. Particle size increases with the pyramid height. (b) HRTEM image showing the direct formation of 3D island of Ag on Si, (c) histogram of the particle size distribution, (d) SAD pattern of the interface showing epitaxial growth of Ag on Si.* 110

4.21 *(a) Low-magnification BF XTEM image of S3, (b) histogram of the particle size distribution, (c) high-magnification XTEM image of S3,(d) BF XTEM image showing almost all the spherical particles are associated with triangular particle underneath, (e) SAD pattern from a region in (d) showing epitaxial relation between Ag and Si. [110] Zone axis diffraction pattern where diffraction spots of Ag are indexed by red and Si by the yellow color. (f) HRTEM image of the portion marked by a red square in (c), showing the facet is along the 422 direction and the Moiré fringe of spacing is* 9.670.04 *Å.* 111

4.22 *(a) SE image of P-Si produced by SDR method. (b) Ag deposited on P-Si by GDR. (c) XTEM image of Ag deposited on P-Si. (d) STEM-HAADF image of Ag on P-Si. (e) EDX elemental spectra from the region marked by a red rectangle in (d).* 113

4.23 *(a) BF TEM image of Si NW produced by MACE process on planar Si* (100)*. (b) HRTEM image of a single Si nanowire. (c) SAD pattern of Si NW along* [110] *zone axis showing diffraction spots. (d) HRTEM image of the interface between Ag and Si. (e) Closer look of the portion marked by black square in (d) showing Si* (111) *and Ag* (111) *plane. (f) FFT pattern of the same region showing diffraction spots for Ag and Si.* 114

4.24 *(a) Formation of Si nanowire on planar Si using* 0.2 *M* H_2O_2 *as etchant (b) HRTEM image (c) Wien filtered HRTEM image of a single nanowire showing absence of any amorphous Si layer. (d) FFT pattern of the region shown in (c) showing very good crystalline structure of the nanowire.* 116

4.25 *. (a) BF TEM image of Si NW formed on P-Si by MACE process. (b) High-magnification image from the portion marked by a red square in (a). (c) FFT pattern from Si nanowire. (d) High-magnification image of a single Si nanowire. (e) HRTEM image of a single Si NW showing the formation of zig-zag sidewalls of Si. (f) Wien filtered image of (e) showing the etching direction. (g) STEM-HAADF image. (h) EDX elemental spectra from the portion marked by yellow square in (g) showing the presence of Si and Ag. (i) EDX mapping (Si-K map, Ag-L map, and composite map) from the portion marked by a magenta rectangle in (g).* 119

4.26 *(a) XSEM image of Si NW after the removal of Ag by* HNO_3*. (b) XSEM view of P-Si/Si nanowire after redeposition of Ag on it. (c,d) Plan-view SEM image after annealing at* 550C *for* 1 *minute at* O_2 *and* N_2 *atmosphere, respectively. The inset shows a BSE image to confirm the presence of Ag on the top of Si nanowire.* 120

4.27 *SE images. (a), (b), (c), (d) and (e) represents Pd nanoparticles features when deposited on Ge (*100*) for* 1 *minute (*$G1$*),* 2 *minutes (*$G2$*),* 10 *minutes,* 20 *minutes and* 60 *minutes respectively. (f), (g), (h), (i) and (j) represents Pd nanoparticles Pd nanoparticles features when deposited on Si (*100*) for* 1 *minute (*$S1$*),* 2 *minutes (*$S2$*),* 10 *minutes,* 20 *minutes and* 60 *minutes respectively and (k), (l), (m), (n) and (o) represents Pd nanoparticles features when deposited on pyramidal Si for* 1 *minute (*$PS1$*),* 2 *minutes (*$PS2$*),* 10 *minutes,* 20 *minutes and* 60 *minutes respectively* 121

4.28 *BF XTEM images: (a), (b) and (c) shows G10, G20, and G60 samples respectively; (d), (e) and (f) shows S10, S20, and PS60 samples respectively; (g), (h) and (i) shows PS10, PS20, and PS60 samples respectively. (j), (k) and (l) shows magnified images of the G60, P60, and PS60 sasmples, respectively. Insets show the magnified images of the Pd nanostructure.* 124

4.29 *(a) HRTEM image of a Pd shaft deposited on* $G10$ *sample. Inset shows the FFT pattern from the region marked by the red rectangle in part a. (b) IFFT image showing Pd(*111*) plane and its direction with respect to the substrate. (c) SAD pattern taken along [*110*] zone axis showing diffraction spots of Si and Pd. (d) HRTEM image of a single Pd cluster (*$S10$*) which generates nanorod-shaped Pd nanoparticles showing formation of dislocations and grain boundary and strain-induced defects. (e) IFFT image. (f) SAD pattern from* $S60$ *sample showing good crystallinity. (g) HRTEM image of a single Pd shaft showing the formation of a twin boundary at the midportion. (h) SAD pattern taken along [*110*] zone axis showing the formation of a tilted heteroepitaxy between Pd and Si for the* $PS20$ *sample. (i and j) HRTEM image of a single Pd shaft and FFT image from the interface of* $PS20$*, respectively.* 126

5.1 *SERS spectra of* 5×10^{-5} *M R6G for (a)* 1 *minute Ag deposited and* 1 *minute* O_2 *annealed sample (*$S1$*) (b)* 3 *minutes Ag deposited and* 1 *minute* O_2 *annealed sample (*$S2$*). (c) Variation of SERS spectra with the molar concentration of R6G for* $S1$*.* 135

5.2 *UV-Vis absorbance spectra of (a) samples made on planar Si (100) and (b) samples made on P-Si, respectively.* 138
5.3 *FDTD calculated electric field distributions of (a) 60 nm radius spherical Ag particles in combination with endotaxial Ag particles, (b) 125 nm spherical Ag particles with 50 nm endotaxial Ag particles. (c) and (d) calculated EF (in log scale) in the X-Z plane from the same particles, respectively.* 139
5.4 *FDTD calculated electric field distributions of coupled 60 nm radius spherical Ag particles in combination with the endotaxial Ag particles (a) when the interparticle distances are 10 nm, (b) when interparticle distances are 25 nm. (c) and (d) calculated EF (in log scale) in the X-Z plane for both the cases shown in (a) and (b), respectively.* 140
5.5 *SERS spectra of 10^{-5} M R6G at three different random site for three different substrates: (a) P-Si/Ag, (b) P-Si/Ag annealed at N_2 and (c) P-Si/Ag annealed at O_2* 141
5.6 *(a) SERS spectra of 10^{-5} M R6G taken for S1, S2, and S3 samples just after preparation (day 1). (b) SERS spectra of the same three samples after 28 days.* 143
5.7 *SERS spectra of different concentration of R6G for S3 and R6G (10^{-1} M) on P–Si.* 144
5.8 *(a) SE image, (b) PAN CL image showing the formation of hot spots on both the spherical particle and triangular particle, (c) CL emission spectra from the spherical particle (red curve) and from bottom triangle (blue curve), (d and e) Mono CL image at 372 and 525 nm, respectively, (f) SE image of second particle, (g) MONO CL image showing the hotspot is contained mainly by the sphere at 424 nm, and (h) MONO CL image where the hotspot is also contained by the bottom triangle at 464 nm.* 147
5.9 *UV–visible spectra of S1, S2, and S3.* 148
5.10 *(a) FDTD calculated electric field distribution of triangular Ag particles with the spherical Ag particle combination on 3D Si substrate under 632 nm excitation wavelength and (b) calculated EF in the x–z plane from the coupled Ag nanoparticles.* 149

5.11 *(a) SERS spectra of* 10^{-5} *M R6G on different substrates and* 10^{-1} *M R6G on P-Si. (b–e) Variation of water contact angle for different substrates.* 151
5.12 *(a) X–Z view of FDTD simulated e-field distribution of Si NW on Si pyramid. (b) Ag sphere on P-Si/Si-nanowire configuration showing maximum enhancement at the mid-portion between two spheres. (c) E-field distribution when two spheres are separated by a longer distance. The polarization direction is taken along X-axis.* 152
5.13 *(a), (b) SERS spectra of* $G20$ *and* $G60$*, respectively for different concentrations of R6G. (c), (d) SERS spectra of* $S20$ *and* $S60$*, respectively, for different concentrations of R6G.* 154
5.14 *(a), (b), (c) and (d) shows intensity versus concentration graph for* $G20$*,* $G60$*,* $S20$ *and* $S60$ *respectively.* 156
5.15 *(a) and (b) shows SERS spectra of* $G20$*,* $S20$*, and* $PS20$ *and* $G60$*,* $S60$*, and* $PS60$ *substrates taken with* 10^{-6} *M concentration of R6G. (c) and (d) shows intensities of the Raman spectra for* 10^{-10} *and* 10^{-11} *M concentrations of R6G for the* $PS20$ *and* $PS60$ *samples, respectively.* 157
5.16 *(a), (b), (c), (d), (e) and (f) show SERS spectra of* 10^{-6} *M concentration of R6G after* 1 *month for* $G20$*,* $G60$*,* $S20$*,* $S60$*,* $PS20$ *and* $PS60$ *sample, respectively.* 159
5.17 *SERS intensity for different substrates for* 3 *different peaks of R6G. The highest is observed for* $PS60$ *(R6G concentration is* 10^{-6} *M).* . 160
5.18 *(a), (b) and (c) shows FDTD-calculated near-field electric field distribution of Pd on Ge(100), Pd on Si(100) and Pd on P–Si. (d), (e) and (f) shows calculated EFs in the logarithmic scale for the same three substrates respectively.* 161
5.19 *FDTD calculated near-field electric field distribution for more than one Pd nanoparticle of (a) Pd on Ge (*100*) (b) Pd on Si (*100*) and (c) Pd on P-Si. Calculated EF in log scale for the same* 3 *substrates are shown in (d), (e) and (f) respectively.* 163

6.1 *(a) Graph of a typical input waveform in CV experiment (b) Typical cyclic voltammogram. E_{pa} and E_{pc} are the anodic and cathodic peak potentials, and i_{pa} and i_{pc} are the anodic and cathodic peak currents, respectively. Source: Elsevier* 166

6.2 *CV comparison plot for (a) S*10*, S*20 *and S*60 *(b) PS*10*, PS*20 *and PS*60 *(c) G*10*, G*20 *and G*60 *in* 1 M Na_2SO_4 *solution as electrolyte and at a scan rate of* 60 mV/s 169

6.3 *(a) and (b) shows CV study with different molar concentrations of glucose using PS*60 *and G*60 *substrates as working electrodes, respectively. (c) and (d) shows CV study with different molar concentrations of AA using PS*60 *and G*60 *substrates as working electrodes, respectively.* 170

6.4 *(a) and (b) shows linear response of peak reduction current with scan rate (with* R^2 *error) for glucose detection using PS*60 *and G*60 *as working electrode respectively. (c) and (d) linear response of peak reduction current with scan rate (with* R^2 *error) for AA detection using PS*60 *and G*60 *as working electrode respectively* 171

6.5 *(a and b) Amperometric current density–time curves for glucose sensing using PS*60 *and G*60 *as working electrodes, respectively. (c and d) Amperometric current density–time curves for AA sensing using PS*60 *and G*60 *as working electrodes, respectively.* 172

6.6 *(a) and (b) linear response graph of glucose concentration (with residual errors) with the current density for PS*60 *and G*60*, respectively. (c) and (d) linear response graph of AA concentration with the current density for PS*60 *and G*60*, respectively.* 173

6.7 *(a and b) Selectivity of glucose (working potential* 0.6 V*) over other electroactive materials using PS*60 *and G*60 *as working electrodes. (c and d) Selectivity of AA (working potential* 0.3 V*) over other electroactive materials using PS*60 *and G*60 *as working electrodes.* . 175

List of Tables

3.1 *Standard redox potential of different of different elements.* 76

4.1 *Average crystallite size with standard deviations from the XRD measurement.* 87

5.1 *Average EF with standard deviations from SERS measurement for different Raman peak of* 5×10^{-5} *M R6G.* 136

5.2 *Comparison of SERS EF between different samples with our work based on Ag.* 137

5.3 *EF from SERS measurement for different Raman peak of* 10^{-5} *M. R6G* 142

5.4 *EF for different interval of time for S3.* 144

5.5 *EF from SERS measurement for different Raman peak of* 1×10^{-5} *M R6G.* 150

5.6 *Average EF with standard deviations from SERS measurement for different Raman peak of* 10^{-6}*M R6G.* 155

6.1 *Comparison of the Analytical Performance of the Proposed AA Biosensor with Other AA Biosensors Reported Previously* 176

6.2 *Comparison of the Analytical Performances of the Proposed Glucose Biosensor with Other Glucose Biosensors Reported Previously.* . . . 177

Chapter 7

Summary

This chapter summarized different findings of this thesis work.

As research on nanomaterials is extending day by day, different processes are developing to assemble nanomaterials on different substrates efficiently. It is because of the fact that for different applications, nanomaterials are required to adhere on a substrate surface efficiently. Not only that, the metal semiconductor interfaces are emerging as a promising candidate for solar light harvesting and also to the effect of different dielectrics on the optical property of nanomaterials. Different processes like MBE, PVD, CVD, laser ablation are already used for this purpose. However, all of the above mentioned processes required heavy instrument, appropriate maintenance and hence they are costly. GDR is a very low-cost process and efficient to deposit metal nanoparticle on semiconductor substrate. It does not require any heavy instrumentation and controlling different parameter are much easier. This process also produces a very much clean interface as it uses no external reducing agent or external voltages. The deposited film morphology can be modified by changing the morphology of the substrate which can be achieved by chemical etching or by ion beam radiation. In this thesis work, we have done an extensive growth and structural analysis by SEM, TEM and XRD technique of Ag deposited on planar and patterned Si. Contrary to other findings, we have obtained an improvement in the optical property of the Ag nanoparticle due to RTA at O_2 atmosphere. This improved optical property is induced by formation of complex shaped Ag nanostructure due to annealing at this environment. The stability of these structures were also studied by keeping them in ambient atmosphere for 28 days and they showed very stable structural and optical properties. These substrates can be used effectively as SERS active substratre.

Besides, one dimensional semiconductor nanowire show unique optical, electrical

properties which are due to quantum confinement effect. However metal decorated semiconductor nanowires were previously made by using heavy instrumentation which makes the production cost higher. Electroless process in our work to produce metal decorated semiconductor nanowire can bring down the production cost much lower with an added tunability So this present thesis work is mainly focused on the creation of pattern on semiconductor substrate and deposition of metal nanoparticles on it by GDR process, to study the evolution of the nanostructures with annealing and to prepare substrate which can be useful for multifunctional applications i.e. SERS, catalysis and hydrophobicity.

We have also discussed the growth of Pd nanoparticles on Si, Ge and pyramidal Si substrates. The growth rate and morphology of the Pd nanoparticles were observed to be heavily dependent on substrate type, morphology and defects on the substrate surface as observed from TEM and SEM observations. Different shaped Pd nanoparticles were produced by this process without any use of surfactants. The substrates were observed to be SERS active and they also showed very good catalytic activity for the detection of glucose and ascorbic acid even in presence of other electro-active species.

In conclusion this thesis work mainly contributes to the following facts (i) oxidation is not that bad always. As we see from chapter 4 and 5 that Ag nanoparticles indeed takes very interesting shapes when annealed in O_2 atmosphere and not only that, these substrates are very much stable and shows very good SERS enhancement which is contrary to the previous findings. (ii) A complete electroless process was used to produce metal nanoparticle decorated Si nanowires which will make this process much cheaper. Whereas previously heavy instrumentation were used

to create such substrates and (*iii*) The structures of Pd nanoparticles were modified without using any surfactants which have an effect on the SERS effect of Pd. By using this method the SERS enhancement of Pd nanoparticles were observed to be greatly increased compared to the previously reported literature besides its efficient catalytic properties.

Summary

Surface-enhanced Raman scattering (SERS) is a very powerful novel analytical tool that provides a very high level of detection sensitivity with molecular precision and has excellent potential to be used as a tool for chemical and biological sensing. The base of SERS is the Raman scattering which has a very low cross-section. In the SERS process, the scattering cross-section can be increased up to 10^{14} times using metal nanoparticles by "localized surface plasmon resonance (LSPR)". It is the dominant reason behind such a huge enhancement observed in SERS. It occurs when the incident light interacts with rough metal surfaces (apex, edges) and produces a sub nano-meter region of immensely concentrated EM field called "hot spots". Gold (Au) and silver (Ag) are the two most used metal for this purpose as they possess superior optical properties compared to others in the UV-Vis region. Here, we have shown that rapid thermal annealing of Ag-based SERS substrate (2D and 3D) actually enhances its performance. This is contributed by the formation of a composite nanostructure consisting of endotaxial Ag with Ag sphere on planar Si substrate and triangular Ag with spherical Ag on pyramidal Si substrate in O_2 atmosphere. The morphology, interface was studied extensively using different complementary techniques. The substrates produced in this process are very much low-cost, reproducible, efficient, and showed very efficient detection of rhodamine 6g (R6g) dye even after keeping them in an ambient atmosphere for one month. The extensive use of Ag and Au in SERS restricts the use of other metals, especially Pt group metals for SERS related applications because of their relatively poor optical properties. To overcome this limit, we also tried to produce SERS active substrate based on Pd nanoparticles which have a very good catalytic efficiency. We have observed that different nanostructure of Pd can be grown on different semiconductor substrates by keeping the other parameters the same (solvent concentration, temperature, deposition time, etc.) during deposition. This process does not involve any surfactants to control the morphology and we observed enhancement factor 10^6 using this process. The substrates were also able

to detect glucose and ascorbic acid (AA) qualitative as well as quantitatively with very good sensitivity and detection limits. This opens up the possibility of using these substrates in various important applications like diagnostic detection, illicitly sold narcotics detection, and civil defense applications in forensic laboratories.

Chapter 1

General Introduction

This chapter describes briefly about the inspiration of this thesis work and outlooks

---

1.1 Introduction

In recent times, research in nanotechnology is getting immense importance and emerging very rapidly. This due to the fact that nanoparticles possess very much different properties compared to their bulk counterparts [1, 2]. Nowadays, nanotechnology finds its usage in many applications and continuous study is going on to control different properties of nanomaterials in a more efficient way. Richard Feynmann, in 1955 during his famous lecture at Caltech asked: "What would happen if we could arrange the atoms one by one the way we want them?" [3]. This quote first introduced the concept of nanotechnology. However, this question remains unanswered in the future for some time. Not only this, the thought behind this question could not affect the scientific community much. Things changed after the introduction of many advanced scientific instruments i.e. SEM, TEM, and AFM. With these instruments scientists get to know what is happening there on the atomic scale, which later gave birth to one of the most important scientific aspects known as "Nanotechnology".

The two most important parameters which are mainly responsible behind the unusual properties of nanomaterials are compared to their bulk counterparts (i) nanomaterials have a larger surface to volume ratio, which makes them more chemically reactive [4, 5] (ii) quantum confinement effect, which is dominant in this regime and is also responsible for several unusual properties shown by nanoparticles [6, 7].

Nanomaterials are classified into four categories by Richard W. Siegel viz zero, one, two, and three dimensional [8]. Nanoclusters, spheres are 0-dimensional structure, fiber, wire are one-dimensional nanostructure, nanoplates, film come under

two-dimensional nanostructure while faceted nanostructure comes under three-dimensional nanostructure. Nanoparticle properties are very much dependent on their shape and size [9–12]. So, tuning their shape precisely and to control their size and shape in a more controlled way is the prime interest of researchers working in this field today.

This thesis work is based on electroless galvanic displacement deposition of metallic nanoparticles (Ag, Pd) on planar and patterned semiconductor substrates (Si and Ge) and their structural evolution due to annealing at different atmospheres. The plasmonic properties of the deposited metal nanoparticles were studied experimentally using UV-vis, Raman scattering process, as well as theoretically using FDTD computer simulations. A brief description of different important factors is presented in this chapter.

1.1.1 Metallic Nanoparticles

Metal nanoparticles with nanometer dimension have attracted immense interest to the researchers due to their unique optical properties. They observed to possess very strong light scattering and absorption ability in the near infra-red and visible region of the EM spectra [13–17]. A phenomenon called LSPR is responsible for the uniqueness in the optical property of the metal nanoparticles. LSPR occurs when the incident EM radiation interacts resonantly with the oscillating conduction band electrons of the metals. During LSPR a highly intense EM field is generated around the nanoparticle and it remained confined within a sub-nanometer range called “hot spot” [18–21]. This confined field is evanescent in nature. Generation and spatial extension of the “hot spots” are totally dependent on the size, shape and interparticle distances between the nanoparticles [21–25]. It plays the most

important role to determine the SERS activity and subsequently the use of metal nanoparticles as bio-sensors. Metal nanoparticles already find their usage in energy storage, sensors, optoelectronics, and catalysis applications [26–30].

Colloidal metal nanoparticles have already shown excellent behavior as sensor and SERS active material [30–34]. However, the most significant drawback of colloidal metal nanoparticles is that it undergoes agglomeration with time which can reduce it's effectiveness drastically. Also, in such a case, as they form a cluster by agglomeration, the study of different optical properties of a single nanoparticle is very much difficult.

This thesis work is devoted to the formation of metal nanoparticles on patterned and planar semiconductor (Si and Ge) substrate and to observe the change in the nanoparticle morphology with annealing at different atmospheres. Also, how the SERS activity and electrocatalytic activity of the metal-semiconductor system varies with different factors i.e. substrate type, deposition time, and annealing temperature.

1.1.2 Galvanic Displacement Reaction

GDR is a part of the electroless reaction in which the difference between the reduction potential of two material is the sole driving force [35–38]. In this process, the metal ion which has lower oxidation potential replace the other metal which finally got dissolved into the solution.

The most important characteristics of GDR are as follows:

(i) The reaction stops when the entire surface of the substrate is covered with the metal which is to be deposited.

(ii) The reaction rate can be controlled by temperature.

(*iii*) The coating uniformity can be improved by stirring.

(*iv*) The control over the reaction rate is not much easy as the process is very fast. However, the control over particle growth can be obtained by using different molecules like CTAB for encapsulation [39].

GDR process is very much used for nanoscale patterning, dip-pen lithography on various semiconductor surfaces [40–42]. It is also used to produce hydrophobic, SERS active, anti-reflecting substrates [43–47]. The detailed about GDR is discussed in chapter 3 of this thesis.

1.1.3 Metal-Assisted Chemical Etching

MACE is mostly used to form semiconductors nanowire. As one-dimensional semiconductor nanostructures show exceptional electrical, optical, and mechanical properties, they find their applications in photovoltaics, thermoelectrics, optoelectronics and also in chemical and biological sensors [48–54]. As nanomaterial properties are very much dependent on their size and shape, a precise tuning over their morphology is very much needed. To obtain control over nanowire's growth bottom-up and top-down approaches are made. RIE process is mostly used to produce semiconductor nanowire but it damages the surface and crystal structure extensively [55, 56]. These drawbacks can be overcome efficiently using MACE process. It is also an electroless process and does not require any external bias. MACE process basically consists of two steps (*i*) deposition of metal nanoparticles on the substrate and (*ii*) etching of the substrate in the presence of HF and an oxidative agent [48]. In this process, the metal particle acts as a catalyst which finally forms a cylindrical channel through the substrate. The etching direction can

be controlled by changing different parameters like HF and an oxidative agent concentration ratio, temperature, etc [57–60]. The process is very simple and does not require any heavy instrumentation and is very much applicable for mass industrial production.

1.1.4 SPR Driven Properties of Nanomaterials

The optical behavior of metals like gold (Au), silver (Ag) and others was attracting people from the ancient ages. Though ancient people of China, Egypt, and Rome did not have the scientific idea, but they were able to prepare Au and Ag nanoparticle solutions with controllable size and composition very much successfully. These solutions were mostly used to make glass paint and luxurious crafts like the "Lycurgus Cup" (Figure 1.1). All of these were going without knowing the scientific origin. It requires centuries for the people to understand that the unique color property of strained glass is due to scattering and absorption of light while interacting with metal nanoparticles. In 1847 Micheal Faraday first made the assumption that "variation in the size of the particle gave rise to a variety of resultant colors" [61, 62]. It was Gustav Mie in 1908 who first showed the existence of plasmons with detailed experiments, and also explained it theoretically with the interaction of the incident electromagnetic wave with a metallic sphere of a given value of dielectric constant [63]. This explanation solved the century-old mystery on the unique color of strained glass. It also opened up a totally new field related to the optical properties of metal nanoparticles while interacting with EM waves. The unique optical properties are the result of the collective oscillation of electrons in the conduction band of metals and known as plasmons. Localized surface plasmons arise when surface electron vibrates resonantly about a positive

ion (lattice point) due to interaction with the alternating nature of incident EM radiation.

Figure 1.1: *The Lycurgus Cup placed in British Museum, London. Made in Rome probably in 4th century AD (a) Shows green color when lightened externally (b) shows red color when lightened internally. The Au and Ag nanoparticles embedded in the glass are responsible for such dichroic effect. (c) Strained glass window in Chartres cathedral. The different colors are due to the presence of metal oxide nanoparticles. Source: internet.*

Surface plasmons are basically of two types [64–67] :

(i) LSP or localized surface plasmons of localized nature.

(ii) SPP is of propagating in nature. The SPP propagates through the interface between metal and dielectric. Both types of surface plasmons find their

applications in sensing, medicine, SERS, and photovoltaics.

1.1.5 LSPR

As we have seen, the surface plasmons are confined to the surface of the metal nanoparticles and it depends heavily on the surface charge density [68, 69]. When the surface plasmons interact resonantly with the incident EM radiation, huge enhancement of the incident field occurs in a very small region around the nanoparticle which is called "hot spot's". These "hot spots" are very much dependent on the size, shape and interparticle distance between the nanoparticles. Hence, tuning these properties is an emerging field of nanoscience and a vast portion of the scientific community is still working on it.

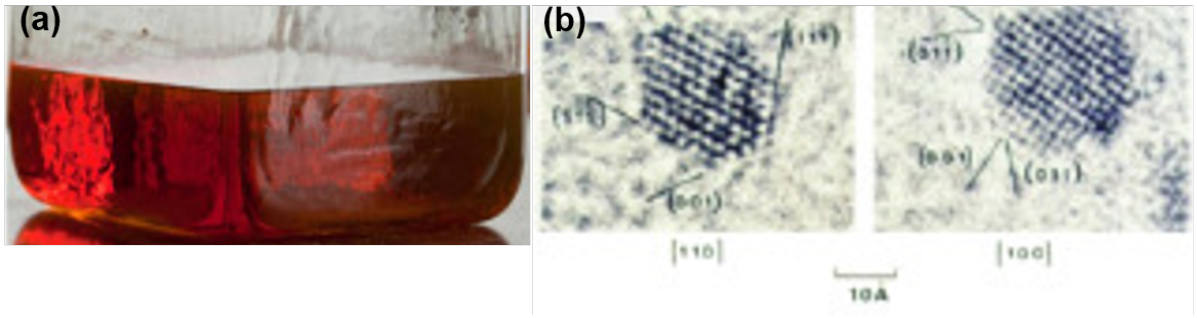

Figure 1.2: *Farady's Au colloid. (a) Farday's Au colloid solution stored in Royal Institution of Great Britain (b) High resolution TEM data of Au colloid. Source: Thomas, J. M., Midgeley, P. A. Chemical Communication (2004)*

1.1.6 Surface-Enhanced Raman Scattering

Raman spectrum gives us information about symmetry, constituent and the environment of the molecule [70–72]. It is extensively used to find out the components, molecular structure, and vibrational modes. Light of wavelength from near infrared to ultraviolet can be successfully used as an excitation source for this purpose.

However, the Raman scattering cross-section is very low which limits its application.

SERS was first discovered by Fleischmann. *et al.* through the detection of pyridine adsorbed on rough metal surface in 1974 [73]. The huge enhancement helped to detect monolayer adsorbed species on the metal surfaces. From this start, the detection of single-molecule is achieved nowadays using the SERS technique. In the last 45 years, SERS found extensive application in different research fields. The advantages of SERS techniques are as follows [74, 75]:

(i) Sensitivity down to the single-molecule level can be obtained by SERS.

(ii) Accurate information about molecular fingerprints can be obtained.

(iii) SERS is less effected by photo-degradation compared to fluorescence and hence suitable for long term monitoring.

(iv) Compared to fluorescence peak SERS peak bandwidth is 10-100 times narrower.

(v) For single wavelength excitation, multiple detections can be obtained.

(vi) Size, shape, and distribution can be tuned easily for SERS active substrate.

1.1.6.1 Electro-Magnetic Enhancement

EM enhancement occurs when the surface conduction electrons interact resonantly with the incident electric field producing a very high local electric field around the nanostructure. The locally enhanced electric field amplitude $E(\omega)$ at frequency ω is generally computed using computational electrodynamic simulation and it is calculated at the position of the molecule. The electromagnetic enhancement is normally taken as $\frac{|E(\omega)|^4}{|E_0|^4}$ over the position of the molecules, where E_0 is the amplitude of the incident electric field. However, this simple expression neglects the

Stoke's shift and if we include it the modified expression will become $\frac{|E(\omega)|^2|E(\omega')|^2}{|E_0|^4}$ where ω' is the Raman frequency. Sometimes ω' is assigned to the frequency (or wavelength) of the dipolar re-radiation. In addition to that, the strong spatial localization of the plasmon field produces a field gradient affecting the SERS signal. However, this can only be calculated if the particle morphology is known exactly. The $\mid E(\omega) \mid^4$ approximation is observed to give the electromagnetic enhancement factor accurate by an order of magnitude [76].

In the case of SERS substrate having a large area, it is observed that the structures which give significant EF at single-particle level (i.e. Au nanostars) does not give an improved EF when they are organized in an ensemble on the substrate. The contrary is observed for a simple Au nanosphere which is contributed by higher surface coverage of Au spheres [77].

1.1.6.2 Chemical Enhancement Mechanism

Unlike EM enhancement CE occurs due to electron transfer between the nanoparticle and the absorbed molecule. The electron transfer can occur to the excited and ground state of the molecule-metal system. The enhancement in this can be obtained by calculating the change in polarizability derivative of the molecule-metal system using electronic structure calculation. The result produced by this calculation is independent of frequency. Valley *et al.* uses this theory and predicted the contribution by an order of two for gold and silver nanoparticle deposited substrates using different substituted benzene thiolates [78]. The enhancement factor obtained by them is different which is contributed by the CE process as the substrates are the same for all the cases.

1.1.6.3 Dependence on The Gap

The strength of hot spots also depends vastly on the nanoparticle junctions, the gap between two nanoparticles, and different other geometrical details. The intensity of the hot spots is observed to be inversely dependent between the distance of the nanoparticles. Classical electromaganetism can be applied for hot spots of size between $2 - 10\ nm$ by neglecting the non-local effect and by considering only the frequency-dependent dielectric property of the material. For a distance of less than $1\ nm$ non-local effects appear which makes the optical response non-linear and a more sophisticated approach is needed to treat such special circumstances efficiently [77, 79].

1.1.7 Substrate Supported Nanoparticles

Though colloidal nanoparticles show very good SERS enhancement down to single-molecule level. They have problems regarding agglomeration which reduces their efficiency for the long term. Noble/metal-semiconductor composite has its own advantages over metal nanoparticles. As semiconductor substrates act as support to hold the metal nanoparticles, this reduces agglomeration and makes the substrate suitable for SERS measurement over a long period [80]. We have shown in this thesis work the advantage of a substrate supported nanoparticles for SERS measurement.

1.1.8 Advantages of 3D Substrate

3D SERS substrates are observed to show higher SERS enhancement compared to their 2D counterparts. One of the reasons for this is that the 3D substrate possesses a larger surface area which produces more “hot spots” and can absorb

more absorbate molecules [81]. Lee *et al.* has observed that the SERS signal enhancement measured at the 3D plasmonic nanostructure was 3.9 times the signal measured at 2D plasmonic nanostructure [82].

In recent years, 3D SERS substrates have been observed to show very good sensitivity, easy tailoring, and higher stability. 3D SERS substrate can be obtained via different processes like MACE, anisotropic etching, RIE and, LIE process [83–88]. Out of these processes, RIE and LIE are of very high cost. On the other hand, chemical etching and MACE are of the very low-cost, able to give high throughput and higher uniformity. In this thesis work, we use anisotropic etching and GDR process to deposit metal nanoparticles on 3D Si to obtain effective and sustainable SERS active substrate.

1.1.9 Advantages of Ag and Pd nanoparticles

Au and Ag are two mostly used metal for plasmonic applications due to their easy tunability of shape and size [89]. Ag nanoparticle shows the lowest resonance loss at optical frequencies. Also, it is used as an anti-reflecting coating for the solar cell as its ability to trap the solar light is best among the metals. However, Ag nanoparticle is very much prone to rapid oxidation when kept at ambient atmosphere [24, 90]. Au nanoparticle, on the other hand, is very much stable against oxidation. Ag also shows very good microbial activity as it forms disulfide bonds, which modifies the protein structure in enzymes and finally leads to the death of microbes. This activity also depends on the shape and size of the nanoparticles [91–93]. In this thesis work, we will show that the SERS effect of Ag nanoparticles can be improved significantly by proper treatment in O_2 atmosphere.

Platinum (Pd) and palladium (Pd) both show very good catalytic properties

and they are already significantly used in fuel cells, hydrogen generation and chemical sensors [94–96]. The applicability of these two materials motivates researchers to use them as SERS active substrate. However, the SERS EF obtained from these two metals were not very encouraging. Srnova *et al.* first studied the SERS with Pd and obtained EF of 190 [118]. Pd deposited by electro-deposition process showed EF of 10^3 [119]. Different other morphologies like hexagon, cubes were tried to finally obtain EF of 10^4 [119]. The SERS effect of Pd was observed to be dependent vastly on the size of the Pd nanoparticles. A decrement in the SERS signal with increasing Pd shell thickness was observed by Fang *et al.* [179]. However, Pd nanoparticles deposited by GDR process, were observed to show very good stability against oxidation as observed by Gutes *et al.* [80]. Ag showed superior SERS enhancement compared to Au but has problem regarding oxidation, Pd can be an effective replacement for that if its EF can be increased by some way. This fact motivated us to use Pd nanoparticles deposited by GDR method for SERS application. Ringe *et al.* found that Pd rich tips can sustain strong and narrow LSPR which can be coupled strongly with the dielectric substrate underneath to produce a very good SERS substrate [180]. Various applications need strong adhesion of particles with the substrate to avoid coagulation, which can lead to undesirable results. EF of 10^3 was obtained by Xu *et al.* using Pd nanoparticles deposited on ITO substrate by electrodeposition process [183]. Previously various surfactants like CTAB and PVP were used to control the morphology of Pd nanoparticles when deposited on various substrates [119]. So it is almost impossible to separate these surfactants which effect the SERS activity.

In this thesis, we have shown that the morphology of the Pd nanoparticles deposited on the semiconductor substrate can be controlled by changing substrates and changing the deposition time. This effects the SERS and catalytic activity of the substrates vastly. The morphology of the nanoparticles was studied extensively using SEM and XTEM. The substrates prepared in this process showing good SERS enhancement and also catalytic activity. The SERS experimental results were explained theoretically using the FDTD method.

1.1.10 Recent Progress on Ag Deposited SERS Substrates

Due to better scattering efficiency, SERS substrates prepared by Ag shows better enhancement than Au [89]. However, the disadvantages of substrates prepared by Ag is the fact that the Ag structure easily gets deteriorated due to oxidation when they are subjected to prolonged exposure to atmosphere [90]. Also, high-temperature treatment reduces the SERS effectiveness of the substrates which is driven by rapid oxidation and agglomeration of the Ag nanoparticles [117]. Pinkhasova *et al.* reported that heating Ag nanoparticles at 300^o C reduce the SERS efficiency due to the formation of silver oxide. However, with increasing the heating temperature to 400^o C the partial reduction of silver oxide leads to increment in the SERS efficiency but it cannot be 100% recovered [157].

In this thesis work, we have shown that RTA of Ag nanoparticle deposited on Si substrate at O_2 environment leads to increment in the SERS enhancement.

1.1.11 Recent Progress on 3D Si SERS Substrate

One-dimensional semiconductor nanostructures are getting immense attention nowadays due to their outstanding electronic and optical properties. Due to their compatibility in semiconductor industry, research on Si nanowire is increasing rapidly over the past decade. They are also used to produce biosensors, thermo-electric battery and different electrodes [123–125]. Laser ablation, MACE, VLS, MBE techniques are used to produce Si nanowires [126–129, 165]. Between these processes, MACE is a very low-cost, less complicated and easy process. In MACE, the reduction of the oxidative agent took place on the metal particle surface which acts as a cathode. The Si substrate underneath the metal particle acts as an anode to produce SiO_2 which gets dissolved into the solution in the presence of HF producing Si nanowire [165]. Li *et al.* were the first to produce porous Si by etching in HF/H_2O_2 [128]. After that, the effect of different parameters like effect of different metal nanoparticles (Au, Ag, Pt, Pd and Cu), HF/H_2O_2 ratio and concentration of doping was studied vastly by different research groups [129, 166]. Si nanowires also find their applications in SERS detection and in catalysis extensively [167–170]. Si-nanowire acts as very good support to hold the metal nanoparticles which can give significant SERS enhancement. Metal nanoparticle decorated Si-nanowires were previously made by CVD, VLS process or by a mixed process of CVD and GDR. CVD is a very sophisticated technique and requires heavy instrumentation. GDR, on the other hand, is a very simple, low-cost and easy process. Controlling different parameters like diameter, density, orientation, porosity of Si-nanowire is very much easy with this process [171]. Also, it is very much clean as no external reducing agents are used.

Here, we have investigated the formation of Si-nanowire on both pyramidal Si and planar Si. We have observed Si-nanowire with zig-zag and crystalline sidewall on P-Si, and amorphous but smooth sidewall on planar Si (100).In the case of planar Si, the etching occurs along (100) direction while on pyramidal Si it is along [311] direction on P-Si. We also produced spherical shaped Ag particle decorated Si-nanowire using GDR and RTA process which is SERS active and hydrophobic

1.1.12 Epitaxy and Endotaxy

Epitaxy indicates the growth of a crystalline film on a substrate where the overlayer is in registry with the substrate. Two kinds of epitaxy are mostly observed (*i*) Homoepitaxy, where the substrate and the overlayer both are of the same material. (*ii*) Heteroepitaxy, where both layers are of different materials. In the silicon industry, heteroepitaxy is the most used process. Depending on the interface energies, strain generation at the interface due to lattice mismatch, different growth mode occurs. The three most observed growth processes are (*i*) Layer by layer growth mode or FM growth process (Figure 1.3a) (*ii*) Island growth or VW growth process (Figure 1.3b) and (*iii*) Layer plus island or SK growth mode (Figure 1.3c) [97–99]. In general, hetero-epitaxial growth under the lattice strain introduces many defects at the interface. However, it also produces tilted hetero-epitaxy where lattice strain at the interface is minimized through the introduction of a tilt angle.

Endotaxy is a different kind of epitaxy where the growth of crystalline structure occurs within the substrate. It indicates precipitation of coherent phase in the bulk matrix where the bulk matrix produces a coherent interface around the precipitate

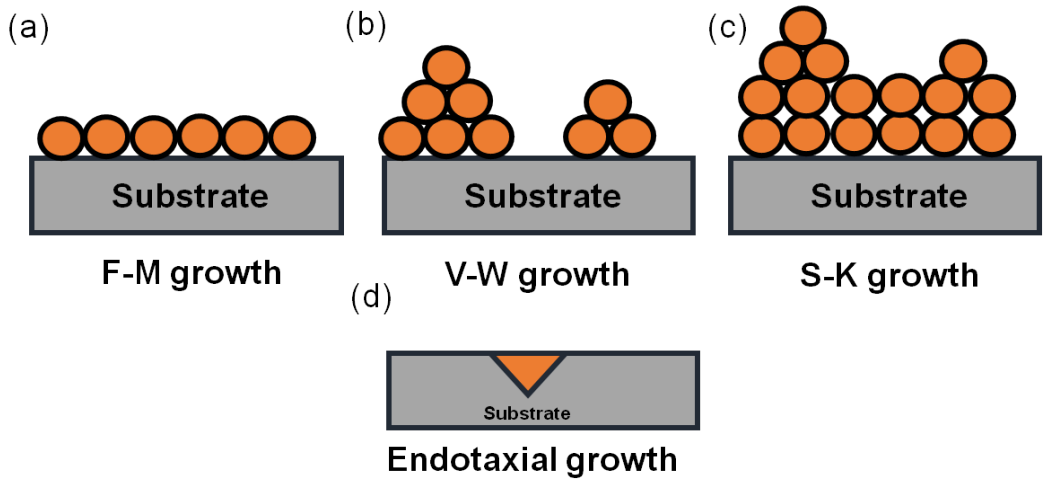

Figure 1.3: *Different growth mechanisms (a) F-M growth (b) V-W growth (c) S-K growth and (d) Endotaxial growth*

phase (Figure 1.3d)[100]. By using different processes like MBE [101], ALD epitaxial or endotaxial structure can be obtained [102]. Endotaxial structure of different metals like Pt, Co, Ni, Fe, Ti [103–106] can be formed by the MBE process, which is of very high cost and robust. Previously, endotaxial Ag on Si is reported by Juluri *et al.* by MBE process [105]. So, In general, sophisticated physical vapor deposition techniques, like MBE in UHV or ion implantation followed by high-temperature annealing are used to grow endotaxial structures of Ag[105, 131–133]. However, all of these are challenging, expensive, and time-consuming. Among these processes, GDR is a very low-cost process, and it also produces a very clean interface due to the absence of any external reducing agent. In GDR, the difference in electrostatic potential between the substrate and the metal to be deposited is the driving force behind the deposition [135]. Metal ions are reduced with electrons supplied by virtue of Si half-cell reaction. The electrostatic potential of Ag is 0.8 V whereas for Si it is -0.875 V w.r.t SHE which indicates a smooth deposition of

Ag on Si in this process. Ag nanoparticles embedded in a semiconductor substrate are found to increase absorption. It also shows the SERS effect due to their strong near-field coupling effect [105, 134].

In this thesis, we have shown that endotaxial Ag nanoparticles and spherical Ag nanoparticles composite formed on planar Si(1 0 0) surface when annealed at O_2 atmosphere. The substrate hence produced can serve as a good substrate for SERS. We have chosen this system because the oxide growth rate in Ag-Si(1 0 0) system is prolonged compared to Au-Si(1 0 0) and Ag-Si interface is less reactive compared to Au-Si. At room temperature, Si atoms can out-diffuse through several angstrom thick Au layer. This diffusion process results in broken Si-Si bonds which makes the system more reactive and prone to oxidation. Ag is observed to form an abrupt metal/semiconductor junction, and the rate of growth of the oxidized layer is slow for an Ag-Si system. The formation of endotaxial Ag nanoparticle is observed to be dependent on the deposition time, annealing atmosphere, and the nature of the substrate.

1.1.13 Annealing Induced Structural Variations of Nanoparticles

Annealing of nanoparticles is an essential part of nanotechnology. Through annealing of nanoparticles, their size, shape, inter-particle distances, particle density can be modified according to our requirement. Thermal annealing can also improve the adhesion between the substrates and the nanoparticles and decomposes the residual oxide at the higher temperatures. Special structural arrangement can also be generated if the proper condition is applied. OR is the most common process to observe during annealing [107]. Wilhelm Ostwald in 1896 introduced OR

and showed that the process was driven by surface energy minimization [108]. In the OR process smaller particle is dissolved due to their high surface energy and creates a larger particle of spherical shape to minimize the surface energy (Figure 1.4). This process is mostly observed for nanoparticles synthesized in colloidal form but can also occur for substrate supported nanoparticles. Surface diffusion, vapor phase diffusion and diffusion through the substrate are the different mechanism by which particles grow in size.

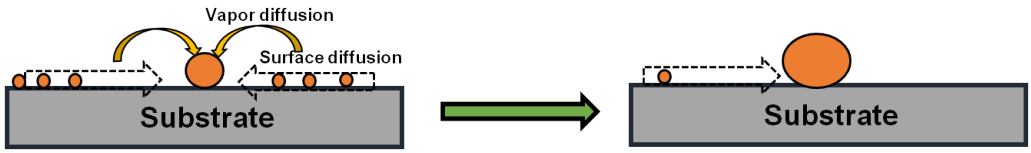

Figure 1.4: *Thermal diffusion of nanoparticles*

The radius of a particle and it's chemical potential is related by the Gibb's Thomson equation which is [109]

$$\mu = \mu_0 + \frac{2\gamma V}{r} \tag{1.1}$$

where μ_0 is the chemical potential of a particle with a radius equal to infinity, γ is the amount of work needed to create unit surface, V is atomic volume and r is the radius of the nanoparticles. So from this relationship, we can clearly observe that the smaller particles have higher chemical potential and hence, they will dissolve and diffuse to the bigger nanoparticle to reduce its chemical potential. In this thesis work the effect of annealing on metal nanoparticles deposited on the planar and patterned substrate is discussed in detail.

1.1.14 Finite-Difference Time-Domain Simulation

FDTD simulation is one of the most important tools to study the optical properties i.e. near field intensity distribution, absorption, scattering, etc for nanostructures of different materials. K. Yee first introduced the concept of FDTD simulation in the early 70s. In FDTD simulation two segments are used i.e. space and time. Cells of size smaller than the wavelength consists of the space part. "Leap frog" algorithm is used to solve Maxwell's equation for each cell to evaluate all $\overrightarrow{H}$ and $\overrightarrow{E}$ field values. The Yee scheme of FDTD is shown in Figure 1.5, which consists of a cubic volume element of total volume δ and a side length of δx, δy, and δz for space discretization. The electric and magnetic field components are arranged at half increment in space and time (the step size for time discretization is δt).
Now from Maxwell's equation

$$\frac{\partial \overrightarrow{E}}{\partial t} = \frac{\overrightarrow{\nabla} \times \overrightarrow{H} - \overrightarrow{J}}{\epsilon} \tag{1.2}$$

$$\frac{\partial \overrightarrow{H}}{\partial t} = \frac{\overrightarrow{\nabla} \times \overrightarrow{E} - \overrightarrow{M}}{\mu} \tag{1.3}$$

where the permittivity and permeability of the medium are denoted by ϵ and respectively. The electric current density $\overrightarrow{J}$ is given by,

$$\overrightarrow{J} = \overrightarrow{J}_{source} + \sigma \overrightarrow{E} \tag{1.4}$$

and magnetic current density can be written as,

$$\overrightarrow{M} = \overrightarrow{M}_{source} + \sigma \overrightarrow{H} \tag{1.5}$$

from equation 1.2, 1.3, 1.4, and 1.5 one can get the vector component of the electric and magnetic field which is considered to be the heart of FDTD simulation. As

an example, the x-component of $\overrightarrow{E}$ can be written as,

$$\frac{\partial E_x}{\partial t} = \frac{1}{\epsilon}[\frac{\partial H_x}{\partial y} - \frac{\partial H_y}{\partial z} - J_{sourcex} + \sigma E_x] \tag{1.6}$$

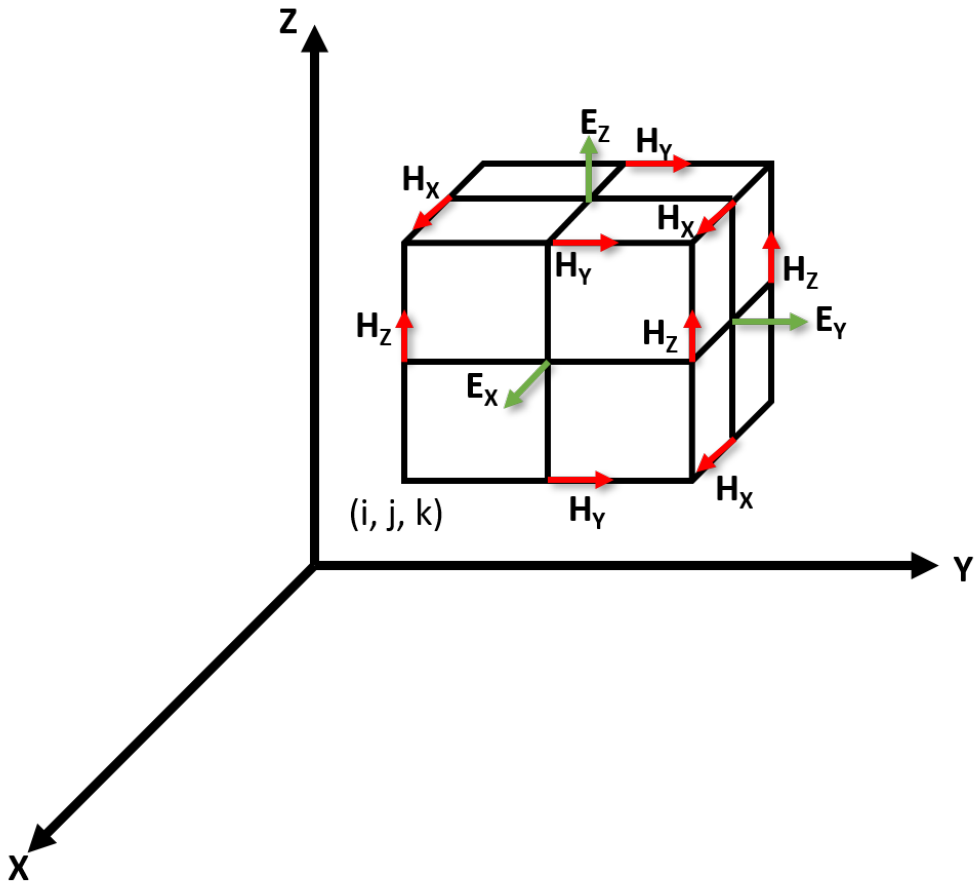

Figure 1.5: *Components of different electric and magnetic field vectors within Yee's grid.*

A finite-difference equation in discrete form can be obtained from Maxwell's equation using Yee's definition of the rectangular coordinate system. According to that the component of E_x at time step $(n + \frac{1}{2})$ at one space point of the lattice $(i, j + \frac{1}{2}, k + \frac{1}{2})$ which indicates the spatial location $(i \triangle x, j \triangle y, k \triangle z)$ is given as,

$$\frac{E_x\mid_{i,j+\frac{1}{2},k+\frac{1}{2}}^{n+\frac{1}{2}} - E_x\mid_{i,j+\frac{1}{2},k+\frac{1}{2}}^{n-\frac{1}{2}}}{\triangle t} = \frac{1}{\epsilon_{i,j+\frac{1}{2},k+\frac{1}{2}}}$$
$$[\frac{H_z\mid_{i,j+1,k+\frac{1}{2}}^{n} - H_z\mid_{i,j,k+\frac{1}{2}}^{n}}{\triangle y} - \frac{H_y\mid_{i,j+\frac{1}{2},k+1}^{n} - H_y\mid_{i,j+\frac{1}{2},k}^{n}}{\triangle z}$$
$$- J_Source_x\mid_{i,j+\frac{1}{2},k+\frac{1}{2}}^{n} - \sigma\mid_{i,j+\frac{1}{2},k+\frac{1}{2}} E_x\mid_{i,j+\frac{1}{2},k+\frac{1}{2}}^{n}] \quad (1.7)$$

as the coefficients are fixed throughout the simulation they can be pre-calculated:

$$E_x\mid_{i,j+\frac{1}{2},k+\frac{1}{2}}^{n+\frac{1}{2}} = (K_a(m))E_x\mid_{i,j+\frac{1}{2},k+\frac{1}{2}}^{n-\frac{1}{2}}$$
$$+ (K_b(m))[H_z\mid_{i,j+1,k+\frac{1}{2}}^{n} - H_z\mid_{i,j,k+\frac{1}{2}}^{n} + H_y\mid_{i,j+\frac{1}{2},k}^{n} - H_y\mid_{i,j+\frac{1}{2},k+1}^{n}$$
$$- J_{Sx}\mid_{i,j+\frac{1}{2},k+\frac{1}{2}}^{n} \triangle] \quad (1.8)$$

where $(K_a(m))$ and $(K_b(m))$ are constants depending on the medium. The detailed can be found in ref [110]. So, from the equations shown above it can be inferred that every component of the electric field at a particular space point in time can be obtained from its value at the same point in previous time step, the neighboring magnetic field, and from material properties. The field components are calculated at each space point, for a particular time from the stored data and the process continues. To record the field component at each space point for analysis a "monitor" is placed in the simulation mesh.

The data for E and H with each frequency for a cell can be obtained by doing discrete Fourier transformation of the time data store at the end of the simulation. To take care of the fact that there is no huge variation of filed components between two adjacent cells the cell dimension must be smaller than the illumination wavelength, which is obtained from the Courant equation,

$$S = \frac{c \triangle t}{\triangle} \quad (1.9)$$

where S is the Courant number which must be $\leqslant \frac{1}{\sqrt{no.of dimensions}}$ for stability of the simulation. For 3D simulation, it must be $\leqslant \frac{1}{\sqrt{3}}$. During the practical simulation the sufficient resolution to the desired geometrical structure is provided by defining a proper cell size $\triangle$, which is given by,

$$\triangle = \frac{\lambda_{min}}{10 n_{max}} \tag{1.10}$$

from which $\triangle t$ can be obtained using the previous equation.

To find out the E-field intensity distribution and enhancement factor a commercial FDTD simulation package (Lumerical Inc, Canada) was used in this thesis work. The details can be found in the website (https://www.lumerical.com/products/fdtd/).

1.2 Outline of The Thesis

This thesis work is organized as follows: With this introduction in **Chapter 1** in **Chapter 2** a detailed illustration of various experimental techniques like TEM, SEM, XRD, Raman spectroscopy, and XTEM sample preparation is presented. In **Chapter 3** a basic introduction on GDR, application of GDR on Si, Ge substrates, and MACE process is discussed. **Chapter 4** deals with the growth of Ag on planar Si substrate and pyramidal Si substrate and how the Ag film morphology changes with annealing in different atmospheres. Formation of Si-NW on planar and pyramidal Si is also discussed in detail. Finally, deposition of Pd nanoparticle on various planar and patterned semiconductor substrate is discussed in detail in the chapter. **Chapter 5** deals with the SERS activity of the different metal nanoparicles deposited on semiconductor substrates in detial and it also, shows the theoretical reason behind the enhancement by using FDTD ssimulation. **Chapter**

6 The electrocatalytic activity of Pd deposited on planar and patterned semiconductor substrate is discussed in detail. It also, shows that the substrates can be used as an effective electrochemical glucose and AA sensor.Finally, in **Chapter 7** we have discussed the summary and conclusions from this thesis work.

Chapter 2

Experimental methods

This chapter describes in detail about transmission electron microscopy (TEM), its different operational procedure, components , cross-sectional sample preparation for TEM and also basic operation of CL-SEM, RAMAN, Electrochemical workstation, UV-Vis spectrometer and XRD

2.1 Introduction

Different kinds of noble metal-nanoparticles were deposited by electroless deposition method on planar and patterned semiconductor substrates. In this chapter, the growth method is discussed in detail. To study the evolution of the nanoparticles deposited on different semiconductor substrates (planar and patterned), various experimental techniques were used. TEM technique is the heart of this thesis work. Through HRTEM process and other associated techniques like SAD, HAADF-STEM images, and EDX the crystalline structure of the nanoparticles, their interfaces, morphology, and chemistry were studied extensively. The crystallinity of the structures was also studied using XRD technique. The overall morphology of different nanostructures was also studied using SEM. The optical properties of the nanoparticles were studied using CL spectroscopy, UV-vis spectroscopy, and Raman spectroscopy.

2.2 Synthesis of Different Metal Nanostructures on Semiconductor Substrates

2.2.1 Synthesis of Ag on Planar Si and Formation of Endotaxial Ag

Si(1 0 0) [p-type] substrates were first ultrasonicated in ethanol, acetone, and DI water for 5 *minutes* to remove the organic contaminations. The substrates were then cleaned by RCA method to finally form a native oxide layer on the Si substrate. After cleaning, the substrates were rinsed in ethanol and de-ionized water and stored in a vacuum desiccator until further use. GDR process was used to deposit Ag nanoparticles on patterned Si. In this process, the substrates were

immersed in 2% HF solution for 1 *minute* to remove the native oxide layer. The substrates were then immediately transferred into a solution consists of $AgNO_3$ (5 mL, 5 mM) and HF (5 mL, 4.8 M).Ag was deposited by the previously mentioned GDR process for 1 *minute* and 3 *minutes*, respectively. The as-deposited substrates were then subjected to RTA at 550^o C in O_2 and N_2 atmosphere, respectively with a heating and cooling ramp of 10^o C per second. No intermixing between Ag and Si is observed at this temperature as the annealing temperature was much below the eutectic temperature (836^o C) of Ag-Si system [136]. Henceforth, notation S1 and S2 will be used for Ag deposited on Si substrate for 1 *minute* and annealed at O_2 atmosphere for 1 *minute* and for Ag deposited on Si substrate for 3 *minutes* and annealed at O_2 atmosphere for 1 *minute*, respectively. Notation $S3$ will be used for Ag deposited on Si substrate for 3 *minutes* and annealed at N_2 atmosphere for 1 *minute*. The substrates were washed using ethanol and de-ionized water and kept in the vacuum desiccator.

2.2.2 Ag Deposition on Pyramdial Si and Formation of Coupled Ag Nanostructure

Initially, Si substrates were ultrasonicated in acetone, ethanol, and de-ionized water for 5 minutes to remove any organic contamination. The substrates were then subjected to SDR method [158]. Where the substrates are initially dipped into a solution consisting of $30wt\%$ NaOH in de-ionized water at 75^oC for 3 *minutes* to remove few μm thick layers from both sides. In the second step, the substrates were dipped into a solution of $2wt\%$ NaOH and 10% IPA for 45 *minutes* to finally obtain pyramidal Si substrate. The substrates were washed using ethanol and de-ionized water and kept in vacuum desiccator. The GDR depositions were carried

out for different times (10 s, 30 s, 60 s and 90 s) to obtain uniform coverage of Ag nanoparticles. The substrates were then subjected to RTA (JETFIRST, jipelec) at 550^o C for 1 *minute* in N_2 and O_2 atmosphere respectively. The ramp rate was set as 10^o C per second. We will use notation $S1$ to indicate Ag deposited on Si (P-Si/Ag), S2 to indicate N_2 annealed P-Si/Ag (for 1 minute), S3 to indicate O_2 annealed P-Si/Ag (for 1 minute).

2.2.3 Production of Si-Nanowire on Pyramidal Si and GDR of Ag

Si pyramids were formed using SDR method, the detailed of this method is described before. To produce Si-nanowire array Si substrates were first subjected to RCA cleaning to finally produce a layer of SiO_2 on the substrate. Ag was deposited by the previously described GDR process to obtain a uniform coverage on the substrates. The substrates were rinsed by ethanol and DI water respectively to ensure that no loosely bound particles remain and then dried. Si-nanowires were produced by the MACE process in which the substrates were immersed in a solution of HF (4.8 M) and H_2O_2 (0.5 M) for 30 *minutes*. The governing equation for the process can be written as [111],

$$H_2O_2 + 2H^+ = 2H_2O + 2h^+ \tag{2.1}$$

$$Si + 4HF_2^- + 2h^+ = SiF_6^{2-} + 4HF + H_2(g) \tag{2.2}$$

Metal particles deposited at the substrate act as the cathode in this process.
The Schematic diagram of GDR and MACE process is shown in Figure 2.1a and Figure 2.1b, respectively. By immersing the substrates in concentrated HNO_3 solution the Ag nanoparticles accumulating at the base region of Si-nanowire were

removed. Ag nanoparticles were re-deposited on Si-nanowire by GDR method and then the substrates were subjected to RTA at 550^o C at O_2 and N_2 atmosphere respectively to produce nanoparticle decorated Si-nanowire.

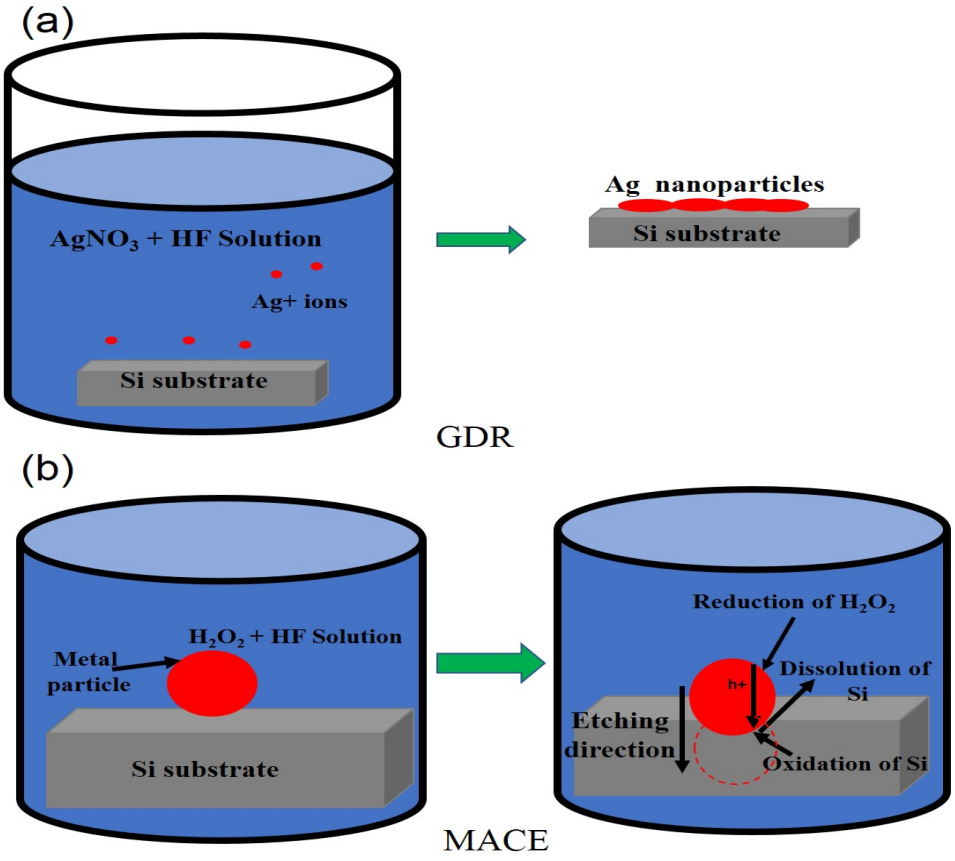

Figure 2.1: *(a) Schematic of GDR. (b) Schematic of MACE process.*

2.2.4 Electroless Deposition Process of Pd

Electroless deposition of Pd was carried out on p-type Si(100) and on Ge(100) substrate. Both the substrates were cleaned by ultrasonication in ethanol, acetone and de-ionized water to remove any organic contamination. P-Si substrates were produced using previously mentioned SDR method. To deposit Pd on P-Si and

on planar Si, the substrates were immersed in a solution of 2% HF for 1 *minute* to remove the native oxide layer. Next, they were immediately transferred to a solution consisting of $PdCl_2$, HF and KCl mixed in such a way to obtain Pd^{2+} concentration of 0.15 M and F^- concentration of 20 mM. KCl was required to produce sufficient $PdCl_4^{2-}$ ion. However, planar Ge substrates were directly inserted into the plating solution after ultrasonic cleaning. The substrates were immersed for different times to observe the effect of deposition time on morphology. So, we will use different notations to indicate different substrates. Pd deposited for 10, 20 and 60 *minutes* on planar Ge(100) substrate will be indicated as G10, G20, and G60 respectively. Similarly, Pd deposited for 10, 20 and 60 *minutes* on planar Si(100) substrate will be called S10, S20, and S60, respectively, Pd deposited for 10, 20 and 60 minutes on pyramidal Si(100) substrate will be called PS10, PS20, and PS60, respectively.

2.3 Characterization and Application Techniques

2.3.1 Transmission Electron Microscopy (TEM)

Louis de Broglie first introduced the wave nature of electron in 1925 having wavelength very much lower than the visible light. Then in the year 1927, Davisson and Germer first demonstrated the diffraction phenomenon of electrons which confirms the claim made by de Broglie. In 1932, Knoll and Ruska first developed the electron microscope consisting of electron lenses, which gives Ruska the Noble prize in the year 1986, just two years before his death in 1988. Ruska's idea helped to build the first commercial TEM in UK in the year 1936. However, the regular production of TEMs was started by Siemen and Halske in Germany from 1939.

From that time, various companies dedicate themselves towards the development and production of sophisticated TEMs worldwide (i.e. Hitachi, JEOL, Philips etc).

2.3.1.1 Light Microscopy

The smallest distance which can be resolved using the light microscope is about $0.1 - 0.2\ mm$, in presence of sufficient illumination by visible light. The smallest distance which can be resolved clearly is called as resolving power of a microscope. According to Rayleigh criterion of resolution it can be written as,

$$\delta = \frac{0.61\lambda}{\mu \sin \beta} \tag{2.3}$$

where λ is the incident radiation wavelength, μ is the viewing medium refractive index and β is the half-angle of the cone of light entering the lens. The quantity $\mu \sin \beta$ is called N.A of the microscope. Considering N.A to be unity, resolution becomes almost half of the incident radiation wavelength. If we consider the average of the visible light wavelength as 550 nm, the resolution of a very good light microscope is 330 nm. This separation corresponds to 1000 atom diameter and it is well above the nanoscale regime. So, for observation of smaller objects microscope with resolving power much smaller than this is required, which can be achieved using TEM.

In 1925, Louis de Broglie shows the relationship between the wavelength of electrons and their energy, which can be written as

$$\lambda = \frac{1.22}{\sqrt{E}} \tag{2.4}$$

where E is the energy of the electron in eV. So, from the above equation, we can see that the wavelength of electrons having energy 200 keV is 2.8 $picometer$, which is very much smaller than the size of an atom.

2.3.1.2 Interaction of Electrons With Matter

An electron is a kind of ionizing radiation. It's interaction with specimen results in different kinds of signals, every signal has their own different origin and can be used to extract different kinds of information which are used in AEM. The different signals which are used in AEM are (*i*) X-ray (*ii*) Elastically and inelastically scattered electrons (Figure 2.2).

SE and BSE are used in the SEM to obtain topographic and elemental information about the specimen.

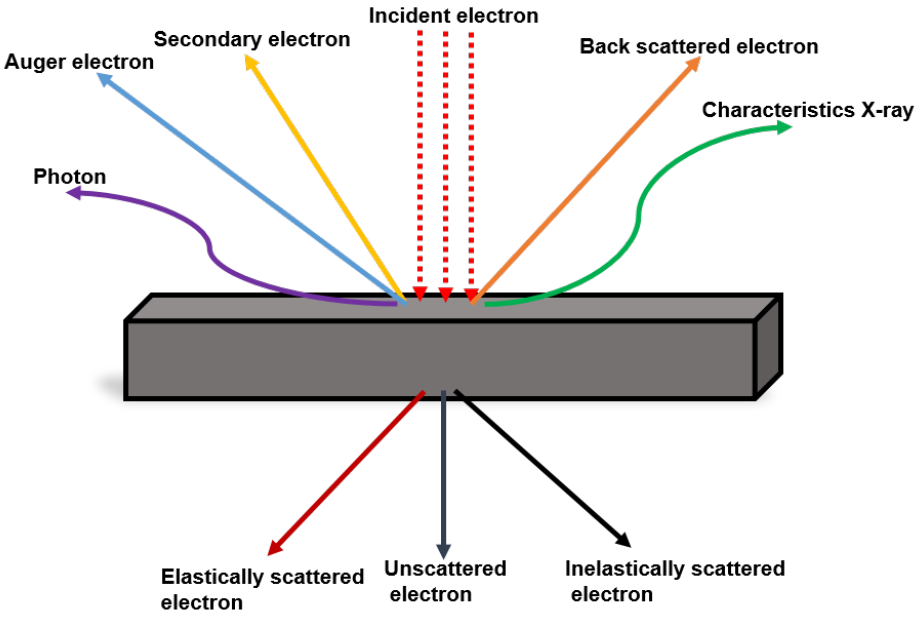

Figure 2.2: *Schematic representation of generation of various signals due to interaction of highly energetic electrons with a thin specimen.*

(*i*) **X-ray:** X-rays are the most important signal which gives the chemical information on the nanometer scale. This also helps to find out the atomic ratio of the constituents elements and also the spatial information. X-rays are generally of two types **Characteristic X-rays and Bremsstrahlung radiation:** When

the incident high energy electrons interact with the electrons in the inner shell and transfer more than the ionization energy corresponds to a particular shell, the electron in the inner shell escape to the Fermi level and the shell becomes vacant which leads the atom into an excited state. To minimize the energy, electrons from outer shell jumps to the inner shell and either emits X-ray or Auger electrons. The energy of the emitted X-ray is dependent on the atomic number of the elements and hence specific for specific material and is called Characteristic X-rays."Bremsstrahlung" is a German word and means "breaking radiation". It produces a continuous background in the X-ray region and originated from decelerated electrons. While most of the electron microscope is equipped with an EDX detector, the Auger electron detection is carried out in specially configured TEM. **Secondary electrons:** It is the result of inelastic interactions between the incident electrons and the outer shell electrons of the atoms. These electrons emit only from the surface of the sample and give the topographic information and are used in scanning electron microscopy. **Backscattered Electrons:** BSE are generated due to elastic collision between the incident electrons with the atoms. The signal comes from a deeper portion of the sample and shows high sensitivity to the difference in atomic numbers. This is also vastly used in SEM to spatially differentiate between various elements. **Energy loss electrons:** When electrons interact with a specimen it can lose energy through various processes. These processes produce energy loss electrons (inelastic electrons) which carry more information compared to X-ray. These inelastically scattered electrons carry information about the electronic structure of the atoms of the specimen from which valance state, bonding, bandgap, and specimen thickness can be measured very much accurately.

2.3.2 Different Components of TEM

TEM is a very complicated instrument. The general parts of a TEM consist of three components

(*i*) The illumination system

(*ii*) Specimen stage

(*iii*) Projection system

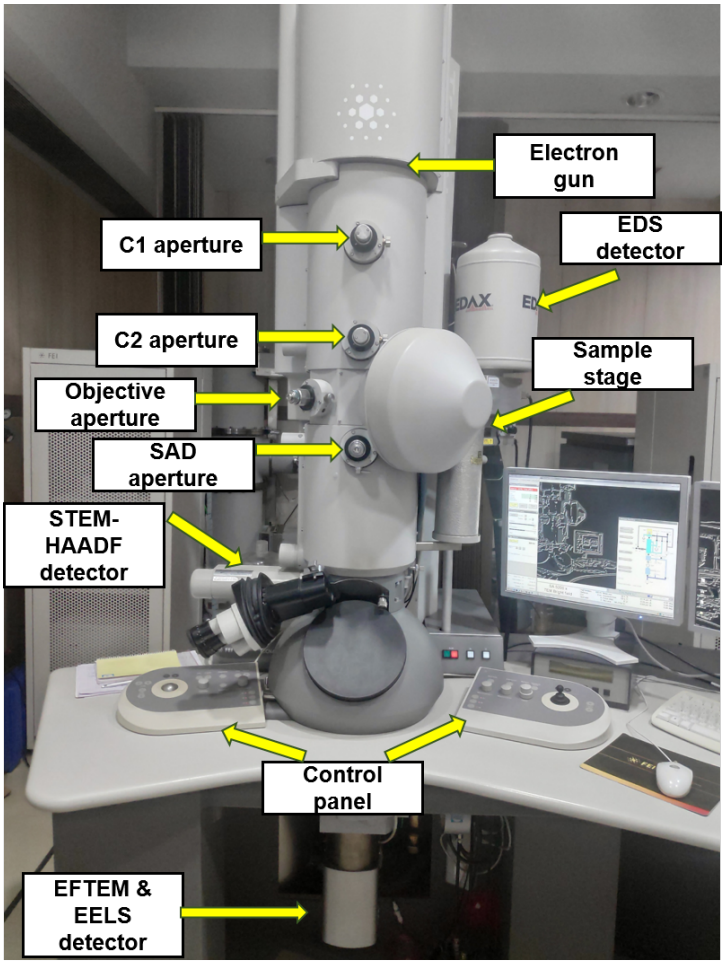

Figure 2.3: *300 keV FEI TECNAI G20 Twin Microscope facility at SINP, Kolkata.*

2.3.2.1 The Illumination System

The illumination system and its controlling unit is the heart of TEM. The major parts of the illumination system are consists of

(i) Electron source or filament

(ii) High voltage system

(iii) Condenser lens

(iv) Objective lens

2.3.2.2 Electron Source or Filament

Two kinds of electron sources are used mostly in TEM. One is the thermionic source which when heated produces electrons and the other is the field emission source which produces electrons on the application of an electric field between the tip and the anode. Schottky field emission gun is a combination of thermionic emission and field emission gun and is also widely used as an electron emission source.

In the thermionic gun, the electrons are needed to supply sufficient thermal energy so that they overcome the barrier and leak out from the surface. This barrier is known as work function. The emission current density depends on the temperature and their relation obeys Richardson-Dushman equation

$$J = AT^2 e(-\phi/kT) \tag{2.5}$$

where A is a constant and is different for different materials, k is Boltzmann constant ($8.5 \times 10^{-5}\ eV/k$). So, from the equation, we can see that higher temperature is required for metals with higher work function. However, a few eV of thermal energy is sufficient to melt most of the metals. Hence, previously TEM's

were made of tungsten filament because of its high melting point (3660 K) and LaB_6 crystal is mostly used as the thermionic source because of its low work function.

FEG's are called cold guns as no thermal heating is required. The strength of the electric-field increases significantly at sharp points, which is the principle behind FEG. If V be the applied voltage and r is the radius of the tip then the electric field at the tip will be $E = \frac{V}{r}$. Tungsten can be made readily a tip of radius $< 0.1\mu\ m$. For the application of 1 kV potential, the value of E becomes $10^{10}\ V/m$. This amount of electric field is sufficient to overcome the work function barrier for the electrons. The tip should be also mechanically strong so that it can sustain the severe stress applied by the electric field. The field emission depends on the orientation of LaB_6 crystal and $< 310 >$ orientation served the best. The tip should remain pristine for effective field emission and this can be achieved only in UHV condition ($< 10^{-9}\ Pa$). The most popular electron guns are Schottky electron guns whose surface is treated with ZrO_2 for improved emission characteristics.

The thermionic gun consists of three parts, they are cathode or electron gun, Wenhelt cylinder, and anode. The cathode is connected to the high voltage power supply. The electrons emerge out from the cathode to the anode with acceleration depending on the applied voltage. The movement of the electrons from the cathode to anode is controlled by the Wenhelt cylinder. A small negative bias is applied to the Wenhelt cylinder and this converges the electron beam to a point called crossover. Electrons are then accelerated towards the anode. FEG consists of a cathode and two anodes. The extractor voltage is provided between the first anode

and cathode. The applied voltage produces an intense electric field so that electrons can tunnel out from the cathode. To avoid any thermo-mechanical fracture of the tip the voltage should be increased very slowly. The electrons are accelerated by the second anode which is placed after the first anode. The combined effect of the anode field acts as an electrostatic lens and creates a crossover, which determines the effective size of the source and its position. However, such configuration does not give a stable source, which can be improved by the incorporation of the magnetic lens inside the gun.

2.3.2.3 Electron Beam Acceleration

After the extraction of the electrons from the electron gun they are accelerated by the high electric field which is applied between an anode (which is a metal plate with a central hole) and the cathode. The applied potential difference between the cathode and anode accelerates the electrons towards the anode and only 1% of the emitted electrons pass through the anode hole. To analyze the property of electrons when they are accelerated by high voltage, we have to consider its wavelength. The kinetic energy of the electrons when they are given a potential 'V' *volt* is given by

$$K.E = \frac{p^2}{2m} = eV \tag{2.6}$$

where p and m are the momentum and mass of the electrons respectively, e is the electronic charge. Now from De Broglie hypothesis the wavelength of the electrons will be

$$\lambda = \frac{h}{p} = \frac{h}{\sqrt{2meV}} \tag{2.7}$$

if we apply an acceleration voltage of 100 keV the velocity of electrons approaches to 0.5 c which is very much comparable to the velocity of light in vacuum. Hence, considering the relativistic effect the more accurate expression for the wavelength of electrons will be

$$\lambda = \frac{h}{p} = \frac{h}{\sqrt{2meV(1 + \frac{eV}{2mc^2})}} \tag{2.8}$$

which gives the wavelength of 1.2 pm for electrons with an acceleration voltage of 300 kV (in absence of any instrumental noise).

2.3.2.4 Lenses and Apertures

The illumination system consists of the electron gun and condenser lenses. The combined role of these two is to extract the electrons from the source and transfer all the way to the specimen. Unlike LM where we change the position of the lenses to focus the beam, in the electron microscope EM lenses are used. The strength of these lenses can be modified by changing the current through the coil around a soft magnetic material core to change the strength of the resulting magnetic field.

The electromagnetic lens consists of two parts. The first part is a cylindrical shape core made of soft iron having a hole through it. This is called as pole-piece and the hole between them is called bore of pole-piece (Figure 2.4a). Most of the lenses are consist of two pole-pieces. There is a gap between the pole-pieces and this bore to gap ratio is a very important parameter for such kind of lens. The second part consists of a copper wire surrounding each pole-piece. A magnetic field is created in the bore whenever current is passed through the coil. The magnetic field is axially symmetric while inhomogeneous along the length. The ray path (or trajectory) of the electrons through it can be controlled by changing the current

through the coils (Figure 2.4b). The coils are feed through cooled water to counter the resistive heating of the coil.

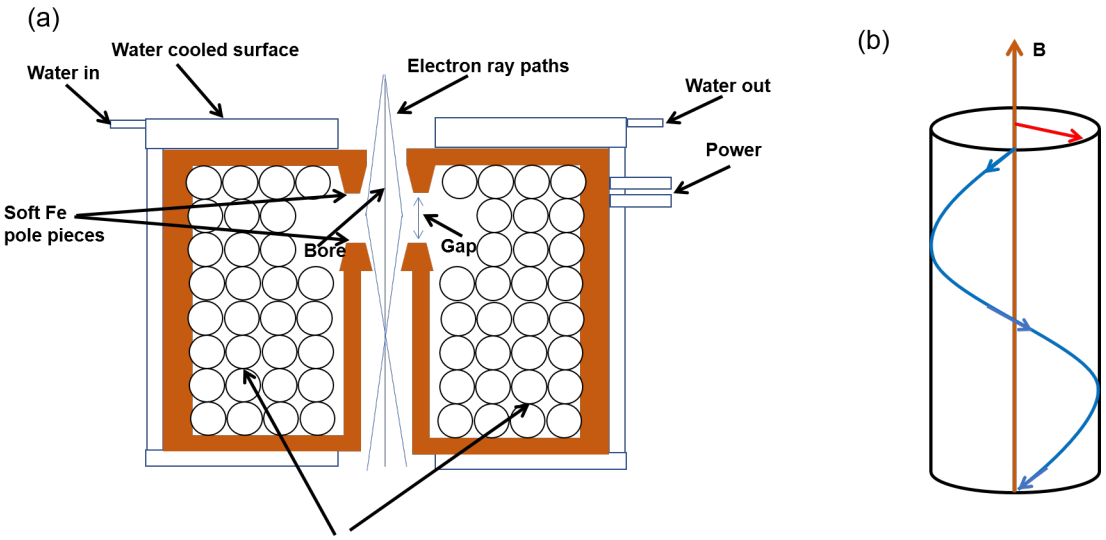

Figure 2.4: *Schematic representation of (a) magnetic lens and (b) path of and electron in a magnetic field.*

To understand mathematically how an electromagnetic lens works, let us consider an electron of charge e enters into a magnetic field of strength B and an electric field of strength E. The Lorentz force acting on the electrons will be

$$\vec{F} = -e(\vec{E} + \vec{v} \times \vec{B}) \tag{2.9}$$

in absence of the electric field

$$\vec{F} = -e\vec{v} \times \vec{B} \tag{2.10}$$

hence the resultant force will be perpendicular to the plane containing both $\vec{v}$ and $\vec{B}$. The direction of the applied field can be determined by using Fleming's left-hand rule.

For an electron entering into a uniform magnetic field nearly 90^o with it, the force on it will be $F = evB\sin 90^o = evB = \frac{mv^2}{r}$ where r is the cyclotron radius which can be written as $r = \frac{mv}{eB}$. As the velocity of the electron is comparable to the velocity of light, we have

$$r = \frac{2m_0E(\sqrt{1+\frac{E}{2E_0}})}{eB} \tag{2.11}$$

where E_0 and m_0 are the rest mass energy and rest mass of the electron respectively. From this, we can derive the value of r as

$$r = \frac{3.37\times10^{-6}\sqrt{[V(1+0.9788\times10^{-6}V]}}{B} \tag{2.12}$$

to derive this equation we have considered that $\theta = 90^0$, i.e. the electron travels straight along the optical axis, which indicates that it does not feel the presence of the lenses. Hence, it must deviate from its straight-line path so that the EM lenses can affect its path. Hence in this conditions, e^- will have two velocity components, v_1 perpendicular to $\vec{B}$ and v_2 parallel to $\vec{B}$. So, $v_1 = v\sin\theta$ and $v_2 = v\cos\theta$. v_2 results motion along the direction of the optical axis. On the other hand, v_1 will produce a circular motion with a radius given by the combined effect of these two. This will result in a helical path of the e^- s along the optic axis. The cyclotron frequency can be written as

$$\omega_c = \frac{2\pi}{T_c} = \frac{eB}{m} \tag{2.13}$$

from these equations, we can estimate the ray path of the electrons through the lens completely.

2.3.2.5 The Specimen Stage System

The specimen stage is one of the most important parts of the TEM. The specimen stage is mostly of two types, side-entry stage, and top entry stage. In the side-entry

stage, the specimen is kept at one end in such a way that the vibration should be minimum. The design of the stage should be such that it does not disturb the vacuum of the TEM column during its insertion. This is achieved through an airlock which is a small chamber where the specimen is initially inserted and it is evacuated before the stage enters into the TEM column. In a side entry stage, the stage is inserted horizontally into the column through the airlock. The rotation of the holder about its long axis activated the airlock evacuation valve and high vacuum valve. It is easier to control the precise motion of the specimen along x, y, and z-direction. Also, the specimen tilt can be obtained easily by turning the external end of the holder. Also, heating and cooling of the specimen stage are easy to arrange in this configuration.

In the top entry stage, the specimen is clamped to a cylindrical holder which consists of a conical collar. The holder is inserted into the TEM collar through an airlock by a sliding and tilting arm which is retracted after insertion. For our experimental purpose, we have used the side entry sample stage.

2.3.3 Projection System

The projection lens is there to produce a final image or diffraction pattern through the entire TEM screen which has a diameter of several centimeters. To minimize distortion in the final image, the projector lens is made to be a very strong lens with the focal length of a few millimeters.

2.3.3.1 TEM Screen and Camera

To visualize the image a phosphor screen is used. The screen consists of a metal plate, which is coated with a thin layer of fluorescent powder which fluorescence in

the yellow-green region in the visible spectrum. Traditionally the phosphor material consists of zinc sulfide with very small metal impurity. The screen is observed through a viewing window which is of high lead concentration and sufficiently thick to efficiently absorb X-rays which are generated when the electrons incident on the screen.

To record the TEM image or diffraction pattern CCD sensors are used. It consists of millions of Si photodiodes. Each Si photodiode produces an electrical signal proportional to the intensity level. As a very highly condensed electron beam can damage the photodiodes, they are protected by a phosphor screen on which e^- beam intensity can be adjusted. The image can be viewed digitally on a monitor screen and can be stored digitally in computer memory.

2.3.4 Vacuum System

To avoid undesired scattering of electrons by gas molecules, it is very much essential to maintain a high vacuum inside the TEM column. The electron gun requires a very good vacuum to prevent high-voltage discharge and oxidation of the filament material. To obtain this high level of vacuum different kinds of pumps are used in TEM (Figure 2.5). In our system, we have rotary, oil diffusion pump, ion pump, etc.

2.3.4.1 Rotary Pump

It consists of a rotating assembly operated with an electric motor, It also consists of internal vanes which are separated by a coil spring. This configuration enables it to press against the inside wall of the cylindrical pump and produce an airtight

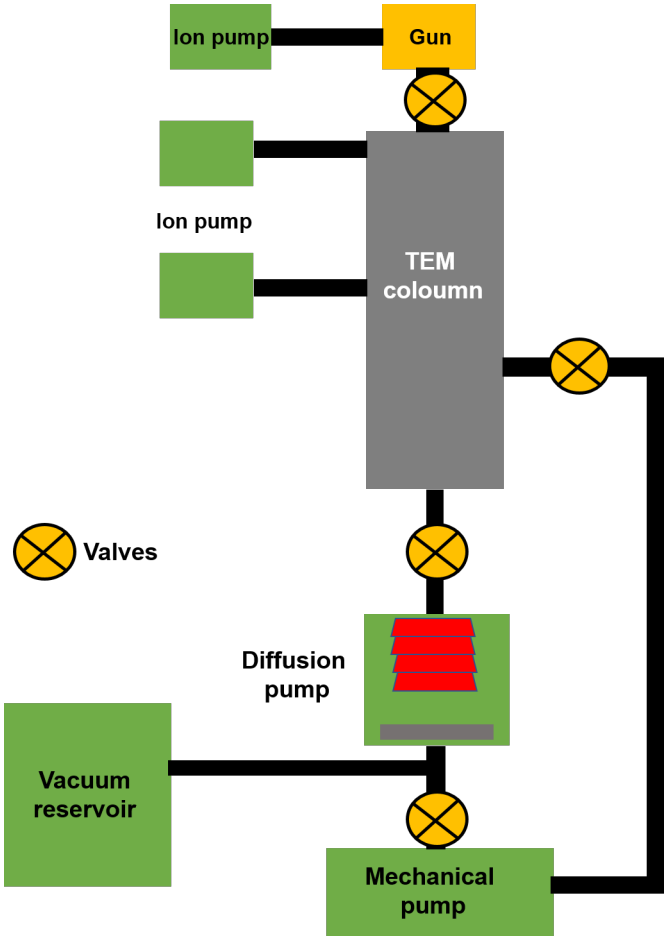

sysytem.png

Figure 2.5: *Schematic diagram of TEM vacuum system.*

seal. The lubrication of the inside chamber is done with oil of low vapor pressure which reduces wearing and friction of sliding surfaces. To obtain a considerable expansion of the volume of the gas at the outlet the rotation axis is offset from the cylinder axis. The gas drawn at the inlet expands considerably before it goes out through the opposite valve. The air is then compressed and goes out from the outlet. In the meantime, there is already an expansion of air drawn from the inlet of the next cycle and the action continues. The rotary pump is a "rough" pump which can bring down the pressure to 1 Pa, which is 10^5 order less than

atmospheric pressure. But this vacuum level is not sufficient for efficient electron emission.

2.3.4.2 Oil Diffusion Pump

The diffusion pump is used to produce a "high" vacuum ($< 10^{-3}\ Pa$). A typical cylindrical diffusion pump uses a low vapor pressure liquid having a very high boiling point. The liquid is boiled using a heater situated at the base of the cylinder. The vapor rises through the pump and then an internal baffle assembly deflects them downwards through jets. During their downward motion, the oil molecules collide with air resulting in downward movement of the gasses from the inlet of the pump. The oil molecules come back to the liquid state after colliding with the cooled inside wall of the diffusion pump. The minimum working pressure of a diffusion pump is below 10 Pa to prevent oxidation of the oil. This is obtained by a rotary pump connected to the bottom of the diffusion pump.

2.3.4.3 Turbo-Molecular Pump

Turbomolecular pump is also used to supplement the diffusion pump. An ion pump is also used to obtain a pressure below $10^{-4}\ Pa$, which is suitable for the operation of the gun.

For an efficient operation of a TEM, all the different pumps must work in correct sequences. It is controlled and monitored by vacuum gauges located at different portions of the system and controlled by different valves. Modern TEM's come with an automatic software control vacuum system.

2.3.5 TEM Imaging and Diffraction

The objective lens collects the electrons emerging out from the specimen and produces a diffraction pattern at the back focal plane and finally forms the image in the image plane by recombining them. To switch between the diffraction patterns and image we have to adjust the imaging system lenses. To obtain a diffraction pattern the back focal plane of the objective lens should act as the object plane for the intermediate lens (Figure 2.6a). To obtain an image, the imaging lens system is re-adjusted so that the image plane of the objective lens act as the objective plane for the intermediate lens (Figure 2.6b).

The diffraction pattern taken from the whole sample does not contain any useful information due to buckling. Also, in such a case the diffracted beam is often so intense that it can damage the viewing screen or can saturate the CCD camera. So, in SAD pattern, we select a particular portion of the specimen which is free of buckling and also it reduces the direct beam intensity. To do this we insert an aperture above the sample which allows only those electrons to pass through it and hit the sample. The diffraction pattern is of two types (i) CBED and (ii) SAD. In CBED we use a convergent beam to hit the specimen and the resultant pattern is a circular disk instead of spots. In SAD operation, the parallel beam hits the specimen and produces diffraction spots. Here the aperture is placed in a conjugate plane with the specimen which is at one of the planes where the image of the specimen is formed for the imaging lens. The SAD aperture is placed at the image plane formed by the objective lens as shown in Figure 2.6. The proper adjustment of the aperture is done by viewing on the phosphor screen.

According to Bragg's law, Figure 2.7 shows an incident beam of wavelength W_1

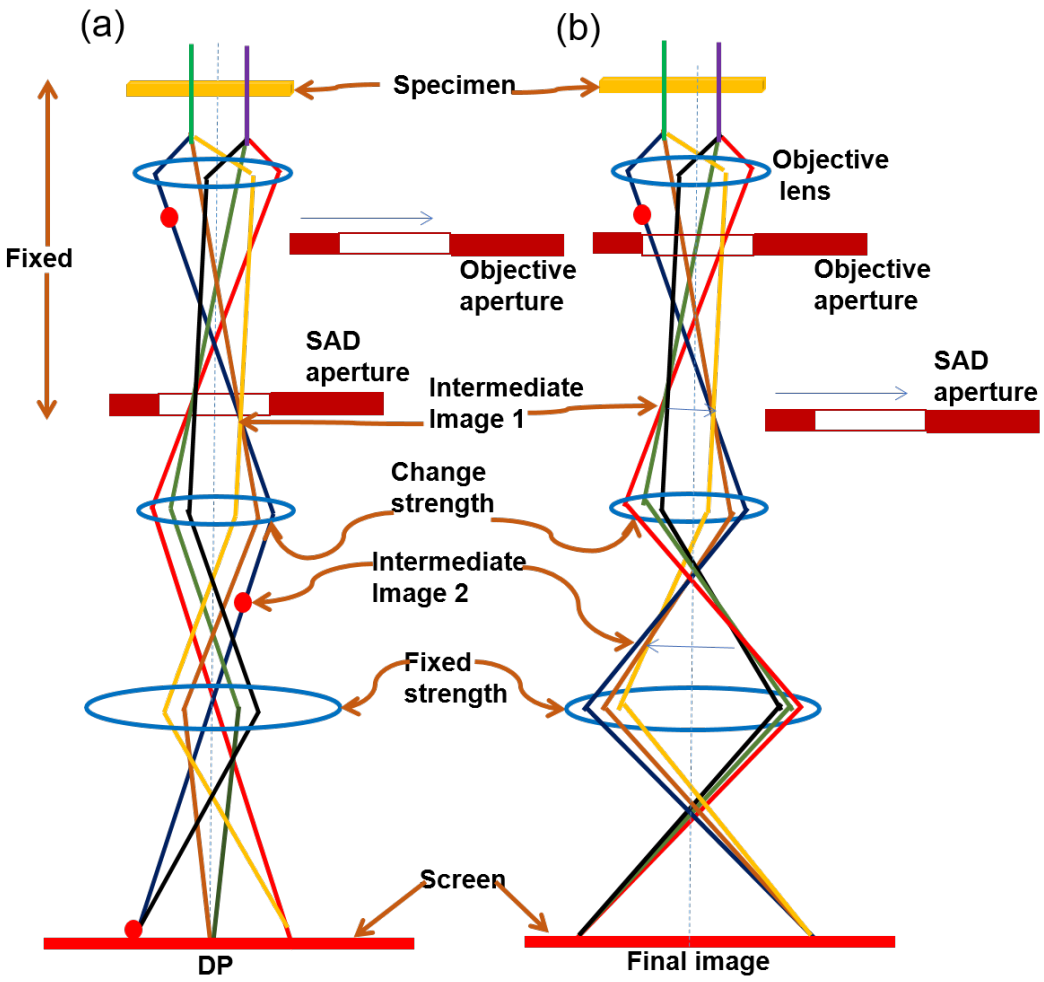

Figure 2.6: *Two most basic TEM operation (a) image mode (b) diffraction mode.*

is scattered by an atomic plane and produces the diffracted wavefront W_D which depends on the scattering process (coherent or incoherent). According to Laue's condition, the simplified diagram for a scattering process of two atoms is shown in Figure 2.7. It shows the wave propagation vector $\overrightarrow{k}$ with plane wavefront, where $\overrightarrow{k}$ is normal to the wavefront. We can write the equation as

$$\overrightarrow{K} = \overrightarrow{k_D} - \overrightarrow{k_1} \tag{2.14}$$

where $\overrightarrow{k_D}$ and $\overrightarrow{k_1}$ are the diffracted and incident wavefronts and $\overrightarrow{K}$ is the change

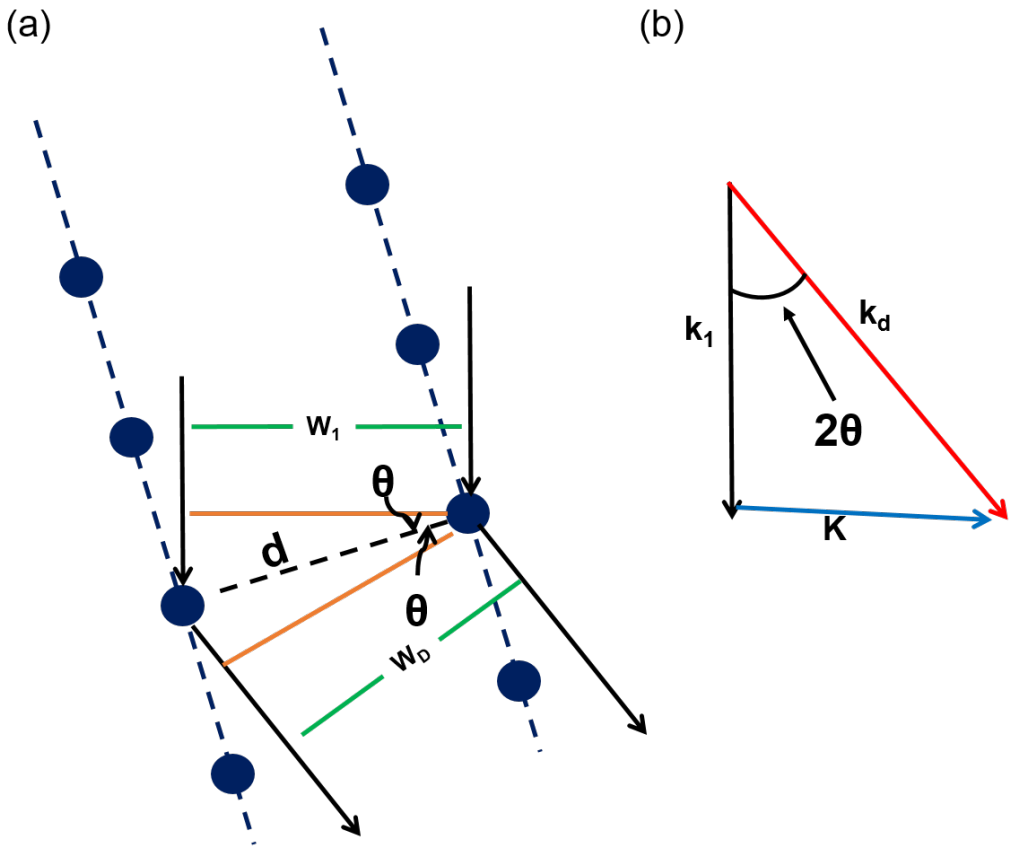

Figure 2.7: *(a) Representation of scattering from two atomic planes where W_1 and W_D are the incident and diffracted waves respectively. (b) incident wave vector is k_1, diffracted wave vector is k_d and K is the difference vector.*

in wave vector due to diffraction. If λ be the wavelength of incident light then,

$$| \overrightarrow{k_1} | = | \overrightarrow{k_d} | = \frac{1}{\lambda} \tag{2.15}$$

Provided there is no change in electron energy during diffraction. From Figure

we also have

$$\sin\theta = \frac{| \overrightarrow{k_2} |}{| \overrightarrow{k_1} |} \Rightarrow | \overrightarrow{k} | = \frac{2\sin\theta}{\lambda} \tag{2.16}$$

If θ equals to the Bragg angle θ_B then

$$| \overrightarrow{k} | = \frac{2\sin\theta_B}{\lambda} \tag{2.17}$$

The path difference between the incident and diffracted wave becomes

$$2d \sin \theta_B = n\lambda \tag{2.18}$$

For n=1 we have

$$2d \sin \theta_B = \frac{\lambda}{d} = \lambda \mid \overrightarrow{k} \mid \tag{2.19}$$

For diffraction, at Bragg angle, the magnitude of $\overrightarrow{k_1}$ is indicated by $\overrightarrow{K_B}$ as

$$\mid \overrightarrow{K_B} \mid = \frac{1}{d} \tag{2.20}$$

$\mid \overrightarrow{K_B} \mid$ is defined so that $\mid \overrightarrow{K_B} \mid = g$.

According to Bragg's law the diffraction planes behave like a mirror for the incident electron beam. The wave vector $\overrightarrow{g}$ is related directly to the diffraction spots in TEM.

2.3.6 Bright-Field and Dark-Field Operation

The SAD pattern consists of a central bright spot originating from the direct beam and some scattered spots whose position and orientation depends on the crystal planar distances and crystallographic orientation and dependent on the nature of the specimen. To obtain a BF image the central spot is selected with the SAD aperture and is aligned along the optic axis. The image taken in this configuration is called BF image (Figure 2.8a). The DF image is taken by selecting a diffracted beam (Figure 2.8b). As the diffracted beam is not aligned along the optic axis the image taken in this configuration will have more astigmatism and aberration. To

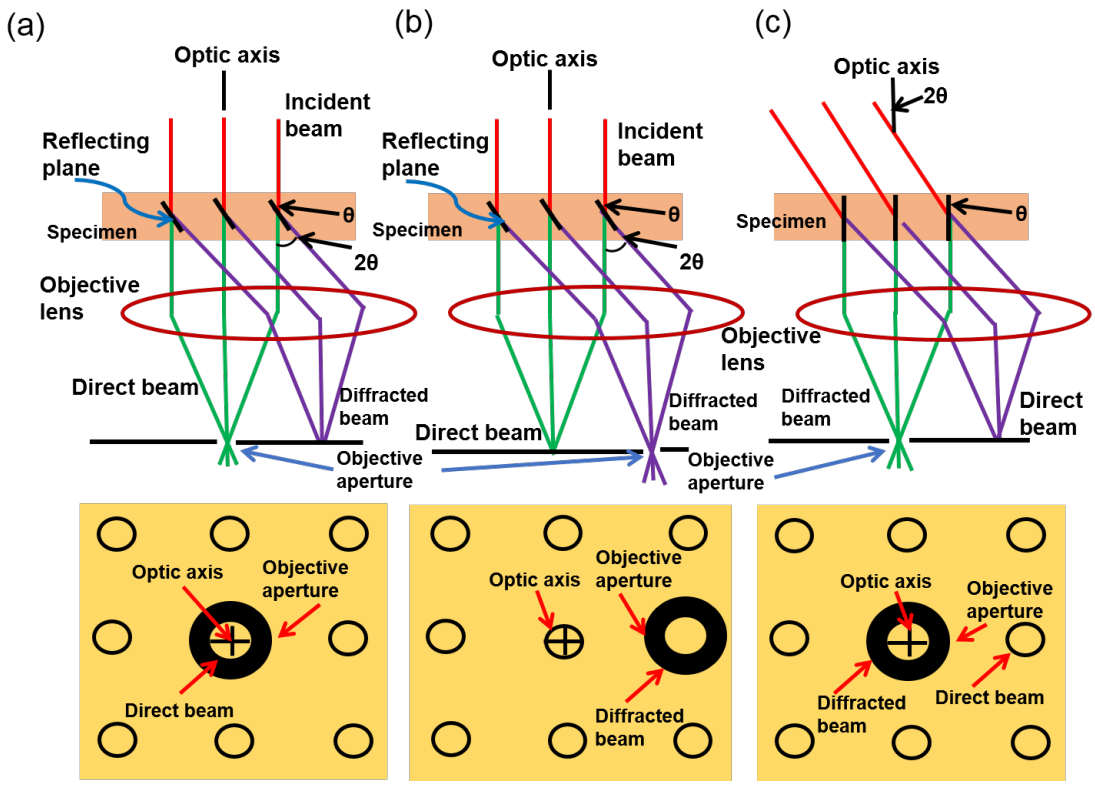

Figure 2.8: *Ray diagram of bright and dark-field mode of operation using objective lens and objective aperture (a) BF mode of operation using direct beam. (b) off-axis DF mode of operation using an off-axis beam. (c) CDF mode where the incident beam is tilted to make the scattered beam travel along the optic axis.*

avoid the situation the diffracted beam is first aligned along the optic axis and this imaging process is known as CDF imaging (Figure 2.8c).

2.3.7 Scanning Transmission Electron Microscope

In STEM mode a convergent beam of electron is used as a probe and to form the final image of the area of interest is scanned using the probe. One thing to remember is that there should not be any change in the direction of the scanning beam otherwise it will be very difficult to interpret the result. In STEM mode the

beam must do the scanning parallel to the optic axis, which is ensured by two pairs of scan coils. They pivot the beam at the front focal plane of the upper objective pole-piece. As lenses are not used in this configuration, the images are free from any chromatic aberration. STEM images are also acquired as BF, DF, and ADF-STEM images. For the acquisition of BF STEM image and aperture is inserted into the plane of TEM to allow only the direct electrons to contribute to the image. The BF detector is inserted into the microscope axis and it intercepts the direct beam electrons. As STEM acquisition is a serial recording process, it takes some time to form a single image of the specimen. To obtain a DF STEM image any or all of the scattered electrons are selected and fall onto the BF detector by simply shifting the stationary diffraction pattern. In ADF images an annular detector is used so that all of the scattered electrons fall to the detector. The advantage of this process is that the contrast of the image is directly proportional to Z^2 as high angle scattering is dominated by Rutherford scattering effects. The electrons which are scattered more than 50 $mrad$ are collected in this process.

2.3.8 Phase Contrast Microscopy

To construct the phase contrast image it is necessary to calculate the intensity of the beam at the exit surface of the specimen (here at point P in the Figure 2.9, as after suitable magnification this will become the image. To construct this, we will consider the fact that any crystal is made of a number of unit cell. The amplitude of a scattered electron from an unit cell can be written as,

$$A_{cell} = \frac{e^{2\pi ikr}}{r} \sum_{i=1}^{n} f_i(\theta) e^{2\pi ikr} \tag{2.21}$$

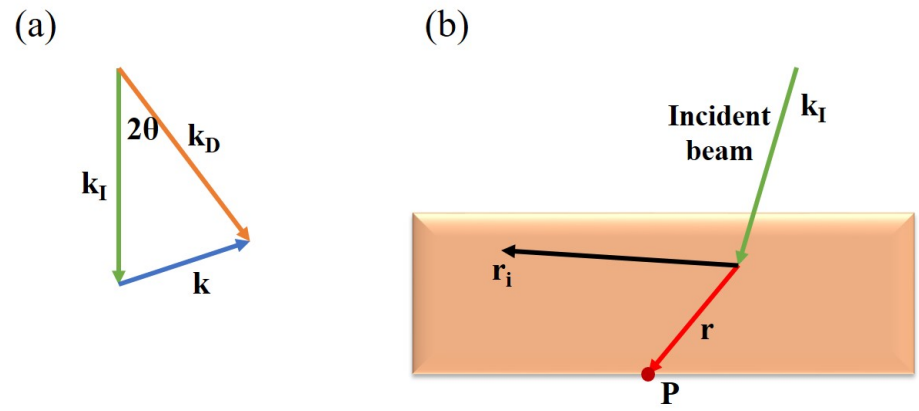

Figure 2.9: *Schematic representation of (a) diffraction of wave through a crystal (b) realationship between spherical wavefront radius r, position vector of the i-th atom r_i and the point P at which the intensity is to be calculated.*

where, $f(\theta)$ is the atomic scattering factor, and the index i goes over all the atoms in the unit cell, θ is the angle of diffraction of the incident beam, k is the wave vector and position of the i-th atom in the unit cell. The term $\sum_{i=1}^{n} f_i(\theta)e^{2\pi ikr}$ can be written as $F(\theta)$ which indicates the structure of the unit cell. So we can write the previous equation as

$$A_{cell} = \frac{e^{2\pi ikr}}{r} F(\theta) \tag{2.22}$$

to find the intensity at point P, the summation is to be done over all the atoms in the unit cell. If the number of unit cell per unit area on a plane parallel to crystal surface is n and the inter-planar distance is a. Then $\frac{a}{n}$ defines the volume of a unit cell V_c. So, considering this the diffracted beam amplitude (in θ direction) can be written as

$$\phi_g = \frac{\pi a i}{\xi_g} \sum_{i=1}^{n} e^{-2\pi i \vec{k}.\vec{r_n}} e^{-2\pi i \vec{k_D}.\vec{r}} \tag{2.23}$$

where $\vec{r_n}$ describes the position of each unit call. The quantity ξ_g is called

"characteristic length" for the $\overrightarrow{g}$, and it can be expressed as,

$$\xi_g = \frac{\pi V_c \cos\theta_B}{\lambda F_g} \tag{2.24}$$

where F_g denotes $F(\theta)$ when θ corresponds to a Bragg angle, ξ_g depends on the wavelength and on F_g. The value of F_g is higher for higher atomic number elements and hence, ξ_g is small for Au but large for Si.

The fundamental understanding of diffraction contrast in TEM can be obtained from "Howie-Whelan" equation. Here, the wavefunction inside the crystal can be considered to be sum of the electron beam passing through it. The amplitude of direct beam is ϕ_0 and ϕ_{g1}, ϕ_{g2},.....ϕ_{gn} represents the amplitude of the diffracted beams. So, the total wavefunction can be written as,

$$\psi^T = \phi_0 e^{2\pi\overrightarrow{\xi_0}.\overrightarrow{r}} + \phi_{g_1} e^{2\pi\overrightarrow{\xi_{g_1}}.\overrightarrow{r}} + \phi_{g_2} e^{2\pi\overrightarrow{\xi_{g_2}}.\overrightarrow{r}} + ... \tag{2.25}$$

where $\overrightarrow{\xi_0}$ and $\overrightarrow{\xi_{g_1}}$are the wave vectors in vacuum. This are indicated as $\overrightarrow{k}$ inside the crystal. In two- beam approximation method only one diffracted beam along with the direct beam is considered. This condition can be acquired by tilting the crystal such that only one strong diffraction occurs while all the others become weak. In such case a small change in ϕ_z due to the passage of small distance dz through the material can be represented as,

$$d\phi_g = \frac{\pi i}{x_g}\phi_0 e^{2\pi i(\overrightarrow{xi_0}-\overrightarrow{\xi_D}).\overrightarrow{r}} dz + \frac{\pi i}{\xi_0}\phi_g dz \tag{2.26}$$

$$d\phi_0 = \frac{\pi i}{x_0}\phi_0 dz + \frac{\pi i}{\xi_g}\phi_g e^{2\pi i(\overrightarrow{xi_D}-\overrightarrow{\xi_0}).\overrightarrow{r}} dz \tag{2.27}$$

where the quantity $\overrightarrow{xi_0} - \overrightarrow{\xi_D}$ represents the change in wave vector when ϕ_0 scatters into ϕ_g. For a perfect crystal $\overrightarrow{\xi_0} - \overrightarrow{\xi_D} = \overrightarrow{g} - \overrightarrow{s}$, where $\overrightarrow{s}$ is the excitation

error. The quantity ξ_0 and ξ_g are the characteristic length for forward scattering and diffracted beam corresponding to a vector $\overrightarrow{g}$. The equations can be rearranged to represent pair of coupled differential equation. Which is given by,

$$\frac{d\phi_g}{dz} = \frac{\pi i}{x_g}\phi_0 e^{2\pi i(\overrightarrow{xi_0} - \overrightarrow{\xi_D}).\overrightarrow{r}} + \frac{\pi i}{\xi_0}\phi_g \tag{2.28}$$

and

$$\frac{d\phi_0}{dz} = \frac{\pi i}{x_0}\phi_0 + \frac{\pi i}{\xi_g}\phi_g e^{2\pi i(\overrightarrow{xi_D} - \overrightarrow{\xi_0}).\overrightarrow{r}} \tag{2.29}$$

from this paired equations we observed that the relative change in ϕ_0 and ϕ_g are 'dynamically coupled" to each other and this pair of equations are known as "Howie-Whelar equation". It leads to the fundamental understanding of diffraction contrast in TEM.

For two beam condition we can write equation 2.25 as

$$\psi = \phi_0(z)e^{2\pi i\overrightarrow{k_I}.\overrightarrow{r}} + \phi_g(z)e^{2\pi i\overrightarrow{k_D}.\overrightarrow{r}} \tag{2.30}$$

now, we will make some substitution by taking $\phi_0(z) = A$ and $e^{2\pi i\overrightarrow{k_I}.\overrightarrow{r}}$ out as a factor and $\phi_g = Be^{i\delta}$, where $B = \frac{\pi^2 \sin(\pi t s_{eff})}{\xi_g \pi s_{eff}}$ and $\delta = \frac{\pi}{2} - \pi t s_{eff}$. So, equation 2.30 becomes

$$\psi = e^{2\pi i\overrightarrow{k_I}.\overrightarrow{r}}[A + Be^{i(2\pi\overrightarrow{g}.\overrightarrow{r}+\delta)}] \tag{2.31}$$

so, the equation can be written as,

$$I = A^2 + B^2 + 2AB\cos(2\pi\overrightarrow{g}.\overrightarrow{r} + \delta) \tag{2.32}$$

so the outward beam oscillates sinusoidally normal to $\overrightarrow{g}$ and the periodicity depends on δ. We can relate these fringes to the interplanar spacing and normal to $\overrightarrow{g}$. This model indicates that for different values of $\overrightarrow{g}$ the intensity varies sinusoidally with different periodicities. It is also valid when the incident beam is slightly off the optic axis.

2.3.9 Moiré Pattern

The Moiré pattern forms due to interference of two lattice planes having nearly same interplanar spacing. Moiré fringes are mainly of two types (i) Translational Moiré fringe, when the planes are parallel to each other, the $\overrightarrow{g}$ vectors will also be parallel. So, if they can be written as $\overrightarrow{g_1}$ and $\overrightarrow{g_2}$ a new lattice spacing will be produced and will be represented by $\overrightarrow{g_{tm}} = \overrightarrow{g_2} - \overrightarrow{g_1}$. $\overrightarrow{g_2}$ and $\overrightarrow{g_{tm}}$ represents the shorter spacing and translational Moiré fringes respectively. The direct space fringes d_{tm} corressponds to g_{tm} can be represented as

$$d_{tm} = \frac{1}{g_{tm}} = \frac{1}{g_2 - g_1} = \frac{d_2 d_1}{d_1 - d_2} \tag{2.33}$$

(ii) Rotational Moiré fringes, if we consider the two vectors to be identical in length and inclined from each other by an angle β. The new $\overrightarrow{g}$ vector in this case will have length of $2g\sin(\frac{\beta}{2})$. So,

$$d_{tm} = \frac{1}{g_{tm}} = \frac{1}{2\sin(\frac{\beta}{2})} = \frac{d}{2\sin(\frac{\beta}{2})} \tag{2.34}$$

The expression for general Moiré fringes for small inclination angle and for two different lattice parameter having very small difference with each other can be written as,

$$d_{gm} = \frac{d_1 d_2}{\sqrt{(d_1 - d_2)^2 + d_1 d_2 \beta^2}} \tag{2.35}$$

2.3.10 Energy-Dispersive X-ray

X-rays are generated when the highly energetic electrons strike the specimen. As X-rays are characteristics of the specimen only hence, by using x-ray spectrometry a detailed elemental analysis can be done in TEM. In X-ray energy dispersive

spectrometer a Si or Ge detector is used. A voltage pulse proportional to the energy of the X-ray is generated by the detector. The pulses are translated into a signal in a particular channel with electronic processing. A spectrum is generated in the energy window which can further be transformed into compositional profile or compositional map (Figure 2.10). To do an EDX we have to first obtain an STEM image and then the elemental information can be obtained by using a spot as a probe. But to obtain a good statistical information usually a drift corrected spectrum image is obtained in STEM mode.

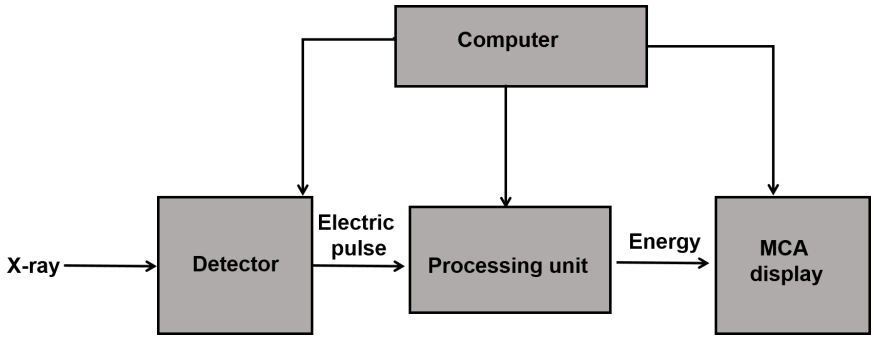

Figure 2.10: *Schematic representation of EDX signal generation processing unit .*

The different working steps of an EDX detector is as follow

(i) A charge pulse proportional to the X-ray energy is generated by the detector.

(ii) The generated pulses are then converted into voltage.

(iii) The voltage pulses are then amplified by a FET.

(iv) The digitalized signal is stored in the desired channel and displayed in a computer.

Unlike STEM image formation, the generation of EDX spectra is very fast. An EDX actually does two kinds of work (i) It detects the X-rays and (ii) It separates

them into a spectrum depending on their energy. The Si detector is not pure Si, as pure Si contains acceptor type impurity and behave as p-type Si. Hence to compensate for this it is lightly doped with Li to create an intrinsic Si. We have used the TIA software of FEI platform to perform all the EDX analyses.

2.3.11 TEM Cross-Sectional Sample Preparation

For TEM analysis the transmitted electrons are used to form the images. Hence the specimen cannot be inserted into their bulk form. They must be electron transparent and hence solid samples have to go through a special sample preparation process before they are inserted into the TEM column. The different process of thinning a sample fro suitable TEM measurements are the following and is shown in Figure 2.11.

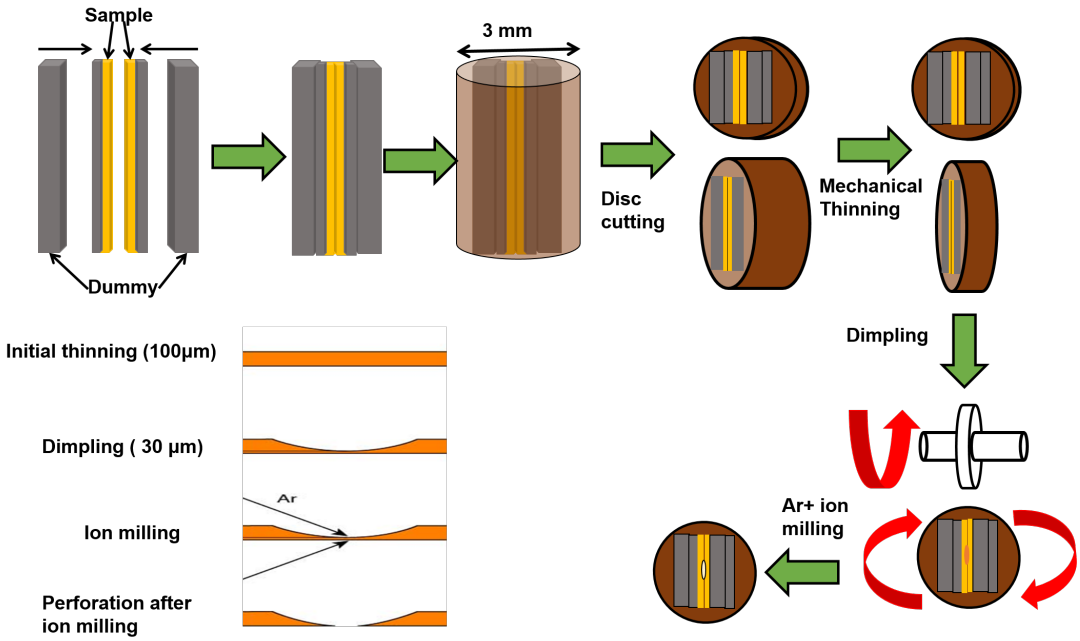

Figure 2.11: *Schematic of TEM cross-section sample preparation process.*

2.3.11.1 Bonding of the Substrate

At the very first step, two substrates (of width 3 mm) on which nanoparticles are deposited are bonded face to face with epoxy. The epoxy consists of a resin and a hardener. These two were mixed at 8 : 1 ratio (resin:hardener) and stirred properly to obtain a uniform color mixture. The epoxy is then applied onto the surface of the substrates and they are bonded face to face. To obtain a strong bonding at the interface between the two substrates the composite is kept pressed by a mechanical arrangement and kept at a hot plate at 130^o C to obtain a strong adhesion.

2.3.11.2 Insertion of The Composite into a Copper Tube and Disc Cutting

After the composite is formed it is inserted into a Cu tube of 3 mm dia. The composite is placed at the center of the tube and dummy substrates are inserted on both sides of it to fill the empty space. The total combination is kept vertically on a glass slide and placed on a hot plate. Epoxy is inserted into the tube to obtain compact bonding between them. The Cu tube is then cut into a disc of 0.5 mm width using a wire saw.

2.3.11.3 Initial Thinning

The disc of 0.5 mm width and 3 mm dia is then thinned mechanically using a disc grinder (Gatan) and silicon carbide paper to obtain suitable thickness for dimpling. Special care must be taken while thinning so that no crack occurs during this process otherwise it will break when the thickness will be very much less. The thickness of the sample becomes $60 - 100\mu$ after initial thinning.

2.3.11.4 Dimpling

During dimpling, only a small portion at the center of the sample is thinned. In this process, the sample is placed on a circular table which can rotate uniformly in the horizontal plane. The grinding wheel rotates in a vertical plane whose rotation speed can be adjusted according to the hardness of the material. The dimpling was done using 3μ size diamond paste. After final dimpling, the thickness of the sample at the mid-portion becomes 30μ. The dimpled side is then polished with 0.25μ size diamond paste.

2.3.11.5 Ion Milling

After dimpling, the sample is still not thin enough for TEM measurement. To make it suitable for TEM observation it has to go through the ion milling process. We have used a PIPS from Gatan for this purpose. During PIPS thinning Ar^+ ions are produced and by using bias they are made to strike the sample at the desired region to obtain the final electron transparent sample. An LCD display is used to monitor the process and also for proper centering of the disc. In our system, the energy of the ions can vary between 1.5 keV to 5 keV and the angle of incidence can be adjusted up to $\pm 10^o$. For most of the ion milling 3.5 keV energy is used. While for cleaning purposes 1.5 keV energy is used. The process is completed when we observe a tiny perforation at the center of the sample in the LCD display.

2.3.12 TEM Characterization

XTEM samples were prepared along [110] and [−110] projections and also along [100] and [−100] projections. The cross-sectional samples were made using the process described in the second chapter. The TEM characterizations were done using an FEI TECNAI G^2 F30-ST microscope operated at 300 keV. It is also equipped with a HAADF detector (Fischione, Model 3000) and EDX for X-ray analysis. The samples prepared along [110] and [−110] projections were oriented along [110] zone-axis and the samples prepared along [100] and [−100] zone axis were oriented along [100] zone axis for TEM observations.

2.3.13 Scanning Electron Microscope

To obtain a detailed topographical information SEM was used. In SEM, SE images are obtained by using raster pattern scanning of electron beam over an area of the sample. The different components of an SEM are shown in Figure 2.12.

Much like TEM, the components of SEM are electron gun, electromagnetic lenses, aperture, scanning coils, electrostatic lens, and detectors. Typically 5 kV to 30 kV high voltage is applied to the electron gun in SEM. The electrons then emerge out from the sharp FEG tip (typically of 100 nm radius) and incident on the sample after passing through a series of a condenser and objective lenses. The working of these lenses is the same as their function in TEM described before. Using the above mentioned voltage to the filament, a nanometer size probe is obtained which is very much pre-requisite to study nanomaterials topography efficiently. The charging effect is a very important phenomenon in SEM which distorts the image and also disturbs the vacuum. Hence to avoid this a few nm conductive layer is coated upon non-conductive samples. Special care should be

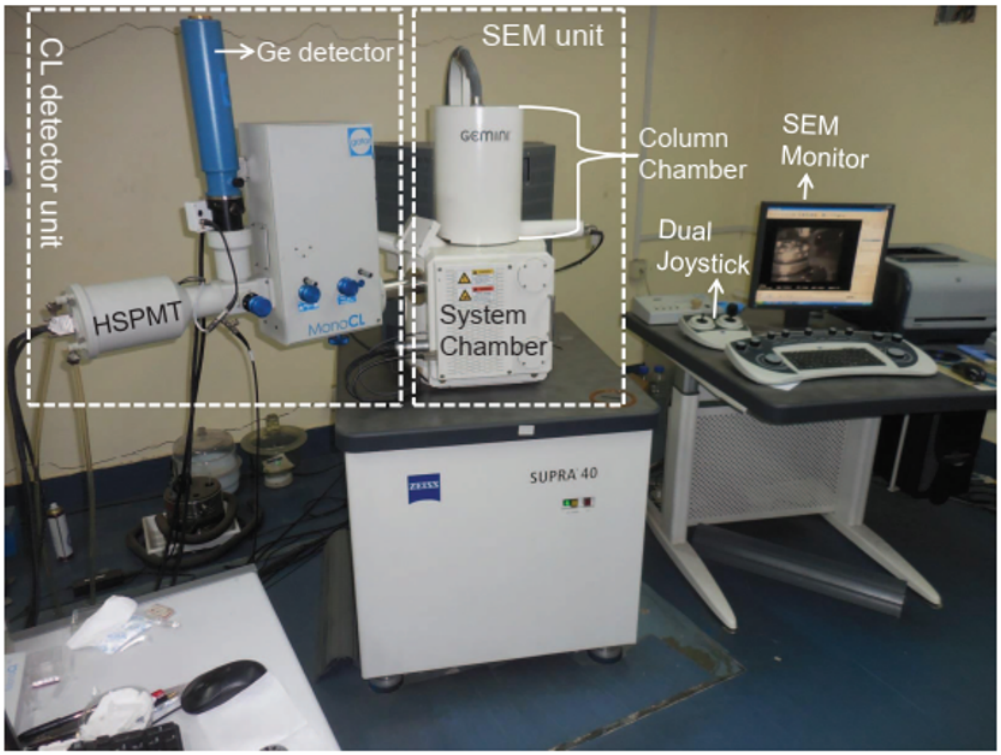

Figure 2.12: *Photograph of Gatan CL-SEM installed at SINP, Kolkata .*

taken while inserting the sample into the chamber. The vacuum of the sample chamber is maintained by a turbo pump backed by a rotary and the chamber pressure is maintained at 1×10^{-5} $mbar$. The FEG should be maintained at UHV condition to avoid any contamination and to obtain a longer lifetime fro the filament. Different kinds of interactions occur when highly energetic electrons incident on a sample resulting generation of various kinds of signals. The two most used signal in SEM is the secondary electron and backscattered electrons. Secondary electrons are generated from $5 - 50$ nm depth from the surface and hence contain topographic information. Backscattered electrons escape from 100 times larger depth compared to SE and the signal intensity depends on the atomic number of an element and hence contain the elemental information.

2.3.13.1 Cathodoluminescence in a SEM

The customized CL SEM set up at SINP was installed by Carl Zeiss, Germany, and Gatan UK. It consists of two main units (i) Unit to produce a nanometer-size probe (ii) Optical detection unit (Mono CL3, Gatan). The schematic of the system is shown in Figure 2.13.

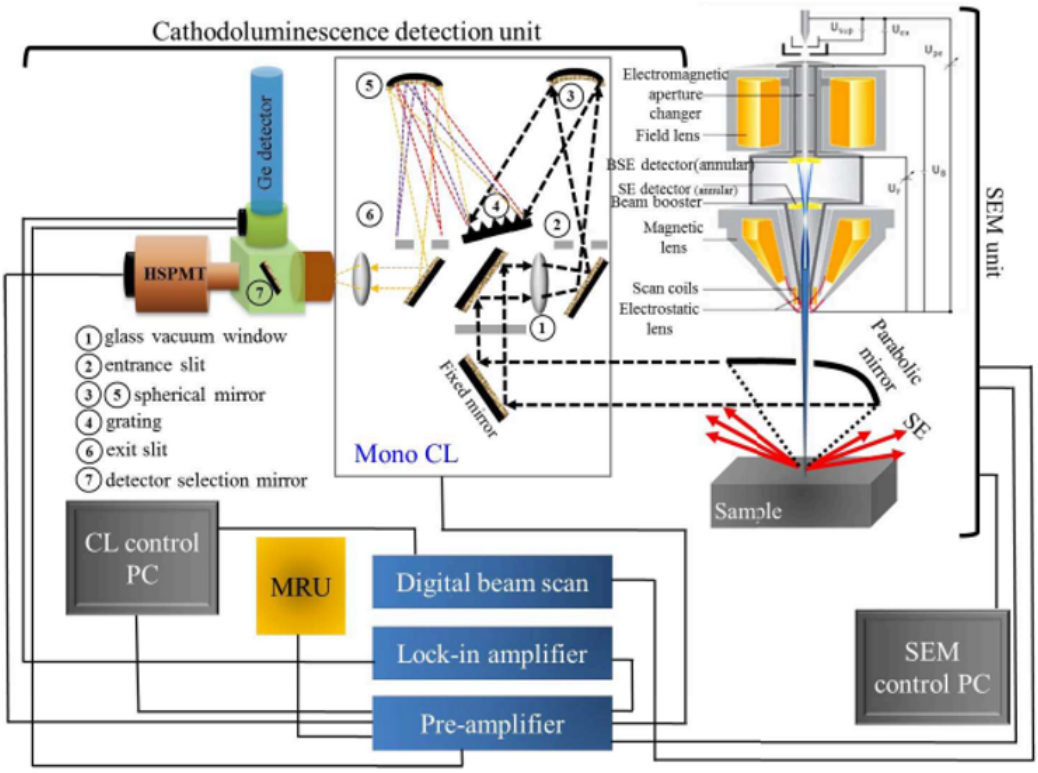

Figure 2.13: *Detailed schematic diagram of the CL-SEM system .*

A paraboloidal mirror, which is a part of the optical detection unit is placed inside the SEM chamber. The electron beam incident on the sample after passing through a hole (in the paraboloidal mirror) of 1 mm dia. The emitted signal from the sample within a solid angle of 1.42π sr is collected by the mirror. The collected

light signal is then collimated and fed to an optical monochromator of 300 mm focal length. The light signal from the monochromator is directed to a HSPMT which is Peltier cooled. The sample is kept at the focal point of the paraboloidal mirror so that maximum photon can reach to the detector and also to obtained a significant signal to noise ratio.

The CL SEM has two modes of operation (i) Mono CL mode, in this mode photon map at a particular wavelength can be obtained from the sample. The electron beam can either scan an area of the sample or it can be fixed at a point on the sample to generate photons. The emitted photons are then collimated and finally fed to a HSPMT detector to obtain the spectra. In (ii) PAN CL mode no monochromator is used and the emitted photon of all wavelength is fed into the HSPMT detector.

2.3.13.2 SEM Characterization

Quanta FEG (FEI) was used for SEM analysis. Normal plane view and XSEM mode were used for detailed morphological analysis. SE images were acquired to obtain the topographical information and BSE images were acquired to obtain detailed elemental information as the signal obtained from BSE image is dependent on the atomic number of the elements. The operating voltages were varied between 5 kV and 15 kV depending on the resolution required.

2.3.14 Raman Spectroscopy

Raman spectroscopy involves measuring the frequency shift of inelastically scattered photons by a sample. The interaction of incident EM radiation with different motion of the molecules (vibration/rotation) changes the polarizability of the molecules and results in Raman scattered light. However, the Raman scattering is a very rare event. A single Raman scattering takes place in $10^6 - 10^8$ scattering events. The Raman scattering can be of two types (i) Stokes Raman scattering, in this kind of scattering the scattered light has lower frequency compared to the incident light. In (ii) the Anti-Stokes scattering scattered light has greater frequency compared to incident light. The intensity of the Stoke's line is much greater than the intensity of Anti-Stoke's line. In anti-Stokes scattering event, the incident photon takes energy from the molecular bond which is initially at excited vibrational state. The shift in the energy of the photon is entirely dependent on the chemical composition of the molecule which is responsible for the scattering. So, the Raman spectrum is a fingerprinting tool for the identification of different chemicals.

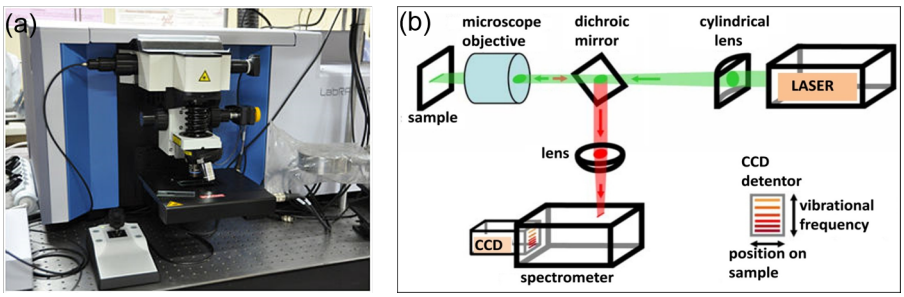

Figure 2.14: *(a) Labram HR 800 installed at SINP, Kolkata (b) Schematic of different unit and working process of a Raman spectrometer.*

The Raman intensity collected in a Raman spectrometer can be written as,

$$I_{RS} = \frac{8\pi^4\alpha^2}{\lambda^4 r^2}(1 + (\cos\theta)^2) \tag{2.36}$$

where α is the polarizability of the molecule, λ is the incident light wavelength, r is the distance between the scattering center and detector, θ is the scattering angle and I_0 is the incident light wavelength. SERS is a very useful tool for the detection of a very low concentration of analyte and their structural information. In SERS the incident EM light interacts with the localized surface plasmon resonances of the metal nanoparticles and generates a very high intense EM field. From different theoretical and experimental studies, it is observed that the SERS intensity is directly proportional to the fourth power of local electric field intensity and also dependent on the morphology of the metal nanoparticles. We have used a micro Raman spectrometer (Labram HR, Jobin Yvon) equipped with Peltier cooled CCD detector at room temperature. It is equipped with He-Ne laser with a wavelength of 632.8 nm as the excitation source. The block diagram of the Raman spectrometer is shown in the Figure 2.14b.

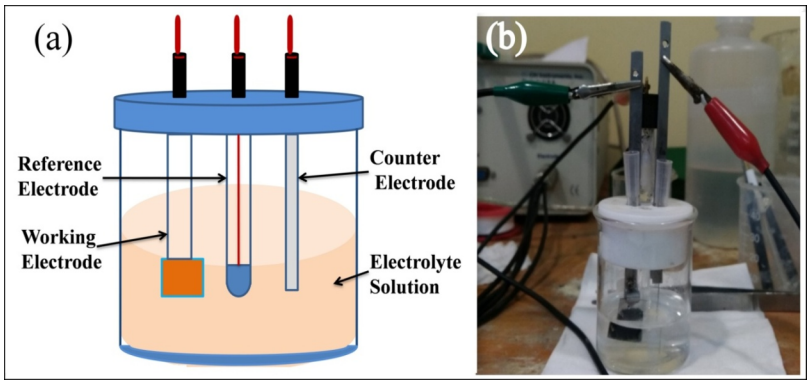

Figure 2.15: *(a) Schematic of three electrode configuration of a electrochemical workstation (b) Photograph of a three electrode system in working condition.*

2.3.14.1 SERS Measurements

SERS measurements were carried out using R6G as the dye molecule. The SERS substrates were prepared by drop-casting 20 μ L solution of 10 μ M R6G and the substrates were kept for 12 $hours$. The SERS spectra were taken using LABRAM HR 800 Raman spectrometer and using Labspec 4 software. He-Ne laser of excitation wavelength of 632.8 nm was used for this purpose. The data were taken for 10 seconds of integration time and 3 acquisition. The laser beam size was $1\mu m \times 1\mu m$ with a beam power of 100 μW. The spectrometer was calibrated using the Raman peak of Si at 525 cm^{-1}. A 100$\times$ aperture (N.A = 0.9) was used. N_{Bulk} which is the number of molecules in the bulk sample is calculated from this by assuming that R6G deposited on the Si substrate uniformly and have formed a single monolayer.N_{SERS} was calculated by using the fact that the R6G molecules were also adsorbed on pyramidal Si uniformly. To ensure homogeneity, the SERS substrates were taken from three different points.

2.3.15 Electrochemical Workstation

A typical electrochemical cell consists of a reference electrode, a working electrode and a counter electrode which are immersed in an ionic conductor (electrolyte solution). We used CHI 660C electrochemical workstation which is interfaced with a computer system to perform all the electrochemical work. The substrate of interest works as the working electrode, a platinum wire acts as the counter electrode and Ag/AgCl (kept in 3 M KCl) worked as the reference electrode, thus forming a three-electrode system (Figure 2.15). The working electrode is placed as close as possible to the reference electrode to avoid a significant ohmic drop. The potential difference between the working electrode with respect to the reference electrode can

be controlled digitally. We represent all the potential with respect to the potential of Ag/AgCl electrode. The substrates were cleaned by acetone and ethanol before the measurement. Due to low cost and high conductivity $1M\ Na_2SO_4$ solution was used as the electrolyte.

2.3.16 FDTD Simulation Set Up for Different Structures

2.3.16.1 Endotaxial Ag

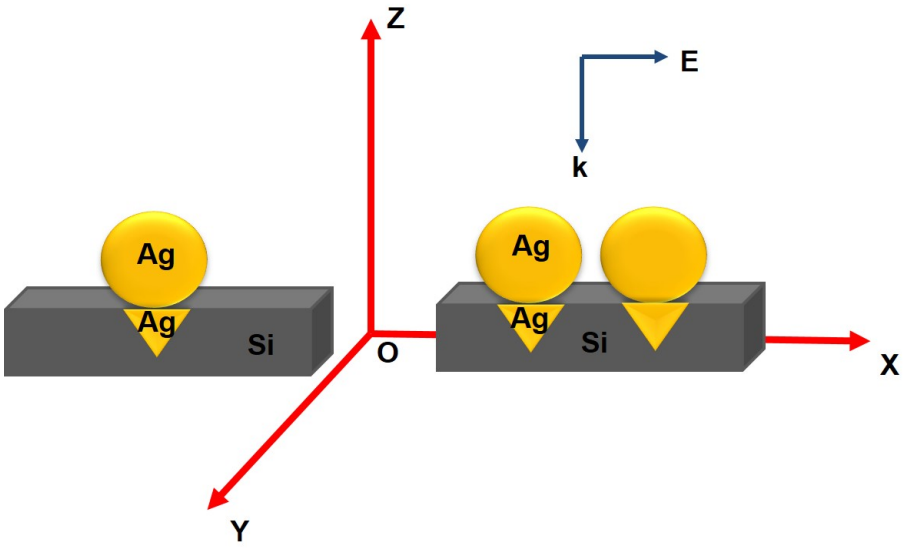

Figure 2.16: *Structural geometry used for FDTD simulation.*

3D FDTD simulation was used to obtain the near-field intensity distribution and SERS enhancement factor. According to TEM observation, the coupled Ag nanostructure was laid on Si substrate with embedded Ag triangle into the Si matrix. The geometry of the substrates and the coupled structure is shown in Figure 2.16. A TFSF source propagating along negative z-axis and having polarization

along the x-axis is used to excite the composite system. The total simulation region was taken as $500 \times 500 \times 500\ nm^3$ and PML boundary condition was applied in all directions. The simulation time was set as 500 fs so that all the energy decays out. Excitation wavelength with center at 632 nm and having a span of 100 nm on both sides was used. The field monitors were placed in the x-z and y-z plane to observe the near field intensity distribution.

2.3.16.2 Ag on Pyrmidal Si

The coupled nanostructure was taken as a combination of Ag sphere of radius 100 nm which is situated over a triangular Ag nanoparticle of side length of 155 nm according to SEM and TEM observations. The coupled system was placed on a pyramidal shaped Si of side length $2000 \times 2000 \times 2000\ nm^3$. The system was excited by a total-field scattered field source injecting along z-direction and having polarization along x-axis. The total simulation region was $1500 \times 1500 \times 1500\ nm^3$ and the boundary condition was taken as a perfectly matched layer. To give the energy field enough time to decay out simulation time of 500 fs was selected. The mesh size was set to $1.5 \times 2 \times 2\ nm^3$ for all the simulations. To understand the near field intensity distribution, field monitors were placed along y-z, x-y and x-z plane surrounding the nanostructure. An excitation wavelength of 632 nm was used for simulation purposes.

2.3.16.3 Ag on Pyramidal Si/Si-Nanowire Binary Structure

Ag nanoparticles were considered to be a sphere of 100 nm diameter situating at the top of Si-nanowire. The other parameters are the same as endotaxial Ag. The

mesh size was set as $1.5nm \times 2nm \times 2nm$ for all the measurements. The field-monitor was set at the x-z plane to observe the near field intensity distribution.

2.3.16.4 Pd on Different Semiconductor Substrates

The simulation geometry was arranged according to our observations in SEM and TEM. The initial Set up is same as described before, only the mesh sizes were taken as $1.5 \times 1.5 \times 1\ nm^3$ along x, y and z-direction respectively.

Chapter 3

Galvanic displacement reaction

This chapter describes the basic understandings on Galvanic displacement reactions (GDR) and metal-assisted chemical etching (MACE) on semiconductor and metals

3.1 Introduction

Metal semiconductor integration structure plays a very crucial role in modern IC technology. In recent days, the electrolytic process is used extensively which replaced aluminum (Al) with copper (Cu) based technology. Galvanic displacement process is obtaining intense attention nowadays. It has the potential to be used as the most adopted process for IC fabrication due to its simplicity, low-cost, and easy tunability.

In GDR, metal ions are reduced by substrate material when the substrate is immersed in the plating solution. The deposition requires no external powers source and a reducing agent [111]. So, understanding the reaction mechanism is very much important before going into the application of the GDR process.

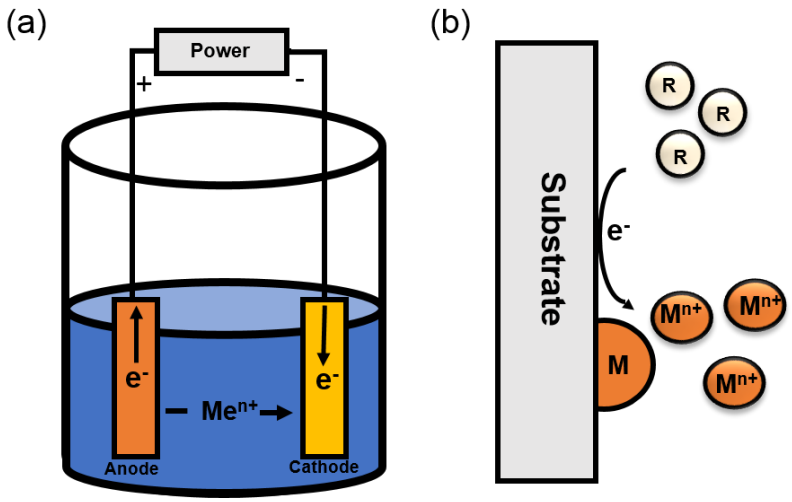

Figure 3.1: *Schematic of (a) Electrocatalytic process (b) Electroless process*

3.2 Electrodeposition Process

In an electrolytic process, substrate surface modification occurs in an electrolyte when an external voltage is applied between two electrodes as shown in Figure 3.1a. In a typical electrolytic process different properties of the film like film uniformity, film thickness, etc depends on electrolyte concentration, temperature, and external voltages. Electrolytic process can be divided into three categories:

3.2.1 Autocalytic and Substrate Catalytic Process

In autocatalytic process, the metallic ions are reduced in the solution in the presence of a reducing agent. The reducing agent spontaneously produces electrons to produce metallic ions. The reduction rate depends on the concentration and temperature of the reducing agent. As the name autocatalytic suggests, the oxidation-reduction process remains confined at the surface of the depositing metal. The deposition of Ni from hydrophosphite solution is an example of an autocatalytic process. Compared to electrodeposition process autocatalytic process has more control over film uniformity, thickness by simply adjusting electrolyte concentration and deposition time. In the substrate catalytic process the reducing agent can not reduce the metal ion from the solution and the deposition stops when the whole substrate is covered completely.

3.2.2 Galvanic Displacement Process

Compared to the substrate catalytic or autocatalytic process where the metal ions are reduced with the help of a reducing agent present in the solution. Galvanic displacement process does not require any such reducing agent. In this process, the substrate itself provides the electrons to reduce the metal ions. The reduction

potential of the substrate should be lower compared to that of the metal to make the reduction and the deposition process to continue. In this process, the reaction also stops when the entire surface is covered. Various parameters like temperature, plating time can be varied to control the growth rate.

GDR process is used for gold coating in ICs. HP group also produced gold nanoparticle decorated Si nanostructures using this process[112]. It is also used to produce nanoscale patterned surface, effective SERS active substrate and solar-cells [113].

In this thesis work, we have done GDR on Si and Ge substrate and hence it is very much important the electrochemical properties of them.

3.3 Si

Numerous investigations on the electrochemical properties of Si is reported already. A Schottky diode like formation occurs when Si is immersed in an electrolyte solution with the formation of a space charge layer at the junction. When Si is in contact with an unnoble electrolyte the dominant electron exchange occurs in the valence band. When Si is in contact with a noble electrolyte further electron exchange can occur with redox electrolyte in the presence of surface state of Si [111].

The standard reduction potential of Si with respect to a SHE is $-0.875\ V$. In most of the cases the GDR process for Si is carried out in HF solution, so understanding of Purbaix diagram which is the potential / PH diagram of $Si-F-H_2O$ system is important and is shown in Figure 3.2a. From the diagram, it is observed that Si is not thermodynamically stable in water and oxidized immediately as the

equilibrium line of Si lies below the equilibrium line of water to the H_2 reduction system. This diagram is used to determine electrolyte concentration, pH, and fluoride concentration for electrochemical reactions consisting of Si. At low pH, Si shows inert behavior due to native oxide formation. Using HF the oxide film can be dissolved at open circuit potential. In water solution and in the presence of fluoride ions, the formation of silicon hexafluoride occurs which readily gets dissolved. The surface in this process is passivated by the complete formation of Si-H termination bond. Depending on the pH of HF and NH_4F solution formation of $-SiH_2$ and $-SiH_3$ occurs. Figure 3.2b indicates the dissolution process of Si in the fluoride solution for different pH ranges (pH 4 to pH 8).

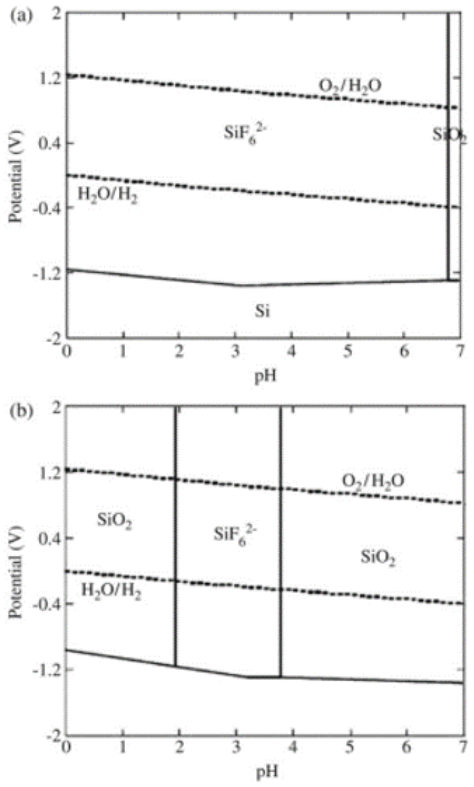

Figure 3.2: *(a) and (b) Potential-pH diagram for $Si-F-H_2O$ system for different concentration of F^- ion. Image: ref 111*

In presence of water molecule the Si-H surface bonds hydrolyzed at the kink site. Si gets dissolute through the weakening of the Si-Si back bond. For pH value of less than 4, no reaction takes place due to a very low concentration of F^- ions. For pH values of greater than 4, Si dissolution occurs through Si-H bond thermal activation. Fluoride ions play a crucial role in it. Finally, Si dissociates through the formation of the Si-F bond in the presence of the water molecule (Figure 3.3).

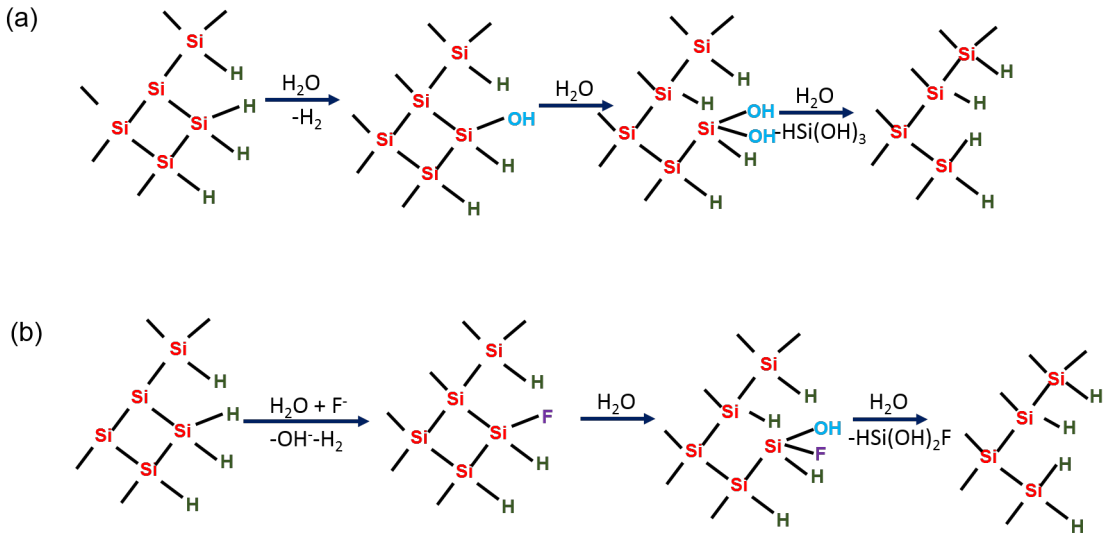

Figure 3.3: *Schematic of H-terminated Si dissolution in (a) water (b) in HF.*

the chemical reaction of redox couple is

$$M^{n+}(aq) + Si^0(s) + 6F^-(aq) = M^0(s) + SiF_6^{2-}(aq) \tag{3.1}$$

where s and aq indicates solid and aqueous phases respectively. The reaction process mentioned previously can be divided into two half cell reaction

$$M^{n+}(aq) + ne^- = M^0(s) \tag{3.2}$$

$$SiF_6^{2-}(aq) + 4e^- = Si^0(s) + 6F^-(aq) \tag{3.3}$$

$$E^0(Si^{4+}/Si^0) = -1.20V_{SHE} \tag{3.4}$$

the metal deposition rate in this process is proportional to HF concentration. The Si surface gets rough at the metal deposition points and after the reaction, the Si immediately gets oxidized at the defect positions (like steps, kinks, etc), which are more chemically active compared to the H^- terminated Si surface. The deposition rate can be controlled by introducing surface defects with ion bombardment and also the doping level of Si substrate affects the deposition rate.

3.4 Galvanic Displacement on Ge Substrate

However, galvanic displacement on Ge occurs without any external oxidant and since the reaction product, GeO is water soluble. The reaction goes as follow:

$$Ge + H_2O = GeO + H_2 \tag{3.5}$$

compared to Si, Germanium undergoes dissolution in various acidic media like H_2SO_4, $HClO_4$, and HCl.

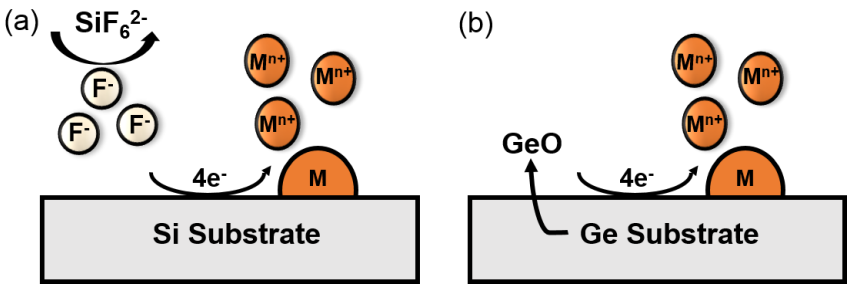

Figure 3.4: *Galvanic displacement process on (a) Si substrate and (b)Ge substrate.*

Thermodynamically GDR process is easier for metals with high redox potential.

Deposition of gold, silver, palladium are easier compared to Cu and Ni. The redox potential for different metals is listed in Table 3.1.

Elements	**Redox potential(in V)**
Au^{3+}/Au	1.42
Ag^{+}/Ag	0.8
Cu^{2+}/Cu	0.34
Pt^{2+}/Pt	1.2
Pd^{2+}/Pd	0.83
Ru^{2+}/Ru	0.8
Ni^{2+}/Ni	-0.23
Ge/Ge^{4+}	-0.12
Si/Si^{4+}	-0.86

Table 3.1: *Standard redox potential of different of different elements.*

3.5 Displacement of Noble Metals

The reduction of noble metal nanoparticles by Si in an aqueous solution of fluoride ion is very much important in the microelectronic industry. As fluoride ions are used to etch the native oxide from Si surface, metal contamination will lead to deposition of undesirable metal deposition which will affect the performance of the device. Balashova *et al.* and Krikshtopaitis *et al.* studied the deposition of Cu and Au metal on Si and Ge in the presence of fluoride ion about forty years ago [114]. They observed that the deposition rate gradually decreases with time.

Morphology of Au film deposited on Ge (111) and on Si (111) was studied by Magagnin *et al.* They found that the adhesion of Au film with Si is weak. However, they observed a strong adhesion of Au on Ge substrate [35, 115, 116]. This is attributed to the formation of a chemical bond between Au and Ge. Pt and Pd were observed to form such kind of chemical bonds with both Si and Ge.

Different kinds of Ag nanostructures were produced on Si and they showed very good SERS properties. However, oxidation always leads to decrement in the SERS properties of the substrates [90, 117]. In this thesis work, we have shown that rapid thermal annealing at the O_2 atmosphere increases the SERS activity of Ag nanoparticles due to the formation of a special composite structure. The GDR process occurs in a mixed solution of silver nitrate ($AgNO_3$) and HF. The reaction equation can be written as,

$$Si(s) + 6F^-(aq) + 4Ag^+(aq) = 4Ag(s) + SiF_6^{2-} \tag{3.6}$$

The reduction equation is

$$Ag^+(aq) + e^- = Ag(s)$$

(3.7)

There are many steps which are rate-determining:

(i) Ag^+ diffusion on Ag surface.

(ii) Diffusion of F^- ion and its reaction with Si to finally produce SiF_6^{2-}.

(iii) Dissorption of SiF_6^{2-}.

Overall the growth rate is dominated by diffusion of Ag. As metallization is very much important for the production of integrated devices, Cu is used to replace Al to fulfill the requirement of metal on MEMS devices. Copper deposition by GDR is studied extensively and it is observed to show a very good adhesion with Si.

3.5.1 Displacement of Pt group metals

The Pt group metals (Pt, Pd) show very good catalytic properties [26, 94, 95]. Also, they possess very good stability at high temperatures. The SERS effect of Pd is studied for many years but the EF is observed to be very low [39, 118, 119]. In this thesis work, we have shown that Pd substrate can be very useful as both SERS active substrate and as an electrochemical sensor of glucose and AA.

Gorostiza *et al.* studied the growth of Pt on Si (100) in HF solution. They observed the formation of Pt nuclei along with Si etch pits [120]. Compared to Pt on Si, Pd on Si, Ge is less studied and to the best of our knowledge, no report exists on the growth of Pd on patterned Si. High purity Pd film deposition on Si and Ge substrates was observed by Ye *et al.* [121]. The substrate acts as a reducing agent and high purity Pd film occurs to deposit at the substrate surface.

3.5.2 Effect of Surfactants

As modulation of nanostructure is very much important for different applications like SERS, electrochemistry, etc. Different surfactants like PVP, AA were used to control the growth rate of the nanoparticles for Au, Ag, and Pd [122]. Differently shaped Ag nanoparticles were obtained by using PVP and by reducing silver nitrate solution at 160^oC. Also, Ag can be used as a template to form Au nanostructure as Au^{3+} ion etches Ag atoms from Ag nanoparticle surface. Differently shaped Pd nanoparticles are also produced using PVP as a surfactant [39]. However, removing the surfactant is not possible for the nanoparticles deposited on substrates. So, the SERS enhancement of these nanoparticles will be very much affected by the surfactants. In this thesis work, we have shown that by varying the substrate morphology the metal deposition rate can be controlled. This can lead to different

shaped nanostructure for the same deposition condition.

3.6 Metal Assisted Chemical Etching

Semiconductor nanowires have potential applications in thermoelectrics, optoelectronics, photovoltaics, and also in chemical and biological sensors [123–125]. The remarkable mechanical, optical, and electrical properties are due to their high surface to volume ratio and quantum effect. However, it is very much important to tune their structure efficiently for the above-mentioned applications. Bottom-up growth processes like CVD, MBE were used to produce Si nanowire, but these processes require very much sophisticated instrumentation, time and hence complicated [126, 127]. Metal-assisted chemical etching process is used nowadays to produce Si nanowire because this process is very much easy and does not require any heavy instrument.

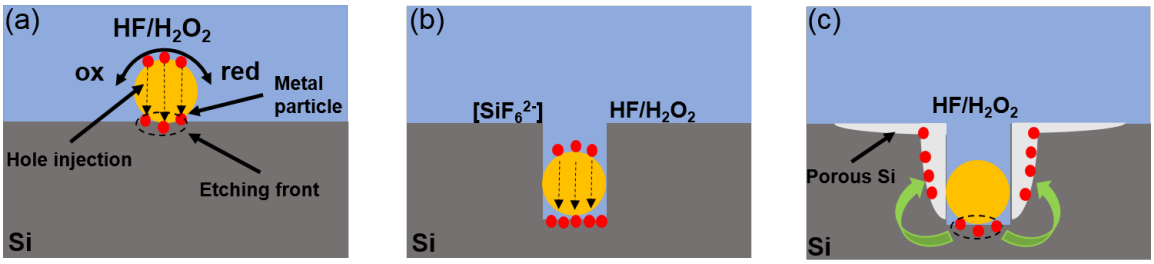

Figure 3.5: *Different steps of metal-assisted chemical etching process for an isolated metal nanoparticle. (a) Reduction of H_2O_2 at the meta particle surface and insertion of hole into the Si surface (b) oxidation of Si surface and subsequent dissolution leads the metal particle to penetrate inside the substrate (c) diffusion of holes towards the Si surface and subsequent oxidation of Si leads to formation of porous Si.*

In this process, a noble metal film (like Au, Ag, Pt, Pd) is first deposited on the

substrate (Figure 3.5a). In the second step, the etching occurs in a solution consists of HF and an oxidative agent. All of this can be performed in a chemical lab making this process cheap and appropriate for mass production. Due to such simplicity compared to other processes research on MACE process is growing rapidly and a substantial amount of work has already been done. Li and Bohn in 2000 observed formation of channels on Si substrate [128]. The channel formation occurs when noble metal films deposited on the substrates are placed in a solution consists of HF and oxidative agent. Chartier *et al.* observed the formation of porous Si at the channel walls and underneath the film [129]. However, the exact explanation of the formation process is still not feasible. Different mechanisms are proposed to explain this phenomenon.

During MACE, holes are generated at the junction of the electrolyte and the metal particles by a redox reaction. The metal particles act as a catalyst in the reduction of the oxidative agent (H_2O_2). The generated holes than reach to the Si surface through the metal particles. The electrolyte containing HF reach to the gap between the metal particles and Si. As a result of this, the oxidized Si dissolves and gets removed from the substrate surface. The particles sink into Si and the process continues (Figure 3.5b). The concentration of holes is maximum at the junction of metal particles and Si and the etching permanently occurs at this point. The etching reactions can be written as

$$H_2O_2 + 2H^+ = 2H_2O + 2h^+ \tag{3.8}$$

$$Si + 2H_2O + 4h^+ = SiO_2 + 4H^+ \tag{3.9}$$

$$SiO_2 + 6HF = H_2SiF_6 + 2H_2O \tag{3.10}$$

Porous Si is also formed in this process in the regions far from the metal particles (Figure 3.5c). Because the density of holes decreases as we go far from the metal particle and in these places Si only dissolved locally producing porous Si. However, the porosity of Si can be effectively controlled by the HF/H_2O_2 ratio. At high H_2O_2 concentration porosity of Si is observed to increase. Also by creating a local density variation in this ratio zig-zag Si nanowire can be produced. In this thesis work, we have shown that the sidewalls of Si nanowire produced from planar Si and pyramidal Si are very much different and the HF/H_2O_2 ratio is mainly responsible behind this. The concentration of Ag^+ ions also plays a very decisive role behind this. Geyer *et al.* have observed that as soon as Ag^+ ions are removed from the solution etching stops and no channel formation occurs.

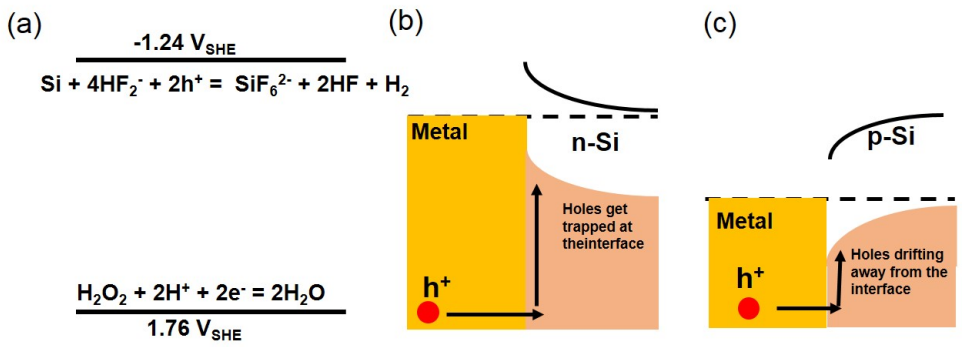

Figure 3.6: *(a) Schematic of reduction potential for the two MACE half reaction process vs V_{SHE} (b) and (c) Au-Si interface band diagram for n-type and p-type Si substrate respectively.*

Ruby A. Lai proposed a Schottky barrier catalysis mechanism behind the MACE process [130]. By using this mechanism they could explain the dependence of MACE process on doping concentration, doping type, and etchant solution

composition. According to their mechanism, the metal ions not only participate in catalyzing the oxidation but they also form a Schottky type barrier with the Si at the junction which controls the spatial dispersion of the holes. The band-bending in an n-type Si occurs such that it can trap more injected hole at the surface, which promotes the oxidation and dissolution of Si (Figure 3.6a). For a p-type Si the band bending occurs such that it cannot trap most of the injected holes at the surface and results in slower oxidation and dissolution of Si (Figure 3.6b).

Chapter 4

Structural Study of Nanoparticles Deposited on Semiconductor Substrates by Electroless Method

---

This chapter describes the structural study of different noble metal (Ag, Au and Pd) nanoparticles using SEM, TEM and XRD method.

4.1 Introduction

The LSPR and other near and far-field optical properties (*i.e.*scattering, absorption of nanomaterials are heavily dependent on the size, shape and interparticle distances [21–25]. On the other hand, the final morphology of nanoparticles deposited on substrate is highly dependent on the growth rate, substrate type and on the nanoparticle-semiconductor interface. Hence, to correlate the optical and catalytic properties of nanostructure with its morphology a detailed structural analysis is very much required. XRD can provide a rich information on different structural parameters but it always show an average measurement taken over an ensemble of particle.So, to make a direct space single particle observations on the growth rate, morphology and interfaces, electron microscopy measurement is very much required. SEM can give us both topographic and elemental information by SE and BSE imaging method. However, it is unable to give an atomic scale information. To obtain a real space atomic scale information TEM is used. It can provide a very precise measurement about the size, shape, inter-atomic spacing of a single nanoparticle with a minimal error. Also, from the EDX imaging and mapping a clear visualization about the location of different constituent elements can be obtained very easily. These special features make TEM a very efficient instrument in nanoscience. In this chapter, we will describe a detail structural characterization of the growth and morphology of metal nanoparticles (Ag, Au and Pd) deposited on planar and patterned semiconductor (Si, Ge) substrates by GDR method and their structural evolution due to RTA process in different atmosphere.

4.2 Structural Evolution of Ag Deposited on Planar Si

4.2.1 Morphology: SEM Analysis

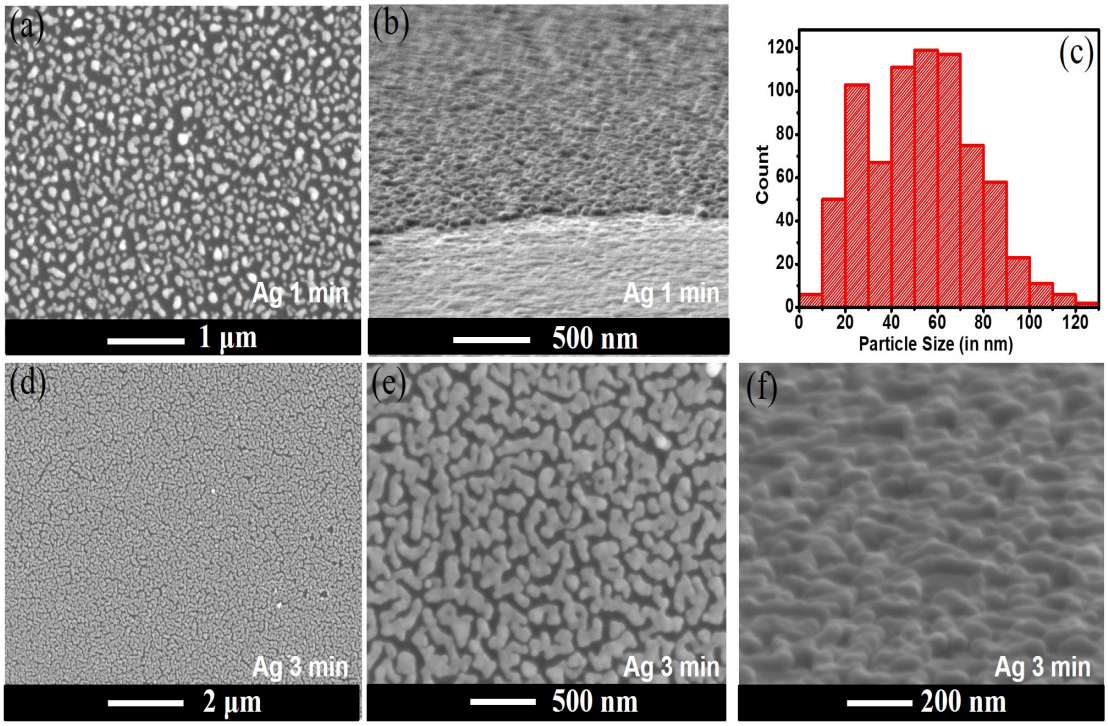

Figure 4.1: *SE image of (a) Ag deposited on Si* (100) *by galvanic displacement method for* 1 *minute, (b) Bird's eye view of (a), (c) Histogram of particle size distribution, (d) Ag deposition on Si for* 3 *minutes, (e) magnified view of (d) showing a spaghetti-like structure, (f) Bird's eye view of (d) showing a flat top morphology of Ag nanoparticles.*

SE image of Ag nanoparticles, deposited on planar Si(1 0 0) substrate for 1 *minute* deposition time is shown in Figure 4.1a. From SEM images 37% coverage and an average particle size of 52.9 ± 11.1 *nm* are obtained. Figure 4.1b shows the flat top surface of the particles and with increasing the deposition time we obtain higher coverage of 78% as observed from Figure 4.1d. The Ag nanoparticles initially

remain disconnected and for higher deposition time they extended and finally form a percolated network (Figure 4.1e). The percolation process seems to increase the particle uniformity and the surface remains flat (Figure 4.1f). Ag follow SK or layer plus island growth mode [137].

4.2.2 Study of Crystallinity: XRD analysis

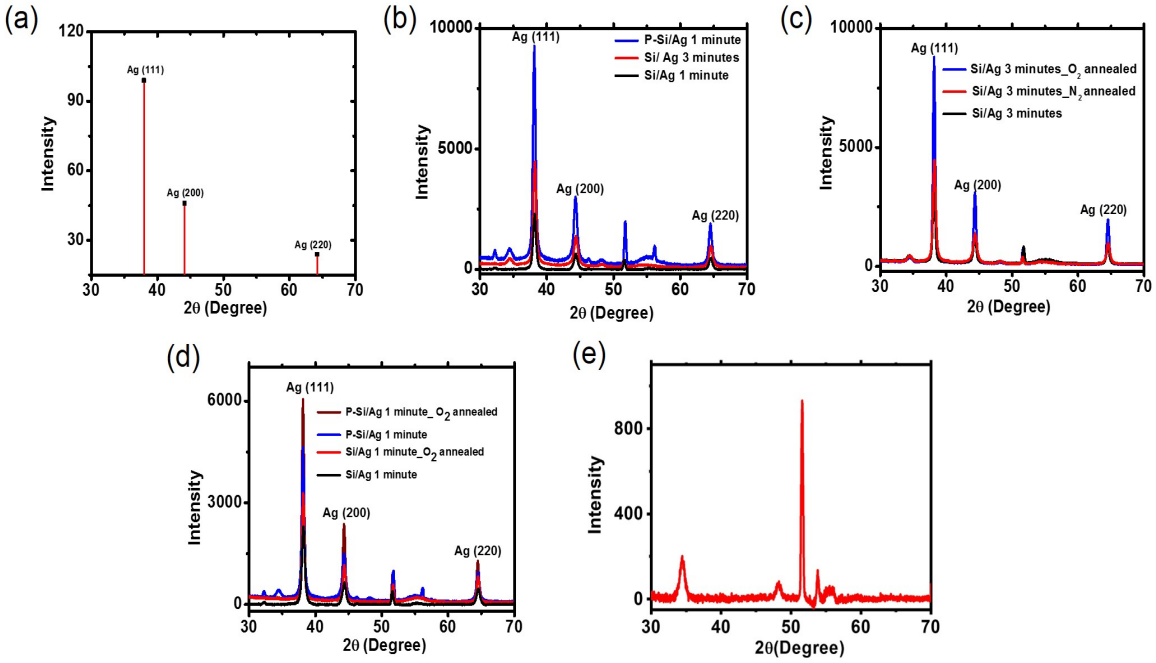

Figure 4.2: *(a) XRD peaks of cubic Ag according to JCPDS data. (b) XRD pattern of Ag deposited on Si for* 1 *minute and* 3 *minutes, respectively. (c) XRD pattern of Ag deposited on Si for* 3 *minutes and annealed at* N_2 *and* O_2 *atmosphere, respectively. (d) Ag deposited for* 1 *minute and annealed at* O_2 *atmosphere for planar Si and P-Si, respectively (e) GIXRD pattern of blank Si*

Figure 4.2 shows the crystallinity of the substrates obtained from GIXRD measurement. The peaks obtained corresponds to (1 1 1), (2 0 0) and (2 2 0) plane of cubic Ag (JCPDS card No. $87-0597$, space group. Fm-3m). The un-identified peaks are arising from Si substrate as shown in Figure 4.2e. The peak intensity

corresponds to Ag (1 1 1) plane is most intense as it has lowest surface energy and hence, most Ag atoms got oriented in this direction to remain in stable thermodynamic state. The sharp nature of the peaks indicates a high crystallinity of Ag. Figure 4.2a shows the XRD pattern of Ag according to JCPDS data. Figure 4.2b shows the XRD pattern of Ag deposited in Si for 1 *minute* and 3 *minutes*, respectively. Table 4.1 shows the grain size of different samples which were calculated using Scherrer's formula [138].

Substrate	**Average Crystalline Size (in nm)**	**Standard Deviation (in nm)**
Si/ Ag 1 *minute* deposition	14.5	1.3
Si/Ag 1 *minute* deposition O_2 annealed	18.3	1.1
Si/ Ag 3 *minutes* deposition	14.9	1.8
Si/Ag 3 *minutes* deposition O_2 annealed	20.4	0.8
Si/Ag 3 *minutes* deposition N_2 annealed	18.1	1.1
P-Si/Ag 1 *minute* deposition	16.9	1.8
P-Si/Ag 1 *minute* deposition O_2 annealed	21.3	0.8

Table 4.1: *Average crystallite size with standard deviations from the XRD measurement.*

This clearly shows the increment in the grain size due to increased deposition time and annealing. Also, it is observed from Figure 4.2c that when as-deposited Ag substrates are annealed at O_2 and N_2 atmosphere, respectively, the increment in the grain size is more for annealing at O_2 atmosphere which shows enhance mobility of the Ag adatoms during annealing at O_2 environment. The absence of any Ag oxidation peak indicates that the Ag particles are in their pure metallic form. Figure 4.2d shows an increment in the Ag crystallite size when they are deposited on pyramidal Si indicating a higher growth rate of Ag on pyramidal Si compared to planar Si.

4.2.3 Structural Study: TEM Analysis

Figure 4.3a shows BF TEM image of 1 *minute* Ag deposited on planar Si(100). The average particle size is 55.7 ± 11.9 nm, which matches well with SEM measurement. The average height is peaked at 57.8 nm with an aspect ratio of 0.46. The STEM-HAADF image is shown in Figure 4.3b. Figure 4.3c shows the EDX mapping obtained from the orange rectangle in Figure 4.3b. It shows the presence of Ag on Si and no penetration of Ag into Si is observed in this case. Formation of the Moiré pattern is observed from Figure 4.3d which occurs due to the overlap of Ag(1 1 1) and Si(1 1 1) plane. The FFT image (Figure 4.3e) shows a slight rotation of 4.16^o of Ag(1 1 1) with respect to Si(1 1 1) plane. Such kind of epitaxy is very much unique and reduces the interfacial strain significantly. Epitaxial formation of Ag on Si is evident from Figure 4.3f. Figure 4.3g shows the high-magnification BF XTEM image of the same. XTEM images in Figure 4.3h and Figure 4.3i shows formation of quasi-continuous Ag layer due to 3 *minutes* deposition time. This

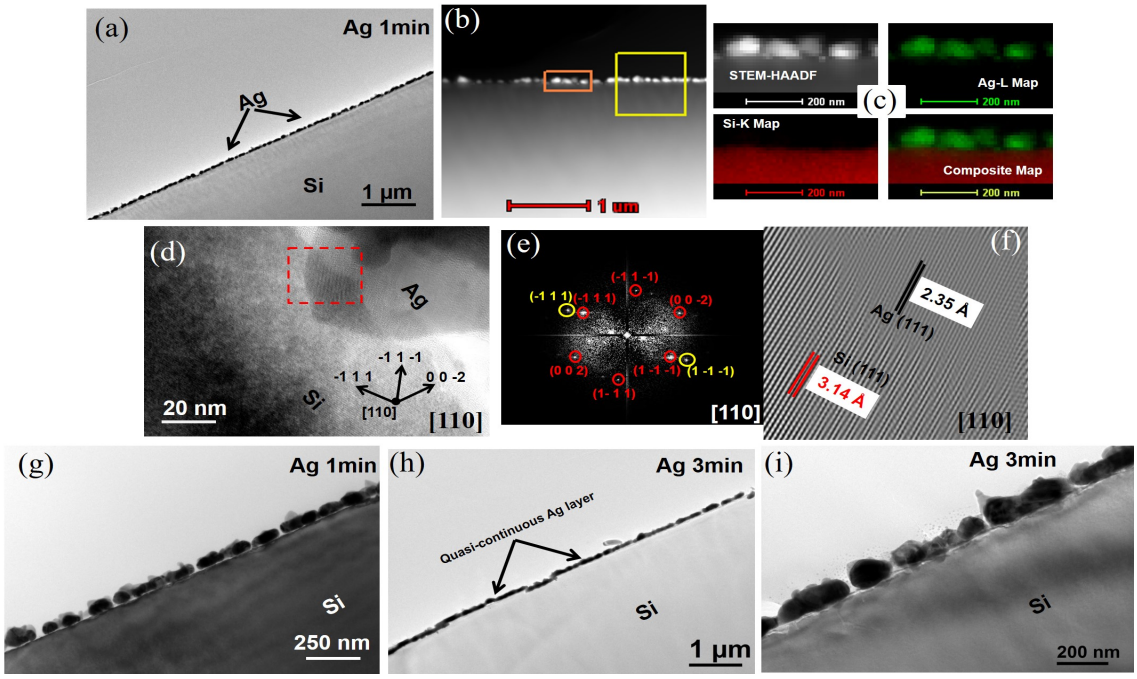

Figure 4.3: *(a) Low magnification BF XTEM image showing Ag deposition on Si for* 1 *minute, (b) STEM-HAADF image (c) STEM-HAADF image from the area marked by the rectangular portion in (b) and corresponding EDX maps (Ag-L map, Si-K map and composite map), (d) HRTEM image of the interface between Ag and Si. (e) and (f) FFT pattern and inverse FFT image from the region marked by red square in (d), respectively, (g) High magnification image of (a) showing almost identical height of the nanoparticles, (h) Low magnification bright-field image of* 3 *minutes Ag deposition on Si showing the formation of quasi-continuous layer, (i) High magnification image of (h).*

structure corresponds to the spaghetti-like formation as described earlier. The aspect ratio obtained in this case is 0.32 indicating a faster growth rate along the lateral direction of the particles with increasing deposition time.

Both 1 *minute* and 3 *minutes* deposited Ag on Si, the particles become spherical after annealing at O_2 atmosphere at 550^o C for 1 *minute* (Figure 4.4a). The average particle size for S1 and S2 is obtained as 121.1$\pm$26.3 *nm* and 253.8$\pm$56.5 *nm*,

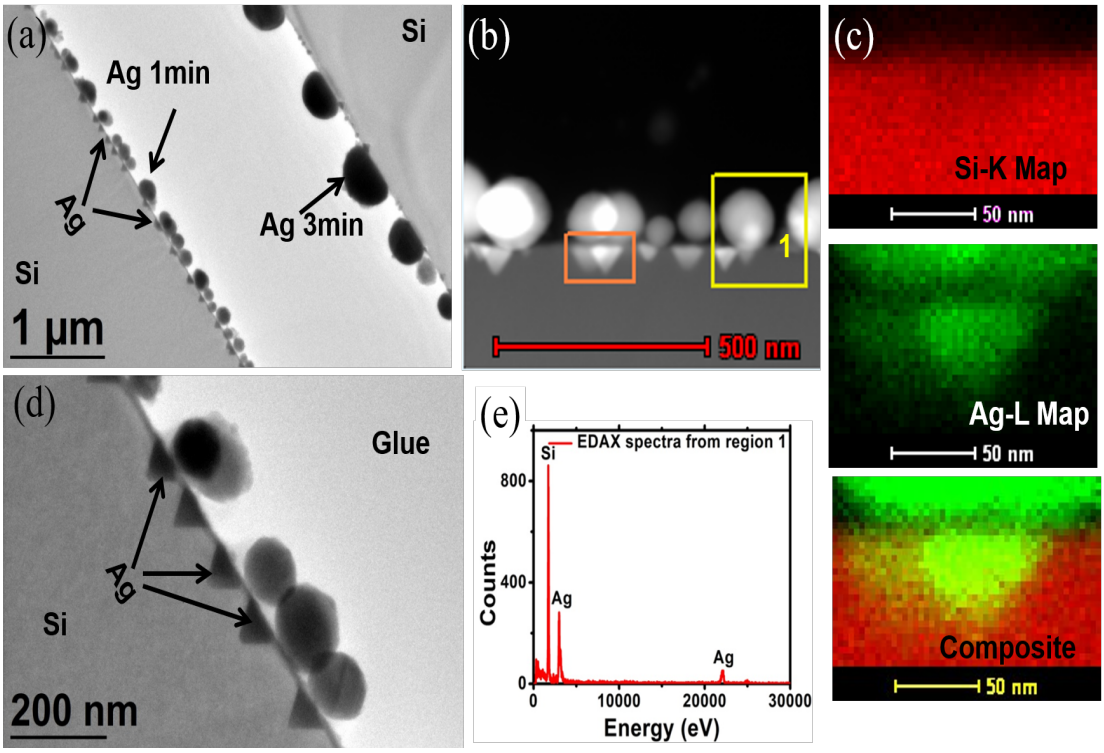

Figure 4.4: *(a) Low magnification BF XTEM image of S1 and S2, (b) STEM-HAADF image of S1, (c) EDX elemental map from the rectangular region in (b), (d) Enlarged view of S1 showing the formation of buried Ag nanoparticle, (e) EDX spectrum from region 1 in (b).*

respectively. Which shows an almost two times increment from the as-deposited sample. Due to the "OR" process, the smaller particles get dissolved due to their high surface energy and the bigger particles increases in size resulting in a decrement in the particle density. In addition to the spherical particles, triangular like particles are also observed inside the Si substrate. However, there is a clear variation in the size of triangular particle obtained from S1 and S2 as obtained from Figure 4.4a. The insertion length of the triangular nanoparticles for S1 and S2 is 60.1 ± 11.7 and 42.4 ± 6.7, respectively. The metal nanoparticles remain in a highly unstable configuration at the substrate due to their high surface energy, so when

the substrate is rapidly annealed, the enhanced kinetics helps the nanoparticles penetrate into Si via interstitial-substitutional reaction [139]. Also, Si tends to diffuse through Ag at temperature $150-200^{o}\,C$, which helps Ag to completely buried into Si and finally to produce the endotaxial structure. From interface energy consideration, if the interface energy σ_{Ag/SiO_2} is less than σ_{Ag} then the nanoparticles will get embedded into the Si. Now the surface energy for Ag is $\sigma_{Ag} = 1.25Jm^{-2}$ and that for SiO_2 is $\sigma_{SiO_2} = 0.29Jm^{-2}$. The value of the surface energy of the interface can be obtained from Young's equation which can be written as [139],

$$\sigma_{Ag/SiO_2} = \sigma_{SiO_2} - \sigma_{Ag}\cos\theta \tag{4.1}$$

The average contact angle of the nanoparticles with the substrates was obtained as $137.3^{o} \pm 6.6^{o}$, was calculated from different TEM images. Considering this, the value of σ_{Ag/SiO_2} comes as 1.209 which definitely lower than the value of σ_{Ag}. Hence, the formation of endotaxial structure is thermodynamically favorable. As the particles in S1 have a lower CA compared to that of S2, the number of endotaxial particles will be greater in the case of S2 compared to that of S1, that is the present case. The endotaxial particles get elongated along the substrate surface and they form a sharp Ag-Si interface. Figure 4.4c shows the EDX elemental map from the orange rectangular shown in Figure 4.4b, which clearly shows the embedded particles are indeed Ag. An almost one to one correspondent relationship is observed between the spherical Ag and triangular Ag from Figure 4.4d.

The formation of endotaxial structure is only possible when there is direct contact between Ag and Si. Such kind of direct contact is obtained in GDR process

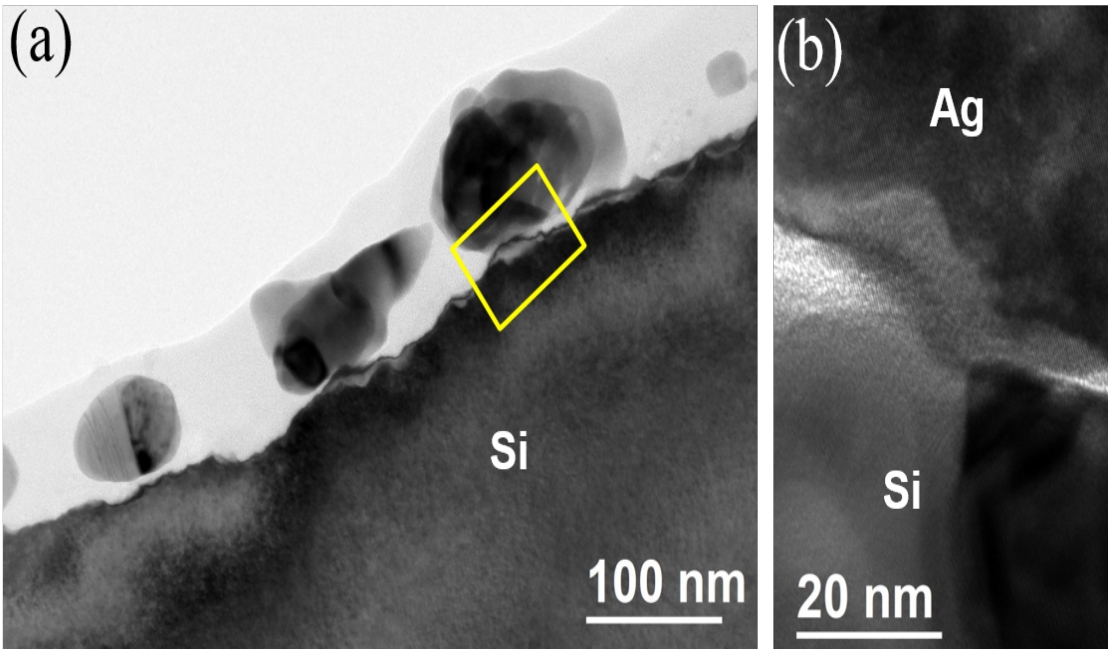

Figure 4.5: *(a) Bright-field XTEM image of 1minute Ag deposition on Si (100) showing formation of direct contact points between Ag and Si, (b) Enlarged view from the region bounded by yellow rectangle in (a).*

and is shown in Figure 4.5. Oxidized Si layer at the interface can prevent the penetration of Ag into the Si matrix. However, the rapid ramp rate during RTA heating ruptures the oxidized Si layer and made the penetration possible. Such kind of endotaxial Ag formation was not seen when Ag is normally annealed at the same temperature in the presence of the O_2 atmosphere.

4.2.4 HRTEM Analysis of Endotaxial Particles

The thinnest portion was taken for HRTEM analysis and the image is shown in Figure 4.6a. The arrows indicate different crystallographic directions. The FFT image (Figure 4.6b) taken from region 1 of Figure 4.6a shows epitaxial relationship

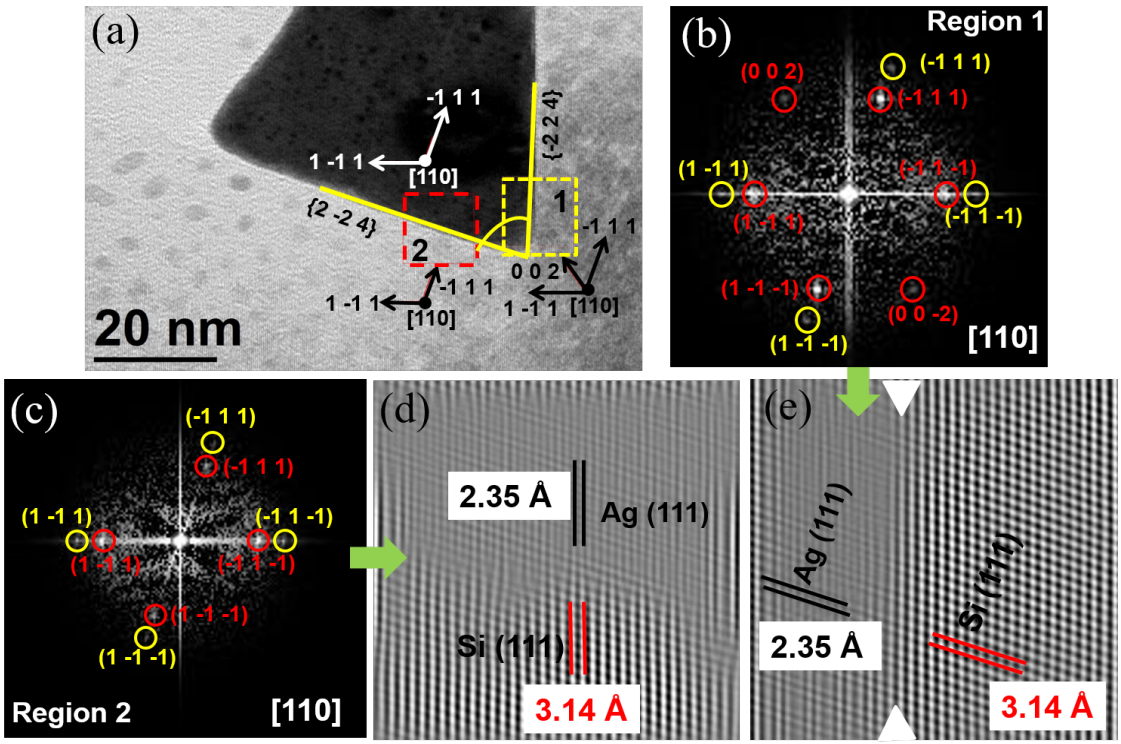

Figure 4.6: *(a) HRTEM image of an endotaxial particle for sample S*1*, (b) and (c) are FFT patterns from the region 1 and 2 in (a), respectively showing epitaxial relationship between Ag and Si on both facets, (d) and (e) IFFT image of (c) and (b), respectively showing orientation of Si (1 1 1) and Ag (1 1 1) plane along the facets.*

between Si and Ag as, $Si(-111)\|Ag(-111)$ and $Si(1-1-1)\|Ag(1-1-1)$ parallel planes,and in both the cases the in-plane direction is $Si[110]\|Ag[110]$.

The same epitaxial relationship is obtained from the FFT image taken from region 2. All measurement was done by aligning the sample along [1 1 0] zone axis. In this case, also the epitaxy between Si and Ag is obtained via DME process. The lattice mismatch between Si (111) and Ag (111) plane is about 25% but in DME process a 3×3 domain of Si matches with a 4×4 domain of Ag and reduces the

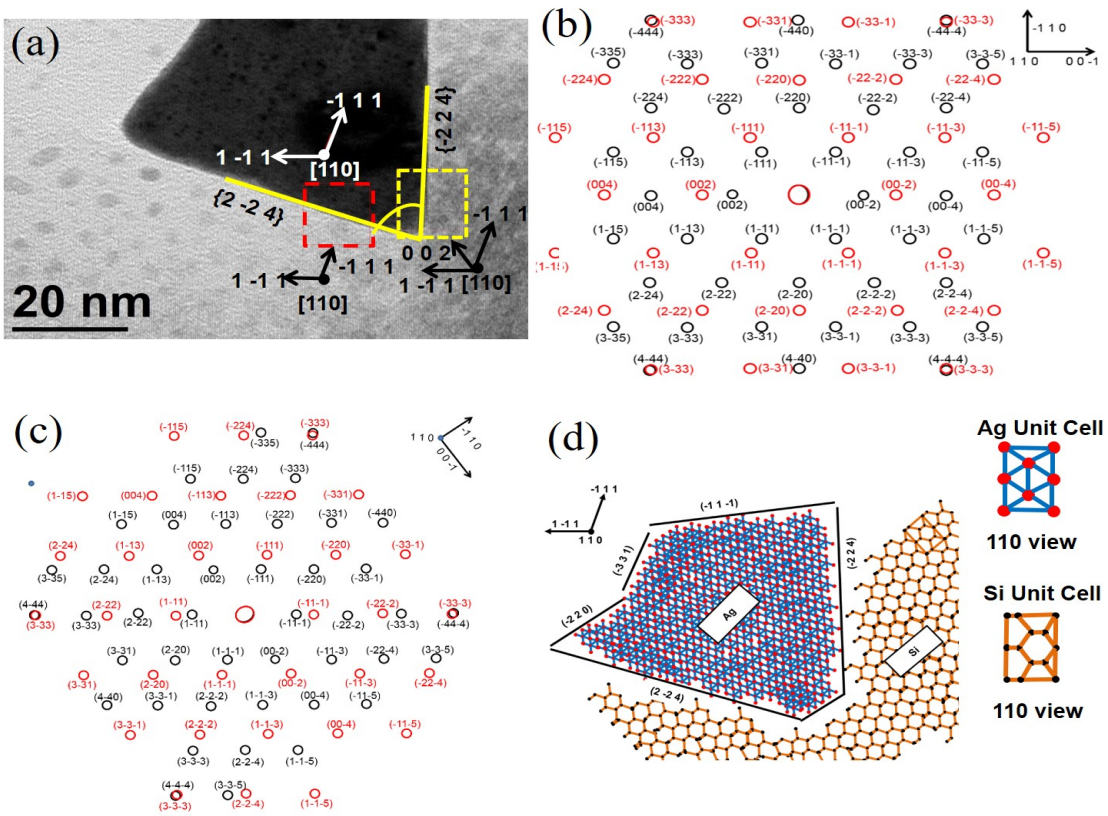

Figure 4.7: *(a) HRTEM image of an endotaxial Ag particle in Si which is taken as reference to analyze the structure, (b) Simulated diffraction pattern of Si and Ag along 110 zone axis, (c) rotated diffraction pattern (57 clockwise) to obtain similar FFT pattern showed in Figure 4(b). (d) Reformation of endotaxial particle of (a) showing the facet directions, the [110] view of Ag and Si is also shown.*

lattice mismatch to 0.6% only, resulting epitaxial growth. No formation of clustering or defect was observed along the interface of the embedded nanoparticle. According to Martin *et al.* the small distortion generated in this case is averaged out by a large number of Si atoms situated below, resulting absence of any significant defects along the interface [140]. The dominant epitaxy was observed to occur along [-1 1 -1] and [-1 1 1] direction from Figure 4.6c and Figure 4.6e, respectively. Figure 4.7 shows the BF TEM image of an endotaxial structure which was taken

for detailed structural analysis. Crystal Maker software (CrystalMaker Software Ltd, UK) was used to obtain the view of unit cell of Ag and Si along [1 1 0] zone axis and their corresponding simulated diffraction pattern which is shown in Figure 4.7b. The previously obtained diffraction pattern shown in Figure 4.7b was obtained by rotating the simulated diffraction pattern in the x-y plane by 57^o. The crystal structure finally shown in Figure 4.7d is almost similar to that shown in Figure 4.7a. This shows that -224 and $2-24$ facet bound the particle from both sides with $3-31$ facet connecting them. $2-20$, -331 and $-11-1$ facet consist the upper surface of the particle.

Figure 4.8a shows the STEM-HAADF image of S2 sample and Figure 4.8b shows the EDX elemental mapping taken from the orange rectangular region of Figure 4.8a. This shows that the number and length of the endotaxial structures reduce greatly in number compared to S1. The bright-field TEM image of S1 is shown in Figure 4.8c. Figure 4.8d shows the bright-field TEM image of the sample annealed at N_2 atmosphere showing the formation of only spherical shaped particles due to OR process.

Effect of aging on the samples S1 and S2 were also studied through HRTEM analysis after keeping the samples in the ambient atmosphere for 1 month. BF TEM image of the two samples is shown in Figure 4.9a. The lower portion shows S1 sample and the upper portion shows sample S2. For S1, the average insertion length was found to be $58.8 \pm 8.1\ nm$. The shape of the spherical particles was observed to deviate significantly for both S1 and S2. Some defects were observed

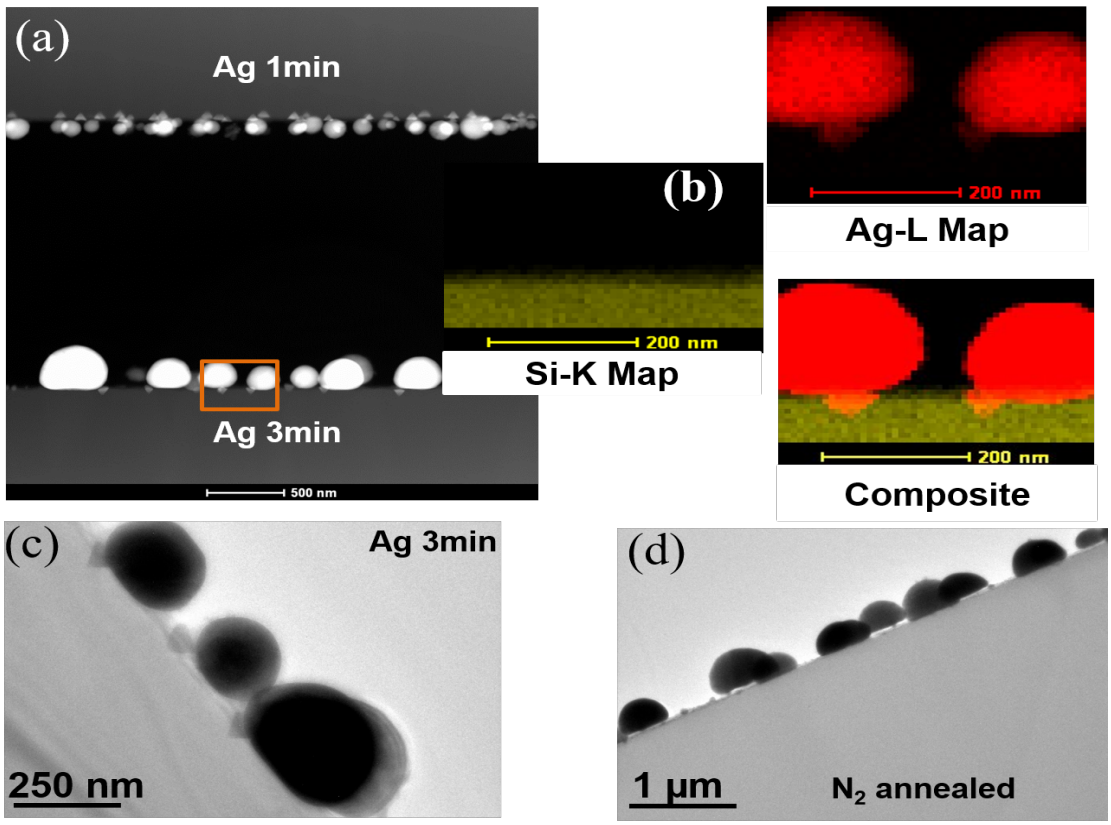

Figure 4.8: *(a) STEM-HAADF image of S1 and S2, (b) EDX elemental mapping from region bounded by the orange rectangle in (a), (c) XTEM image of S2, (d) XTEM image of Ag deposited for 3 minute and N_2 annealed (S3).*

at the interface between endotaxial Ag and Si due to interfacial strain as shown in Figure 4.9c. The high-magnification image (Figure 4.9c) clearly shows the deviation in shape for the spherical particle while the endotaxial particles remain same as before. A layer of SiO_X was observed to form on almost at the top of every Ag particle and is shown in Figure 4.9d. EDX elemental map shown in Figure 4.9f confirms the presence of Si and O on top of the Ag particle surface.

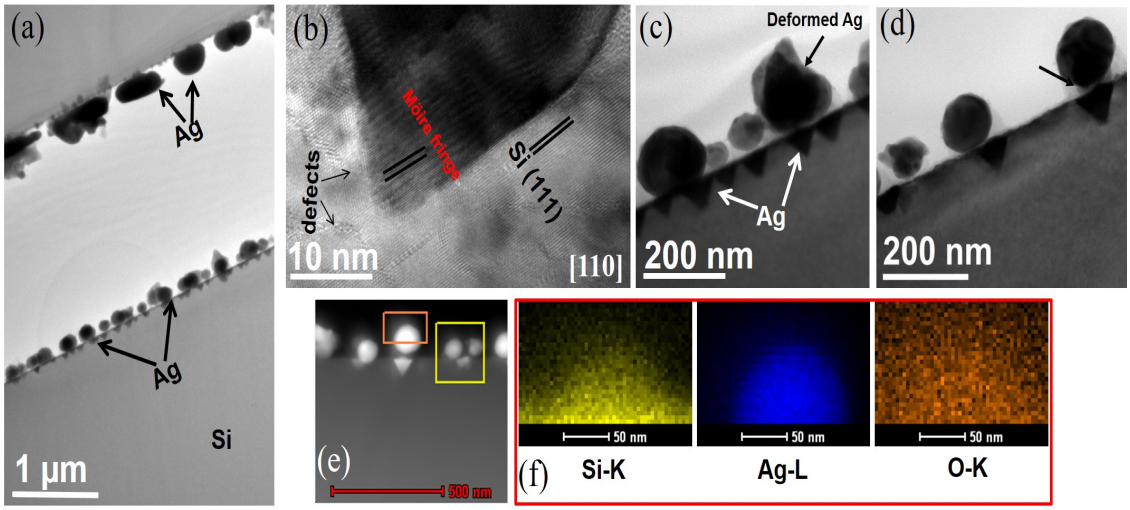

Figure 4.9: *(a) STEM-HAADF image of S1 and S2, (b) EDX elemental mapping from region bounded by the orange rectangle in (a), XTEM image of S2, (d) XTEM image of Ag deposited for* 3 *minute and* N_2 *annealed (S3).*

Unlike planar Si, Ag particles formed a percolated network after 1 *minute* deposition on pyramidal Si which is shown in Figure 4.10a. Figure 4.10b shows the XSEM image of the same. We previously observed that Ag particle grow heteroepitaxially on pyramidal Si by making a tilt angle to reduce the interfacial strain. After annealing the substrate at 550^o C for 1 *minute* in O_2 atmosphere combined triangular and spherical Ag formed on Si substrate as shown in Figure 4.10c. The triangular particle does not get embedded in the Si matrix in this case and they form along the slope of the pyramid, which is evident from the STEM-HAADF image (Figure 4.10d). During annealing at the N_2 atmosphere, only spherical particle formation seems to occur as shown in Figure 4.10e.

So, the formation of triangular particles is observed only in the case of annealing at O_2 atmosphere and not in N_2 atmosphere. Step brunching, faceting, and pitting of metal nanoparticles can be induced by adsorbates like O, S (X) etc. O

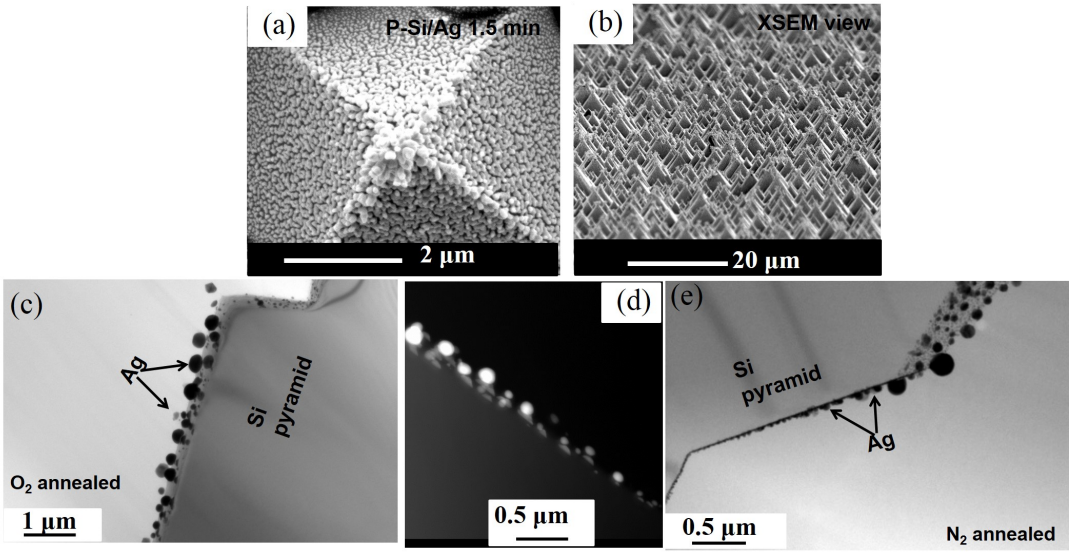

Figure 4.10: *(a) SE image of Ag deposited for* 1 *minute on P-Si substrate, (b) XSEM view of (a). (c) BF XTEM image of* O_2 *annealed Ag on P-Si showing the formation of the triangular particle in addition to spherical Ag. (d) STEM-HAADF image of (c) showing the position of Ag triangle on the substrate, (e) BF XTEM image of* N_2 *annealed Ag on P-Si showing the formation of only spherical particle.*

was observed to increase the kinetics of Ag ad-atoms resulting formation of Si lattice defect [141–144]. The localized stress in Si formed triangular etch pits, which act as the nucleation center for the triangular particle. Metal particles(M) form a cluster with the chalcogens and this changes the mass transport process. The cluster (M-X) dominants the transport process instead of a single metal atom. On the dielectric substrate, they are observed to transform freely compared to metallic counterpart [143]. So during annealing at O_2 atmosphere, an ad-species called Ag_mO is formed which transport Ag through the substrate. This Ag_mO decomposes to Ag whenever they hit the surface of another Ag [139]. They preferably stick to the edges than to the surface of the Ag and leads to the formation of triangular Ag. The formation occurs along Si [111] direction to minimize the surface

energy and triangular particle forms along the slope of the pyramid. While the reason behind the formation of the endotaxial structure was explained previously.

4.3 Effect of Annealing on Gold Thin Film on Silicon Surfaces Deposited by Electroless Deposition

4.3.1 TEM Analysis

The thickness of the Au film is $87 \pm 6\ nm$. The magnified image of the interface is shown in Figure 4.11b. Figure 4.11c shows the HRTEM image of the thin film showing the formation of defects at the inside and on the top portion of the film. The Au film is observed to be consists of Au (111) plane having an inter-planar spacing of 2.25 $\mathring{A}$ as observed from the HRTEM image and the FFT pattern shown in Figure 4.11d and e, respectively. The EDX spectrum confirms the presence of Si and Au (Figure 4.11g).

Figure 4.12a shows the morphology of the Au film after RTA annealing. It is observed that Au particle took a spherical form with a number of triangular shaped buried nanoparticles into Si. The average diameter of the spherical Au is 400 nm having an aspect ratio of 0.625 and the insertion length of the triangular nanoparticle is 70 nm. The HRTEM image (Figure 4.12b) shows that the side facets of the buried nanoparticle are consist of (4 2 2) facets which are connected by a (3 1 1) facet. The FFT image (Figure 4.12c) taken from the interface shows an epitaxial relationship between Au (111), Si (111) and Au (220) and Si (220) plane, and the in-plane direction is Au [110] $\parallel$ Si [110]. The Moiré fringe pattern of inter-planar spacing of 9.34 $\mathring{A}$ shows that there no rotation between Si (111)

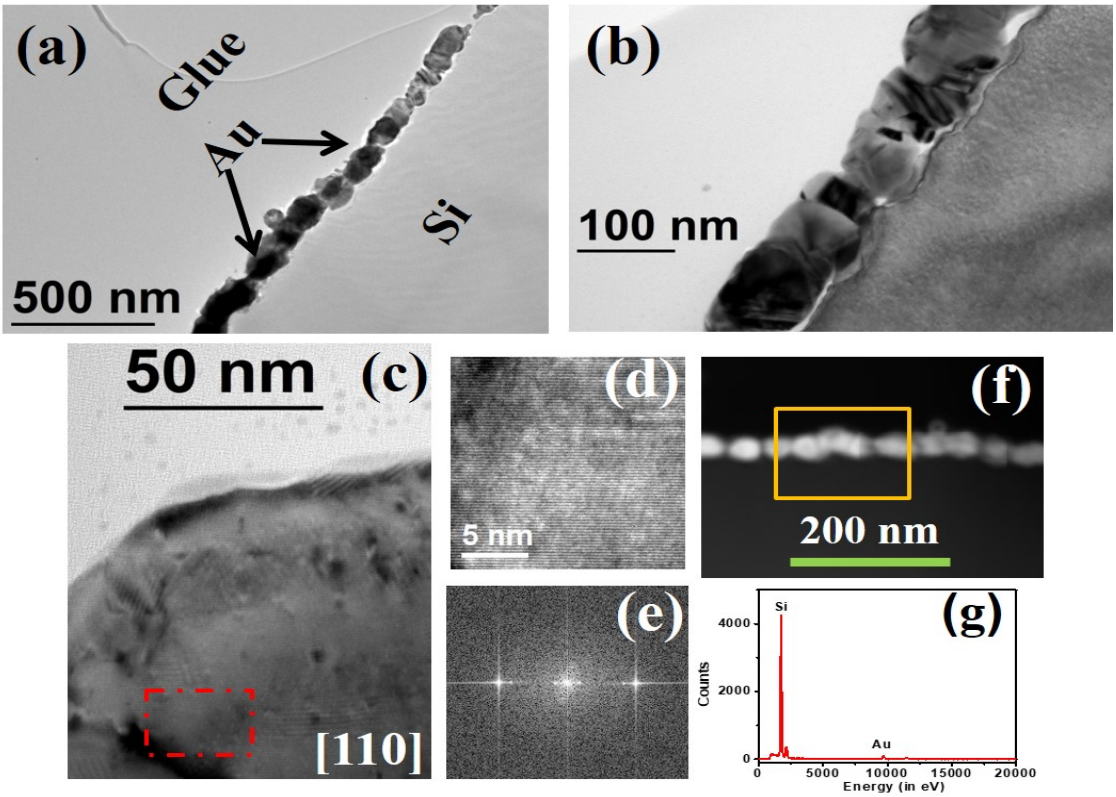

Figure 4.11: *(a) BF TEM image of Au deposited on Si for* 15 *minutes by GDR. (b) Magnified image of (a). (c) HRTEM image of Au film showing formation of various defects at the middle and top portion of the film. (d) and (e) HRTEM image and FFT pattern from the region bounded by red rectangle in (c) showing formation of Au (111) plane. (f) STEM-HAADF image. (g) EDX spectra from the region bounded by yellow rectangle in (f) confirming presence of Si and Au*

and Ag (111) plane. The presence of Au into Si is also confirmed by the EDX line profile shown in Figure 4.12e. Figure 4.12f shows the morphology of the film after annealing at $550^o\,C$ for 1 hour in a muffle furnace. This clearly shows the formation of a continuous thin film having a thickness of 300 nm. Endotaxial structures were observed to form in this case also has a thickness of 75 nm. In the case of Ag, the endotaxial structures were formed mainly during annealing at O_2 atmosphere and not in other environments. However, here the endotaxial structures were observed

to form during annealing at O_2 atmosphere and also for environmental annealing. The lower eutectic temperature of the Au-Si system must play a role behind such formation. The detailed mechanism can only be understood using an in-situ microscope.

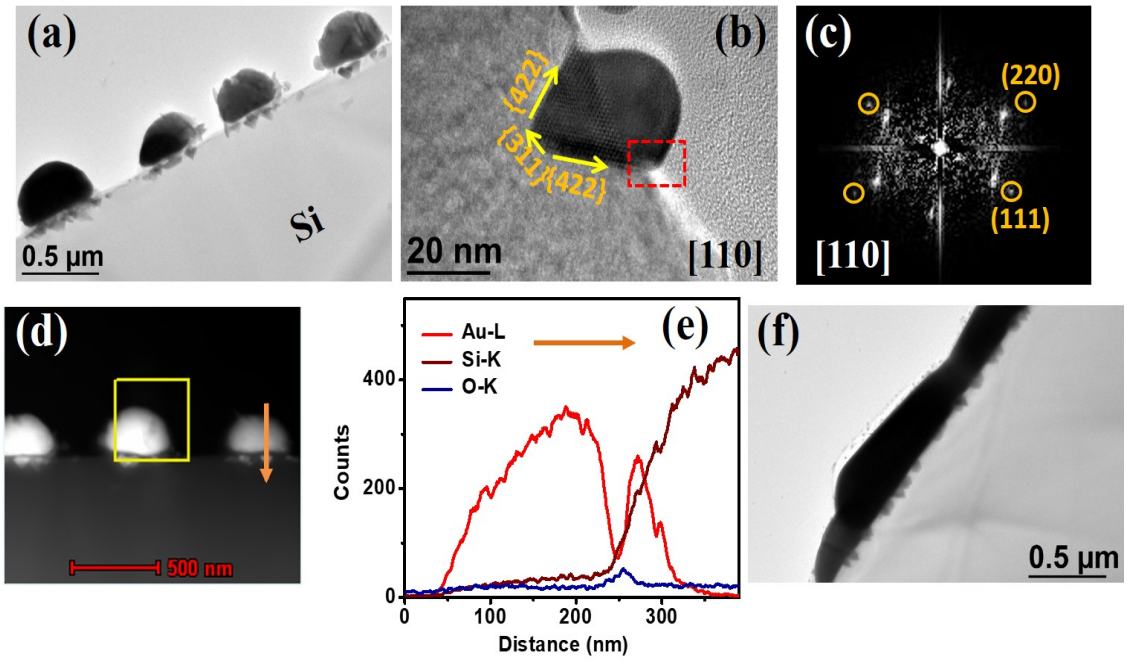

Figure 4.12: *(a) BF TEM image of RTA annealed Au nanoparticles showing formation of isolated spherical Au nanoparticles with endotaxial particles. (b) HRTEM image of a single Au particle showing formation of Moïre fringes. (c) FFT pattern from the interface indicating an epitaxial relationship between Au and Si. (d) STEM-HAADF image showing Au nanoparticles with higher contrast. (e) EDX line profile taken along the line shown in (d) Confirming the endotaxial particle is made of Au. (f) BF TEM image of normal annealed Au thin film on Si at ambient atmosphere. Formation of endotaxial Au on Si is observed in this case also.*

4.4 Structural Study of Ag Deposited on Pyramidal Si and Their Evolution Due to RTA

4.4.1 Morphology Analysis: SEM Observations

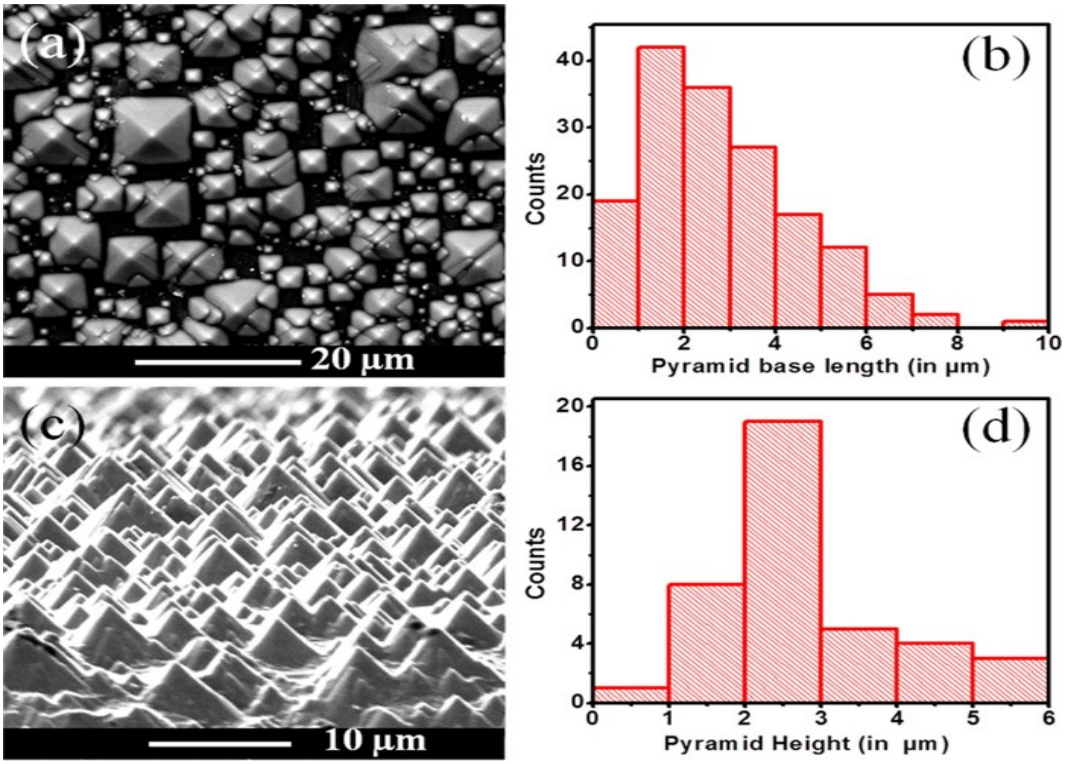

Figure 4.13: *(a) SE images of micropyramids on Si, (b) histogram of base length distribution, (c) XSEM view, and (d) histogram of height distribution.*

SE image of pyramidal Si is shown in Figure 4.13a and the size distribution of the pyramids is shown in Figure 4.13b. It shows an average base length of 2.9 μm of the pyramids. The XSEM view of the pyramids is shown in Figure 4.13c with the height distribution in Figure 4.13d. It shows an average height of 2.8 μm for the pyramidal structures.

To ensure uniform deposition of Ag on Si, different deposition times were taken ($10s, 30s, 60s$ and $90s$) and the evolution is shown in Figure 4.14a-d. The growth

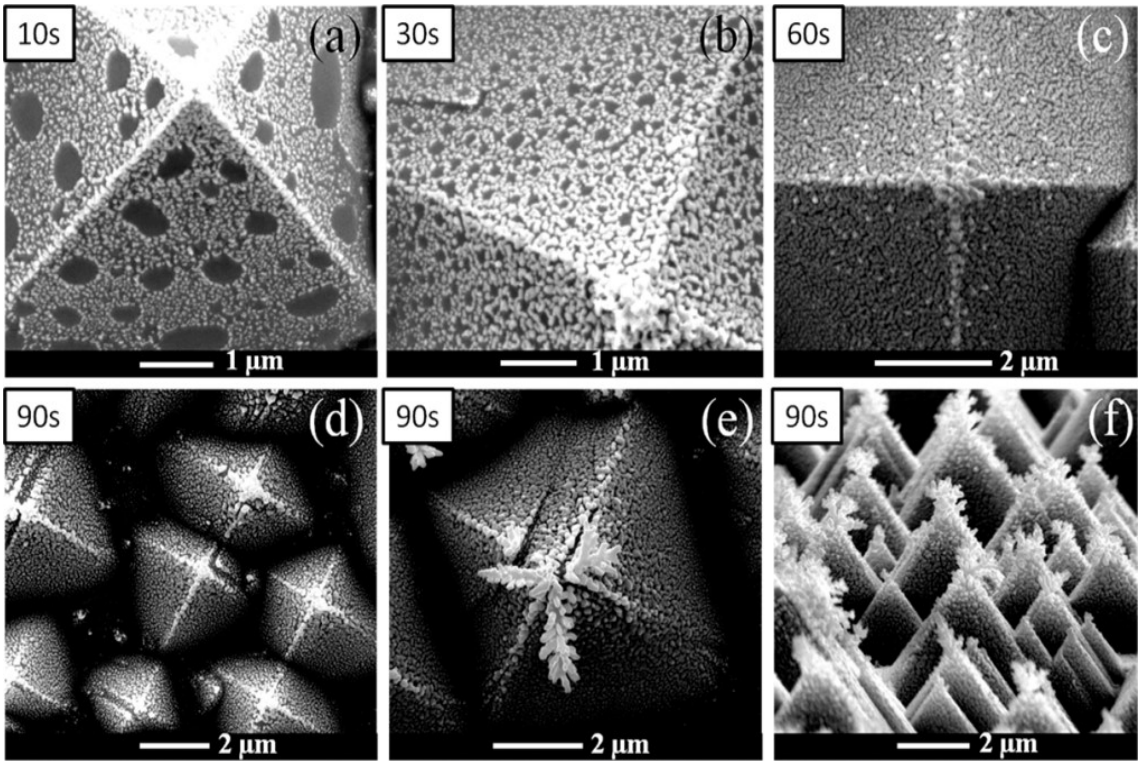

Figure 4.14: *Plane view SE image of Ag deposited on Si pyramids for different reaction times: (a)* 10*, (b)* 30*, (c)* 60*, and (d)* 90 *s; (e) magnified view of (d) showing dendritic Ag nanostructure formation on top of the pyramid, and (f) XSEM view of (d) showing the presence of dendritic structure at the top in most of the pyramids.*

rate of the nanoparticles was observed to be higher at the top and edges of the pyramid while slower growth rate was seen at the middle and at the bottom of the pyramid. Initially, Ag was deposited on Si by keeping some oval-shaped gap (Figure 4.14a-d) while the radius of the gap is decreasing with increasing deposition time and uniform morphology is obtained after 90 *seconds* deposition time and form a spaghetti-like morphology. Such growth of Ag on Si (111) was previously seen at UHV condition [159]. Formation of some dendritic structures was also seen from the XSEM images, at the top of the pyramid due to the highest growth rate (Figure 4.14e-f). A remarkably opposite kind of growth was observed when Ag was

deposited on planar Si (100). For smaller deposition time Ag nanoparticles deposit uniformly over the substrate (Figure 4.15a), while for lower deposition time (180 *seconds*) formation of oval-shaped holes was observed (Figure 4.15b) between two Ag clusters. The pyramidal Si substrates were then subjected to RTA at different atmosphere to observe the evolution of the nanoparticles due to heat treatment.

Figure 4.16a shows the SE image of the samples annealed at 550^o C for 1 *minute*

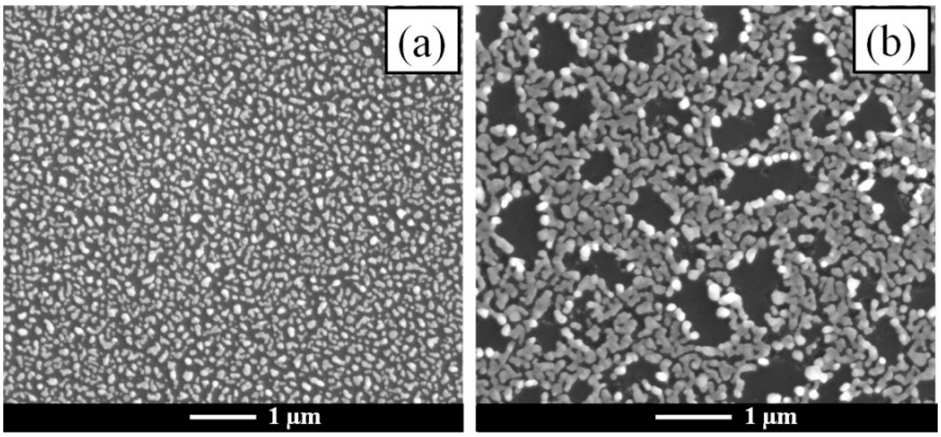

Figure 4.15: *Ag nanoparticles deposited by galvanic displacement method on Si (*100*) substrate for reaction time of (a)* 60 *and (b)* 180 *s.*

in N_2 atmosphere. The BSE images of the sample are shown in Figure 4.16b and Figure 4.16c, which shows a clear contrast between Ag and Si. It was observed that compared to as-deposited sample, particle size increases and the particles situated at the top and at the edges have higher size compared to those at the middle and bottom. Increment in particle size indicates the occurrence of a process known as "OR" where the smaller particles get dissolved due to their higher surface energy and resulted bigger particle formation [135]. However, some smaller particles are observed to remain in this process as shown in Figure 4.16c which indicates an incomplete OR process due to N_2 annealing.

When the samples were annealed at O_2 atmosphere and in same condition, a

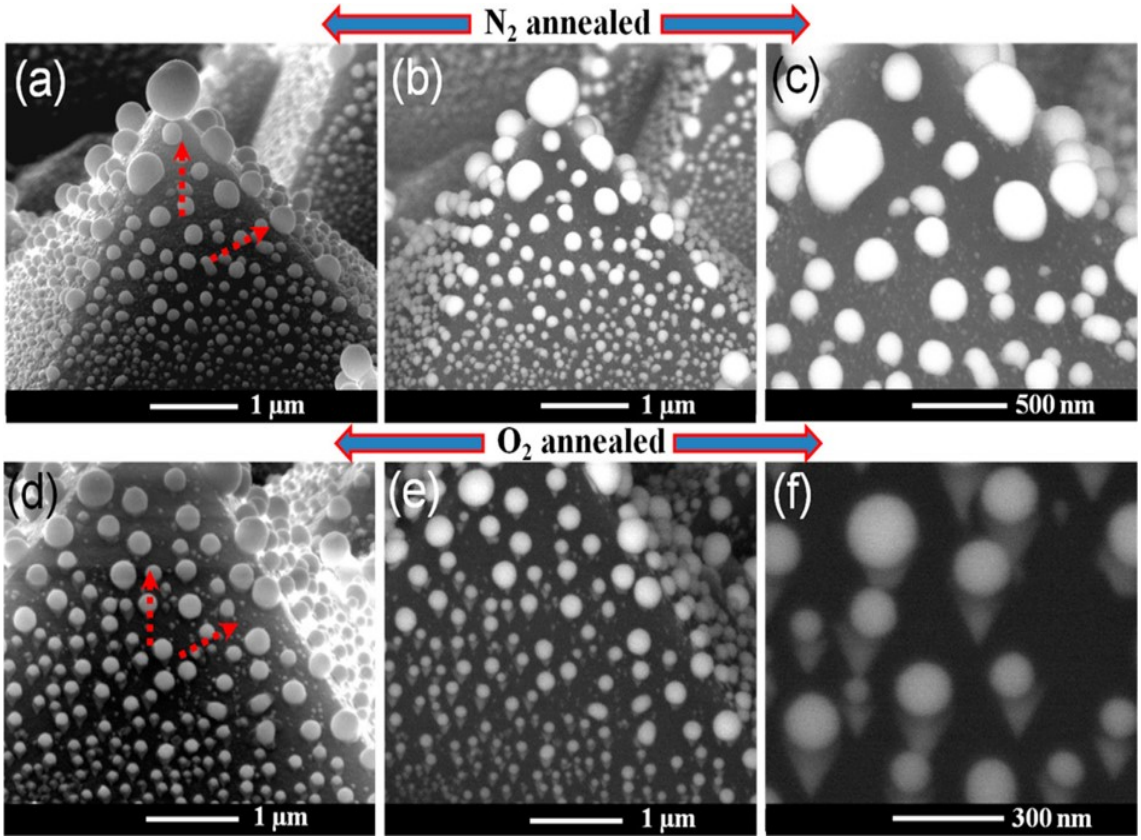

Figure 4.16: *XSEM images: (a) SE image of S2 sample showing the particle size variation from bottom to the top of the pyramid, (b and c) corresponding BSE images showing the atomic contrast between Si and Ag, (d) SE image of S3 sample showing the formation of spherical-shaped particles along with the triangular one, (e and f) corresponding BSE images confirm that the triangles are also made of Ag.*

dramatic decrement in the number of small particles is observed. The BSE image (Figure 4.16f) shows a clear formation of triangular-shaped Ag nanoparticles in this case. Wall *et al.* also observed formation of triangular Ag island on Si (100) due to annealing at 500^o C [160]. They also observed that the number of triangular islands increased with increasing temperature. This formation is kinetically limited at low temperatures. Triangular etch pits are observed to form at low

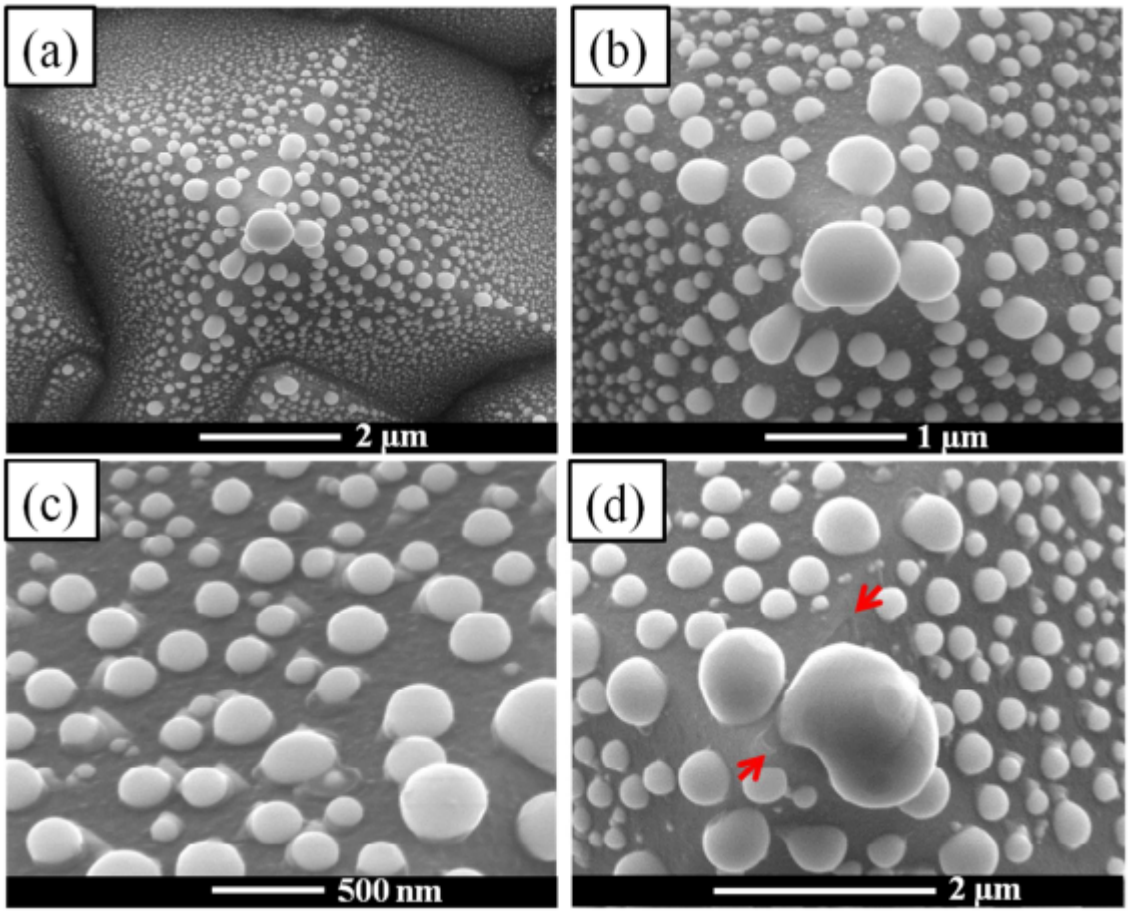

Figure 4.17: *(a)-(b) Top-view SEM image of S2, (c)-(d) Top view SEM image of S3 showing that the triangles are at the bottom of spheres and Si etch pit formation (shown by red arrow) during annealing at O_2 atmosphere, respectively*

temperature on Si (111) in presence of Ag. We have also observed such kind of etch pit formation which is shown in Figure 4.17d. This kind of etch pit formation occurs due to the introduction of Si lattice defects, which is the result of higher diffusion of Ag into Si during annealing. The higher diffusion of Ag on Si is result of formation of an adspecies called Ag_mO which diffuses Ag more easily on Si due to its lower detachment barrier [139].

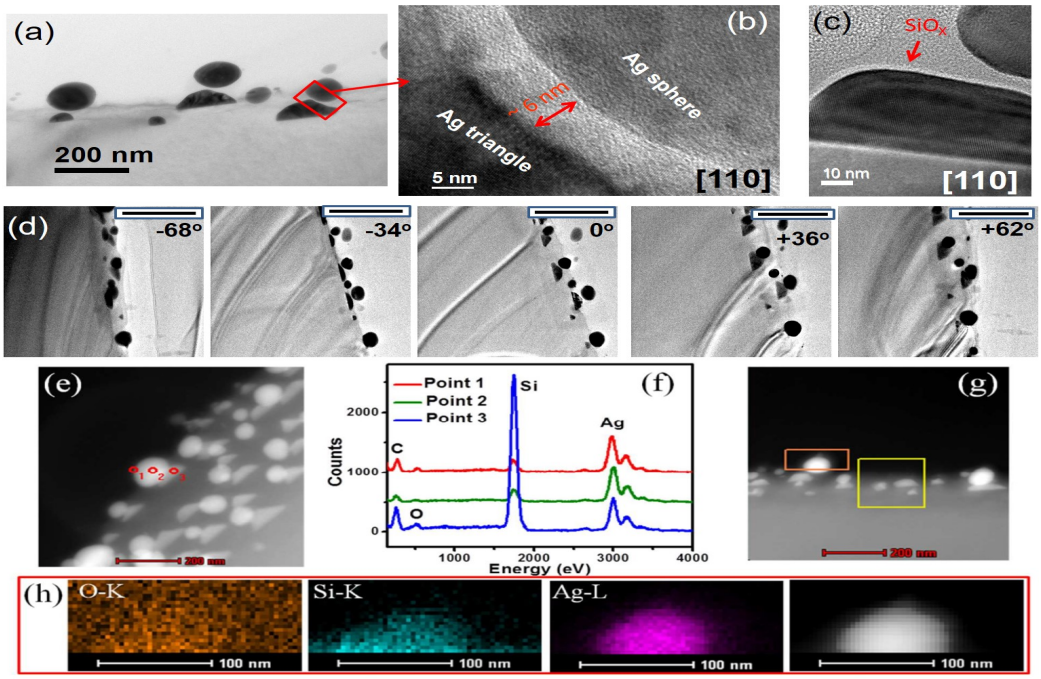

Figure 4.18: *(a) [100] XTEM image of S3 showing the separation between triangular and spherical particle, (b) corresponding HRTEM image, (c) HRTEM image from another pair of triangular and spherical particle clearly showing a thin layer of SiO_X covering triangular particle. (d) TEM tomography data showing such separation with different projections [−68, −34, 0, +36 and +62], (e) STEM-HAADF image, (f) EDX spectra from three different points shown in (e) clearly showing the presence of Si upto the surface (electron beam of spot size 2 nm), (g) STEM-HAADF image, (h) Magnified STEM-HAADF image and EDX elemental maps from a region marked in (g) showing the presence of Si and O upto the surface region.*

Ag_mO will decompose to Ag whenever they are attached to the surface of an Ag nanoparticle. However, at high temperature, Ag_mO has a higher chance to react with surface Si atoms. Ag ad-atoms prefer to stick to the edge compared to the facet of the triangular island, which is possible when the diffusion through the substrate is more likely than diffusing through nanoparticle surface resulting formation of triangular-shaped Ag island with Si etch pits. So the triangular-shaped etch pits act as the nucleation center behind the formation of triangular

Ag nanoparticles. The spherical Ag on top of triangular Ag are formed due to OR process. From extensive HRTEM observation a thin layer of SiO_X is observed to form between the triangular and spherical Ag (Figure 4.18). This thin layer provides better stability to the triangular particles as they get a layer of protection from the atmosphere. Previously it was observed that Ag diffuses slowly through SiO_2 compared to Ag and that may be responsible behind the formation of spherical Ag on top of almost every triangular Ag.

4.4.2 Analysis of Crystalline Structure: TEM Observation

To study the crystalline structure and the interface between Ag and Si we have done extensive TEM analysis. The BF XTEM image of $S1$ is shown in Figure 4.19a and the corresponding particle size distribution is shown in Figure 4.19e. It shows an average particle size of $35 \pm 5\ nm$. The increment in the particle size from the base towards the top is also evident from Figure 4.19a and 4.19b. The EDX elemental spectra were acquired from the portion indicated by red rectangle in Figure 4.19b and are shown in Figure 4.19c. The elemental mapping (Figure 4.19) is taken from the orange rectangle in the STEM-HAADF image (Figure 4.19). The HRTEM image (Figure 4.19f) shows the interface of Ag and Si and it shows high crystalline nature of Ag in this portion. The Fourier filtered image from the marked portion indicates a rotation between Ag (111) and Si (111) plane. The angle between them is measured to be 36.14^o. This kind of tilted hetero-epitaxy was seen previously when Ag was deposited on Ge by electroless process the formation of defects occurs at the interface to reduce the strain[21].

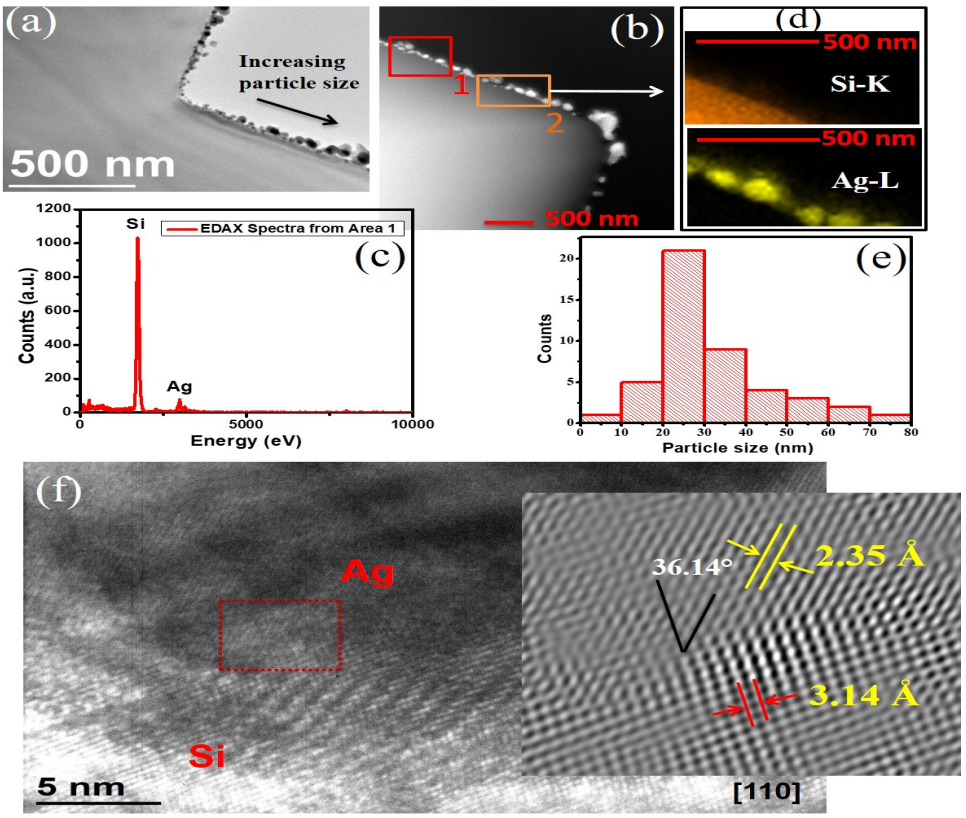

Figure 4.19: *(a) Low-magnification BF XTEM image of S1, (b) STEM-HAADF image, (c) EDX spectrum from region 1 is shown in (b), (d) elemental map from region 2 using Si–K and Ag–L energy, (e) histogram of particle size distribution, and (f) HRTEM image at the interface. (Inset) Fourier-filtered image of the red-dotted region of the interface showing crystallographic relation between Si (111) and Ag (111) planes.*

The BF TEM image of S2 is shown in Figure 4.20a. We have observed an increment in the contact angle of the Ag nanoparticle from the base towards the summit. Which is due to increment in the surface energy along this direction. From the particle size distribution curve (Figure 4.20c) it is observed that the smaller particles decrease in number and the average particle size becomes 85 ± 13 *nm*. The particles obtained a quasi-spherical shape (Figure 4.20b). The growth is a VW growth as no necking is observed. The SAD taken along [110] zone axis

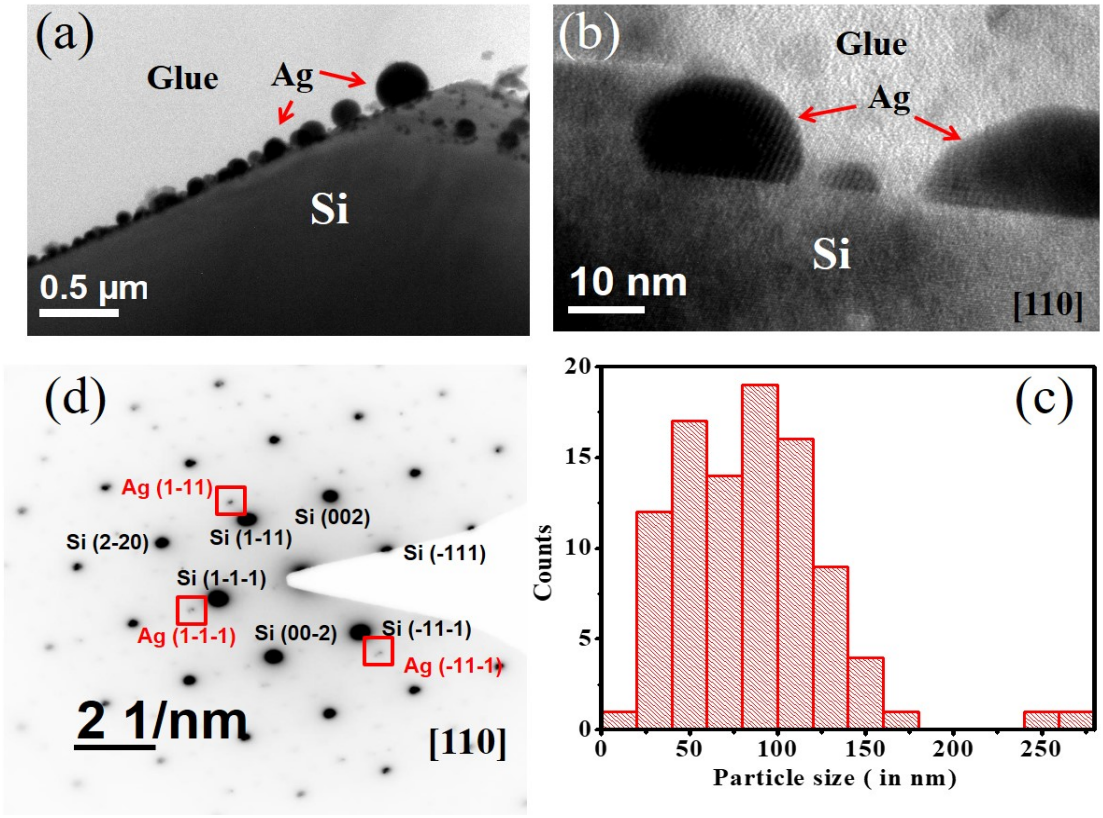

Figure 4.20: *(a) BF XTEM image of S2 showing formation of only spherical particle on Si due toN_2 annealing. Particle size increases with the pyramid height. (b) HRTEM image showing the direct formation of 3D island of Ag on Si, (c) histogram of the particle size distribution, (d) SAD pattern of the interface showing epitaxial growth of Ag on Si.*

shows a very good epitaxial relationship between Ag (111) ‖ Si (111) plane and parallel in-plane direction is Ag [110] ‖ Si [110].

The TEM images of S3 show the sample annealed at O_2 atmosphere. From the particle size distribution (Figure 4.21b) the average particle size was obtained as 105 ± 14 nm, indicating higher size of the particles compared to S2 due to OR process. Triangular particles under the spherical particle are clearly seen from

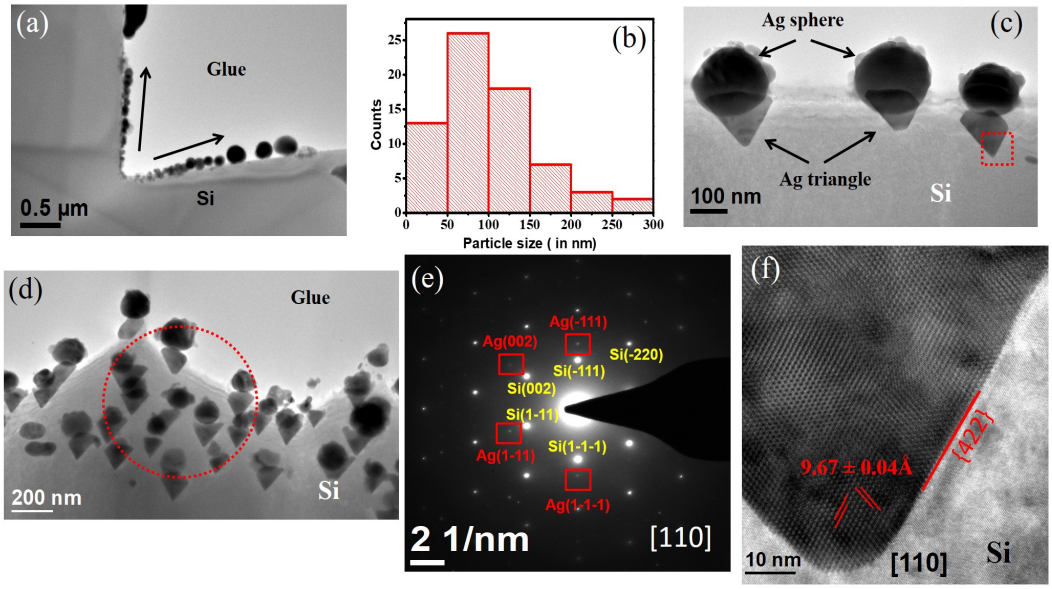

Figure 4.21: *(a) Low-magnification BF XTEM image of S3, (b) histogram of the particle size distribution, (c) high-magnification XTEM image of S3,(d) BF XTEM image showing almost all the spherical particles are associated with triangular particle underneath, (e) SAD pattern from a region in (d) showing epitaxial relation between Ag and Si. [110] Zone axis diffraction pattern where diffraction spots of Ag are indexed by red and Si by the yellow color. (f) HRTEM image of the portion marked by a red square in (c), showing the facet is along the 422 direction and the Moiré fringe of spacing is* 9.670.04 *Å.*

the XTEM image (Figure 4.21c). The HRTEM image of the composite structure shows that the surface of the spherical Ag is rough (Figure 4.21d). In some cases, the triangular particles are not observed to be perfectly symmetric. The spherical particles are also observed to be situated at one end of the triangular particle, however the small size gap between the two cannot be seen in this configuration. However, it is clear that the annealing environment plays a key role to determine the final structure.

The most dominant factor to determine the final morphology and shape of the

nanoparticles is the mobility on the substrate. Adhesion energy is directly related to surface energy of the substrate and it can be written as,

$$E_{ad} = \gamma_m(1 + \cos\theta) \tag{4.2}$$

where θ and γ_m are the equilibrium CA of the particles and the surface energy respectively. The average CA for S3 and S2 is obtained to be 113.6^o and 133.2^o respectively from different TEM and SEM images. Which clearly indicates a lower value of adhesion and consequently a higher mobility of Ag in the presence of O_2 atmosphere.

The SAD pattern of S3 is shown in Figure 4.21e. This also shows an epitaxial relationship between Si (111) and Ag (111) plane and the parallel in-plane direction is Si[110] $\parallel$ Ag[110]. So irrespective of the environment Ag always maintain an epitaxial relationship with Si. The epitaxy between Ag and Si can be explained by DME which is described in the previous chapter. HRTEM image of a triangular structure is shown in Figure 4.21f. The Moiré fringes of spacing $9.67\mathring{A}$ due to overlap between Ag (111) and Si (111) plane. The triangular particles are not embedded inside the Si matrix, which can be confirmed from the Moiré fringe formation.

4.5 Morphology of Si Nanowire Produced on Planar and Pyramidal Si

4.5.1 FESEM and TEM Study

The SE image of pyramidal Si formed by SDR method is shown in Figure 4.22a. The edges of the pyramid contains the highest number of particles due to higher

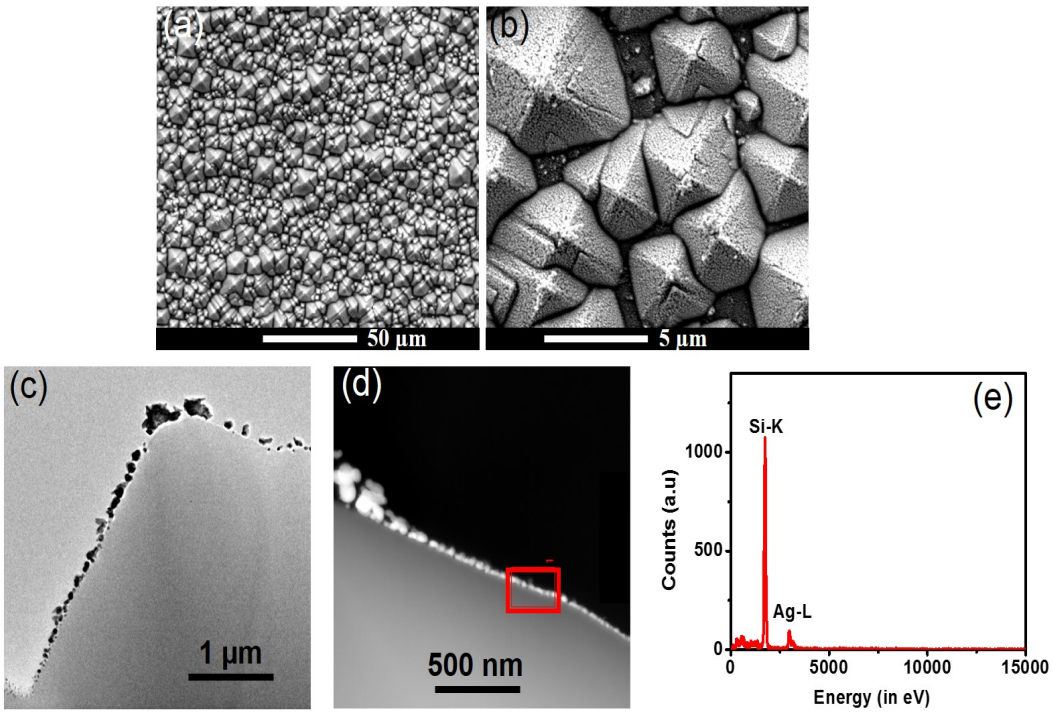

Figure 4.22: *(a) SE image of P-Si produced by SDR method. (b) Ag deposited on P-Si by GDR. (c) XTEM image of Ag deposited on P-Si. (d) STEM-HAADF image of Ag on P-Si. (e) EDX elemental spectra from the region marked by a red rectangle in (d).*

surface energy. The detailed study on the Ag-Si interface is described in the previous sections in this chapter. Figure 4.22c shows the BF XTEM image of the same. It is observed from the image that the size of the particle increases as we go from the base towards the top of the pyramid. This may occur as concentration of Ag^{+} ion is higher at the top compared to the base of the pyramid. The presence of Si and Ag is confirmed from the EDX elemental spectra (Figure 4.22e) obtained from region 1 of the STEM-HAADF image (Figure 4.22d).

BF XTEM image of Si-nanowire produced on planar Si (100) is shown in Figure

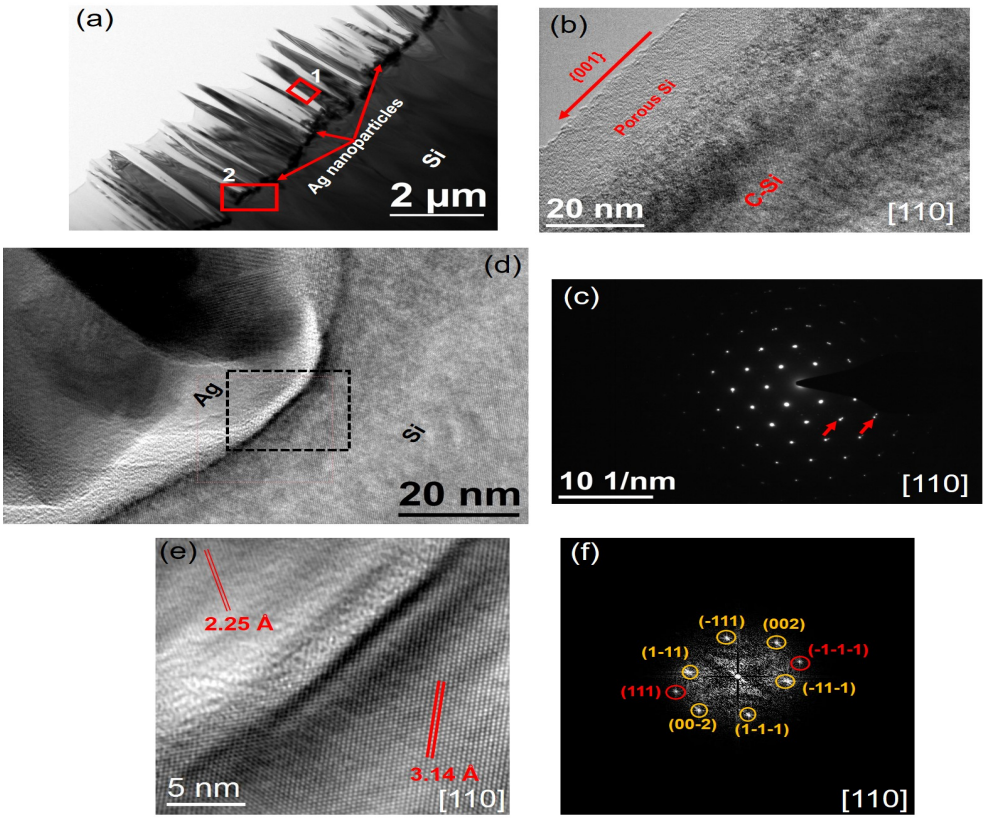

Figure 4.23: *(a) BF TEM image of Si NW produced by MACE process on planar Si* (100)*. (b) HRTEM image of a single Si nanowire. (c) SAD pattern of Si NW along* [110] *zone axis showing diffraction spots. (d) HRTEM image of the interface between Ag and Si. (e) Closer look of the portion marked by black square in (d) showing Si* (111) *and Ag* (111) *plane. (f) FFT pattern of the same region showing diffraction spots for Ag and Si.*

4.23a. The average length of the nanowires is 11.2 ± 2.4 μm with width ranging from 50 nm to 200 nm. The etching is observed to be uniform in this case as all the Ag nanoparticles are residing at the bottom of the Si-nanowire. The HRTEM image is shown in Figure 4.23b. The sidewalls of the Si nanowires are amorphous in nature having a thickness of 15 nm. The amorphous and porous Si structure both are produced with the introduction of the oxidant H_2O_2 during the MACE process. Kim *et al.* showed that the porosity density can be modified by

changing the H_2O_2 concentration [173]. We have also observed the formation of crystalline sidewalls when the concentration of H_2O_2 was reduced to 0.2 M while the other parameters remain unchanged which is shown in Figure 4.24. So, it is clear that H_2O_2 plays an important role to determine the nature of the sidewalls of Si-nanowire. The amorphous structure was produced by dissolving Si with the help of Ag nanoparticle in the presence of H_2O_2. Si has a lower reduction equilibrium potential compared to that of Ag and H_2O_2. Hence, Si valance band will be filled with holes with reduction of H_2O_2 in the presence of metallic ions. Thus Si gets oxidized initially and forms a complex H_2SiF_6 by reacting with HF. This compound is water-soluble and gets dissolves to finally form porous Si structure and nanowire Si. The Ag particles also undergo side-wise movement resulting in lateral etching to finally produce porous Si. The nanowire shows crystalline nature at the mid-portion and the etching is occured along (001) direction. The formation of a small-angle grain boundary in the Si nanowire is evident from the SAD pattern (marked by arrow) shown in Figure 4.23c. The SAD pattern was taken along [110] zone axis. The HRTEM image of the Ag-Si interface shows the formation of a brighter region, which may indicate formation of an intermediate oxide layer. This oxide formation occurs whenever there is a deficit of HF at the interface. The FFT image taken from the region marked by black square in Figure 4.23e shows Ag (111) of inter-planar spacing 2.35$\mathring{A}$ and Si (111) plane of inter-particle spacing of 3.14$\mathring{A}$ [21]. These two planes are oriented at an angle of 32.4^o relative to each other as observed from the FFT image (Figure 4.23f). Generally, hetero-epitaxial growth occurs through the formation of interfacial misfit dislocation and bi-axial strain at the interface. Further stress produces defects at the interface. Tilted

epitaxy is a unique way to reduce the stress at the interface which reduces the number of defects drastically at the interface.

On P-Si, the etching was observed to be quite different. From the BF TEM image

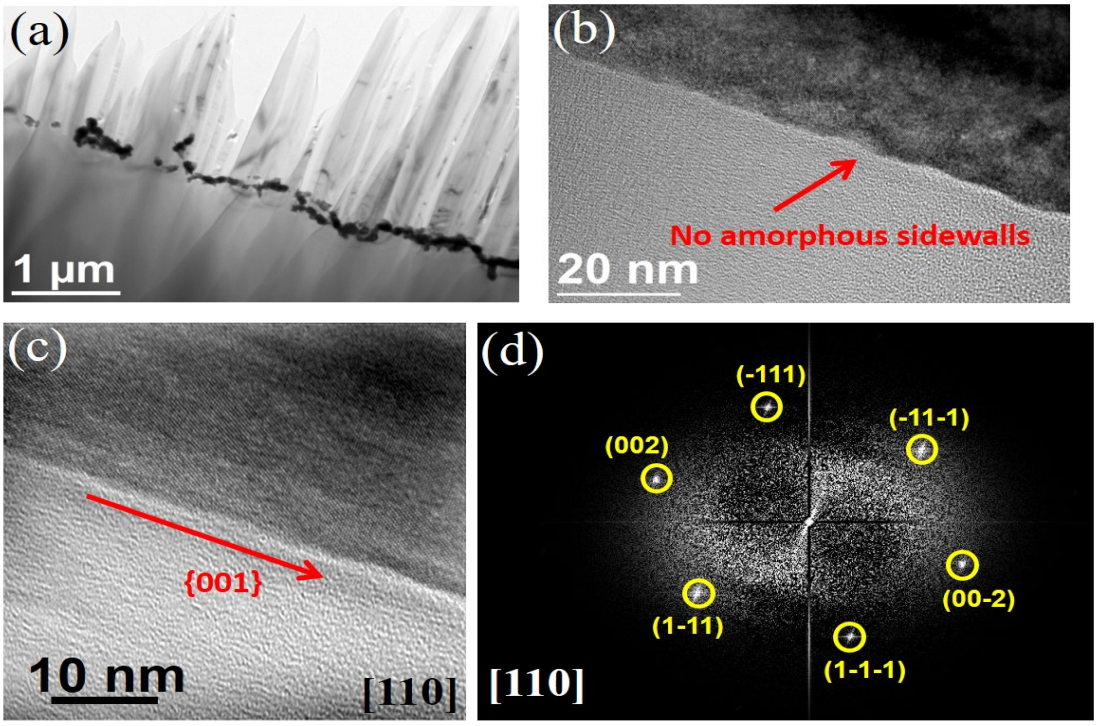

Figure 4.24: *(a) Formation of Si nanowire on planar Si using* 0.2 *M* H_2O_2 *as etchant (b) HRTEM image (c) Wien filtered HRTEM image of a single nanowire showing absence of any amorphous Si layer. (d) FFT pattern of the region shown in (c) showing very good crystalline structure of the nanowire.*

(Figure 4.25a) it is observed that the etching rate increases from the top towards the bottom of the pyramid producing nanowire of higher length at the bottom. Also, the Ag nanoparticles are observed to be situated at different positions of the nanowire unlike planar Si, where all Ag nanoparticles were residing at the bottom of the nanowire after the etching process. A very interesting fact is observed when Figure 4.23a and Figure 4.25a are compared. At planar Si, the Ag nanoparticles

are observed to form a continuous network at the bottom of the nanowires while for etching on P-Si substrate the Ag nanoparticles form a discontinuous network and almost became individual particle, which indicates higher dissolution rate of Ag during etching in P-Si configuration. As other planes of silicon contain higher atomic density compared to (100) plane, hence, for etching along non (100) plane requires higher removal of Si bonds. The dissolution occurs through the formation of H_2SiF_6, which occurs in presence of Ag and H_2O_2, hence Ag will dissolute more during etching along non (100) plane indicating higher resistance for etching on P-Si. Figure 4.25 shows the FFT image of a single Si-nanowire. The HRTEM image of a single Si nanowire is shown in Figure 4.25e, which shows formation of zig-zag nanowire. From the IFFT image (Figure 4.25f) it is observed that the etching occurs along $[1-1-3]$ and $[-11-3]$ direction simultaneously to produce the zig-zag sidewalls. Figure 4.25g shows the STEM-HAADF image of the sample. The EDX spectrum shown in Figure 4.25h is taken from the yellow region of Figure 4.25g and shows presence of Si and Ag. The EDX elemental mapping shown in Figure 4.25i confirms the fact that Ag particles are situated at different positions of Si-nanowire. During MACE process Ag particles act like a micro-cathode at the surface of the Si substrate and also act as a catalyst for reduction of H_2O_2. Si gets oxidized at the portions where Ag particles get attached to them, which is the front surface of the Ag nanoparticles. This oxidation of Si generates holes and electrons developing lower potential at the anode site and higher potential at the cathode site. This potential difference generates a current flow from the cathode to the anode. The flow of electrons occurs inside the Ag particles and holes flow anode to cathode outside Ag particle. These movements produce an electric field

which drives the Ag particle towards the anode and results in the formation of Si nanowire. An abrupt local change of reactant concentration at the interface can lead to the formation of zig-zag Si nanowire. In presence of HF and H_2O_2 the cathodic current density for a p-type semiconductor can be written as [173],

$$j = -zek_c n_c c_{ox} \exp(-\frac{E_A}{k_B T}) \tag{4.3}$$

where e is the charge of an electron, the number of electrons transferred during the reaction is denoted by z, c_{ox} is the oxidant density, k_c is the rate constant, n_c is the electronic density, k_B and $E_a$are the Boltzmann constant and the activation energy for the cathodic reaction respectively.

The competition between oxidation of Si via hole injection and Si oxide removal in the presence of HF through the removal of Si back bond determines the etching rate. As the rate of generation of holes is determined by H_2O_2 reduction rate at the metal surface, it directly indicates the number of holes injected into Si. Etching along non compact (100) plane occurs when H_2O_2 concentration is low. However, etching along more compact non (100) occurs for high concentration of H_2O_2. At the reaction interface the concentration of H_2O_2 quickly gets reduced in the presence of HF, resulting increment in j, thereby producing a large concentration gradient of H_2O_2. Etching rate will get reduce with a decrement in the cathodic current. However, a new influx cycle will be generated due to this concentration gradient and the etching switches direction and the process continues periodically. This oscillatory process may give rise to the formation of zig-zag Si nanowire on P-Si.

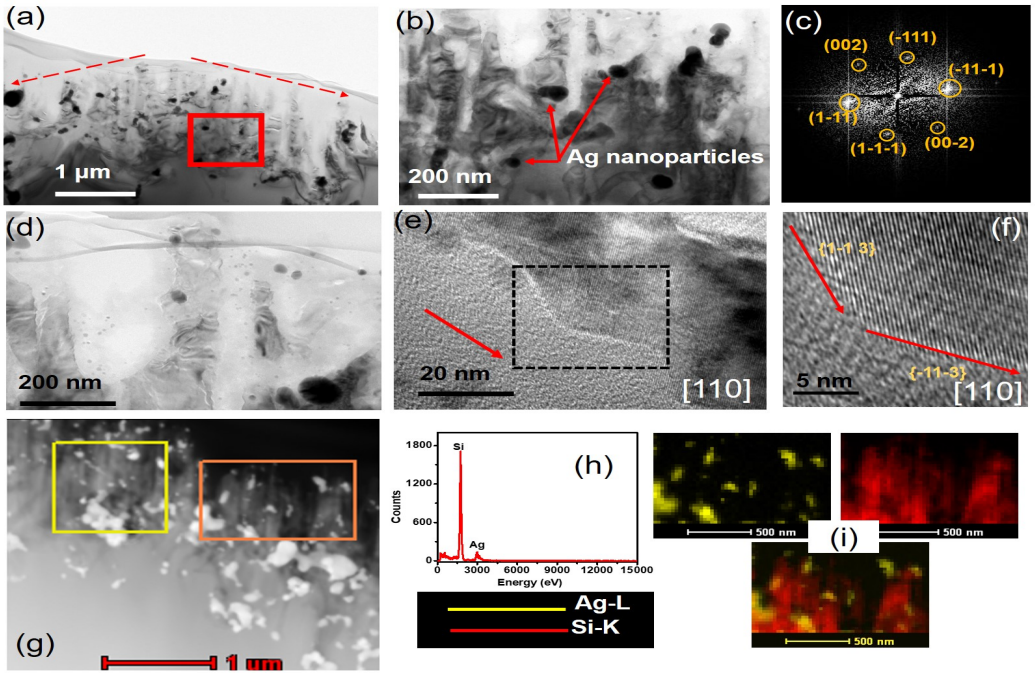

Figure 4.25: . *(a) BF TEM image of Si NW formed on P-Si by MACE process. (b) High-magnification image from the portion marked by a red square in (a). (c) FFT pattern from Si nanowire. (d) High-magnification image of a single Si nanowire. (e) HRTEM image of a single Si NW showing the formation of zig-zag sidewalls of Si. (f) Wien filtered image of (e) showing the etching direction. (g) STEM-HAADF image. (h) EDX elemental spectra from the portion marked by yellow square in (g) showing the presence of Si and Ag. (i) EDX mapping (Si-K map, Ag-L map, and composite map) from the portion marked by a magenta rectangle in (g).*

Si-nanowire after the removal of Ag nanoparticles is shown in Figure 4.26a. The Ag nanoparticles are observed to form at the top of the Si-nanowire and produce a percolated network when they are redeposited on the composite Si structure as shown in Figure 4.26b. The formation of spherical Ag nanoparticles on top of Si-nanowire is observed due to annealing at both O_2 and N_2 atmosphere (Figure 4.26c and Figure 4.26d). The size of the Ag sphere becomes bigger when they are annealed at O_2 atmosphere compared to that of N_2 atmosphere. This may due

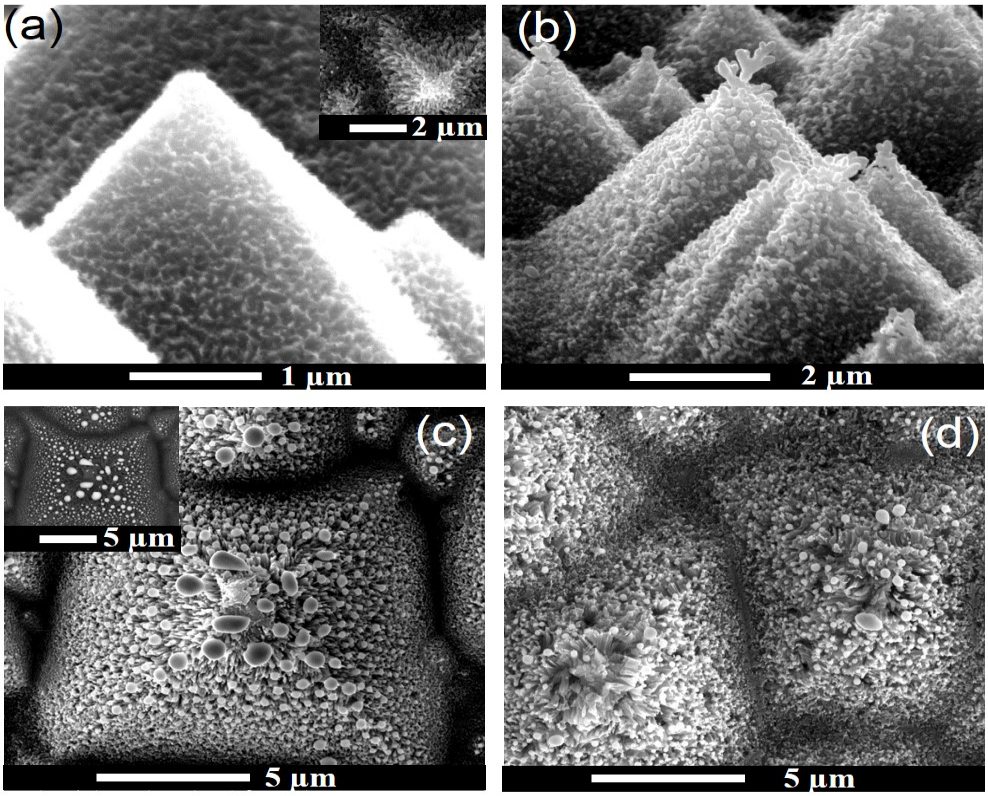

Figure 4.26: *(a) XSEM image of Si NW after the removal of Ag by HNO_3. (b) XSEM view of P-Si/Si nanowire after redeposition of Ag on it. (c,d) Plan-view SEM image after annealing at 550C for 1 minute at O_2 and N_2 atmosphere, respectively. The inset shows a BSE image to confirm the presence of Ag on the top of Si nanowire.*

to the fact that as mobility of Ag atoms enhances in presence of O_2 atmosphere, increased Ostwald ripening occurs in this situation [139]. This results in the formation of bigger shaped Ag nanoparticles due to annealing at O_2 atmosphere. The presence of smaller size Ag nanoparticles is observed due to annealing at N_2 atmosphere from the SE image shown in Figure 4.26d.

4.6 Pd Nanoparticles on Semiconductor Substrates

4.6.1 Morphology: SEM Analysis

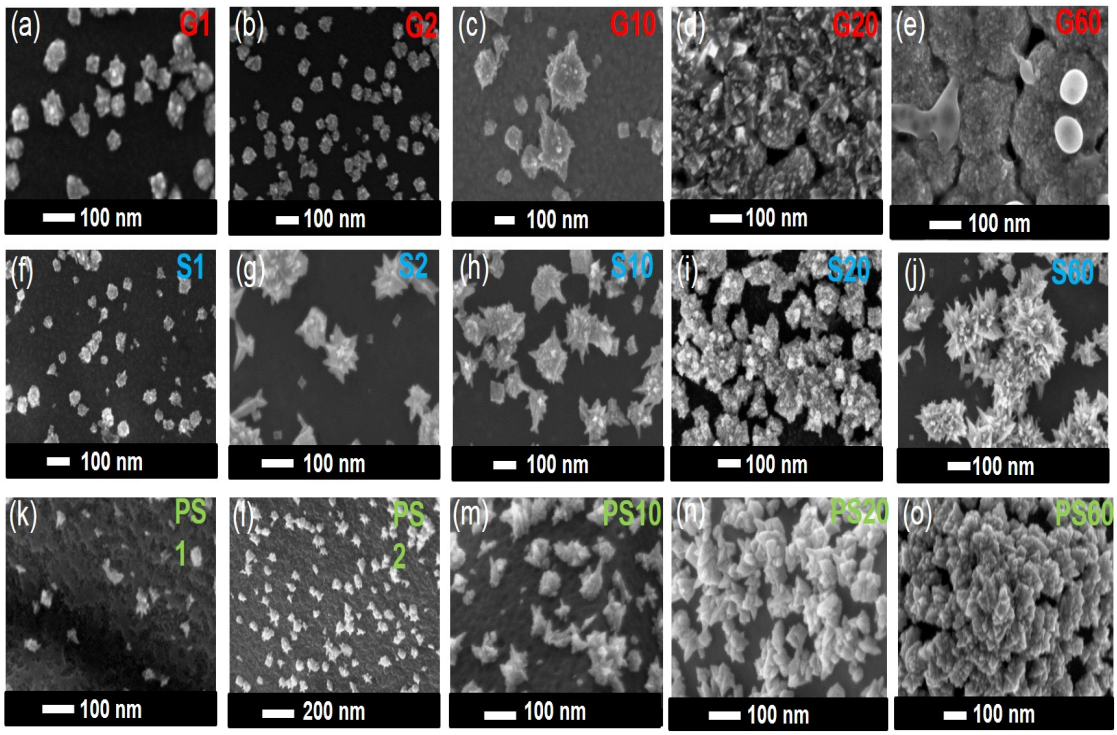

Figure 4.27: *SE images. (a), (b), (c), (d) and (e) represents Pd nanoparticles features when deposited on Ge* (100) *for* 1 *minute* (*G*1), 2 *minutes* (*G*2), 10 *minutes*, 20 *minutes and* 60 *minutes respectively. (f), (g), (h), (i) and (j) represents Pd nanoparticles Pd nanoparticles features when deposited on Si* (100) *for* 1 *minute* (*S*1), 2 *minutes* (*S*2), 10 *minutes*, 20 *minutes and* 60 *minutes respectively and (k), (l), (m), (n) and (o) represents Pd nanoparticles features when deposited on pyramidal Si for* 1 *minute* (*PS*1), 2 *minutes* (*PS*2), 10 *minutes*, 20 *minutes and* 60 *minutes respectively*

The morphology of Pd nanoparticles deposited on different substrates for different times is shown in Figure 4.27. Average size of particle is 41 ± 4 *nm* for 1 *minute* deposition on Ge. The particles have spherical shaped core with different sizes shaft around it. The size of the spherical core increases significantly but

no significant enhancement in the size of the shafts was observed with increasing deposition time (Figure 4.27b). In 10 *minutes* time, the shape became spherical with sharp metal edges (Figure 4.27c). A layer of continuous Pd film is observed here and it is also confirmed by TEM observations. A cluster of dendritic structures with high roughness is observed for a deposition time of 20 *min* as shown in Figure 4.27d. Spherical shaped particles having diameter in the range of $300-500$ *nm* are observed for 60 *minutes* deposition time resulting formation of almost a continuous layer. The surface of the particles becomes rough producing greater electro-active surface area as observed from the SE image shown in Figure 4.27e. On Si(100) the growth rate of the particles is observed to be very slow compared to that of Ge. Urchin-like structure with smaller symmetric shaped core is formed for 1 and 2 *minutes* deposition as observed from Figure 4.27f and Figure 4.27g. The inner core increases with increasing deposition time but the rate of increment is smaller compared to Ge(100). Particle of 35 *nm* diameter is formed for 10 *minutes* deposition time (Figure 4.27h). Particles having spherical shaped core and sharp metal edges are formed for 20 *minutes* deposition (Figure 4.27i). For 60 *minutes* deposition, the number of sharp metal edges increases and obtains a sharp petal-like shape covering almost the whole spherical core as shown in Figure 4.27j. On P-Si a faster growth rate is observed. Due to higher surface energy along the ridge, the growth is highest in these portions. The particles also took urchin-like shape for higher deposition time and it produces a rough surface with higher coverage (Figure 4.27k-m). For 60 *minutes* deposition time 76% coverage was obtained. The sharp metal edges produced in this case are very much helpful to produce significant SERS enhancement.

4.6.2 TEM Analysis

We have done extensive TEM study for detailed structural understanding. Figure 4.28a shows the BF XTEM image of Pd deposited on Ge substrate for 10 *minutes*. It is observed that the Pd nanoparticles form an urchin-like structure. Which consists of spherical shaped core on which metal edges are situated. The width and height of the urchin structure are 150.2 ± 25.2 nm and 117.8 ± 18.5 *nm*. The shafts have a very sharp corner which can enhance the incident EM wave effectively. The average length of the shaft is 37.5 ± 15.6 *nm* with a tapered angle of 38.52^o. A continuous layer of thickness 15.9 *nm* is observed at the bottom of the urchin structure. The film consists of Pd (111) plane as observed from the HRTEM images of the interface and from the FFT pattern. The sharp metal edges are also observed to consist of Pd (111) plane of inter-planar spacing of $2.25\mathring{A}$. The individual flower-like structure gets demolished due to aggregation but the dendritic structure remains intact for 20 *minutes* deposition as shown in Figure 4.28b. The thickness of the continuous layer becomes 64.4 ± 3.1 *nm* with a decrement in the shaft length. The width of the shafts becomes 9.9 *nm*. Formation of some small humps is observed on the side of the shafts as shown from the inset. A relatively flatter morphology with a film thickness of 300 *nm* is obtained for 60 *minutes* deposition time.

The growth rate of Pd is completely different on planar Si. It is observed from Figure 4.28d that the growth rate of Pd nanoparticles is very slow supporting the SEM observations. The EDX spectra show the presence of Si and Pd. The Pd nanoparticles initially form a nanorod structure that gets agglomerated to finally

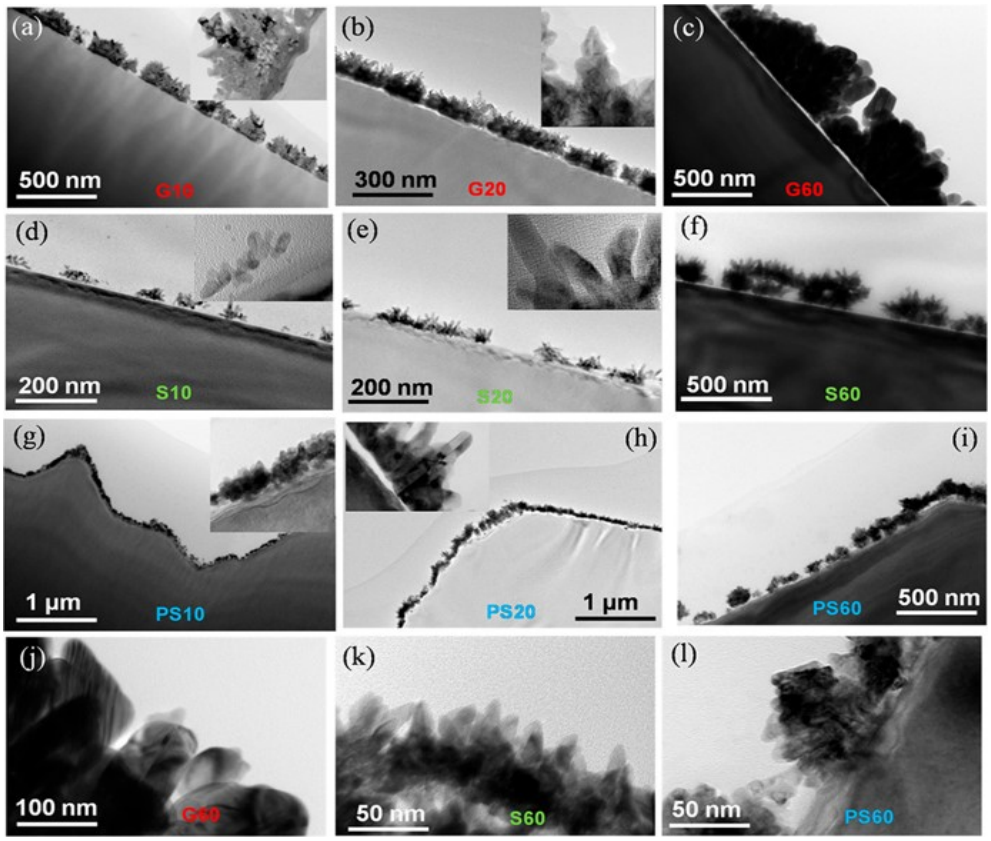

Figure 4.28: *BF XTEM images: (a), (b) and (c) shows G10, G20, and G60 samples respectively; (d), (e) and (f) shows S10, S20, and PS60 samples respectively; (g), (h) and (i) shows PS10, PS20, and PS60 samples respectively. (j), (k) and (l) shows magnified images of the G60, P60, and PS60 sasmples, respectively. Insets show the magnified images of the Pd nanostructure.*

produce urchin-like shape. The average length of nanorod is 29.5 *nm*. From the inset, it is observed that the nanorod starts to grow from a cluster of height 6 *nm* and 10.6 *nm* width. The nanorods grow from these cluster following growth along a particular direction. The length of the nanorod increases for increasing deposition time. The average length of nanorod becomes 38.3 ± 5.9 *nm* and width 7.2 *nm*. So, it is observed that with increasing deposition time the length of the shafts increases while the width decreases. An increased coverage is obtained for

higher deposition time as shown in Figure 4.28f and that leads to the formation of urchin-shaped nanostructure of 77.5 ± 12.5 nm shaft length and 17.1 ± 2.1 nm width.

The growth of Pd is much faster on P-Si compared to that of planar Si. The bright-field TEM image shown in Figure 4.28g shows the Pd nanoparticles after 10 *minutes* deposition on Si. The continuous layer of thickness 45 nm is observed for only 10 *minutes* deposition time. In this case, the particles become flower-like with smaller shaft. Formation of shafts along the perpendicular direction is observed for higher deposition time (Figure 4.28h). The formation of a twin boundary at the mid-portion of the shaft is observed which got extended to the top of the structure as shown in the inset. Formation of single twin boundary is observed to form at the base of the nanostructure. This shows that the formation of shafts occurs from single twinned nanoclusters. For 60 *minutes* of deposition, flower-like structurse appear, having a thickness of 95.2 ± 16.6 nm.

4.6.3 Crystal Structure Analysis

The HRTEM image of a single Pd shaft deposited on Ge is shown in Figure 4.29a. The presence of Pd (111) plane is evident from the IFFT image shown in Figure 4.29b. Figure 4.29c shows the [110] zone axis SAD pattern of the deposited Pd nanoparticles. This shows the polycrystalline nature of the film with diffraction spots corresponds to (111), (200), (220) and (311) plane of Pd. The HRTEM image of the initially formed cluster on Si (100) is shown in Figure 4.29d. Dislocation like defects is observed in the cluster as shown in Figure 4.29e. Formation of (111), (200) and (311) plane is evident from the SAD pattern taken along [110] zone axis. The formation of twin boundary at the midsection is also observed from

the HRTEM imagen shown in Figure 4.29g. Tilted epitaxy is observed to form between Pd (111) plane and Si (111) plane from the HRTEM image and form the FFT image shown in Figure 4.29i and Figure 4.29j respectively.

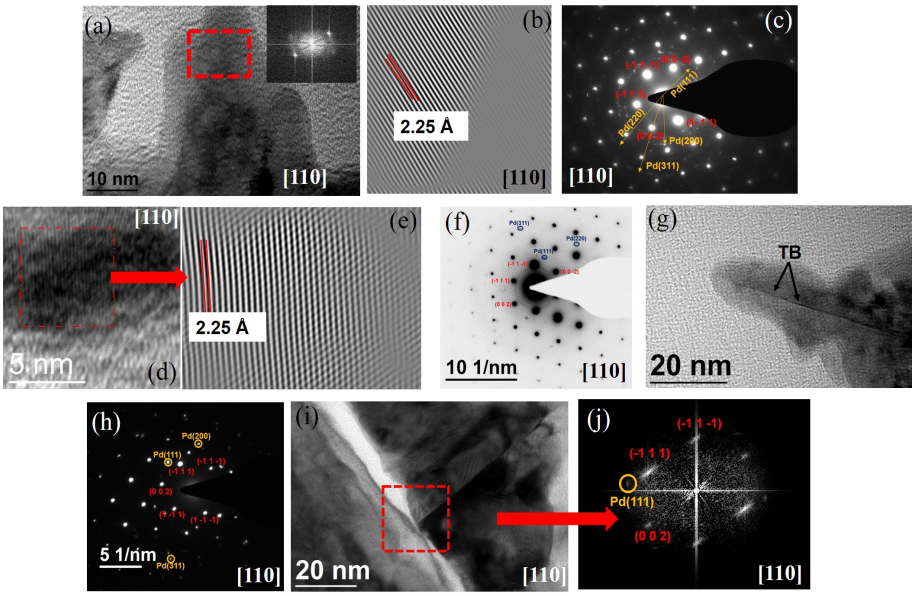

Figure 4.29: *(a) HRTEM image of a Pd shaft deposited on G*10 *sample. Inset shows the FFT pattern from the region marked by the red rectangle in part a. (b) IFFT image showing Pd(*111*) plane and its direction with respect to the substrate. (c) SAD pattern taken along [*110*] zone axis showing diffraction spots of Si and Pd. (d) HRTEM image of a single Pd cluster (S*10*) which generates nanorod-shaped Pd nanoparticles showing formation of dislocations and grain boundary and strain-induced defects. (e) IFFT image. (f) SAD pattern from S*60 *sample showing good crystallinity. (g) HRTEM image of a single Pd shaft showing the formation of a twin boundary at the midportion. (h) SAD pattern taken along [*110*] zone axis showing the formation of a tilted heteroepitaxy between Pd and Si for the PS*20 *sample. (i and j) HRTEM image of a single Pd shaft and FFT image from the interface of PS*20*, respectively.*

The growth rate and final morphology of the deposited film are vastly dependent on the surface energy and defect on the substrate surface. The surface energy

of H-passivated Si is 0.3 Jm^{-2} and for SiO_2 it is also the same [97]. The surface energy of Pd and Ge is 2.01 Jm^{-2} and 1.835 Jm^{-2} [196, 197]. Hence, from surface energy consideration, it is clear that if the same metal is deposited on Ge and Si, the growth rate will be obviously higher in Ge compared to Si. Different defect spots act as the nucleation center for an initial Pd^{2+} ion deposition. On Si substrate, Pd ions are reduced to finally form Pd nanocluster. In this case, the nanoclusters and Si substrates act as local cathode and anode for further Pd deposition resulting deposition of Pd ions on the nanocluster. After obtaining a critical cluster size, reduction of Pd ions and oxidation of Si occurs concurrently leading to anisotropic growth to finally produce urchin-like structure consisting of dendritic shaft. Halide ion (Cl^-) plays a very important role to drive the anisotropic formation by adsorbing to Pd (111) surface [198]. Song *et al.* observed formation of dendritic Pd structure in presence of SO_4^{2-} ion [199]. Pd nanorod and nanoflake structures were made by Kim *et al.* using an electrodeposition process without any external reducing reagent [182]. Depending on the applied potential they varied the reaction rate which finally leads to the formation of different nanostructures. Formation of thick and short nanorod like Pd nanostructures was made by Song *et al.* by applying a lower potential implying a slower growth rate [199]. We have also observed formation of nanorod like structure initially on planar Si indicating slower growth. On planar Si higher growth rate along the vertical direction leads to the formation of the nanorod. In Ge, Pd was observed to form a spherical shaped core initially which was observed previously using PVP as a surfactant, but here we are using no such surfactant to control the morphology. The number of nucleation spots increases for P-Si as it is formed by anisotropic etching process introducing

a number of defects on its surface which justifies the higher growth rate of Pd on P-Si [200]. Conrad *et al.* observed formation of smaller particle number density by electron beam damage on smooth surface [201]. However, on rough surfaces, the number density increases 10 times. Smaller number of Pt nanoparticles is observed to form on Si substrate having fewer defects [201]. In our case, the increased number density with reduced agglomeration confirms the fact that P-Si substrate contains more defect spots. In OR process the particles become larger by agglomeration but on the surface with high roughness and defect spots the mobility of the particles gets reduced while the nucleation rate increases due to presence of defect spots. In previous works, the morphology of the nanoparticles was varied either by changing the applied voltage or by using different surfactants. But in this work, we use the surface energy and surface defects to control the growth rate and morphology of the nanostructures.

4.7 Conclusions

From the above discussions we have seen that the structure and final morphology of both Ag and Pd depends heavily on the substrate morphology (planar and patterned) and also on the deposition time. Also, from RTA process of Ag on planar and patterned Si in N_2 and O_2 atmosphere, it is observed that the kinetics of Ag gets enhanced very much in presence of O_2 atmosphere which leads to the formation of coupled Ag triangular and spherical structure on pyramidal Si and also formation of endotaxial Ag on planar Si. Also, the morphology of Si-nanowire produced by MACE process is observed to be very much dependent on the Si substrate morphology and H_2O_2 concentration. We have also studied the growth

morphology of Pd nanostructures on different substrates and with pre-patterned substrates using a very clean method and without any use of surfactants. The growth rate, size and shape of these nanoparticle depend largely on the substrate material and finally produces different structures for same deposition time. These structures are very much useful for different sensor and solar cell applications.

Chapter 5

SERS Application and Near-Field Study Using FDTD Simulation and Cathodoluminescence Spectroscopy

---

This chapter describes the SERS effectiveness of the noble metal nanoparticle deposited substrates and their near-field study using FDTD simulation

---

5.1 Introduction

Raman scattering occurs when energetic photons scattered inelastically during interaction with a matter. During this interaction, the incident photon either losses its energy if its help to promote the molecule to its excited vibrational energy state from the ground state or it can gain enrgy in case the reverse process occur. So, an information about the vibrational mode of materials can be obtained from this inelastic scattering phenomenon of photons.The Stokes band normally has a greater intensity compared to the anti-Stokes band. The power of Raman spectra detected by a detector can be written as,

$$P_R = kN\sigma_k I \tag{5.1}$$

where P_R is $(photon/s)$ is the power detected by the detector, k is a constant depending on the instrument, the number of molecules illuminated is denoted by N. σ_k is the Raman cross-section of the k-th mode over all emission direction and integrated over the bandwidth, and I is the intensity of the illumination incident on the sample.Though, Raman scattering provide a fruitful information on the structure of molecules, it is a very weak phenomenon. The ratio of Raman cross-section to fluorescence cross-section is 10^{-6}, which implies its weakness.

In SERS technique, the LSPR generated by interaction of EM wave with metal nanoparticles helps to enhance the Raman scattering generated by molecules which are placed near the particle. The SERS and Raman scattered power can be written as,

$$P_{SERS} = G_{SERS}P_{RAMAN} = G^{EM}_{SERS}G^{Chem}_{SERS}P_{Raman} \tag{5.2}$$

where the total Raman EF is represented by G_{SERS} which is the product of two

factors *i.e* G_{SERS}^{Chem} enhancement caused by EM process and G_{SERS}^{Chem} enhancement caused by chemical process.

5.1.1 EM Enhancement

EM enhancement arises from the localization of light at the substrate surface and it depends mostly on the structural features of the substrate and is independent of the analyte molecule. It provides and enhancement up to 10^{10} which can make SERS a single molecular probe. The EM enhancement is contributed by two factors:

(i) The local field enhancement This occurs due to excitation of surface plasmon and produce an extensively amplified electric field in a sub-nm region called "hot spots". The molecules residing in these hot spots will experience a much stronger electric field compared to the other.

(ii) Re-radiation enhancement The radiation power from molecules (which acts as a dipole when produced in an electric field) depends hugely on the nearby field environment that gets modified due to the presence of the metallic substrates. The induced molecular dipole ($\rho(\omega_R)$) vibrating at the Raman frequency due to excitation of the molecule by an electric field having frequency ω_L is given by,

$$\rho(\omega_R) = \tau_R(\omega_R, \omega_L)E(\omega_L) \tag{5.3}$$

where, the Raman polarizability of the molecule is denoted by $\tau_R(\omega_R, \omega_L)$. The radiation power being proportional to the square of the dipole modulus is given by,

$$P_{Raman} = \frac{\omega_R^4}{12\pi\epsilon_0 c^3}|\tau_R(\omega_R, \omega_L E(\omega_L)|^2 \tag{5.4}$$

where, ϵ_0 is the free space permittivity and c is the speed of light in vacuum. The local field enhancement due to the presence of a metallic substrate near the molecule can be written as,

$$M^z_{loc}(\omega_L) = \frac{|E_{loc}(\omega_L)|^2}{|E(\omega_L)|^2} \tag{5.5}$$

where the superscript z indicates the polarization axis of the incident radiation. The re-radiation enhancement is highly dependent on the surrounding environments dielectric constant and is known as spontaneous emission. The molecules placed near the substrate act as a dipole from which radiation is emitting, Though the incident and re-radiated wave has different physical origin, the spectral dependence are very much similar. Both the incident emission and re-radiated emission can excite the surface plasmon and can localized the light in a very sub-nm region. The excitation by the re-radiation process is considered to be enhancement by a laser of excitation frequency ω_R. So, combining this the SERS enhancement can be written as,

$$G^{EM}_{SERS}(E^4) = M^z_{Loc}(\omega_L))M^z_{Loc}(\omega_R)) = |\frac{E_{Loc}(\omega_L)}{E(\omega_L}|^2|\frac{E_{Loc}(\omega_R)}{E(\omega_R}|^2 \tag{5.6}$$

where the enhancement by the laser frequency and at the Raman) frequency is denoted by $M^z_{Loc}(\omega_L)$ and $M^z_{Loc}(\omega_R)$ respectively. For small Raman shift [$\omega_L \cong \omega_R$), the equation can be modified as

$$G^{EM}_{SERS}(E^4) \cong |M^z_{Loc}(\omega_L)|^2 = |\frac{E_{Loc}(\omega_L)}{E(\omega_L}|^4 \tag{5.7}$$

5.1.2 Chemical Enhancement

Chemical enhancement does not enhance the local electric field around the nanoparticle like EM enhancement but it plays an important role to determine the shape

and shift of the Raman peaks. It is studied intensively by many researchers but more attention is given to EM enhancement. Mostly, two kind of mechanism contribute to chemical enhancement (i) Non-resonant chemical effect, where no new electronic state is formed due to metal and molecular interaction. As, there is much difference between the molecular orbital energies to the Fermi energy of the metal. But it leads to a change in the electronic and geometrical structure of the molecule which includes a very small shift in the Raman peak position and intensity. (ii) Resonant charge transfer effect, where a new metal-molecule charge transfer state is created due to the interaction between the metal and molecular orbital. This occurs if the lase excitation wavelength is in resonance with some Raman modes, more particularly to the ones which are also coupled with allowed electronic transitions which is called resonant Raman scattering.

In this chapter we will describe the SERS effectiveness of our substrates mostly by EM enhancement and theoretically by FDTD simulations.

5.2 SERS Measurement of Ag Deposited on Planar Si

The SERS activity of the substrates was measured using R6G as the analyte molecule. The Raman enhancement was measured using the formula [145, 146]

$$EF = \frac{I_{SERS}}{I_{Bulk}} \times \frac{N_{Bulk}}{N_{SERS}} \tag{5.8}$$

where I_{SERS} is the area under the peak of a particular vibrational Raman mode of the adsorbed analyte andI_{Bulk} is the same for the analyte only. The number of molecules present in the bulk sample is denoted by N_{Bulk} and N_{SERS} is the number of analyte molecules present in the SERS sample. R6G of 10^{-1} M concentration

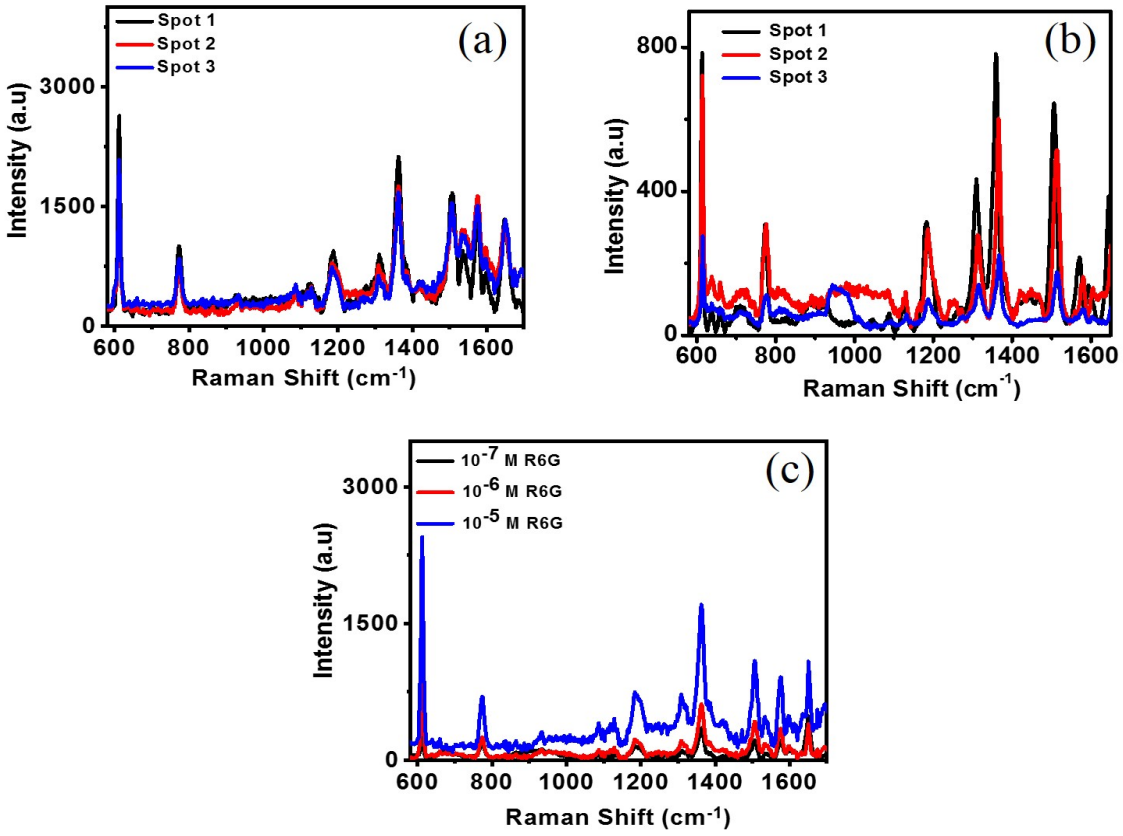

Figure 5.1: *SERS spectra of* 5×10^{-5} *M R6G for (a)* 1 *minute Ag deposited and* 1 *minute* O_2 *annealed sample (S*1*) (b)* 3 *minutes Ag deposited and* 1 *minute* O_2 *annealed sample (S*2*). (c) Variation of SERS spectra with the molar concentration of R6G for S*1*.*

adsorbed on planar Si was used to obtain the reference spectra. Figure 5.1 shows the SERS spectra which includes Raman peak of R6G at 612, 772, 1182, 1312, 1364 and 1512 cm^{-1}. The dominant peak was observed at 612 cm^{-1} and at 1364 cm^{-1} for both S1 and S2.

To ensure the homogeneity, the SERS spectra were taken from 3 random points for both S1 and S2 and is shown in Figure 5.1a and Figure 5.1b, respectively. The SERS enhancement of S1 is almost 2 to 3 times greater than that of S3 for almost

Raman Peaks (cm^{-1})	**EF of S1)**	**EF of S2**
613	$(1.5 \pm 0.1) \times 10^6$	$(6.5 \pm 0.8) \times 10^6$
773	$(6.9 \pm 1.9) \times 10^5$	$(2.0 \pm 0.6) \times 10^5$
1185	$(8.1 \pm 1.5) \times 10^5$	$(2.7 \pm 1.1) \times 10^5$
1316	$(2.7 \pm 0.9) \times 10^5$	$(1.8 \pm 0.4) \times 10^5$
1364	$(1.2 \pm 0.3) \times 10^6$	$(3.2 \pm 0.9) \times 10^5$
1512	$(4.7 \pm 0.5) \times 10^5$	$(5.1 \pm 1.2) \times 10^5$

Table 5.1: *Average EF with standard deviations from SERS measurement for different Raman peak of* 5×10^{-5} *M R6G.*

all the peaks. Table 5.1 shows the EF for both the samples for different peaks. The EF obtained for the peak at 612 cm^{-1} for both S1 and S2 is $(1.5 \pm 0.1) \times 10^6$ and $(6.5 \pm 0.8) \times 10^7$, respectively. The comparison of EF for our substrates with other research work reported previously is shown in Table 5.2.

5.2.1 Optical Property: UV-Vis Spectroscopy

The UV-vis spectra of the samples made on planar and pyramidal Si (100) were taken in diffuse reflectance mode and they were converted to absorbance using Kubelka-Munk method which is shown in Figure 5.2 [154]. Two absorption bands can be seen from Figure 5.2a and in the $300 - 700$ nm range. The absorption band at 433 nm is very much sharp initially but gets broadened with increasing Ag coverage and with annealing. The peak at 533 nm is broader compared to the peak at 533 nm. This peak has a significant role in the SERS enhancement as it is close to the laser excitation wavelength of 632.8 nm. The UV-vis spectra of

Sample	Dye	SERS EF	ref
Ag thin film	Crystal violet	5.3×10^5	[148]
PVP capped Ag molecule	MBA	10^6	[149]
Ag on P-Si	R6G	10^8	[150]
Ag nanoparticle with Graphene quantum dot	R6G	7×10^5	[151]
Ag NP on PDMS	R6G	10^9	[152]
Au/Ag bi-metal nanoparticle with MoS_2 hybrid	R6G	9×10^9	[153]
Ag nanoparticle composite on planar Si	R6G	10^6	-

Table 5.2: *Comparison of SERS EF between different samples with our work based on Ag.*

Ag deposited on P-Si substrate also shows the same kind of behavior as shown in Figure 5.2b.

5.2.2 FDTD Simulation

3D-FDTD simulation was used to understand the real reason behind the enhancement and also to know whether the inclusion of the endotaxial Ag has any significant contribution to it. We have considered two systems for that purpose. One system consists of only Ag sphere of 60 nm radius residing on Si substrate and the other system consists of an Ag sphere of 60 nm radius on top of an Ag triangular particle (side length of 60 nm). The triangular particle was considered to be embedded inside the Si substrate. Figure 5.3a clearly shows an increment of the order of 2 in case of the coupled system. From the simulated EF image, it is observed that the maximum enhancement occurs at the nono-sized gap between

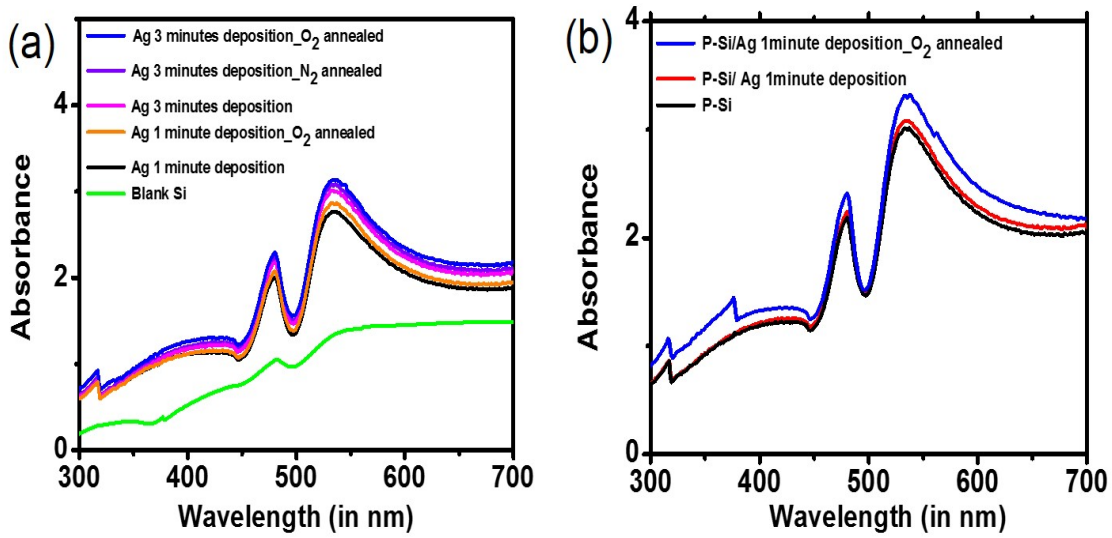

Figure 5.2: *UV-Vis absorbance spectra of (a) samples made on planar Si (*100*) and (b) samples made on P-Si, respectively.*

the two particles. The surface of Ag sphere also generates significant enhancement but it is lower compared to the enhancement produced in the nano-gap. We have obtained the maximum EF of 10^8 from the simulation which is higher than the experimentally observed value. This is trivial as the experimentally obtained value is then averaged over a whole particle which must be lower than the maximum value obtained from theoretical calculations. We have obtained EF of 10^{11} for S2 sample from theoretical calculation (Figure 5.3d) but from the TEM images, we have clearly observed higher inter-particle separation for S2 compared to S1. According to the observations made by Kim *et al.* it is very much clear that the enhancement depends vastly on the inter-particle separation and with increasing the particle separation the enhancement decreases dramatically [155].

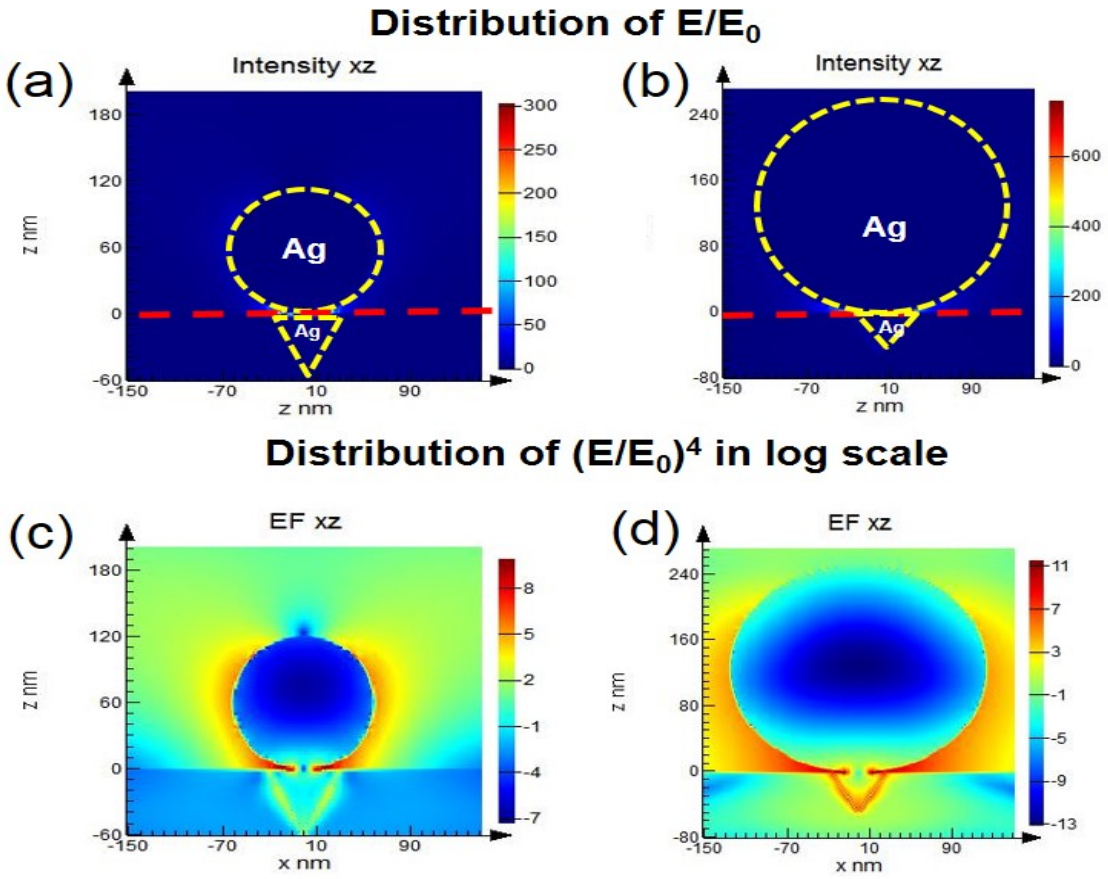

Figure 5.3: *FDTD calculated electric field distributions of (a)* 60 *nm radius spherical Ag particles in combination with endotaxial Ag particles, (b)* 125 *nm spherical Ag particles with* 50 *nm endotaxial Ag particles. (c) and (d) calculated EF (in log scale) in the X-Z plane from the same particles, respectively.*

To study the role of inter-particle separation on enhancement, we have done further FDTD simulation study. When we set the interparticle distance as 10 *nm* an enhancement of 2400 was observed. With increasing the distance to 25 *nm* (Figure 5.4a and Figure 5.4b) a decrement of 4 to 5 order is observed, resulting in almost 10^5 order decrement at the mid-portion of two nanoparticles which is shown in Figure 5.4c and Figure 5.4d. Su *et al.* showed that coupling becomes negligible when the interparticle distance becomes 2.5 times greater than the short

axis length. This results in a decrement in EF for S2 compared to S1.

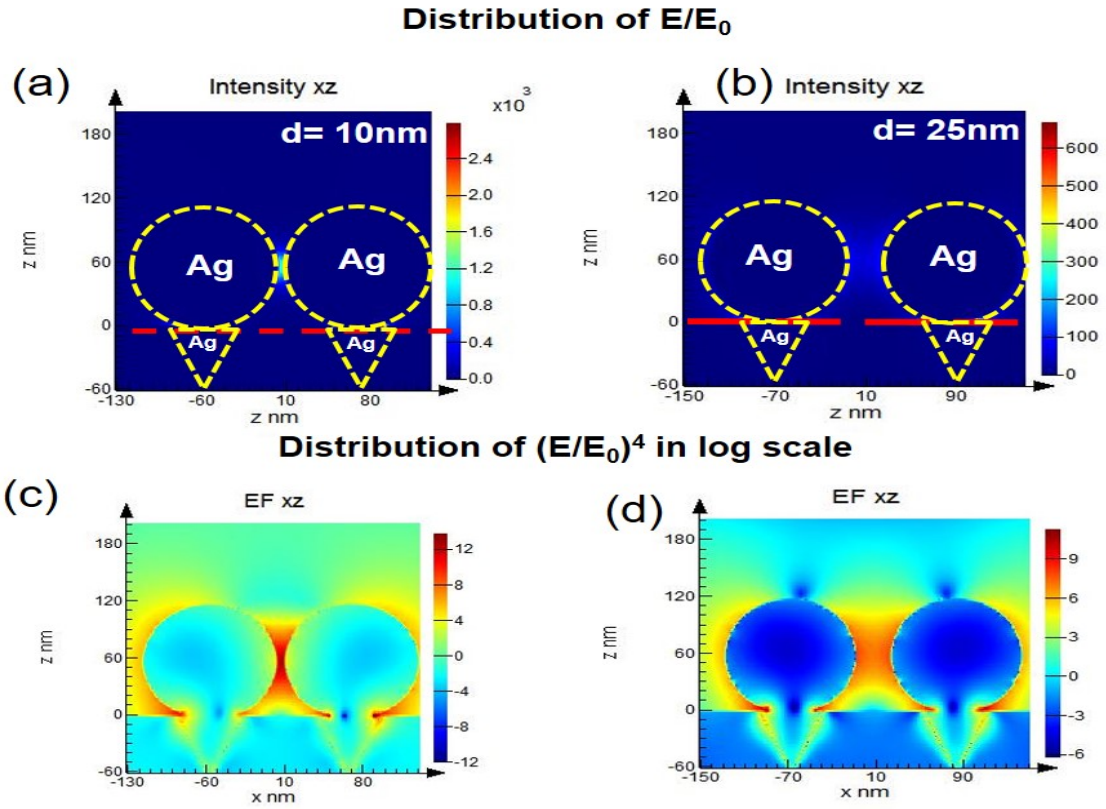

Figure 5.4: *FDTD calculated electric field distributions of coupled* 60 *nm radius spherical Ag particles in combination with the endotaxial Ag particles (a) when the interparticle distances are* 10 *nm, (b) when interparticle distances are* 25 *nm. (c) and (d) calculated EF (in log scale) in the X-Z plane for both the cases shown in (a) and (b), respectively.*

5.3 SERS Activity of Ag Deposited on Pyramidal Si

The SERS activity of the substrates was evaluated using R6G as dye. SERS spectra of all the substrates (S1, S2 and S3) were calculated using the formula [145–147],

$$EF = \frac{I_{SERS}}{I_{Bulk}} \times \frac{N_{Bulk}}{N_{SERS}} \tag{5.9}$$

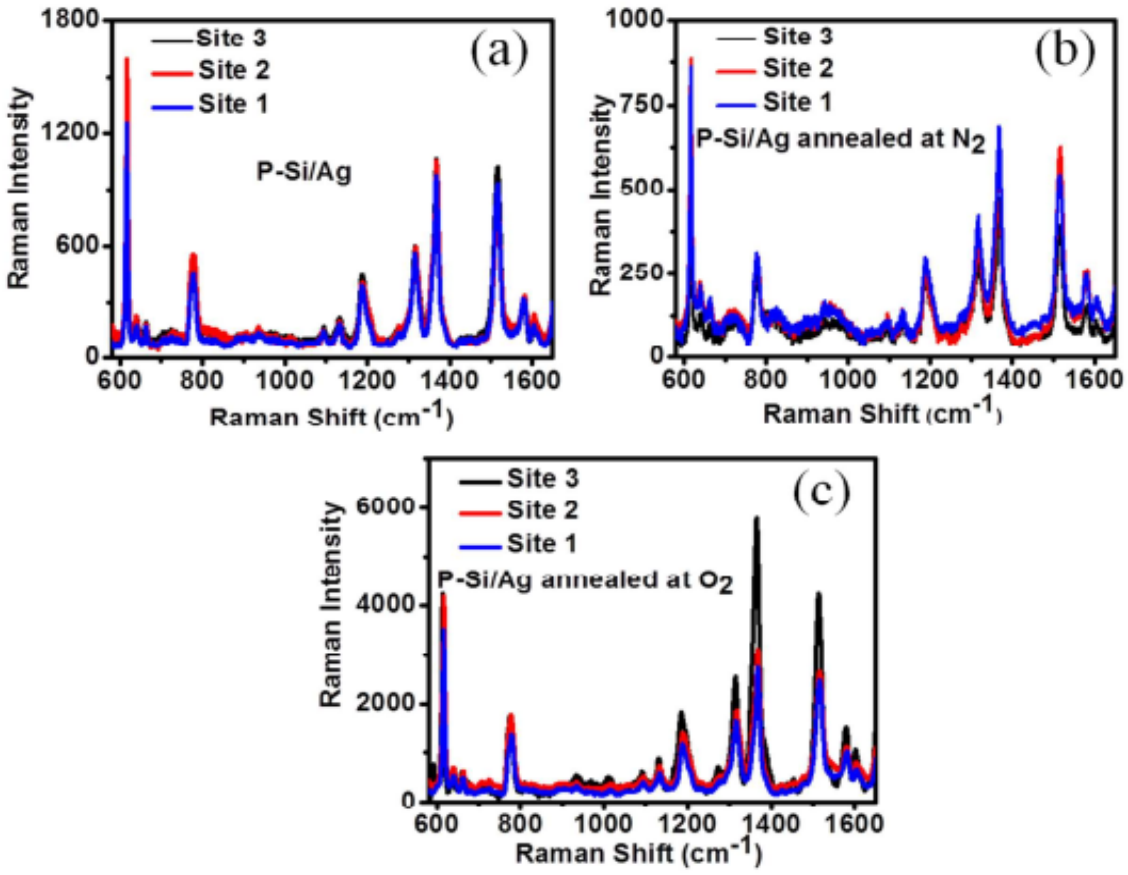

Figure 5.5: *SERS spectra of* 10^{-5} *M R6G at three different random site for three different substrates: (a) P-Si/Ag, (b) P-Si/Ag annealed at* N_2 *and (c) P-Si/Ag annealed at* O_2 .

Where I_{SERS} is the area under the peak of a particular vibrational Raman mode of the adsorbed analyte, I_{Bulk} is the same for the analyte only, the number of molecules present in the bulk sample is denoted by N_{Bulk} and N_{SERS} is the number of analyte molecules present in the SERS sample. To prepare the SERS substrates, the substrates were kept in the solution for 12 hours. R6G of 10^{-1} M concentration adsorbed on P-Si was taken as the reference spectra and 10^{-5} M concentration was used to measure the SERS activity of S1, S2 and S3. Figure 5.5 shows that all the

samples show SERS peak at 613, 774, 1185, 1312, 1364 and 1509 cm^{-1} which are the well-known peak of R6G as observed by previous researchers [145–147]. The most intense peak at 613 cm^{-1} is due to C-C-C in-plane vibration of R6G molecule and the peak at 1364 cm^{-1} is originated by vibration of aromatic C-C bond stretching. It is very much interesting to see that, S3 was giving 3.5 and 2 times higher enhancement compared to S2 and S1 considering all the peaks of the SERS spectra. The SERS EF for S1, S2 and S3 with standard deviation is shown in the Table 5.3 . Highest EF was observed for S3 for the peak at 613 cm^{-1} $[(9.5 \pm 0.8) \times 10^7]$ and it is very much comparable to the EF of the substrates or nanoparticles prepared by Ag. The EF of S2 is observed to be lower than that of S1, which is trivial as S1 contains particles which are of irregular shape and contains sharp edges where EM field can be concentrated. S2 on the other hand mostly contains spherical shaped Ag nanoparticles where EM field does not have chance to get enhance significantly.

Raman Peaks cm^{-1}	**EF** ($\times 10^7$ **of S1**)	**EF** ($\times 10^7$ **of S2**)	**EF** ($\times 10^7$ **of S3**)
613	4.5 ± 0.5	2.7 ± 0.2	9.5 ± 0.8
773	3.8 ± 0.3	2.3 ± 0.1	8.1 ± 0.8
1185	4.7 ± 0.3	2.7 ± 0.2	7.9 ± 1.5
1316	3.5 ± 0.1	1.5 ± 0.2	6.3 ± 1.1
1364	4.3 ± 0.2	2.4 ± 0.2	6.6 ± 1.7
1512	4.5 ± 0.4	1.8 ± 0.2	7.0 ± 1.5

Table 5.3: *EF from SERS measurement for different Raman peak of* 10^{-5} M. *R6G* .

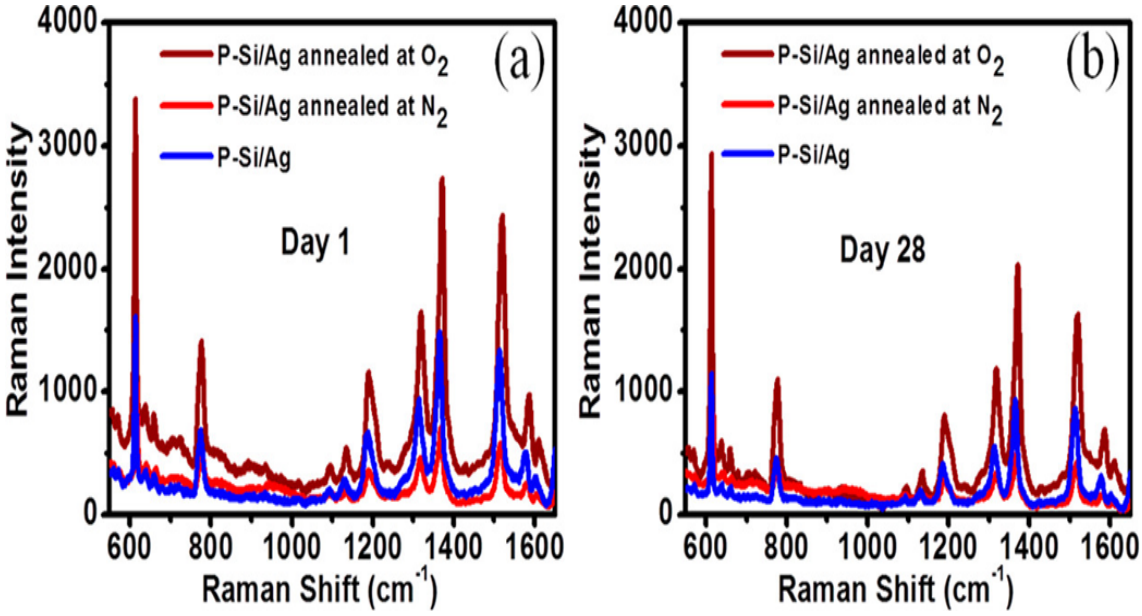

Figure 5.6: *(a) SERS spectra of* 10^{-5} *M R6G taken for S1, S2, and S3 samples just after preparation (day 1). (b) SERS spectra of the same three samples after 28 days.*

To ensure the homogeneity, the SERS data were taken from three different regions of all the substrates and are shown in Figure 5.5. Also, the SERS data were taken at an interval of 7 days up to 28 days to study the impact of atmosphere on these nanoparticles. Figure 5.6 shows the comparative SERS spectra of the three samples at day 1 and at day 28. The intensities of all the SERS peak for all the three substrates were decreasing, however, the decrement is less for S3 (18%) compared to S2 (26%) and S1 (31%) for the peak at 613 cm^{-1} (Table 5.4). This proves the superiority of S3 over S2 and S1 in terms of EF and stability. From the FDTD simulation we have observed that the coupling between the two Ag nanoparticles provides the major contribution behind the enhancement and the formation of SiO_x layer on top of the triangular particles provides the stability. As sample S3 showed the highest enhancement, it was further studied to obtain

the limit of detection. It is observed that significant enhancement was obtained for 10^{-7} M concentration of R6G and is shown in Figure 5.12.

Raman Peaks cm^{-1}	**Day 1** $(\times\mathbf{10^7})$	**Day 7** $(\times 10^7)$	**Day 14** $(\times 10^7)$	**Day 21** $(\times 10^7)$	**Day 28** $(\times 10^7)$
613	(9.5 ± 0.8)	9.4 ± 0.8	8.1 ± 0.9	8.0 ± 0.6	7.8 ± 0.3
1364	6.5 ± 1.7	6.1 ± 0.6	6.1 ± 0.2	5.9 ± 0.2	5.4 ± 0.4

Table 5.4: *EF for different interval of time for S3.*

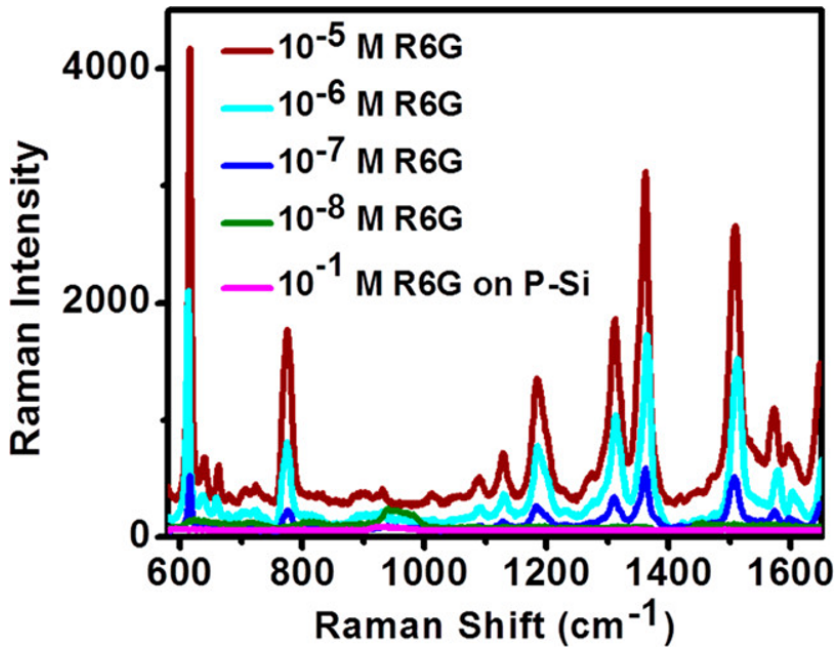

Figure 5.7: *SERS spectra of different concentration of R6G for S3 and R6G (*10^{-1} *M) on P–Si.*

However, considering the model by Lakowicz *et al.* where the adsorbed molecules

were considered to behave as a dipole and metal particles are taken as simple spherical particle then induced electric field can be written as [161],

$$E = \frac{E_0 r^3(\epsilon_m + \epsilon_d)}{(d+r)^3} + (\epsilon_m + 2\epsilon_d) \tag{5.10}$$

where d is the distance between the metal particle and the molecule, r is the radius of the metal particles and the dielectric constant of the metal and the substrate is represented by ϵ_m and ϵ_d respectively. So, it is clear from the equation that the induced electric field changes with metal particle dimension but the change obtained in our case cannot be explained only by considering the change in size.

5.3.1 Cathodoluminescence Measurements

In CL, electron beam excitation is used to produce radiative emission from metal nanoparticles. As the radiative (photon) emission is higher in the regimes where strong LSPR mode occurs, it can directly map the near field intensity distribution [162]. Yamamoto *et al.* were first to spatially resolve the plasmonic mode of Ag using CL spectroscopy [163]. We have also used CL spectroscopy and imaging to find out the exact location of the hotspots produced in the S3 sample.

We have taken CL measurement from the combined structure as the triangular Ag nanostructures are situated at the bottom of the spherical one on pyramidal Si. So, it is very difficult to probe only the triangular nanostructure. Figure 5.8a shows the SE image of the composite nanoparticle and Figure 5.8b shows the PAN CL image of it within the wavelength range of $300 - 800\ nm$. It is clear from the PAN CL image that both the spherical and the triangular particle contains hotspots. The MONO CL mode of operation was also performed to obtain more spectrally

resolved features. Figure 5.8c shows the CL spectra taken from the spherical Ag (red dot in Figure 5.8a) and triangular Ag (blue dot in Figure 5.8a). The strong peak observed at 372 nm is the surface plasmon peak of Ag [21]. The other peaks are observed at 424 nm, 464 nm for the spherical particle and a relatively strong peak at 525 nm for the triangular particle. These peaks are higher-order excitation mode of Ag and their intensity and position depend vastly on the size and shape of the metal nanoparticles.

Figure 5.8d, 5.8e, 5.8g and 5.8h show the MONO CL mapping at $372, 525, 424$ and 464 nm respectively. Using MONO CL mode we could directly map the local electric field. The spatial variation of the emission is caused by the degree of coupling of the incident electron beam excitation with the local electromagnetic field of the local surface plasmon resonance mode. So, from the images of Figure 5.8 we could tell that the peaks observed at Figure 5.8c are the plasmon modes of the combined nanostructure, where an additional peak at 525 cm^{-1} is observed from the triangular nanoparticle and this is also close to the excitation wavelength ($632.8nm$) used for SERS experiment.

5.3.2 UV-Visible Spectroscopy

Figure 5.9 shows the UV-vis absorption spectra of the samples. The UV-vis was obtained in reflectance mode using ParkinElmar Lambda 750 spectrophotometer. The surface plasmon peak of as-deposited Ag is observed to be at 368 nm which is observed to be red-shifted with annealing. Peak at 521 nm and 475 nm is also seen for S3 which is very much close to our CL observation. While for S2 the intensity at 475 nm is reduced compared to that of S3.

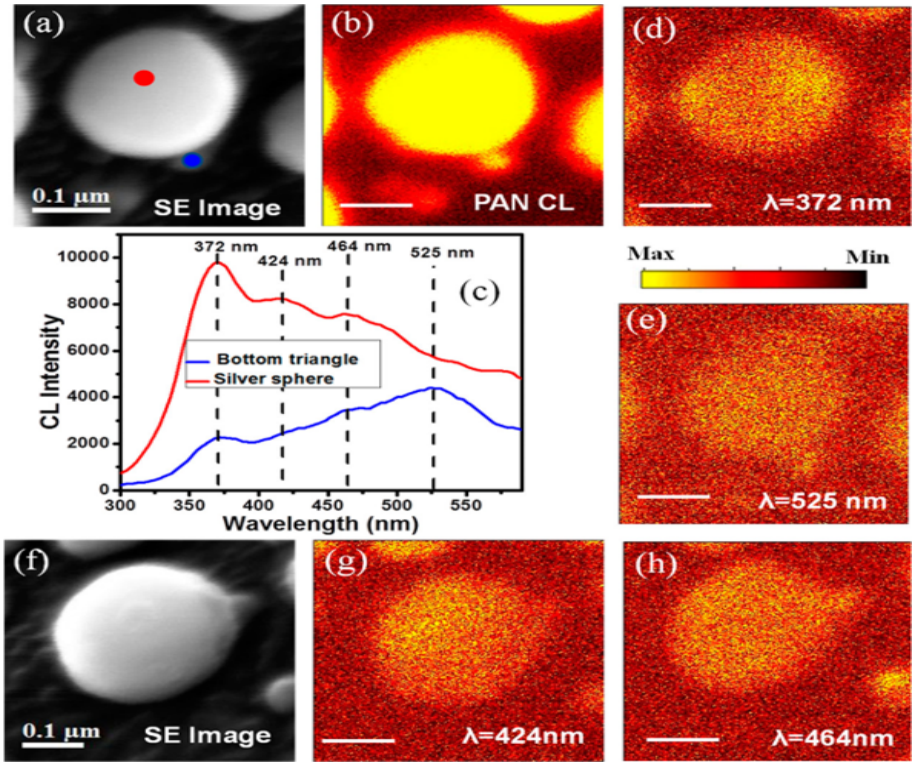

Figure 5.8: *(a) SE image, (b) PAN CL image showing the formation of hot spots on both the spherical particle and triangular particle, (c) CL emission spectra from the spherical particle (red curve) and from bottom triangle (blue curve), (d and e) Mono CL image at* 372 *and* 525 *nm, respectively, (f) SE image of second particle, (g) MONO CL image showing the hotspot is contained mainly by the sphere at* 424 *nm, and (h) MONO CL image where the hotspot is also contained by the bottom triangle at* 464 *nm.*

5.3.3 Near Field Intensity Distribution: FDTD Simulation

We have performed FDTD simulation to understand the enhancement observed for the coupled nanostructure. The x-z view of the near field intensity distribution is shown in Figure 5.10a for 632 *nm* excitation wavelength. The highest enhancement is observed to form at the junction of the spherical Ag and triangular Ag nanoparticle. Thus the coupling between the LSPR of the two nanostructure is considered

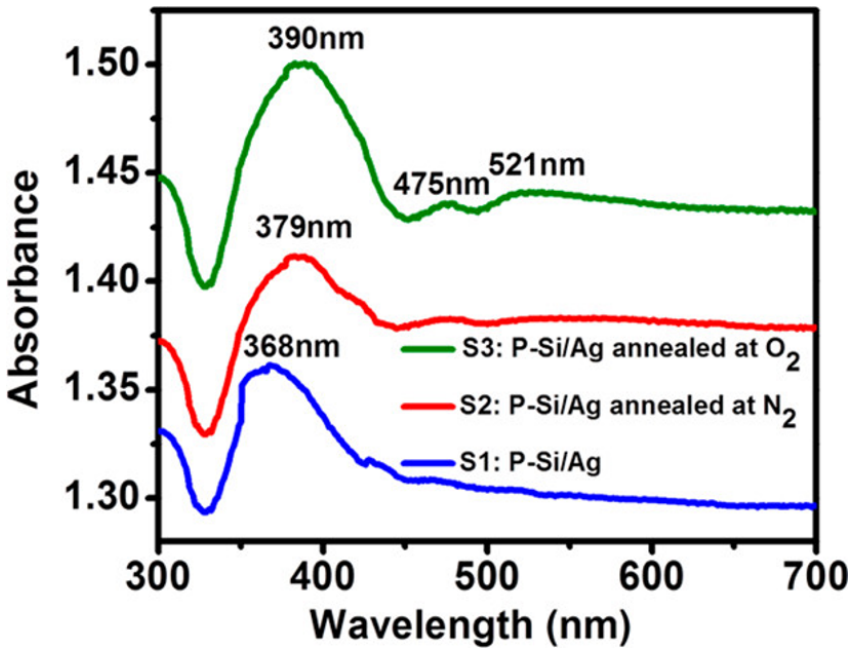

Figure 5.9: *UV–visible spectra of S1, S2, and S3.*

to be responsible behind the large SERS enhancement observed for S3 [164]. Figure 5.10b shows the EF mapping for S3. The enhancement factor is proportional to $(\frac{E^4}{E_0^4})$, where E is the local intensity of the electric field and E_0 is the intensity of the incident electric field. The highest enhancement is observed to occur at the junction (2.8×10^7). The differences between the experimentally observed value and value obtained from simulation are due to (i) CM is also responsible behind SERS enhancement, but in the simulation, we have only considered EM enhancement (ii) The size and distribution of the Ag triangle and Ag sphere combination continuously changes along the height of the pyramid, which will affect the EF but in our simulation we have considered enhancement from a single pair.

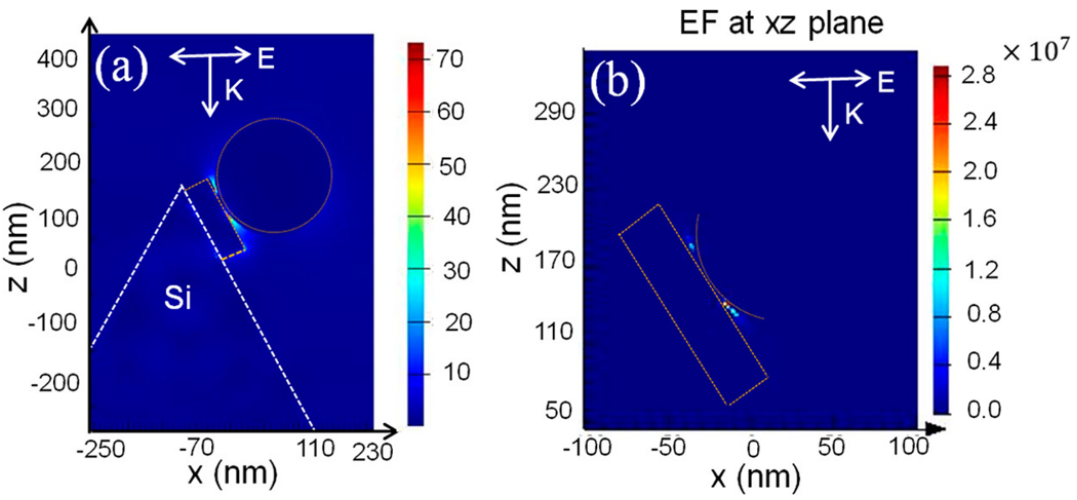

Figure 5.10: *(a) FDTD calculated electric field distribution of triangular Ag particles with the spherical Ag particle combination on 3D Si substrate under* 632 *nm excitation wavelength and (b) calculated EF in the x–z plane from the coupled Ag nanoparticles.*

5.4 SERS Study of Ag Deposited on P-Si/Si-NW Substrate

The Raman spectra of 10^{-1} M R6G and SERS spectra of 10^{-5} M R6G on different substrates are shown in Figure 5.11a. The Raman peak of R6G at 613, 772, 1182, 1312, 1364, 1512 and 1560 cm^{-1} are observed clearly [145–147]. Table 5.5 shows the calculated SERS EF for the peak at 1572 cm^{-1} for all the substrates. A significant enhancement factor of $10^5 - 10^6$ is observed for all the substrates. This shows that the substrates can be used as effective SERS active substrates.

Due to its various roughness scale, the substrate also shows very good hydrophobic property [174]. The CA shown by P-Si sample is 99.85^o which increases to 119.65^o when we deposit Ag on P-Si and is shown in Figure 5.11c. Highest value of contact angle (135.46^o) was obtained for P-Si/Si-nanowire sample shown in Figure 5.11d.

Raman Peaks cm^{-1}	**EF of) P-Si/NW-Si**	**EF of P-Si/NW-Si and Ag N_2 annealed**	**EF of P-Si/NW-Si and Ag O_2 annealed**
613	7.5×10^4	1.1×10^5	1.5×10^5
775	–	1.2×10^4	1.0×10^4
1187	–	3.1×10^4	3.2×10^4
1305	–	3.5×10^5	3.4×10^4
1360	1.1×10^5	1.7×10^5	2.1×10^5
1572	1.6×10^5	2.3×10^6	2.6×10^6

Table 5.5: *EF from SERS measurement for different Raman peak of* 1×10^{-5} *M R6G.*

The contact angle equation of water on rough surfaces can written according to Cassie model as [175],

$$\cos\theta_r = f_1 \cos\theta - f_2 \tag{5.11}$$

where θ and $_r$ are the water CA on the plane and rough surfaces respectively. f_1 and f_2 are the fractional interface areas of the porous structure and of the air in the interface between them respectively.

Water droplet on P-Si almost covers the entire top and valley portions of the pyramid resulting a very small air fraction between them which leads to smaller increments in the water contact angle compared to that on planar Si. With the introduction of nanowire structure on the pyramidal surface a stable interface between the droplet, P-Si/Si-nanowire binary structure and the air portion between

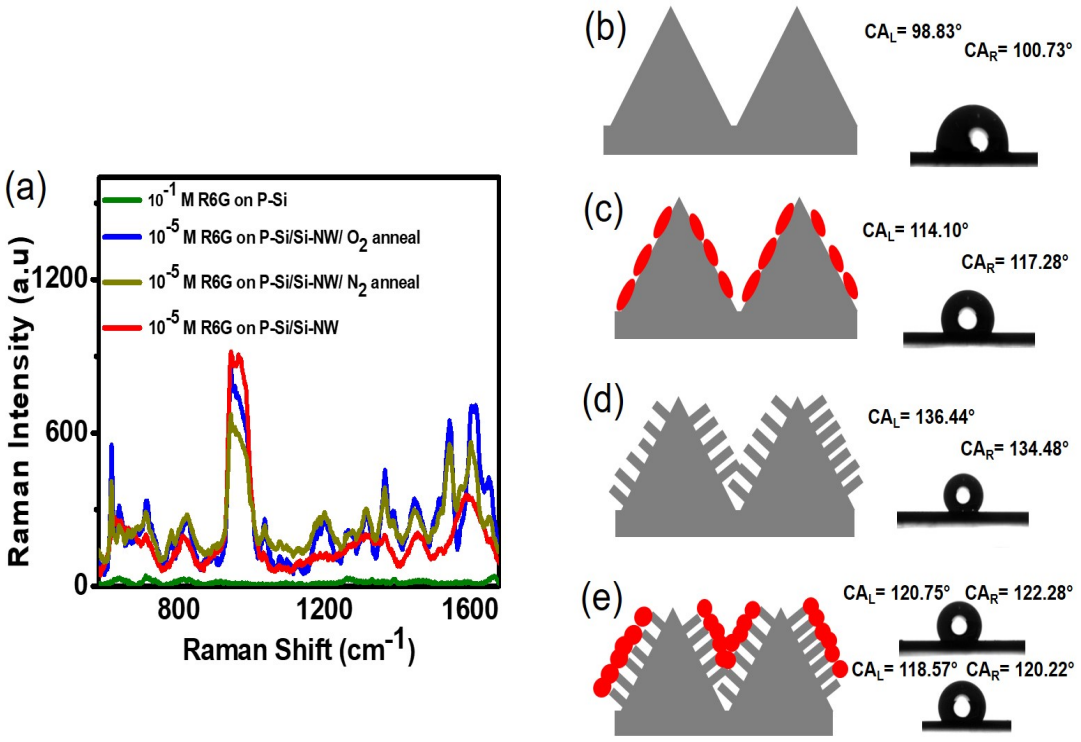

Figure 5.11: *(a) SERS spectra of* 10^{-5} *M R6G on different substrates and* 10^{-1} *M R6G on P-Si. (b–e) Variation of water contact angle for different substrates.*

them is produced. According to the observation made by Li *et al.* for P-Si/Si-nanowire binary structure 93.3% air portions can be obtained. Which gives the value of $f_2 = 0.933$ and $f_1 = 0.067$ resulting a C.A of almost 162^o [175]. In our case, we obtain the $C.A = 135^o$ for the binary structure.

5.4.1 FDTD Simulation of Ag deposited on Si-Nanowire

FDTD simulation was used to study the interaction of incident EM waves with different structures. The direction of propagation and direction of polarization of the incident wave is shown in Figure 5.12. The incident EM wave is observed to get enhanced at the tip of Si-nanowire as shown in Figure 5.12a. From Figure 5.12b it

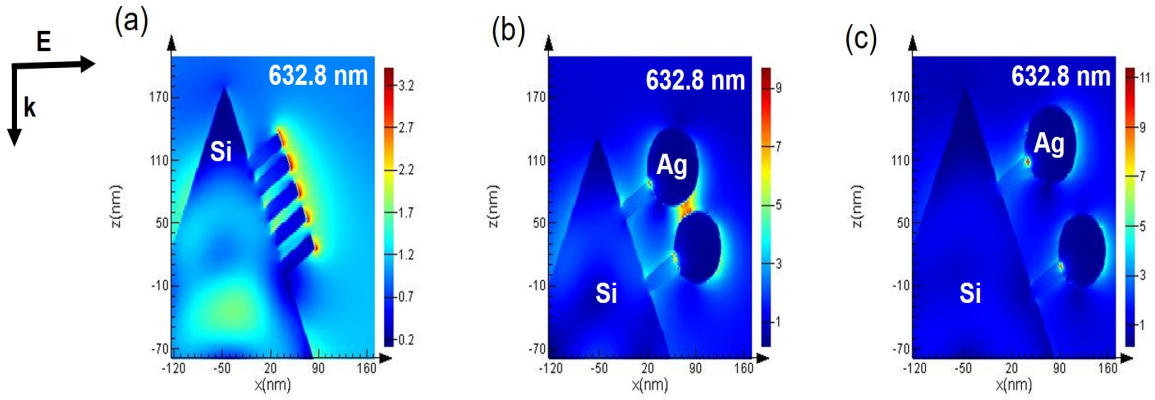

Figure 5.12: *(a) X–Z view of FDTD simulated e-field distribution of Si NW on Si pyramid. (b) Ag sphere on P-Si/Si-nanowire configuration showing maximum enhancement at the mid-portion between two spheres. (c) E-field distribution when two spheres are separated by a longer distance. The polarization direction is taken along X-axis.*

is clear that the near field intensity increases when Ag nanoparticles are situated at the top of Si-nanowire compared to only Si-nanowire. For our simulation purpose, we took two Ag particles of radius 50 *nm* separated by a distance of 20 and 50 *nm*. The radius of the particles was taken according to the observations made by SEM. It was also observed that the interparticle distances between the spherical Ag nanoparticles increase as we go from the bottom towards the top of the pyramid. Hence, to observe the effect of inter-particle distances on the near field intensity two separation distance was taken and it was observed that the intensity decreases with increasing particle separation. We have observed EF of 10^4 which is lower than the experimentally observed value. However, in real samples, a single spherical particle is surrounded by a number of spherical particles in all the direction but we have considered only two particles residing side by side for the simulation purpose. It is known that near field intensity enhances greatly when the two

particles are very close together hence, the experimentally observed EF must be greater than that obtained from the simulation [176, 177]. We have shown that when the inter-particle distances are 50 nm the intensity decreases rapidly at the mid-portion between them (Figure 5.12c). The incident laser also gets periodically reflected after incidence on the pyramidal Si surface, which also contributes to the enhancement significantly. Considering all these factors in a single simulation requires a huge memory and hence we had to limit our simulation for two Ag nanoparticles.

5.5 SERS Activity Measurement of Pd Nanoparticles Deposited on Semiconductor Substrate

The SERS activity of the substrates was measured by using R6G as the probe molecule. To prepare the SERS substrate $50\mu L$ of 10^{-6} M R6G was drop cast on the nanoparticle deposited substrates and then dried overnight. The SERS spectra of the substrates are shown in Figure 5.13. All the samples show the characteristic Raman spectra of R6G as described in the previous chapters. The SERS EF of the different substrates was measured using the method described previously. The highest SERS EF and lowest detection limit of 10^{-10} M was observed for the S60 sample (Figure 5.13d). R6G of 10^{-9} M concentration was detected by the other samples. The intensities of the Raman bands for S60 at 1364, 1512, and 1650 cm^{-1} are 2.5, 3.1, and 2.6 times higher than S20 and 1.8, 2.1, and 1.7 times higher than G20. The SERS spectra were taken from three different points for all the substrates to ensure homogeneity. The average EF with standard deviations are listed in Table 5.6 for all the substrates. EF of $(8.5 \pm 2.1) \times 10^5$ was observed for S60 for the peak at 1650 cm^{-1}. This value is very much comparable to the EF obtained

5.jpg

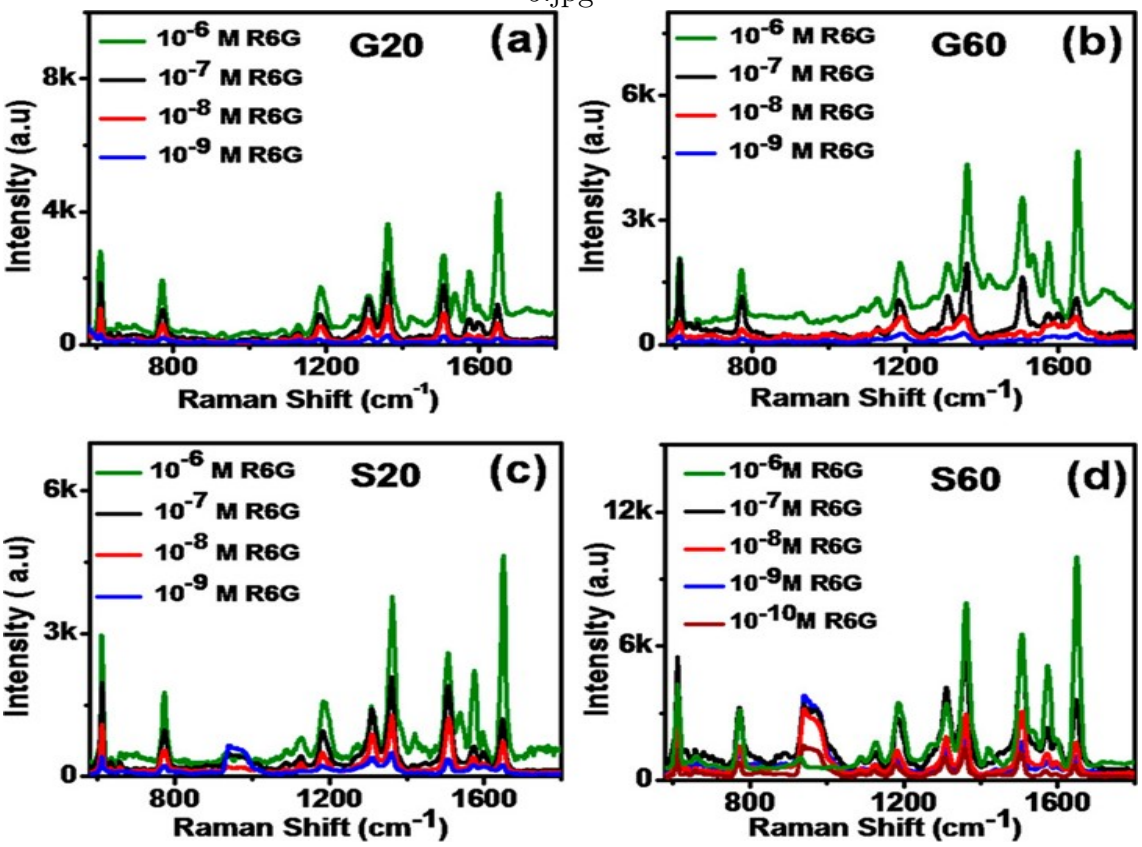

Figure 5.13: *(a), (b) SERS spectra of G*20 *and G*60*, respectively for different concentrations of R6G. (c), (d) SERS spectra of S*20 *and S*60*, respectively, for different concentrations of R6G.*

from chemically synthesized Pd nanoparticles and also Pd nanoparticles deposited on Si substrate. EF for G20 and G60 are$(3.5 \pm 0.3) \times 10^5$ and $(3.4 \pm 0.9) \times 10^5$ for the peak at 1650 cm^{-1}. The highest EF of R6G peaks for the S60 sample can be attributed to the following reasons.

The nanorod clusters produce very sharp metal edges on planar Si giving effective condition for EF enhancement [82, 87]. For S10 the enhancement is also due to the same reason but the very low coverage of nanoparticles does not allow to

Sample Number	**EF at 1362** cm^{-1} $\times\mathbf{10^5}$	**EF at 1512** cm^{-1} $\times\mathbf{10^5}$	**EF at 1650** cm^{-1} $\times\mathbf{10^5}$
G10	2.7 ± 0.1	3.3 ± 0.4	4.9 ± 0.5
G20	2.0 ± 0.1	2.4 ± 0.3	3.5 ± 0.3
G60	2.1 ± 0.4	2.4 ± 0.8	3.4 ± 0.9
S10	1.4 ± 0.2	2.3 ± 0.3	2.5 ± 0.3
S20	1.9 ± 0.3	2.2 ± 0.2	3.3 ± 0.6
S60	4.7 ± 1.4	6.8 ± 1.7	8.5 ± 2.1
PS10	6.1 ± 0.8	12.1 ± 1.3	4.5 ± 0.9
PS20	6.8 ± 1.1	12.6 ± 1.8	8.2 ± 1.8
PS60	16.5 ± 2.3	29.4 ± 7.4	16.8 ± 1.7

Table 5.6: *Average EF with standard deviations from SERS measurement for different Raman peak of* $10^{-6}M$ *R6G.*

produce sufficient number of hot spots. For the Ge substrate, the growth rate is much faster than Si and leads to continuous film of Pd, on which spherical-shaped nanoparticles containing shafts are situated. The ratio of the shaft structure to spherical-shaped core is low here and it does not provide ideal conditions for SERS enhancement. This is also observed in FDTD simulation and discussed in the latter part of this thesis.

The relationship between the concentration of R6G for different samples and

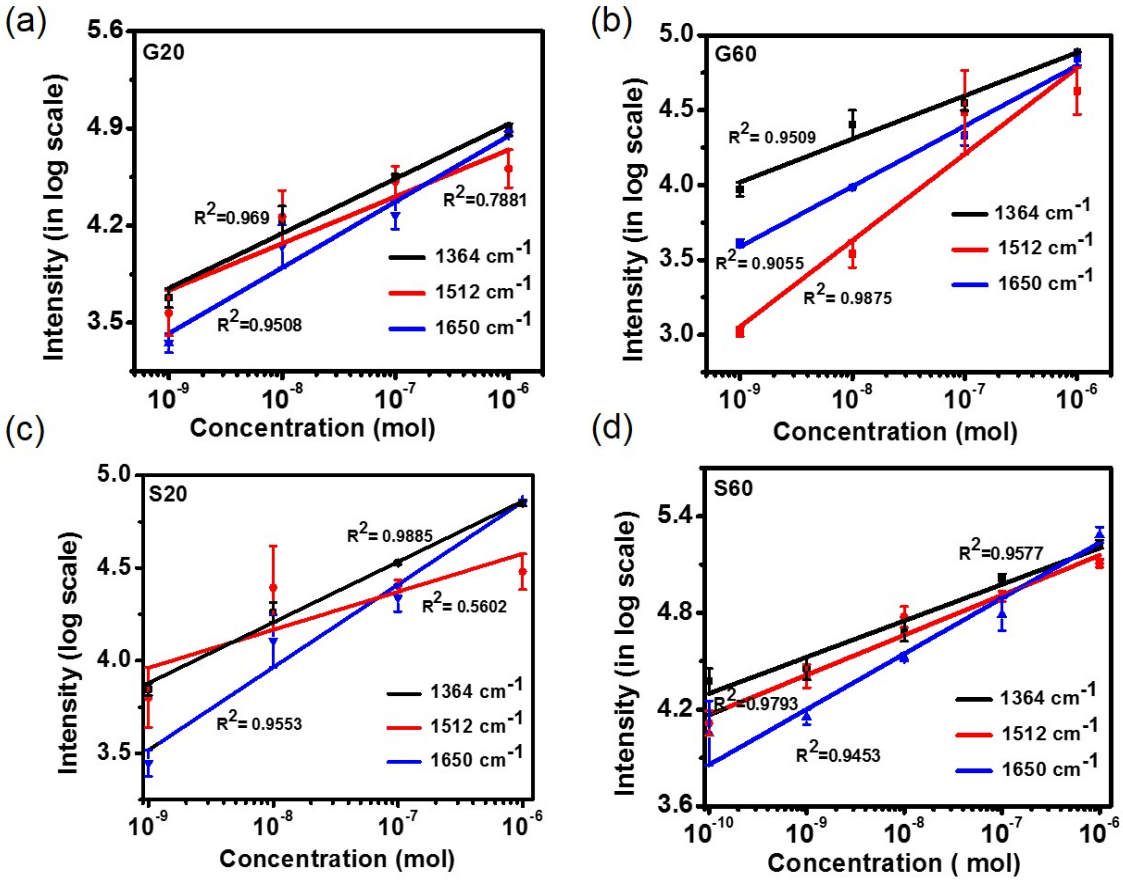

Figure 5.14: *(a), (b), (c) and (d) shows intensity versus concentration graph for G20, G60, S20 and S60 respectively.*

the SERS intensity of the peaks at 1364, 1512, and 1650 cm^1 and is shown in Figure 5.14. The samples show a linear relation with concentration. The values of R^2 (standard deviations) for different samples indicate the fact that all the samples can analyze concentration of R6G quantitatively. The R^2 value of S60 shows the least standard deviations, indicating improved uniformity with increment in the deposition time.

A 3 to 7 times increment in the SERS signal was observed compared to the

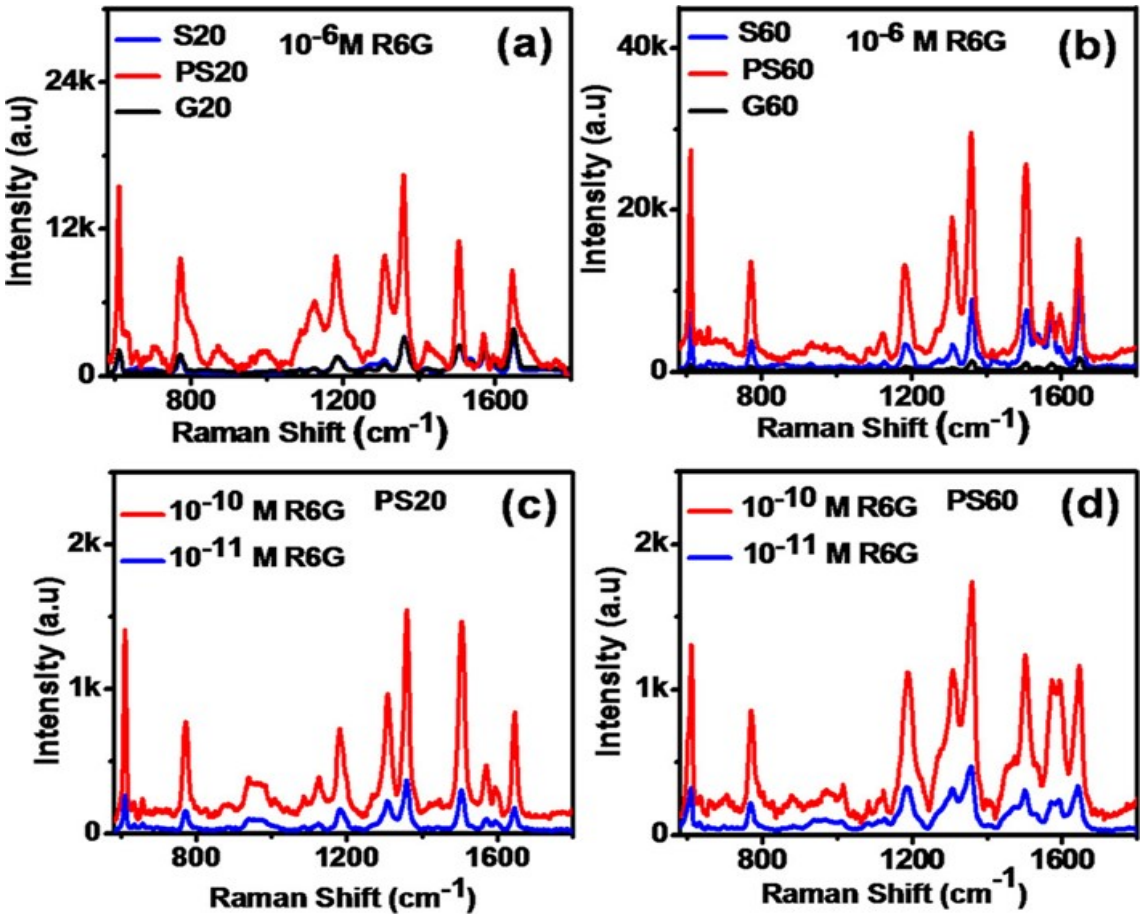

Figure 5.15: *(a) and (b) shows SERS spectra of G*20*, S*20*, and PS*20 *and G*60*, S*60*, and PS*60 *substrates taken with* 10^{-6} *M concentration of R6G. (c) and (d) shows intensities of the Raman spectra for* 10^{-10} *and* 10^{-11} *M concentrations of R6G for the PS*20 *and PS*60 *samples, respectively.*

previous samples for all the peaks of R6G when Pd was deposited on P-Si. As the peak position did not change and also the substrate material remains the same, it is clear that the huge enhancement results from EM origin. From the SERS spectra of Figure 5.15 it is observed that the relative intensity of the peaks at $1312cm^{-1}/1364cm^{-1}$ increases while that of $1572cm^{-1}/1650cm^{-1}$ decreases. The peak at 1312 cm^{-1} has a different origin than the peaks at 1364, 1572, and 1650 cm^{-1}. The change in adsorption geometry of R6G molecule on P-Si compared to

Ge and Si is responsible for such change in relative intensities. The higher intensity at 1364 and 1650 cm^{-1} indicates that the long axis of R6G molecule aligns parallel to the Pd surface (ethylamine up configuration). This configuration increases the interaction with the aromatic ring resulting higher charge transfer. On P-Si surface the intensity of the peaks at 1572 cm^{-1} decreases due to reduced charge transfer. However, to understand the features correctly a detailed theoretical understanding is necessary. Figure 5.15a and Figure 5.15b shows the SERS spectra for PS20 and PS60 sample using 10^{-6} M R6G. For PS20 the EF obtained for the peaks at 1364, 1512 and 1650 cm^{-1} is 8.3×10^5, 1.5×10^6 and 1.1×10^6 respectively. For PS60 these values are 1.9×10^6, 3.8×10^6 and 1.9×10^6 respectively. These values of EF are much higher compared to the previously obtained substrates based on Pd nanoparticles. The huge enhancement can be explained by the following reasons. Significant enhancement of the incident EM signal occurs at the sharp ridge and edges of the P-Si structures. According to Lee *et al.* the enhancement on 3D Si substrate is 3.9 times higher than that on planar Si. Secondly, the periodic pyramidal arrangement will make the incident laser oscillate and the incident light will get trapped which will further contribute to the enhancement. Also, the Pd nanostructures formed on P-Si have a sharp edge compared to the ones formed on planar Si and Ge. Figure 5.15c and Figure 5.15d shows the SERS spectra of the two samples with R6G concentration on 10^{-10} M and 10^{-11} M respectively. Both the substrates show significant SERS enhancement even for such low concentration of the analyte molecule which is remarkable using any substrate with Pd nanoparticles.

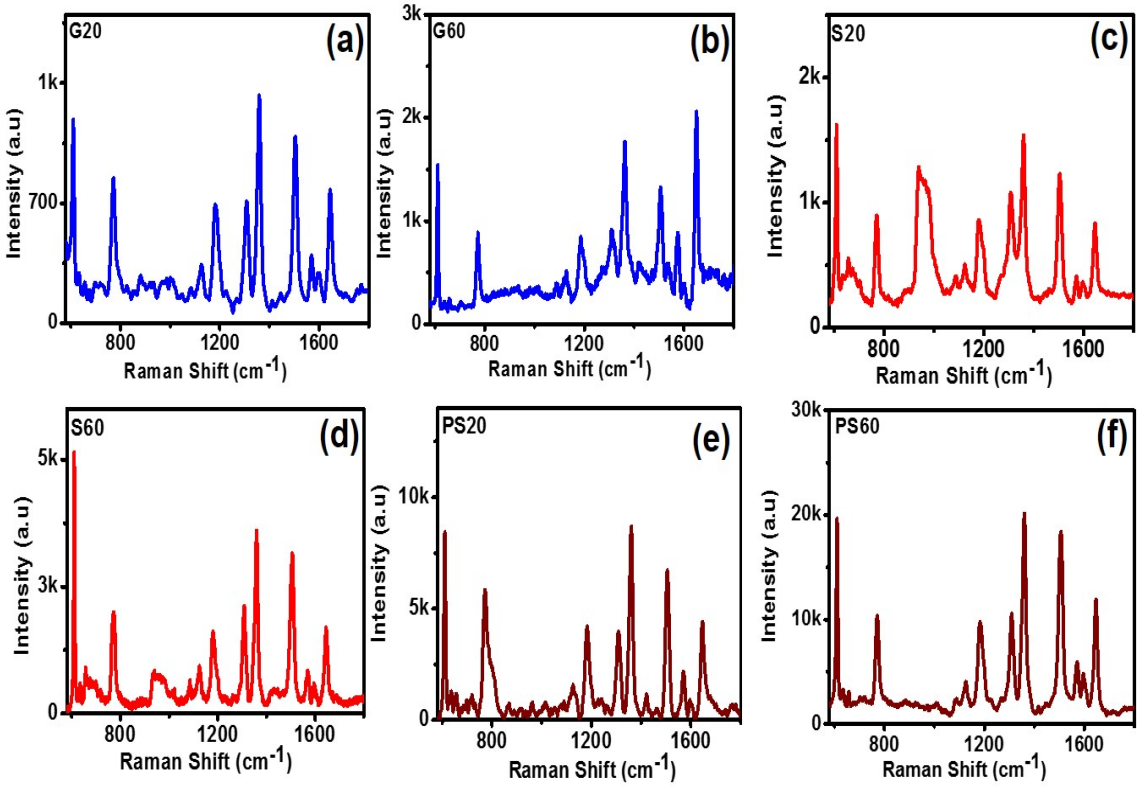

Figure 5.16: *(a), (b), (c), (d), (e) and (f) show SERS spectra of* 10^{-6} *M concentration of R6G after* 1 *month for G*20*, G*60*, S*20*, S*60*, PS*20 *and PS*60 *sample, respectively.*

We have also tested the stability of the substrates by taking the SERS spectra of the samples after keeping them in ambient atmosphere for one month. Figure 5.16 shows the SERS spectra of all the samples after one month and it is observed that the intensity of the SERS peak decreases for all the substrates but significant enhancement still remains. The highest reduction is observed for both *G*60 and *S*20 (52%). While for PS20 and PS60 the reduction in intensity is 30% and 32% respectively. This fact indicates that Pd on P-Si substrate is superior compared to others in terms of EF and also stability. A comparative graph of the SERS

intensity for the three different peaks of R6G is plotted for different samples and is shown in Figure 5.17.

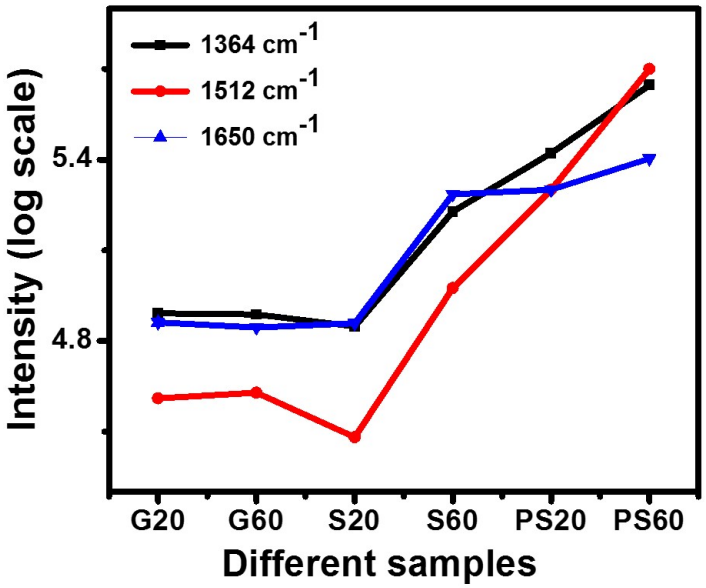

Figure 5.17: *SERS intensity for different substrates for* 3 *different peaks of R6G. The highest is observed for PS*60 *(R6G concentration is* 10^{-6} *M).*

5.5.1 FDTD Simulation Study

FDTD simulation was done to understand the near-field intensity distribution around the nanostructures for three different substrates. Figure 5.18a shows the near-field intensity distribution of Pd deposited on Ge substrate. It is observed that the highest enhancement occurs at the tip of the Pd nanostructures. However, the enhancement at the nanostructure surface is much lower. The EF is proportional to the ratio of $\frac{|E|^4}{|E_0|^4}$, where E_0 is the intensity of incident electric field and E is the intensity of the local electric field. The EF obtained by the simulation is 1.6×10^5 which is slightly lower than the experimentally observed value (Figure

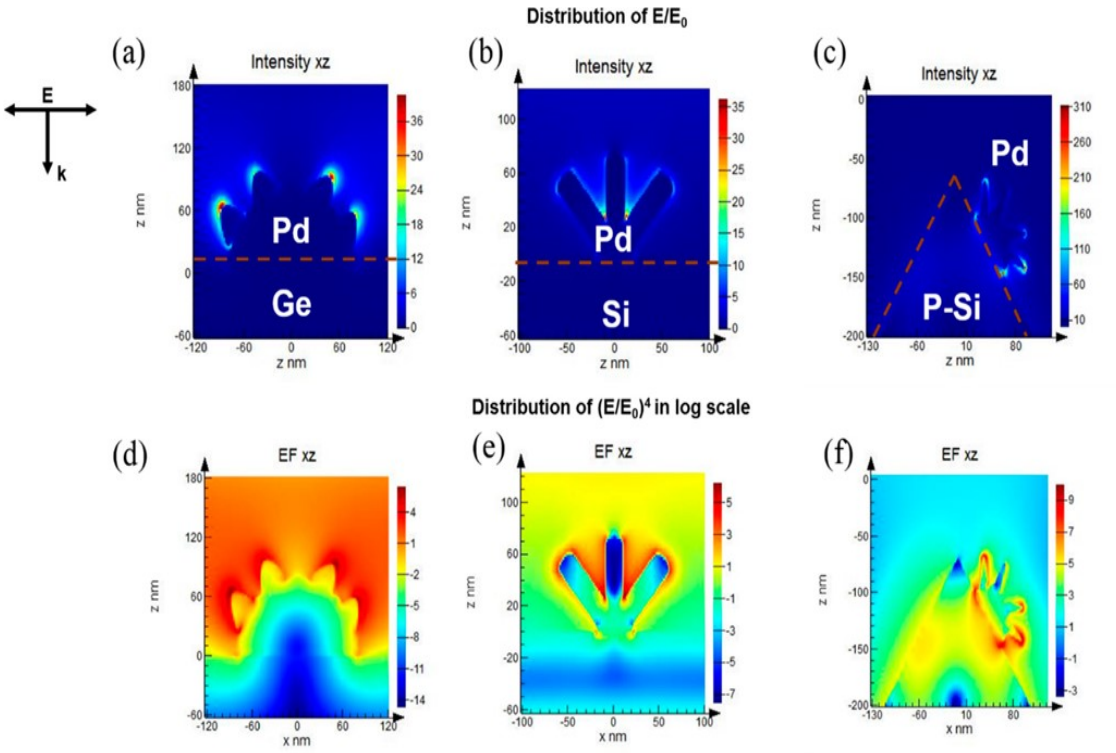

Figure 5.18: *(a), (b) and (c) shows FDTD-calculated near-field electric field distribution of Pd on Ge(100), Pd on Si(100) and Pd on P–Si. (d), (e) and (f) shows calculated EFs in the logarithmic scale for the same three substrates respectively.*

5.18d). This can be attributed to the fact that, in real sample, the number of shafts on spherical Pd is different in different spheres. The incident EM field gets enhanced at the gaps between two spheres when two shafts are situated very closely. So, when two spheres lie very close to each other, incident EM field can also get enhanced between the two spheres. By using a finer mesh we have also done FDTD simulations considering more than one particle for all the substrates and indeed observed large enhancement of the incident EM radiation between the particles which is shown in Figure 5.19. For simulation purposes, we have considered only four shafts on Pd nanoparticles situated on Ge. But from different TEM images, we have observed seven to eight numbers of shafts on the nanostructures which in

practical case must effect in the enhancement. We restrict the simulation for four shaft due to limited computing facilities. In case of Pd on planar Si, a single cluster is observed to form with six to nine nanorods, however, for simulation purposes we have considered a cluster formed with only three nanorods which must have affected the enhancement. The scale bar indicates enhancement of the order of $10^5 - 10^6$ for Si and Ge and 10^9 for P-Si. From the log-normal distribution, it is also clear that the distribution of hot spots is very much widespread. As the enhancement factor obtained from the experiment is averaged over all the hot spots, it must be lower than the highest enhancement shown in the simulation. Figures 5.18b and c show the local electric field intensity for Pd on Si and P-Si respectively. It shows that significant enhancement occurs at the sharp edges and also at the nanogap between the nanorods or nanoparticles. However, significant enhancement is also observed to occur due to pyramidal structure of the substrate which is contributed by the factors described earlier.

5.6 Conclusions

In conclusion, stable SERS active substrates are made based on Ag and Pd nanoparticles. For Ag deposited on planar and pyramidal Si, we obtain from FDTD simulation that the nano-gap between the sphere and triangle is observed to be the source of hotspots which plays the most dominant role to enhance the Raman signal. To the best of our knowledge this is the first report where the effect of annealing environment on the SERS activity of Ag deposited on pyramidal Si is reported. Also, using the composite structure (Ag triangle and Ag sphere) a balancing between forward scattering and absorption of the incident EM field can be

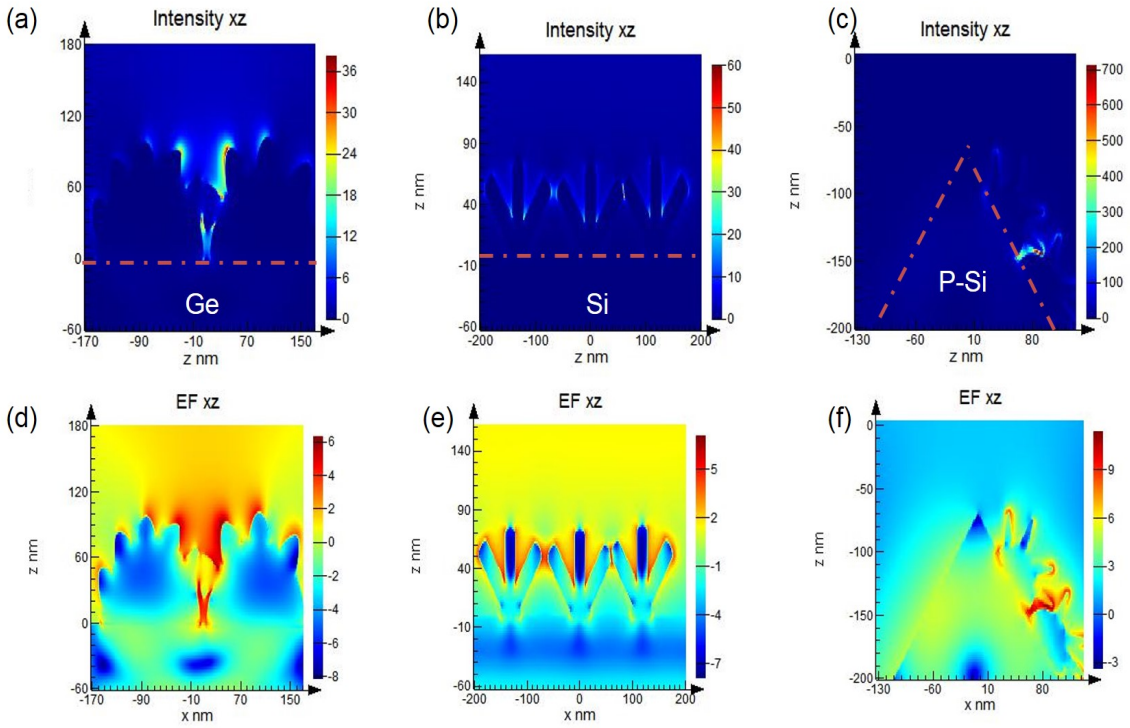

Figure 5.19: *FDTD calculated near-field electric field distribution for more than one Pd nanoparticle of (a) Pd on Ge* (100) *(b) Pd on Si* (100) *and (c) Pd on P-Si. Calculated EF in log scale for the same* 3 *substrates are shown in (d), (e) and (f) respectively.*

obtained which is very much important for plasmon based solar cell applications. Also the SERS activity of different Pd based substrates is also heavily dependent on the structure. We have observed 2 order (10^6) higher enhancements compared to the previously reported result (10^4) using same Pd nanoparticle. A 3D surface (pyramidal structure) produces higher enhancement of the SERS signal of R6G compared to the planar substrate

Chapter 6

Electrochemical Detection of Glucose and AA Using Pd Nanoparticle Deposited on Semiconductor Substrate

---

This chapter describes the effectiveness of the Pd deposited semiconductor substrates as an electrochemical Glucose and AA sensor

---

6.1 Introduction

CV is a versatile method to study the electrochemical properties of electroactive surfaces. It helps to understand the redox reaction mechanism, reversibility of any reaction and also the kinetics of electron transfer of an electro-active species present in the solution. Also, a rapid information on the heterogeneous electron-transfer kinetics, adsorption and coupled chemical reaction can readily be obtained from this. It is the mostly adopted method to find the effectiveness of a material for different applications.

In CV a three-electrode configuration is used where potential is scanned at the working electrode with respect to reference electrode and current flows through a counter electrode, which is monitored in an analyte solution which remains unstirred. The potential between working electrode and reference electrode is varied linearly with time and is scanned back and forth between two extreme values at a constant rate of few mV/s to few V/s, the waveform of the potential is triangular. A current flows through the analyte during this process and the current flows between the working electrode and counter electrode is plotted against the voltage by which the CV curve of the analyte is obtained. The current between the electrode is highly dependent on the nature of the working electrode, composition of the analyte and the scan rate. The reduction and oxidation potential of the analyte and its diffusion co-efficient can be found with very good accuracy. The working electrode material can be considered to have good pseudo-capacitive properties with better rate capability if the peak anodic current increases with increasing the voltage scan rate. As, during higher scan rate more electro-active species appear at the working electrode surface, the number of redox reactions increases. However,

there is a chance of missing the reduction or oxidation peak during slow scan as the reduction or oxidation products can have sufficient time to undergo chemical reaction in the analyte which may not be electro-active.

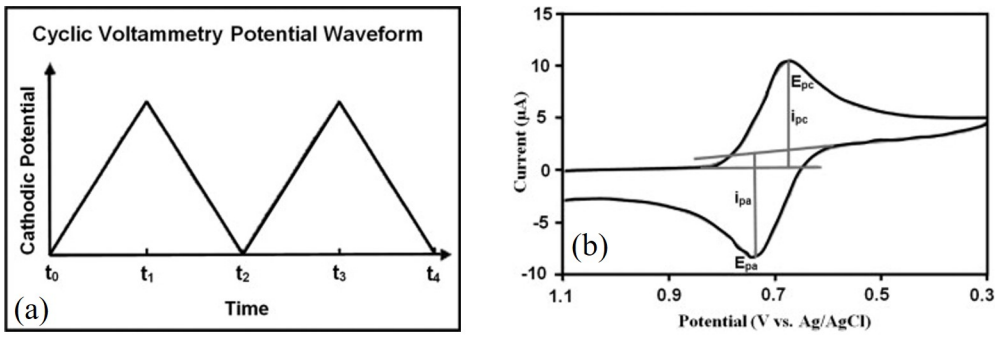

Figure 6.1: *(a) Graph of a typical input waveform in CV experiment (b) Typical cyclic voltammogram.* E_{pa} *and* E_{pc} *are the anodic and cathodic peak potentials, and* i_{pa} *and* i_{pc} *are the anodic and cathodic peak currents, respectively. Source: Elsevier*

Figure 6.1 shows a typical CV diagram of an electrochemical reversible process, where $i_{p,c}$ and $i_{a,c}$ are the anodic and cathodic peak current and $E_{p,a}$, $E_{p,c}$ are the corresponding peak potential. The peak current at 25^o C is given by Randless Sevick expression,

$$I_p = (2.69 * 10^5) n^{1.5} A C D^{0.5} V^{0.5} \tag{6.1}$$

Different factors *i.e.* number of electrons transferred during redox reaction, the factors limiting the rate of the reaction can be found by CV. The diffusion rate of the analyte can be obtained from the difference between the two peak potentials. The nature of the system can also be predicted from the CV curve. The system is reversible, quasi-reversible and irreversible depending on the ration of the cathodic to anodic peak current ratio. If the ratio is 1 then the system is reversible, if it is

nearly equal to 1 then the system is said to be quasi-reversible and if one of the peak is absent then the system is said to be irreversible.

During amperometric sensing experiment the potential across the electrode is kept fixed at either at the reduction or oxidation potential of the analyte and the corresponding current is measured. In this condition, the current only changes when the applied potential is equal to the oxidation or reduction potential of the analyte. The current i during amperometric sensing can be written as,

$$i = \frac{nFAcD^{0.5}}{\pi^{0.5}t^{0.5}} \tag{6.2}$$

where n is the number of electrons transferred/molecule during oxidation and reduction, t is the time elapsed during the application of the potential. The diffusion co-efficient for the analyte molecule can be found out from this equation.

Diabetes mellitus arises due to deficiency of insulin and can leads to serious health problems in the human body, decreasing life expectancy. The normal sugar level in the body is $80 - 120\ mg/dl$, but anything over $200\ mg/dl$ is an alarming sign and needs to treat accordingly [184]. Glucose detection is very much important to detect and treat diabetes. AA is also a very important vitamin in human diet and also works as an anti-oxidant. It is used for the treatment of infertility, common cold, mental illness, HIV and also in cancer [185, 186].

So the detection of AA and glucose is not only important in neurochemistry and biological field but they are vastly important in biological and pathological research purposes. Hence, efficient detection of these two is highly required. Enzyme based sensor shows good detection efficiency for these two but they suffer from poor stability and also get very much affected by the electro-oxidized species [187, 188].

These difficulties can be overcome by non-enzymatic amperometric sensors and metal nanoparticles have already shown vast effectiveness to serve this purpose. Electrochemical method is a very simple, low-cost detection method. Effective sensors based on glucose, hydrogen peroxide (H_2O_2) and AA were already been made by different metal nanoparticles like Au, Ag, Pd, Pt, Mn and Fe [189–195, 195]. However, to made the sensor using metal nanoparticles the particles are needed to be drop cast on the substrate before use and this process does not provide good adhesion and can destroy the stability of the sensors. During deposition of metal nanoparticles on semiconductor using GDR method a chemical bond forms between them which provide very good adhesion and make the substrate stable giving less disturbance in the signal.

6.2 Electrochemical Cyclic Voltammetry Study

The CV characteristics of all the samples using 1 M Na_2SO_4 as electrolyte at a scan rate of 60 mV/s is shown Figures 6.2. An enhanced current density is observed for PS60 and G60 electrodes compared to S20. As the electrochemical response of G60 and PS60 is better than other samples, further study on biosensing was carried out by using these two substrates as electrodes.

6.2.1 Glucose and Ascorbic Acid Sensing Study

Nonenzymatic electrochemical sensing study for the detection of Glucose and AA by G60 and PS60 samples was done using 1 M Na_2SO_4 as the electrolyte which is shown in Figure 6.3. The oxidation peak of Pd was observed near 0 V. This

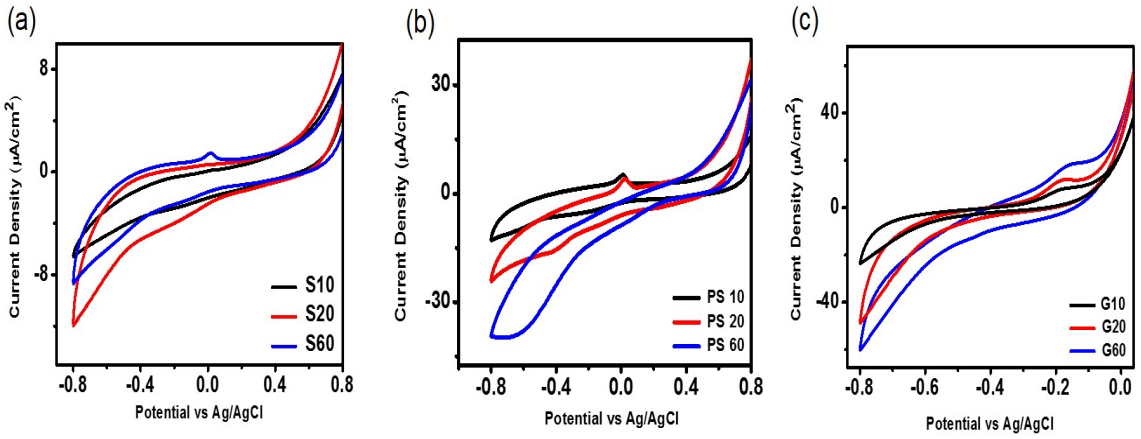

Figure 6.2: *CV comparison plot for (a) S*10*, S*20 *and S*60 *(b) PS*10*, PS*20 *and PS*60 *(c) G*10*, G*20 *and G*60 *in* 1 M Na_2SO_4 *solution as electrolyte and at a scan rate of* 60 mV/s

oxidation peak of Pd was also observed by Wang *et al.* for dendritic Pd nanostructures and by Burke and Casey for bulk Pd structures [202, 203]. According to their observation the reduction peak of palladium oxide occurs at $-0.37\ V$ during the negative scan.

They also observed an increment in the oxidation/reduction peak current with increasing methanol concentration. From Figure 6.3b it is observed that the detection of glucose is prominent at the reduction potential of H_2O_2 (at -0.6V). Figure 6.3c and d shows the Pd oxidation and reduction cycle at 0 V and $-0.3\ V$ respectively and the reduction current is observed to increase significantly with increasing AA concentration. The PS60 and G60 electrodes adsorb the AA molecule from the electrolytic mixture, and then AA gets oxidized by hydrolysis process and converts it to dehydroascorbic acid. This process releases two protons and two electrons, which convert Pd^{2+} to Pd^0 [204]. The increment in the peak current density of

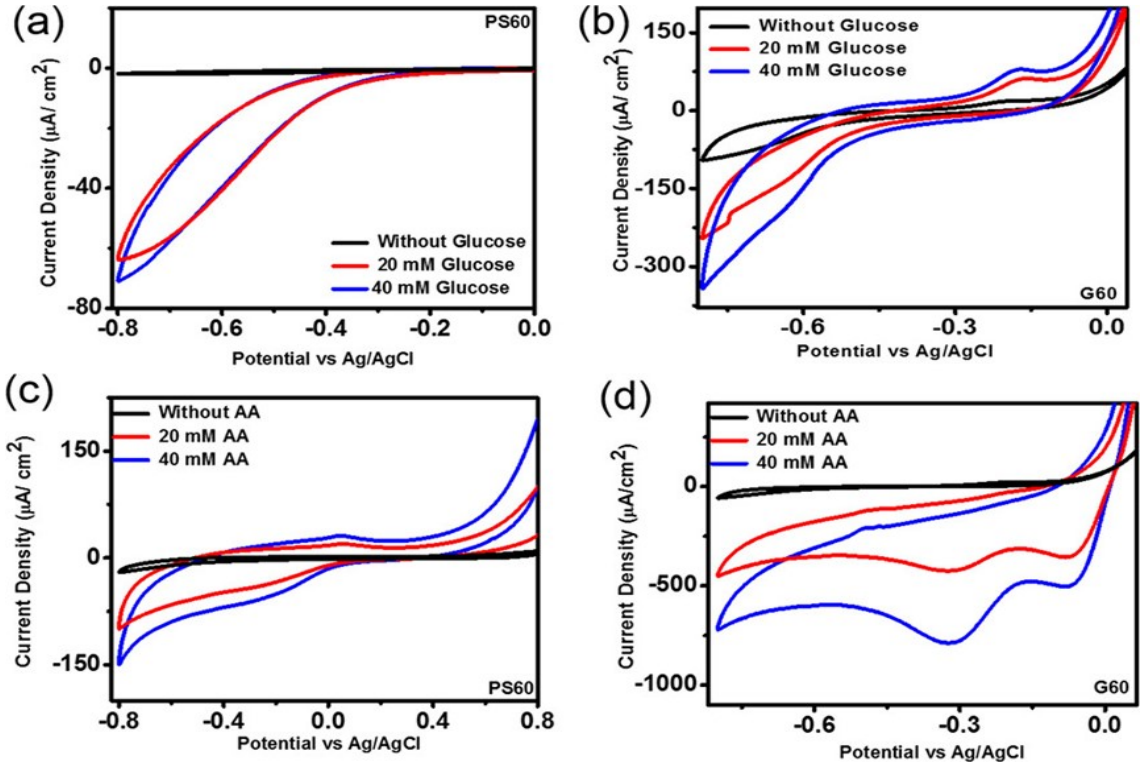

Figure 6.3: *(a) and (b) shows CV study with different molar concentrations of glucose using PS*60 *and G*60 *substrates as working electrodes, respectively. (c) and (d) shows CV study with different molar concentrations of AA using PS*60 *and G*60 *substrates as working electrodes, respectively.*

PdO/Pd redox system on PS60 is weaker than that of G60, indicating larger electroactive surface area for G60 sample. As the reduction current of PdO formed at the surface dominates the CV properties, the adsorbed species at the surface region is the most dominating here.A linear change in the reduction current with the scan rate is also observed from (Figures 6.4), which indicates a surface-confined process.

The amperometric sensing study of glucose and AA was performed at $-0.6\ V$ and $-0.3\ V$ respectively and is shown in Figure 6.5. The amperometric current

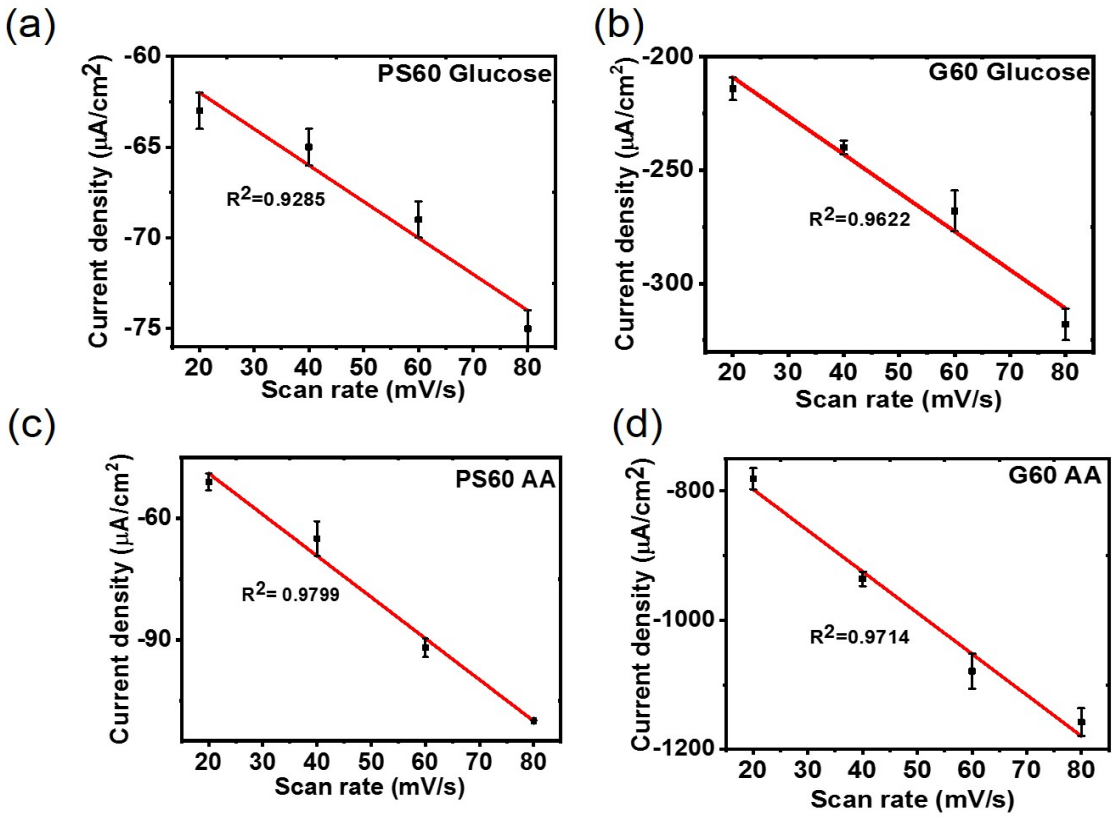

Figure 6.4: *(a) and (b) shows linear response of peak reduction current with scan rate (with R^2 error) for glucose detection using PS*60 *and G*60 *as working electrode respectively. (c) and (d) linear response of peak reduction current with scan rate (with R^2 error) for AA detection using PS*60 *and G*60 *as working electrode respectively*

density-time curve for sensing of glucose using PS60 and G60 sample is shown in Figure 6.5a and in Figure 6.5b. Stable current steps were obtained whenever glucose were added to the electrolyte. Figure 6.5c and Figure 6.5d show the same for AA sensing using PS60 and G60 as the working electrode.

Figure 6.6 shows the calibration curve used for the amperometric sensing study for different substrates. For glucose sensing using PS60 and G60 as the working electrode, the calibration curve can be fitted with the equation, $I_{PS60,glu} =$

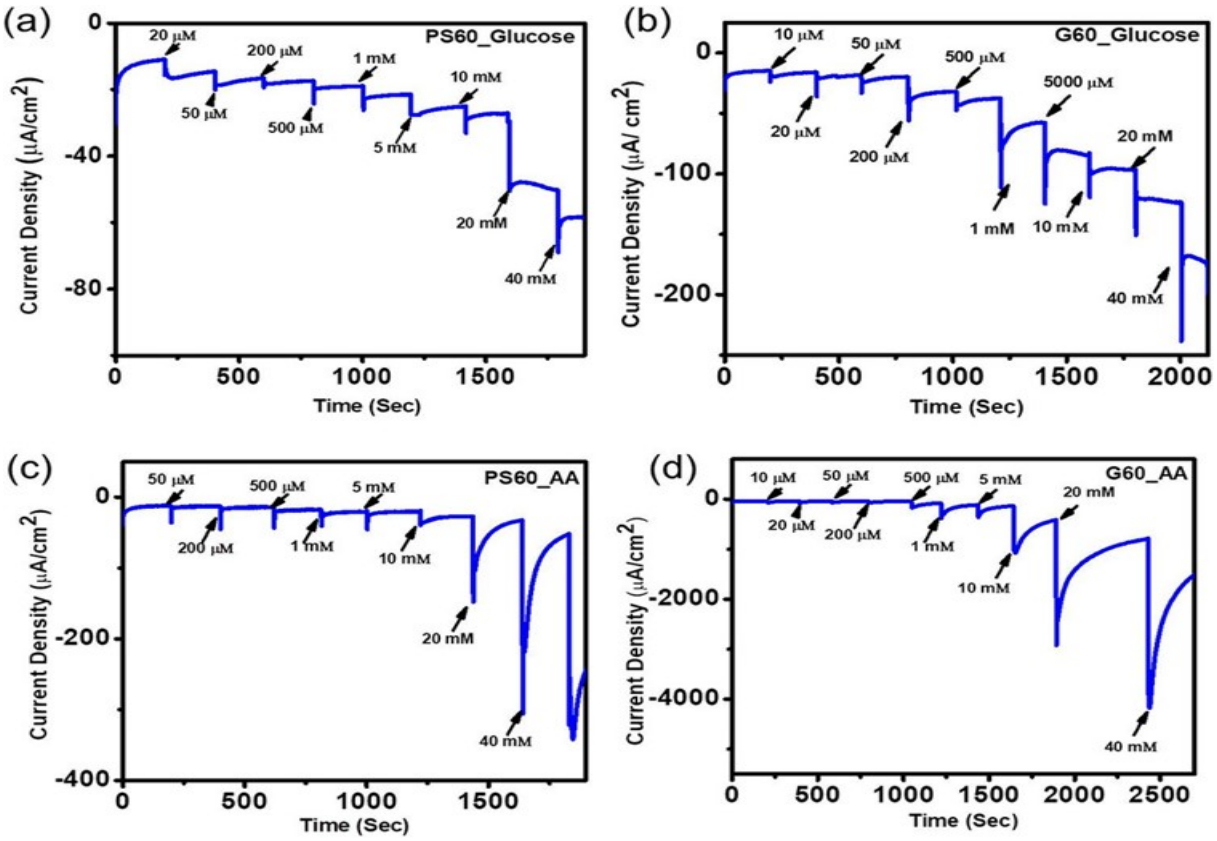

Figure 6.5: *(a and b) Amperometric current density–time curves for glucose sensing using PS*60 *and G*60 *as working electrodes, respectively. (c and d) Amperometric current density–time curves for AA sensing using PS*60 *and G*60 *as working electrodes, respectively.*

$-19.273 - 1.04C_{glu}$ and $I_{G60,glu} = -58.75 - 2.65C_{glu}$ respectively. The calibration curve for AA sensing using these two samples can be fitted with the equation, $I_{PS60,AA} = -17 - 0.92C_{glu}$ and $I_{G60,AA} = -33.29 - 18.67C_{AA}$ respectively. The highest sensitivity values for both glucose and AA were obtained for G60 (2.658 and $18.67\mu AmM^{-1}cm^{-2}$, respectively). The detection limits for PS60 and G60 for AA are 4.35 and $2.01\mu M$, respectively, and the detection limits for the same two substrates for glucose are 2.86 and $7.19\mu M$, respectively (S/N=3).

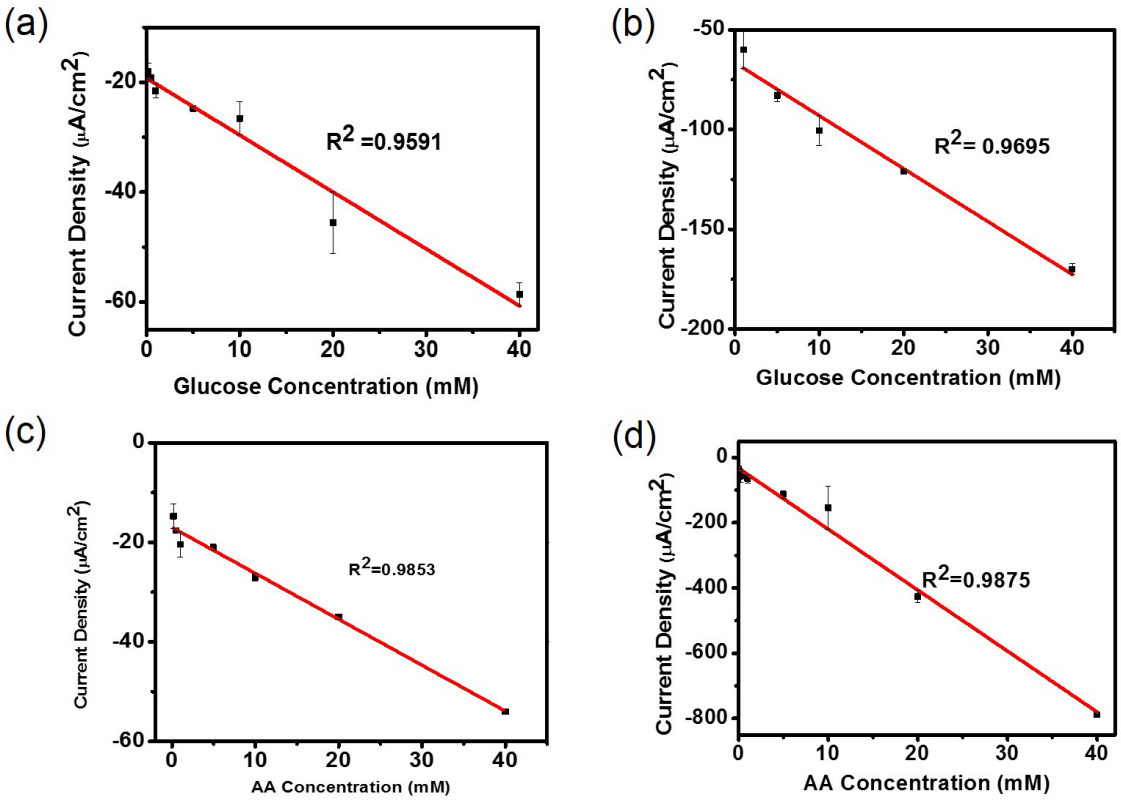

Figure 6.6: *(a) and (b) linear response graph of glucose concentration (with residual errors) with the current density for PS*60 *and G*60*, respectively. (c) and (d) linear response graph of AA concentration with the current density for PS*60 *and G*60*, respectively.*

The comparison of our samples with the previously made electrochemical non-enzymatic biosensors for AA and glucose detection is shown in Table 6.1 and 6.2 respectively. Which show that the sensitivity of our sample is very much comparable to the previously reported results. Due to the presence of more active catalytic sites the sensitivity of G60 sample is highest.

6.2.2 Interference Study

Selectivity towards the desired material in the presence of other electro-active material is a very important property a sensor has to possess. Figure 6.7 shows the current density-time graph for the working electrodes to test the selectivity. The working potential was fixed at the detection potential ($-0.6\ V$ for glucose detection and $-0.3\ V$ for AA detection) of glucose and AA. The interference effect was observed in presence of DA, tap water, UA, hydrogen-peroxide (H_2O_2). All the sensors show a significant change in the current density whenever glucose and AA were added to the electrolyte. The current also changed for the addition of other electro-active material but this change is very small and also the current attains the previous stable value after some time. So, from the current density-time curve it is clear that the substrates also have very good selectivity for glucose and AA detection.

6.3 Conclusions

The Pd deposited semiconductor substrates show very good sensing properties for the detection of glucose and AA. The highest sensitivity ($18.67 \mu A m M^{-1} c m^{-2}$) for AA is observed for Pd deposited on G60 in the linear range of 20 $\mu\ M$ to 40 mM, and for glucose, the highest sensitivity ($2.658 \mu A m M^{-1} c m^{-2}$) is also observed for the same substrate in the linear range of 1 mM to 40 mM. The lowest detection limits for AA and glucose are 2.19 and 7.19 $\mu\ M$, respectively, for the same substrate. Clearly, the substrates we prepared have strong implications in identifying new SERS substrates using low-cost materials as well as electrochemical nonenzymatic sensors. It would be much more beneficial if the smaller interference

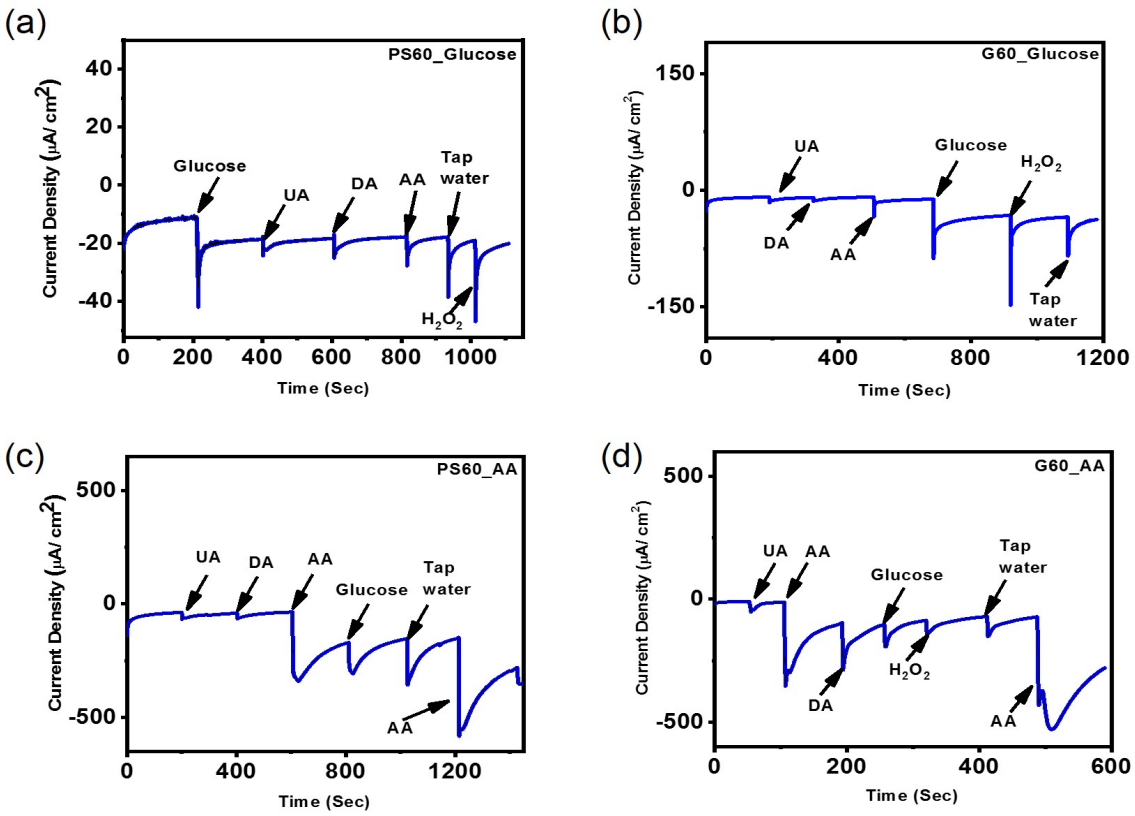

Figure 6.7: *(a and b) Selectivity of glucose (working potential* 0.6 *V) over other electroactive materials using PS*60 *and G*60 *as working electrodes. (c and d) Selectivity of AA (working potential* 0.3 *V) over other electroactive materials using PS*60 *and G*60 *as working electrodes.*

from other electroactive material can be minimized further by introducing some structural or chemical modification to the Pd nanostructures.

Electrode	**Sensitivity** $\mu m\ mM^{-1}\ cm^{-2}$	**Linear Range**	**Detection Limit**	**ref**
Mesopore Rich Active C-Modified Pyrolytic Graphite Electrode	2.27	0.5-2000 μM	0.3 μM	[192]
Pd Nanoparticle Supported Graphene Oxide	6.18	20-2280 μM	N.A	[193]
Poly(N-Methylpyrrole)/ Pd nanocluster	5.6	0.05-1 mM	7 μM	[194]
Graphene Anchored with Pd-Pt Nanoparticles	8.9	20-900 μM	0.11 μM	[195]
GD of Pd on Ge for 60 min	18.67	20-40000 μM	2.01 μM	Our Work

Table 6.1: *Comparison of the Analytical Performance of the Proposed AA Biosensor with Other AA Biosensors Reported Previously*

Electrode	**Sensitivity** $\mu m\ mM^{-1}\ cm^{-2}$	**Linear Range**	**Detection Limit**	**ref**
Mesoporous Pt	9.6	10 mM	N.A	[205]
$NiTiO_3/NiO$ Nanoparticles	1454	0.1-18.8 μM	0.06 muM	[189]
glucose oxidase-Nanoporous Au	12.1	50 μM to 10 mM	1.02 μM	[190]
bimetallic Pt Nanoparticles	10.7	Up to 15 mM	0.5 mM	[191]
GD of Pd on Ge for 60 min	2.66	1-40 mM	7.09 μM	Our Work

Table 6.2: *Comparison of the Analytical Performances of the Proposed Glucose Biosensor with Other Glucose Biosensors Reported Previously.*

Nomenclature

AA	:Ascorbic acid
ADF	:Annular dark-field
AEM	:Analytical electron microscopy
AFM	:Atomic force microscopy
ALD	:Atomic layer deposition
BF	:Bright-field
BSE	:Backscattered electron
CA	:Contact angle
$CBED$	:Convergent beam electron diffraction
CCD	:Charge-couple device
CDF	:Centered dark-field
CE	:Chemical Enhancement
CL	:Cathodoluminescence
CM	:Chemical enhancement

$CTAB$	:Cetyl trimethyl ammonium bromide
CVD	:Chemical vapor deposition
DF	:Dark-field
DME	:Domain matching epitaxy
EDX	:Energy dispersive X-ray
EF	:Enhancement Factor
EM	:Electromagnetic
$FDTD$	:Finite-different time-domain
FEG	:Field-emission gun
FFT	:Fast Fourier transform
FM	:Frank-van der Merew
GDR	:Galvanic displacement reaction
$GIXRD$	:Grazing incidence X-ray diffraction
$HAADF$	:High angle annular dark-field
HF	:Hydrofluoric acid
$HRTEM$	:High-resolution transmission electron microscopy
$HSPMT$	:High sensitivity photomultiplier tube
IPA	:Iso-propyl alcohol

ITO	:Indium-tin oxide
LCD	:Liquid crystal display
LIE	:Laser interference lithography
LM	:Light microscopy
$LSPR$	:Localized surface plasmon resonance
$MACE$	:Metal-assisted chemical etching
MBE	:Molecular beam epitaxy
$MONOCL$	:Monochromatic CL
NA	:Numerical aperture
OR	:Ostwald ripening
$PANCL$	:Panchromatic CL
$PIPS$	:Precision ion polishing system
PML	:Perfect matched layer
PVP	:Polyvinylpyrrolidone
$R6G$	:Rhodamine 6G
RIE	:Reactive ion etching
RTA	:Rapid thermal annealing
SAD	:Selected area diffraction

SDR	:Saw-damage removal
SE	:Secondary electron
SEM	:Scanning electron microscopy
$SERS$	:Surface-enhanced Raman scattering
SHE	:Standard hydrogen electrode
SK	:Stranki-Krastanov
SPP	:Surface plasmon polariton
SPR	:Surface plasmon resonance
$STEM$	:Scanning transmission electron microscopy
TEM	:Transmission electron microscopy
$TFSF$	:Total-field scattered-field
UHV	:Ultra-high vacuum
$UV-vis$	:Ultra-violet visible
VLS	:Vapor liquid solid
VW	:Volume-Weber
XRD	:X-ray diffraction
$XSEM$	:Cross-sectional scanning electron microscopy
$XTEM$	:Cross-section transmission electron microscopy

Synopsis

During the last decade, remarkable improvement is observed over the growth of nanomaterials. Controlling the growth of nanoparticles is very much important because the optical, chemical and conductive properties of nanomaterials depend heavily on their size and shape [1, 2]. Noble metal nanoparticles having the size in the nanometer regime have attained significant interest due to their unique optical, electrical properties. Localized surface plasmon resonance, which is the collective oscillation of conduction electrons is responsible behind the unique optical properties of noble metal nanostructures [3]. Localized surface plasmon resonance (LSPR) is produced when the surface conduction electrons of metals interact resonantly with the incident electromagnetic wave. This interaction produces a highly intense localized EM field around the nanoparticle which remains confined in a sub-nanometer region and is called "hot spots". These "hot spots" are mainly generated around the sharp apexes, edges, and tips of the metal nanoparticles. This LSPR not only increases the local electromagnetic field around the nanoparticles (near field) but it also enhances the scattering field at the far-field. Surface-enhanced Raman scattering (SERS) is an excellent tool to determine molecular fingerprint up to single-molecule level [4]. This ability of SERS technique has made it very much useful for low concentration sensing and imaging of biomolecules [5, 6]. The SERS enhancement is very much dependent on the formation of "hot spots" which as stated previously is very much dependent on the size, shape and interparticle distances of the nanoparticles. Gold (Au) and Silver (Au) are the two most studied materials to prepare SERS active substrates or nanoparticles. It is due to the well established synthetic method, easy tunability of their plasmon wavelength and very high scattering cross-sections in the NIR and uv-visible region of the spectra which makes them superior compared to other noble metals for SERS application [7]. Au and Ag also show better thermal stability and resistance against corrosion. Ag shows better SERS enhancement and catalytic activity compared to Au due to its increased scattering efficiency in the uv-vis region [8]. However, Au shows very good stability against oxidation but Ag nanoparticles or Ag-based substrates become oxidized very much rapidly in ambient atmosphere and lost its efficiency. Also at high-temperature agglomeration occurs which reduces its efficiency further. Noble metal/semiconductor substrates have much advantages over their colloidal counterparts. As the semiconductor substrate holds the nanoparticles strongly hence agglomeration cannot occur easily at room temperature, which

is an important factor to obtain a stable SERS substrate [9]. Hence overcoming the oxidation related problem at high temperature is very much important for Ag-based semiconductor substrates. This will also increase its application in sensing, catalysis related research. However, extensive use of Au and Ag for SERS related applications limits the use of other noble metals like Platinum (Pt) and Palladium (Pd) in this field. Pd and Pt show very good catalytic activity and they found their application in hydrogen storage, fuel cells [10, 11]. Their effectiveness will increase further if their SERS enhancement can be increased significantly. Pd also shows very good stability against corrosion and oxidation, hence finding a SERS active substrate based on Pd should with significant enhancement factor (EF) will be very much beneficial. Srnova et al first studied the SERS effect of Pd and they observed an EF of 190 [12]. Different types of morphology like hexagonal, cubic Pd nanoparticles were made but an enhancement factor greater than 10^4 is very hard to achieve. Various methods were used previously to produce metal-semiconductor substrates i.e. molecular beam epitaxy (MBE), chemical vapor deposition (CVD), atomic layer deposition (ALD), electrocatalytic deposition, pulsed laser deposition (PLD) and galvanic displacement reaction (GDR) [13–15]. between these processes, GDR is an electroless process that does not require any external voltage source and it is also very much easier and cheap. The difference between the reduction potential of two material with respect to standard hydrogen electrode (V_{SHE}) is the sole driving force behind the reaction. The metal-semiconductor interface obtained in this case is very much clean as no external reducing agent is used in GDR. In this thesis work we have studied growth of metal nanoparticles (Ag and Pd) on planar and patterned semiconductor surfaces. The structure of the as-deposited nanoparticles and their evolution due to rapid thermal annealing at different atmosphere (O_2 and (N_2) is studied extensively using scanning/ transmission electron microscopy (S/TEM), scanning electron microscopy (SEM) and X-ray diffraction. The optical properties of the nanomaterials were studied experimentally using cathodoluminescence spectroscopy, uv-vis spectroscopy. The applicability of the substrates as SERS active material were shown using a Raman spectrometer and the enhancement factor (EF) were calculated theoretically by finite-difference time-domain (FDTD) simulation.

Firstly, I have studied the thermal evolution of Ag nanoparticle deposited on planar Si (100) by GDR process.The two half cell reactions of the deposition process

can be written as,

$$Si + 6F^- \rightarrow SiF_6^{2-} + 4e^- \quad (E^0 = -0.86V) \tag{1}$$

$$Ag^+ + e^- \rightarrow Ag \quad (E^0 = 0.8V) \tag{2}$$

Effect of RTA at different atmosphere (O_2 and N_2) on the nanoparticle structure were also studied extensively by TEM. We have observed that when the as deposited Ag nanoparticles are annealed in O_2 AT 550^oC, a combination of spherical Ag and endotaxial Ag were produced in a regular manner. However, no such endotaxial structure formation was seen during annealing at N_2 atmosphere keeping other parameters the same. The enhanced kinetics of Ag in presence of O_2 atmosphere is the reason behind the formation of such endotaxial structure. Ag nanoparticles on planar Si (100) remains in thermodynamically unstable configuration due to their high surface energy [16]. So when the substrate is rapidly annealed, the enhanced kinetics helps the nanoparticles penetrate into Si via interstitial-substitutional reaction. Also, Si tend to diffuse through Ag at temperature $150 - 200^o$ C, which helps Ag to completely buried into Si and finally produce the endotaxial structure. From interface energy consideration, if the interface energy σ_{Ag/SiO_2} is less than σ_{Ag} then the nanoparticles will get embedded into the Si. Now the surface energy for Ag is $\sigma_{Ag} = 1.25Jm^{-2}$ and that for SiO_2 is $\sigma_{SiO_2} = 0.29Jm^{-2}$. The value of the surface energy of the interface can be obtained from Young's equation which can be written as,

$$\sigma_{Ag/SiO_2} = \sigma_{SiO_2} - \sigma_{Ag}\cos\theta \tag{3}$$

The average contact angle of the nanoparticles with the subbstrates were obtained as $137.33^o \pm 6.66^o$, which was obtained from different TEM images. Considering this, the value of σ_{Ag/SiO_2} comes as 1.209 which definitely lower than the value of σ_{Ag}. Hence, formation of endotaxial structure was thermodynamically favorable. Previously, endotaxial structures were produced using lithography, vapor deposition and all of them are challenging, expensive [17, 18]. Here, using simple electroless process we were able to produce endotaxial structure which according to best of our knowledge was not previously reported. The stability of the endotaxial system was also studied by keeping them in ambient atmosphere for one month. The endotaxial structures were observed to remain unaffected by the atmosphere, however, the spherical particle on top of them got distorted significantly which

also proves the superiority of the endotaxial Ag over the particles residing at the surface.

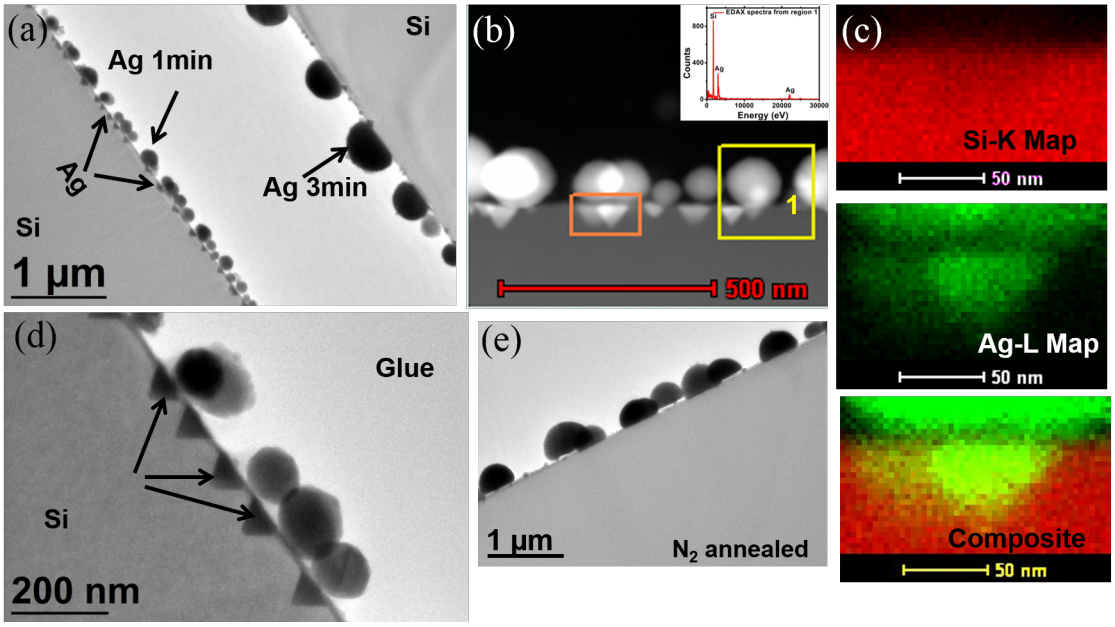

Figure 1: *(a) Low magnification bright-field XTEM image of S1 and S2, (b) STEM-HAADF image of O_2 annealed substrate and the EDX spectrum showing presence of Ag and Si (inset), (c) EDX elemental map from the rectangular region in (b), (d) Enlarged view of S1 showing the formation of buried Ag nanoparticle, (e)Low magnification bright-field XTEM image of S1 and S2, (b) STEM-HAADF image of N_2 annealed substrate showing formation of only spherical Ag particle*

The SERS enhancement of the substrates were examined using rhodamine 6G (R6G) as the dye. The enhancement factor of 10^6 was obtained for the endotaxial and spherical Ag combination. While maximum EF of 10^5 was obtained for spherical Ag particle only. To understand the reason we have done FDTD simulation and it shows that the nano-gap between the spherical and endotaxial Ag contains highly intense EM field which provides the dominant contribution to the enhanced SERS signal observed for the combined structure.

I have also studied the evolution of Ag nanoparticles due to annealing at O_2 and N_2 atmosphere when the deposition was carried out on pyramidal Si. Pyramidal Si was produced by saw-damage removal method. In which planar Si (100) substrates were first immersed in a solution of $30wt\%$ NaOH in de-ionized (DI) water heated at 75^oC for 3 minutes. In this process a few μ m thick layer use to come out from both

sides of the Si substrate. In second step, the substrates were immersed for $40-50$ minutes in a solution containing $2wt\%$ NaOH and 10% isopropyl alcohol (IPA) solution to finally produce pyramidal Si substrate. Ag nanoparticles were deposited on the substrate using the previously described GDR process. The time required to obtain a uniform coating of Ag on Si is 90 seconds. Again, the as-deposited Ag substrates were subjected to RTA at 550^oC in O_2 and N_2 atmosphere respectively. We have observed formation of triangular Ag and spherical Ag combination due to annealing at O_2 atmosphere and formation of only spherical shaped particle due to annealing at N_2 atmosphere. The triangular and spherical structure were observed to form in pair and in this case the triangular Ag do not penetrate into Si but they form along the slope of the pyramid. The size of the nanoparticles also changes from the top towards the bottom of the pyramid. TEM study reveals formation of tilted hetero-epitaxy between Ag and Si. Such kind of epitaxy between Ag and Si can form with the introduction of domain matching epitaxy (DME) where a 3×3 domain of Si matches with a 4×4 domain of Ag which leads to a lattice mismatch of only 0.6% [19].

The SERS effect of the substrates were also studied extensively using rhodamine 6g (R6G) as the dye molecule. The highest EF was obtained as 9×10^7 for the peak at $613cm^{-1}$ of R6G using the O_2 annealed sample. The SERS data were also taken at three points for every measurement to ensure the homogeneity of the samples. The main reasons behind the significant enhancement are (i) The nano-gap between the triangular Ag and spherical Ag which acts as the source of hot spots (ii) The 3D Si also has a significant role to play. It can effectively oscillate the incident EM radiation due to its structural and trap a significant portion of it. The SERS stability of the samples were studied by keeping the substrate in ambient atmosphere for 1 month. The EF was observed to decrease only 18% over the one month time span and gives significant SERS enhancement. Which shows that rapid annealing in O_2 atmosphere actually enhances the ability of the substrate as a SERS active material, which is due to the formation of the complex structure in this environment.

As 3D Si substrates were observed to give higher SERS enhancement compared to their 2D counterparts, we have also observed the SERS enhancement of Ag deposited on Si nanowire [20]. Si nanowire has already achieved much technical

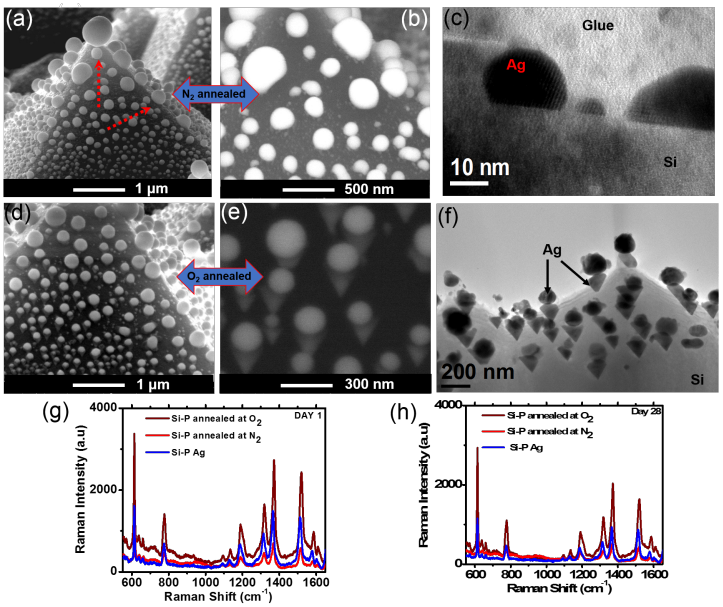

Figure 2: *(a) SE image of N_2 annealed sample showing the particle size variation from bottom to top of the pyramid (b) BSE images showing the atomic contrast between Si and Ag (c) bright-field XTEM image of N_2 annealed sample showing formation of only spherical particle on Si. (d) SE image of O_2 annealed sample showing the particle size variation from bottom to top of the pyramid and also formation of triangular Ag underneath of spherical Ag (e) BSE images confirming that the triangular particles are Ag (f) bright-field XTEM image of O_2 annealed sample (g) SERS spectra at day 1 using 10^{-6} M R6G for all the three samples (h) SERS spectra at day 28.*

importance due to its unique optical, electrical property induced by quantum confinement effect. Different processes were used to produce Si nanowires like molecular beam epitaxy, vapor-liquid-solid method and laser ablation method [21–23]. All of this are very much expensive, time-consuming and require heavy instrumentation. Metal-assisted chemical etching (MACE) method is a electroless process to produce Si nanowire. Compared to other processes this process is very much cheap, easy and controlled tunability can be obtained by this. In this process, the oxidation of Si to SiO_2 occurs in presence of metal ions which acts as a cathode. The reduction of the oxidative agent (mostly H_2O_2) occurs at the noble metal surface and the hole reaches to the substrate to oxidized it. The SiO_2 produced in this process get dissolved into the DI water solution by reacting with HF and

the etching continues.The governing equation can be written as,

$$H_2O_2 + 2H^+ \rightarrow 2H_2O + 2h^+ \tag{4}$$

$$Si + 4HF_2^- + 2h^+ \rightarrow SiF_6^{2-} + 2HF + H_2(g) \tag{5}$$

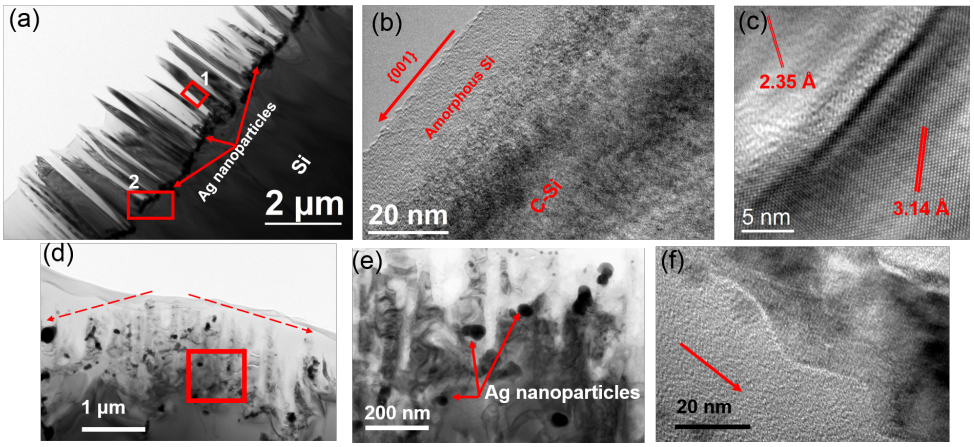

Figure 3: *(a) Bright-field XTEM image of Si nanowire on planar Si produced by MACE process (b) HRTEM image of sidewall of a Si nanowire showing formation of amorphous sidewall (c) HRTEM image of Ag-Si interface. (d) bright-field XTEM image of Si nanowire on pyramidal Si (e) HRTEM image showing presence of Ag nanoparticles at the bottom of the nanowires (f) HRTEM image of a single Si nanowire showing formation of zig-zag sidewalls.*

In this work, we have produced Si nanowire on planar Si as well as on pyramidal Si and did an extensive comparative study on their structure. From high resolution transmission electron microscope (HRTEM) study we have observed that the sidewalls of Si nanowire produced from planar Si substrate has straight and amorphous sidewalls, whereas the sidewalls of the Si nanowires produced from pyramidal Si has crystalline and zig-zag sidewalls. The local variation of the oxidant concentration is assumed to be responsible behind the formation of different sidewalls. Ag nanoparticles were deposited on the Si nanowire by GDR method and they are subjected to RTA at 550^o C in O_2 and N_2 atmosphere respectively. Initially the Ag nanoparticles are observed to be randomly oriented on the Si nanowire but after annealing Ag sphere is observed to form at the top of almost all the Si nanowire. Such kind of arrangement has many special optical properties and obtained previously only by costly VLS or CVD method [21, 22]. But here we could obtain

the same structure by a combination of GDR and MACE which is of very low-cost and easier. The substrates are observed to be both SERS active and hydrophobic. The hydrophobicity property is mainly contributed by the dual roughness scale contributed by the Si nanowire and pyramidal Si structure.

I have also studied the evolution of Pd nanoparticles deposited on Si, Ge and pyramidal Si by GDR process. The governing equation can be written as,

$$2PdCl_4^{2-}(aq.) + Si^o(s) + 6F^-(aq) \rightarrow 2Pd(s) + SiF_6^{2-}(aq.) + 8Cl^- \qquad (6)$$

The rate of growth and final morphology of the Pd nanoparticles are heavily dependent on the surface energy of the substrate and the number of defects present. On planar Si the growth rate is observed to be very slow due to its lowest surface energy among all of them. Highest growth rate was observed for deposition on Ge substrate and growth rate on pyramidal Si lies in between. For small deposition time the Pd particles form an urchin like structure of average size of $120nm$ consisting of spherical core and dendritic shaft as observed from TEM images. With increasing the deposition time the individual spherical shape gets diminished while the dendritic structure remains. For a deposition time of 60 minutes it almost attains a flat top morphology. On planar Si (100) initially nanorod like formation of 30 nm length occurs. Which for higher deposition time produces an urchin like shape with an increment in the nanorod length. The growth rate of Pd is much higher on pyramidal Si. Where an almost continuous layer of Pd of thickness 45 nm is observed for only 10 minute deposition time. So, depending on the surface energy and defect the growth rate is controlled which leads to the formation of different shaped structure. Previously different shape of Pd nanoparticles were produced by using different capping molecules to control the growth rate. However, this capping molecule could not be removed and they reduce the SERS and catalytic efficiency of the substrates [23, 24].

The highest EF we observed for Pd deposited on pyramidal Si and it is $\backsim 3.8 \times 10^6$ which greater than all the SERS active substrates made using Pd. We could detect up to 10^{-11} M of R6G using the substrates. Besides this, the substrates were all observed to have very good catalytic efficiency and can be used as electrochemical sensor to detect glucose and ascorbic acid. The highest sensitivity (18.67 μA mM^{-1} cm^2) for AA is observed for Pd deposited on a Ge substrate for 60 min in the linear range of 2040 mM, and for glucose, the highest sensitivity (2.658 μA mM^{-1} cm^2) is also observed for the same substrate in the linear range of 140 mM.

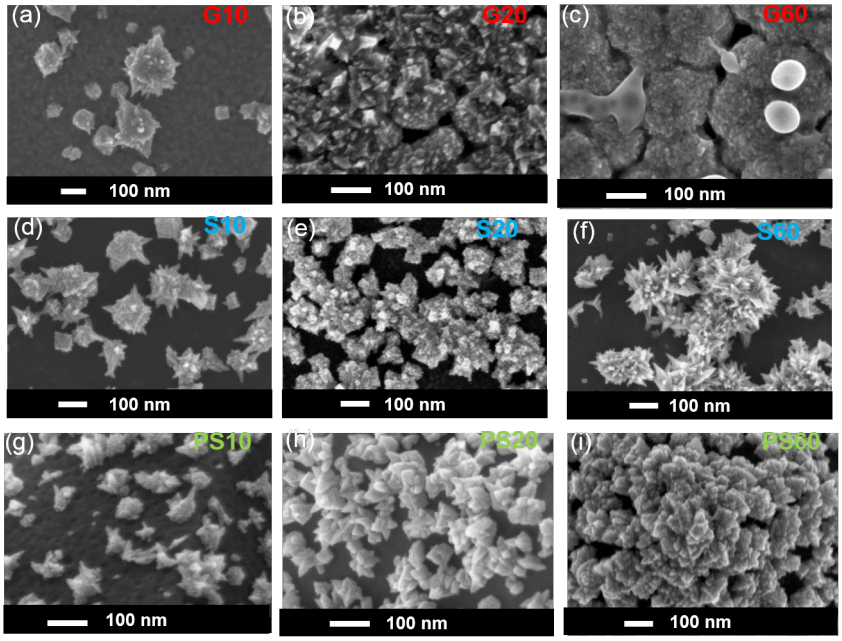

Figure 4: *(a), (b) and (c) shows formation of Pd on Ge for* 10, 20 *and* 60 *minutes respectively, (d), (e) and (f) shows formation of Pd on Si for* 10, 20 *and* 60 *minutes respectively and (g), (h) and (i) shows formation of Pd on pyramidal Si for* 10, 20 *and* 60 *minutes respectively.*

The lowest detection limits for AA and glucose are 2.19 and 7.19 μM, respectively, for the same substrate. Substrates that we prepared are very useful for multifunctional applications like SERS and electrochemical nonenzymatic sensing.

In conclusion, in the thesis work, we have successfully deposited different shaped noble metal nanoparticles on planar and patterned semiconductor substrates. The morphology and shape of the metal nanoparticles are observed to be heavily dependent on the substrate pattern, deposition time and annealing environment. The metal-semiconductor substrates are observed to show good SERS and catalytic effect. They also posses very good stability against oxidation. The three dimensional Si substrate along with sharp metal edges is observed to be responsible behind such enhancement, which was shown in detail by FDTD simulation. The substrates hence produced ins very much capable to produce efficient SERS active and catalytic devices.

Bibliography

[1] R.N. Cassar, D. Graham, I. Larmour, A. W. Wark, K. Flauds, Vib. Spectrosc. **71**, (2014).

[2] A. Ott, S. Ring, G. Yin, W. Calvet, B. Stannowski, Y. Lu, R. Schlatmann, M. Ballauff, Nanotechnology **25**, (2014).

[3] T. Ghosh, P. Das, T. K. Chini, T. Ghosh, B. Satpati, Phys. Chem. Chem. Phys. **16**, (2014).

[4] S. M. Nie, S. R. Emery, Science **275**, (1997).

[5] L. Jensen, G. C. Schatz, J. Phys. Chem. A**110**, (2006).

[6] J. A. Dieringer, K. L. Wustholz, D. J. Masiello, J. P. Camden, S. L. Kleinmann, G. C. Schatz, J. Am. Chem. Soc. **131**, (2009).

[7] L. Vigderman, E. R. Zubarev, Chem. Mater. **25**, (2013).

[8] C. Zhang, S. Z. Jiang, C. Yang, H. C. Li, Y. Y. Huo, X. Y. Liu, A. H. Liu, Q. Wei, S. S. Gao, X. G. Gao, Y. B. Man, Sci. Rep. **5**, (2016).

[9] T. Wang, Z. Zhang, F. Liao, Q. Cai, Y. Li, S. T. Lee, Sci. Rep. **4**, (2015).

[10] F. J. Ibanez, F. P. Zamborini, J. Am. Chem. Soc. **130**, (2008).

[11] S. Horinouchi, Y. Yamanoi, T. Yonezawa, T. Mouri, H. Nishihara, Langmuir **2**, (2006).

[12] I. Srnova, B. Vlckova, V. Baumruk, J. Mol. Struct. **410**, (1997).

[13] R.R. Juluri, A. Rath, A. Ghosh, A. Bhukta, R. Satyavathi, D.N. Rao, K. Muller, M. Schowalter, K. Frank, T. Grieb, F. Krause, A. Rosenauer, P.V. Satyam, Sci. Rep. **4**, (2014) .

[14] J.A. Huang, Y.Q. Zhao, X.J. Zhang, L.F. He, T.L. Wong, Y.S. Chui, S.T. Lee, Nano Lett. **13**, (2013).

[15] J.A. Huang, Y.Q. Zhao, X.J. Zhang, L.F. He, T.L. Wong, Y.S. Chui, S.T. Lee, Nanotechnology **27**, (2016).

[16] R. Lu, Y. Wang, W. Wang, L. Gu, J. Sha, Acta Mater. **79**, (2014).

[17] P. Guha, R. R. Juluri, A. Bhukta, A. Ghosh, S. Maiti, A. Bhattacharyya, A. Srihari, P. V. Satyam, Cryst. Eng. Comm. **19**, (2017).

[18] R. R. Juluri, A. Rath, A. Ghosh, P. V. Satyam, J. Phys. Chem. C **117**, (2013).

[19] T. B. Hur, H. K. Kim, D. Perello, M. Yun, A. Kulovits, J. Wiezorek, J. Appl. Phys. **103**, (2008).

[20] M. K. Lee, T. Y. Jeon, C. W. Mun, J. Kwon, J. Yun, S. H. Kim, D. H. Kim, S. C. Chang, S. G. Park, RSC Advances , (2017).

[21] A. Ghosh, P. Guha, A. K. Samanatara, B. K. Jena, R. Bar, S. K. Ray, P. V. Satyam, ACS Appl. Mater. Interfaces **7**, (2015).

[22] A. Ghosh, P. Guha, R. Thapa, S. Sinthika, M. Kumar, B. Rakshit, T. Dash, R. Bar, S. K. Ray, P. V. Satyam, Nanotechnology **27**, (2016).

[23] L. M. Chen, Y. N. Liu, Cryst. Eng. Comm. **13**, (2011).

[24] D. Xu, X. Yan, P. Diao, P. Yin, J. Phys. Chem. C **118**, (2014).

Bibliography

[1] Khan, I., Saeed, K., and Khan, I. *Arabian Journal of Chemistry* (2017).

[2] Luo, Y., Zhu, C., Du, D., and Lin, Y. *Analytica chimica acta* (2019).

[3] Clinton, W. J. *Weekly Compilation of Presidential Documents* **36**(3), 122–130 (2000).

[4] Chen, Y., Fan, Z., Zhang, Z., Niu, W., Li, C., Yang, N., Chen, B., and Zhang, H. *Chemical reviews* **118**(13), 6409–6455 (2018).

[5] Jin, H., Guo, C., Liu, X., Liu, J., Vasileff, A., Jiao, Y., Zheng, Y., and Qiao, S.-Z. *Chemical reviews* **118**(13), 6337–6408 (2018).

[6] Thomas, G. *Platin. Jubil. Spec. Publ* , 53–66 (2010).

[7] Sun, C. Q. *arXiv preprint cond-mat/0506113* (2005).

[8] Siegel, R. *Nanophase Materials, in "Encyclopedia of Applied physics" 11th ed.* Weinheim: VCH, (1994).

[9] Patsha, A. and Dhara, S. *Nano Letters* **18**(11), 7181–7187 (2018).

[10] Arora, N., Joshi, D. P., and Pachauri, U. *Materials Chemistry and Physics* **217**, 235–241 (2018).

[11] Sudha, P. N., Sangeetha, K., Vijayalakshmi, K., and Barhoum, A. In *Emerging Applications of Nanoparticles and Architecture Nanostructures*, 341–384. Elsevier (2018).

[12] Alves, T., Kolodziej, C., Burda, C., and Franco Jr, A. *Materials & Design* **146**, 125–133 (2018).

[13] Huang, X. and El-Sayed, M. A. *Journal of advanced research* **1**(1), 13–28 (2010).

[14] Das, R. and Soni, R. *RSC Advances* **7**(51), 32255–32263 (2017).

[15] Chouhan, N. *Silver Nanoparticles: Fabrication, Characterization and Applications* , 21 (2018).

[16] Kelly, K. L., Coronado, E., Zhao, L. L., and Schatz, G. C. (2003).

[17] La Spada, L. and Vegni, L. *Materials* **11**(4), 603 (2018).

[18] Kociak, M. and Stéphan, O. *Chemical Society Reviews* **43**(11), 3865–3883 (2014).

[19] De Abajo, F. G. *Reviews of modern physics* **82**(1), 209 (2010).

[20] Das, P. and Chini, T. K. *The Journal of Physical Chemistry C* **116**(49), 25969–25976 (2012).

[21] Ghosh, T., Das, P., Chini, T. K., Ghosh, T., and Satpati, B. *Physical Chemistry Chemical Physics* **16**(31), 16730–16739 (2014).

[22] Cassar, R. N., Graham, D., Larmour, I., Wark, A. W., and Faulds, K. *Vibrational Spectroscopy* **71**, 41–46 (2014).

[23] Wang, P., Liang, O., Zhang, W., Schroeder, T., and Xie, Y.-H. *Advanced Materials* **25**(35), 4918–4924 (2013).

[24] Ott, A., Ring, S., Yin, G., Calvet, W., Stannowski, B., Lu, Y., Schlatmann, R., and Ballauff, M. *Nanotechnology* **25**(45), 455706 (2014).

[25] Chen, H., Ohodnicki, P., Baltrus, J. P., Holcomb, G., Tylczak, J., and Du, H. *RSC Advances* **6**(90), 86930–86937 (2016).

[26] Ibanez, F. J. and Zamborini, F. P. *Journal of the American Chemical Society* **130**(2), 622–633 (2008).

[27] Xie, W. and Schlücker, S. *Chemical communications* **54**(19), 2326–2336 (2018).

[28] Deng, D., Novoselov, K., Fu, Q., Zheng, N., Tian, Z., and Bao, X. *Nature nanotechnology* **11**(3), 218 (2016).

[29] Ma, X., Sun, H., Wang, Y., Wu, X., and Zhang, J. *Nano energy* **53**, 932–939 (2018).

[30] Yang, P., Zheng, J., Xu, Y., Zhang, Q., and Jiang, L. *Advanced materials* **28**(47), 10508–10517 (2016).

[31] Cholula-Díaz, J. L., Lomelí-Marroquín, D., Pramanick, B., Nieto-Argüello, A., Cantú-Castillo, L. A., and Hwang, H. *Colloids and Surfaces B: Biointerfaces* **163**, 329–335 (2018).

[32] Tiwari, V. S., Oleg, T., Darbha, G. K., Hardy, W., Singh, J., and Ray, P. C. *Chemical Physics Letters* **446**(1-3), 77–82 (2007).

[33] He, L., Liu, C., Tang, J., Zhou, Y., Yang, H., Liu, R., and Hu, J. *Applied Surface Science* **434**, 265–272 (2018).

[34] Anju, K., Gayathri, R., Subha, P., Kumar, K. R., and Jayaraj, M. *Microchemical Journal* **147**, 349–355 (2019).

[35] Magagnin, L., Maboudian, R., and Carraro, C. *The Journal of Physical Chemistry B* **106**(2), 401–407 (2002).

[36] Gutes, A., Carraro, C., and Maboudian, R. *Journal of the American Chemical Society* **132**(5), 1476–1477 (2010).

[37] Milazzo, R. G., Privitera, S. M., D'Angelo, D., Scalese, S., Di Franco, S., Maita, F., and Lombardo, S. *International Journal of Hydrogen Energy* **43**(16), 7903–7910 (2018).

[38] Han, W., Stepula, E., Philippi, M., Schlücker, S., and Steinhart, M. *Nanoscale* **10**(44), 20671–20680 (2018).

[39] Chen, L.-M. and Liu, Y.-N. *CrystEngComm* **13**(21), 6481–6487 (2011).

[40] Aizawa, M. and Buriak, J. M. *Journal of the American Chemical Society* **128**(17), 5877–5886 (2006).

[41] Lay, B., Sabri, Y. M., Kandjani, A. E., and Bhargava, S. K. *Journal of colloid and interface science* **547**, 199–205 (2019).

[42] Dryfe, R. A., Walter, E. C., and Penner, R. M. *ChemPhysChem* **5**(12), 1879–1884 (2004).

[43] Qiu, R., Zhang, D., and Wang, P. *Corrosion Science* **66**, 350–359 (2013).

[44] Larmour, I. A., Bell, S. E., and Saunders, G. C. *Angewandte Chemie International Edition* **46**(10), 1710–1712 (2007).

[45] Rizzello, L., Shankar, S. S., Fragouli, D., Athanassiou, A., Cingolani, R., and Pompa, P. *Langmuir* **25**(11), 6019–6023 (2009).

[46] Pei, Z., Hu, H., Li, S., and Ye, C. *Langmuir* **33**(15), 3569–3575 (2017).

[47] Wang, H.-P., Lai, K.-Y., Lin, Y.-R., Lin, C.-A., and He, J.-H. *Langmuir* **26**(15), 12855–12858 (2010).

[48] Geyer, N., Fuhrmann, B., Leipner, H. S., and Werner, P. *ACS applied materials & interfaces* **5**(10), 4302–4308 (2013).

[49] Goldberger, J., Hochbaum, A. I., Fan, R., and Yang, P. *Nano letters* **6**(5), 973–977 (2006).

[50] Tian, B., Zheng, X., Kempa, T. J., Fang, Y., Yu, N., Yu, G., Huang, J., and Lieber, C. M. *nature* **449**(7164), 885 (2007).

[51] Hochbaum, A. I., Chen, R., Delgado, R. D., Liang, W., Garnett, E. C., Najarian, M., Majumdar, A., and Yang, P. *Nature* **451**(7175), 163 (2008).

[52] Hwang, Y. J., Boukai, A., and Yang, P. *Nano letters* **9**(1), 410–415 (2008).

[53] Cui, Y., Wei, Q., Park, H., and Lieber, C. M. *Science* **293**(5533), 1289–1292 (2001).

[54] Patolsky, F., Zheng, G., and Lieber, C. M. *Nature protocols* **1**(4), 1711 (2006).

[55] Park, S.-Y., Di Giacomo, S. J., Anisha, R., Berger, P. R., Thompson, P. E., and Adesida, I. *Journal of Vacuum Science & Technology B, Nanotechnology and Microelectronics: Materials, Processing, Measurement, and Phenomena* **28**(4), 763–768 (2010).

[56] Nuzaihan, M., Hashim, U., Arshad, M. M., Ruslinda, A. R., Rahman, S., Fathil, M., and Ismail, M. H. *PloS one* **11**(3), e0152318 (2016).

[57] Omar, H., Salifairus, M., Alrokayan, S. A., Khan, H. A., Jani, A., Rusop, M., and Abdullah, S. In *2015 IEEE Student Conference on Research and Development (SCOReD)*, 649–652. IEEE, (2015).

[58] Akan, R., Parfeniukas, K., Vogt, C., Toprak, M. S., and Vogt, U. *RSC advances* **8**(23), 12628–12634 (2018).

[59] Miao, B., Zhang, J., Ding, X., Wu, D., Wu, Y., Lu, W., and Li, J. *Journal of Micromechanics and Microengineering* **27**(5), 055019 (2017).

[60] Vinzons, L. U., Shu, L., Yip, S., Wong, C.-Y., Chan, L. L., and Ho, J. C. *Nanoscale research letters* **12**(1), 385 (2017).

[61] Faraday, M. *Philosophical Transactions of the Royal Society of London* (147), 145–181 (1857).

[62] Mayer, K. M. and Hafner, J. H. *Chemical reviews* **111**(6), 3828–3857 (2011).

[63] Mie, G. *Annalen der physik* **330**(3), 377–445 (1908).

[64] Bernardi, M., Mustafa, J., Neaton, J. B., and Louie, S. G. *Nature communications* **6**, 7044 (2015).

[65] Salerno, M., Krenn, J. R., Lamprecht, B., Schider, G., Ditlbacher, H., Félidj, N., Leitner, A., and Aussenegg, F. R. *Optoelectronics Review* (3), 217–224 (2002).

[66] Citrin, D. *Optics letters* **31**(1), 98–100 (2006).

[67] Franzen, S. *The Journal of Physical Chemistry C* **112**(15), 6027–6032 (2008).

[68] Pitarke, J., Silkin, V., Chulkov, E., and Echenique, P. *Reports on progress in physics* **70**(1), 1 (2006).

[69] Atwater, H. A. and Polman, A. In *Materials For Sustainable Energy: A Collection of Peer-Reviewed Research and Review Articles from Nature Publishing Group*, 1–11. World Scientific (2011).

[70] Opilik, L., Schmid, T., and Zenobi, R. (2013).

[71] Fikiet, M. A., Khandasammy, S. R., Mistek, E., Ahmed, Y., Halámková, L., Bueno, J., and Lednev, I. K. *Spectrochimica Acta Part A: Molecular and Biomolecular Spectroscopy* **197**, 255–260 (2018).

[72] Cialla-May, D., Schmitt, M., and Popp, J. *Physical Sciences Reviews* **4**(6).

[73] Fleischmann, M., Hendra, P. J., and McQuillan, A. J. *Chemical physics letters* **26**(2), 163–166 (1974).

[74] Nie, S. and Emory, S. R. *science* **275**(5303), 1102–1106 (1997).

[75] Zong, C., Xu, M., Xu, L.-J., Wei, T., Ma, X., Zheng, X.-S., Hu, R., and Ren, B. *Chemical reviews* **118**(10), 4946–4980 (2018).

[76] Ausman, L. K. and Schatz, G. C. *The Journal of chemical physics* **131**(8), 084708 (2009).

[77] Solís, D. M., Taboada, J. M., Obelleiro, F., Liz-Marzán, L. M., and Garcia de Abajo, F. J. *ACS photonics* **4**(2), 329–337 (2017).

[78] Valley, N., Greeneltch, N., Van Duyne, R. P., and Schatz, G. C. *The Journal of Physical Chemistry Letters* **4**(16), 2599–2604 (2013).

[79] Alvarez-Puebla, R., Liz-Marzán, L. M., and Garcia de Abajo, F. J. *The Journal of Physical Chemistry Letters* **1**(16), 2428–2434 (2010).

[80] Gutes, A., Laboriante, I., Carraro, C., and Maboudian, R. *Sensors and Actuators B: Chemical* **147**(2), 681–686 (2010).

[81] Yang, J., Li, J., Gong, Q., Teng, J., and Hong, M. *Nanotechnology* **25**(46), 465707 (2014).

[82] Lee, M., Jeon, T. Y., Mun, C., Kwon, J.-D., Yun, J., Kim, S.-H., Kim, D.-H., Chang, S.-C., and Park, S.-G. *RSC Advances* **7**(29), 17898–17905 (2017).

[83] Tan, R., Agarwal, A., Balasubramanian, N., Kwong, D., Jiang, Y., Widjaja, E., and Garland, M. *Sensors and Actuators A: Physical* **139**(1-2), 36–41 (2007).

[84] He, Y., Su, S., Xu, T., Zhong, Y., Zapien, J. A., Li, J., Fan, C., and Lee, S.-T. *Nano Today* **6**(2), 122–130 (2011).

[85] Peng, K.-Q., Yan, Y.-J., Gao, S.-P., and Zhu, J. *Advanced materials* **14**(16), 1164–1167 (2002).

[86] Sun, X., Wang, N., and Li, H. *Applied Surface Science* **284**, 549–555 (2013).

[87] Zhang, C., Jiang, S., Huo, Y., Liu, A., Xu, S., Liu, X., Sun, Z., Xu, Y., Li, Z., and Man, B. *Optics express* **23**(19), 24811–24821 (2015).

[88] Seniutinas, G., Gervinskas, G., Verma, R., Gupta, B. D., Lapierre, F., Stoddart, P. R., Clark, F., McArthur, S. L., and Juodkazis, S. *Optics express* **23**(5), 6763–6772 (2015).

[89] Zhang, C., Jiang, S. Z., Yang, C., Li, C. H., Huo, Y. Y., Liu, X. Y., Liu, A. H., Wei, Q., Gao, S. S., Gao, X. G., et al. *Scientific reports* **6**, 25243 (2016).

[90] Bao, L., Mahurin, S. M., and Dai, S. *Analytical chemistry* **76**(15), 4531–4536 (2004).

[91] Siddiqi, K. S., Husen, A., and Rao, R. A. *Journal of nanobiotechnology* **16**(1), 14 (2018).

[92] Srikar, S. K., Giri, D. D., Pal, D. B., Mishra, P. K., Upadhyay, S. N., et al. *Green and Sustainable Chemistry* **6**(01), 34 (2016).

[93] Ahmed, S., Ahmad, M., Swami, B. L., and Ikram, S. *Journal of advanced research* **7**(1), 17–28 (2016).

[94] Ibañez, F. J. and Zamborini, F. P. *Langmuir* **22**(23), 9789–9796 (2006).

[95] Horinouchi, S., Yamanoi, Y., Yonezawa, T., Mouri, T., and Nishihara, H. *Langmuir* **22**(4), 1880–1884 (2006).

[96] Tao, A. R., Habas, S., and Yang, P. *small* **4**(3), 310–325 (2008).

[97] Bal, J. and Hazra, S. *Physical Review B* **79**(15), 155412 (2009).

[98] Dhanaraj, G., Byrappa, K., Prasad, V., and Dudley, M. *Springer handbook of crystal growth*. Springer Science & Business Media, (2010).

[99] Capper, P., Irvine, S., and Joyce, T. In *Springer Handbook of Electronic and Photonic Materials*, 1–1. Springer (2017).

[100] Bonev, I. *Acta Crystallographica Section A: Crystal Physics, Diffraction, Theoretical and General Crystallography* **28**(6), 508–512 (1972).

[101] Cho, A. Y. and Arthur, J. *Progress in solid state chemistry* **10**, 157–191 (1975).

[102] Leskelä, M. and Ritala, M. *Thin solid films* **409**(1), 138–146 (2002).

[103] Kavanagh, K., Reuter, M., and Tromp, R. *Journal of crystal growth* **173**(3-4), 393–401 (1997).

[104] Mahato, J., Das, D., Juluri, R., Batabyal, R., Roy, A., Satyam, P., and Dev, B. *Applied Physics Letters* **100**(26), 263117 (2012).

[105] Juluri, R., Rath, A., Ghosh, A., Bhukta, A., Sathyavathi, R., Rao, D. N., Müller, K., Schowalter, M., Frank, K., Grieb, T., et al. *Scientific reports* **4**, 4633 (2014).

[106] Chen, Y., Ohlberg, D. A., and Williams, R. S. *Journal of Applied Physics* **91**(5), 3213–3218 (2002).

[107] Ferralis, N., Maboudian, R., and Carraro, C. *The Journal of Physical Chemistry C* **111**(20), 7508–7513 (2007).

[108] Voorhees, P. W. *Journal of Statistical Physics* **38**(1-2), 231–252 (1985).

[109] Wynblatt, P. and Gjostein, N. *Acta Metallurgica* **24**(12), 1165–1174 (1976).

[110] Yee, K. *IEEE Transactions on antennas and propagation* **14**(3), 302–307 (1966).

[111] Carraro, C., Maboudian, R., and Magagnin, L. *Surface Science Reports* **62**(12), 499–525 (2007).

[112] Yasseri, A., Sharma, S., Kamins, T., Li, Z., and Williams, R. S. *Applied Physics A* **82**(4), 659–664 (2006).

[113] Sayed, S. Y., Wang, F., Malac, M., Meldrum, A., Egerton, R. F., and Buriak, J. M. *ACS nano* **3**(9), 2809–2817 (2009).

[114] Myamlin, V. A. and Pleskov, Y. V. In *Electrochemistry of Semiconductors*, 23–158. Springer (1967).

[115] Magagnin, L., Maboudian, R., and Carraro, C. *Electrochemical and Solid-State Letters* **4**(1), C5–C7 (2001).

[116] Carraro, C., Magagnin, L., and Maboudian, R. *Electrochimica acta* **47**(16), 2583–2588 (2002).

[117] Formo, E. V., Mahurin, S. M., and Dai, S. *ACS Applied Materials & Interfaces* **2**(7), 1987–1991 (2010).

[118] Srnová, I., Vlckova, B., and Baumruk, V. *Journal of molecular structure* **410**, 201–203 (1997).

[119] Chen, H., Wei, G., Ispas, A., Hickey, S. G., and Eychmuller, A. *The Journal of Physical Chemistry C* **114**(50), 21976–21981 (2010).

[120] Gorostiza, P., Allongue, P., Díaz, R., Morante, J. R., and Sanz, F. *The Journal of Physical Chemistry B* **107**(26), 6454–6461 (2003).

[121] Ye, X. R., Wai, C. M., Zhang, D., Kranov, Y., McIlroy, D. N., Lin, Y., and Engelhard, M. *Chemistry of materials* **15**(1), 83–91 (2003).

[122] Quan, Z., Wang, Y., and Fang, J. *Accounts of chemical research* **46**(2), 191–202 (2012).

[123] McAlpine, M. C., Friedman, R. S., Jin, S., Lin, K.-h., Wang, W. U., and Lieber, C. M. *Nano letters* **3**(11), 1531–1535 (2003).

[124] Hochbaum, A. I., Gargas, D., Hwang, Y. J., and Yang, P. *Nano letters* **9**(10), 3550–3554 (2009).

[125] Zheng, G., Patolsky, F., Cui, Y., Wang, W. U., and Lieber, C. M. *Nature biotechnology* **23**(10), 1294 (2005).

[126] Lerose, D., Bechelany, M., Philippe, L., Michler, J., and Christiansen, S. *Journal of Crystal Growth* **312**(20), 2887–2891 (2010).

[127] Fuhrmann, B., Leipner, H. S., Höche, H.-R., Schubert, L., Werner, P., and Gösele, U. *Nano letters* **5**(12), 2524–2527 (2005).

[128] Li, X. and Bohn, P. *Applied Physics Letters* **77**(16), 2572–2574 (2000).

[129] Chartier, C., Bastide, S., and Lévy-Clément, C. *Electrochimica Acta* **53**(17), 5509–5516 (2008).

[130] Lai, R. A., Hymel, T. M., Narasimhan, V. K., and Cui, Y. *ACS applied materials & interfaces* **8**(14), 8875–8879 (2016).

[131] Huang, J.-A., Zhao, Y.-Q., Zhang, X.-J., He, L.-F., Wong, T.-L., Chui, Y.-S., Zhang, W.-J., and Lee, S.-T. *Nano letters* **13**(11), 5039–5045 (2013).

[132] Li, K., Wang, Y., Jiang, K., Ren, Y., Dai, Y., Lu, Y., and Wang, P. *Nanotechnology* **27**(49), 495402 (2016).

[133] Shin, Y., Song, J., Kim, D., and Kang, T. *Advanced Materials* **27**(29), 4344–4350 (2015).

[134] Li, Z., Jiang, S., Huo, Y., Ning, T., Liu, A., Zhang, C., He, Y., Wang, M., Li, C., and Man, B. *Nanoscale* **10**(13), 5897–5905 (2018).

[135] Ghosh, T., Karmakar, P., and Satpati, B. *RSC Advances* **5**(114), 94380–94387 (2015).

[136] Olesinski, R., Gokhale, A., and Abbaschian, G. *Journal of Phase Equilibria* **10**(6), 635–640 (1989).

[137] Yang, W., Lambeth, D. N., Tang, L., and Laughlin, D. E. *Journal of applied physics* **81**(8), 4370–4372 (1997).

[138] Goudarzi, M., Mir, N., Mousavi-Kamazani, M., Bagheri, S., and Salavati-Niasari, M. *Scientific reports* **6**, 32539 (2016).

[139] Lu, R., Wang, Y., Wang, W., Gu, L., and Sha, J. *Acta Materialia* **79**, 241–247 (2014).

[140] Martin, M. S., Theodore, N. D., Wei, C.-C., and Shao, L. *Scientific reports* **4**, 6744 (2014).

[141] Ozcomert, J., Pai, W., Bartelt, N., and Reutt-Robey, J. *Physical review letters* **72**(2), 258 (1994).

[142] Frank, E. R. and Hamers, R. J. *Journal of Catalysis* **172**(2), 406–413 (1997).

[143] Klust, A. and Madix, R. J. *The Journal of chemical physics* **126**(8), 084707 (2007).

[144] Layson, A. R., Evans, J. W., and Thiel, P. A. *Physical Review B* **65**(19), 193409 (2002).

[145] Pavel, I. E., Alnajjar, K. S., Monahan, J. L., Stahler, A., Hunter, N. E., Weaver, K. M., Baker, J. D., Meyerhoefer, A. J., and Dolson, D. A. *Journal of Chemical Education* **89**(2), 286–290 (2011).

[146] Rao, V. K. and Radhakrishnan, T. *ACS applied materials & interfaces* **7**(23), 12767–12773 (2015).

[147] Hildebrandt, P. and Stockburger, M. *The Journal of Physical Chemistry* **88**(24), 5935–5944 (1984).

[148] Juluri, R., Ghosh, A., Bhukta, A., Sathyavathi, R., and Satyam, P. *Thin Solid Films* **586**, 88–94 (2015).

[149] Yan, M., Xiang, Y., Liu, L., Chai, L., Li, X., and Feng, T. *RSC Advances* **4**(1), 98–104 (2014).

[150] Roy, A., Maiti, A., Chini, T. K., and Satpati, B. *ACS applied materials & interfaces* **9**(39), 34405–34415 (2017).

[151] Ju, J., Liu, W., Perlaki, C. M., Chen, K., Feng, C., and Liu, Q. *Scientific reports* **7**(1), 1–11 (2017).

[152] Guo, Y., Yu, J., Li, C., Li, Z., Pan, J., Liu, A., Man, B., Wu, T., Xiu, X., and Zhang, C. *Optics express* **26**(17), 21784–21796 (2018).

[153] Xu, J., Li, C., Si, H., Zhao, X., Wang, L., Jiang, S., Wei, D., Yu, J., Xiu, X., and Zhang, C. *Optics express* **26**(17), 21546–21557 (2018).

[154] Liu, Y., Ji, G., Wang, J., Liang, X., Zuo, Z., and Shi, Y. *Nanoscale research letters* **7**(1), 663 (2012).

[155] Kim, T.-H., Acapulco Jr, J. A., Hong, S., Lee, S., and Park, S. *Bulletin of the Korean Chemical Society* **36**(3), 815–821 (2015).

[156] Wang, T., Zhang, Z., Liao, F., Cai, Q., Li, Y., Lee, S.-T., and Shao, M. *Scientific reports* **4**, 4052 (2014).

[157] Pinkhasova, P., Chen, H., Sukhishvili, S., Du, H., et al. *RSC Advances* **3**(39), 17954–17961 (2013).

[158] Saini, C., Barman, A., Kumar, M., Satpati, B., Som, T., and Kanjilal, A. *Journal of Applied Physics* **119**(13), 134904 (2016).

[159] Gavioli, L., Kimberlin, K. R., Tringides, M. C., Wendelken, J. F., and Zhang, Z. *Physical review letters* **82**(1), 129 (1999).

[160] Wall, D., Tikhonov, S., Sindermann, S., Spoddig, D., Hassel, C., Horn-von Hoegen, M., and zu Heringdorf, F.-J. M. *IBM Journal of Research and Development* **55**(4), 9–1 (2011).

[161] Lakowicz, J. R. *Analytical biochemistry* **337**(2), 171–194 (2005).

[162] Chaturvedi, P., Hsu, K. H., Kumar, A., Fung, K. H., Mabon, J. C., and Fang, N. X. *ACS nano* **3**(10), 2965–2974 (2009).

[163] Yamamoto, N., Araya, K., and de Abajo, F. G. *Physical Review B* **64**(20), 205419 (2001).

[164] Camden, J. P., Dieringer, J. A., Wang, Y., Masiello, D. J., Marks, L. D., Schatz, G. C., and Van Duyne, R. P. *Journal of the American Chemical Society* **130**(38), 12616–12617 (2008).

[165] Mikhael, B., Elise, B., Xavier, M., Johann, M., and Laetitia, P. *ACS applied materials & interfaces* **3**(10), 3866–3873 (2011).

[166] Asoh, H., Arai, F., and Ono, S. *Electrochimica Acta* **54**(22), 5142–5148 (2009).

[167] Liao, F., Wang, T., and Shao, M. *Journal of Materials Science: Materials in Electronics* **26**(7), 4722–4729 (2015).

[168] Convertino, A., Mussi, V., and Maiolo, L. *Scientific reports* **6**, 25099 (2016).

[169] Cui, H., Li, S., Deng, S., Chen, H., and Wang, C. *ACS sensors* **2**(3), 386–393 (2017).

[170] Li, Y., Dykes, J., Gilliam, T., and Chopra, N. *Nanoscale* **9**(16), 5263–5272 (2017).

[171] Huang, Z., Shimizu, T., Senz, S., Zhang, Z., Geyer, N., and Gosele, U. *The Journal of Physical Chemistry C* **114**(24), 10683–10690 (2010).

[172] Parker Jr, J., Feldman, D., and Ashkin, M. *Physical Review* **155**(3), 712 (1967).

[173] Kim, J., Kim, Y. H., Choi, S.-H., and Lee, W. *Acs Nano* **5**(6), 5242–5248 (2011).

[174] Ensikat, H. J., Ditsche-Kuru, P., Neinhuis, C., and Barthlott, W. *Beilstein journal of nanotechnology* **2**(1), 152–161 (2011).

[175] Li, X., Tay, B. K., Miele, P., Brioude, A., and Cornu, D. *Applied Surface Science* **255**(16), 7147–7152 (2009).

[176] Zhang, H., Liu, M., Zhou, F., Liu, D., Liu, G., Duan, G., Cai, W., and Li, Y. *Small* **11**(7), 844–853 (2015).

[177] Zhang, H., Zhou, F., Liu, M., Liu, D., Men, D., Cai, W., Duan, G., and Li, Y. *Advanced Materials Interfaces* **2**(9), 1500031 (2015).

[178] Tian, Z.-Q., Ren, B., Li, J.-F., and Yang, Z.-L. *Chemical Communications* (34), 3514–3534 (2007).

[179] Fang, P.-P., Li, J.-F., Yang, Z.-L., Li, L.-M., Ren, B., and Tian, Z.-Q. *Journal of Raman Spectroscopy: An International Journal for Original Work in all Aspects of Raman Spectroscopy, Including Higher Order Processes, and also Brillouin and Rayleigh Scattering* **39**(11), 1679–1687 (2008).

[180] Ringe, E., DeSantis, C. J., Collins, S. M., Duchamp, M., Dunin-Borkowski, R. E., Skrabalak, S. E., and Midgley, P. A. *Scientific reports* **5**, 17431 (2015).

[181] Jeong, H. and Kim, J. *ACS applied materials & interfaces* **7**(13), 7129–7135 (2015).

[182] Choi, S., Jeong, H., Choi, K.-h., Song, J. Y., and Kim, J. *ACS applied materials & interfaces* **6**(4), 3002–3007 (2014).

[183] Xu, H., Aizpurua, J., Käll, M., and Apell, P. *Physical Review E* **62**(3), 4318 (2000).

[184] Li, Z.-H., Zhao, X.-L., Jiang, X.-C., Wu, Y.-H., Chen, C., Zhu, Z.-G., Marty, J.-L., and Chen, Q.-S. *Electroanalysis* **30**(8), 1811–1819 (2018).

[185] Raoof, J. B., Kiani, A., Ojani, R., Valiollahi, R., and Rashid-Nadimi, S. *Journal of Solid State Electrochemistry* **14**(7), 1171–1176 (2010).

[186] Zhou, C., Li, S., Zhu, W., Pang, H., and Ma, H. *Electrochimica Acta* **113**, 454–463 (2013).

[187] Bossi, A., Piletsky, S. A., Piletska, E. V., Righetti, P. G., and Turner, A. P. *Analytical chemistry* **72**(18), 4296–4300 (2000).

[188] Hang, L., Zhou, F., Men, D., Li, H., Li, X., Zhang, H., Liu, G., Cai, W., Li, C., and Li, Y. *Nano Research* **10**(7), 2257–2270 (2017).

[189] Pal, N., Saha, B., Kundu, S. K., Bhaumik, A., and Banerjee, S. *New Journal of Chemistry* **39**(10), 8035–8043 (2015).

[190] Wu, C., Sun, H., Li, Y., Liu, X., Du, X., Wang, X., and Xu, P. *Biosensors and Bioelectronics* **66**, 350–355 (2015).

[191] Xiao, F., Zhao, F., Mei, D., Mo, Z., and Zeng, B. *Biosensors and Bioelectronics* **24**(12), 3481–3486 (2009).

[192] Hu, G., Guo, Y., Xue, Q., and Shao, S. *Electrochimica Acta* **55**(8), 2799–2804 (2010).

[193] Wu, G.-h., Wu, Y.-f., Liu, X.-w., Rong, M.-c., Chen, X.-m., and Chen, X. *Analytica chimica acta* **745**, 33–37 (2012).

[194] Atta, N. F., El-Kady, M. F., and Galal, A. *Analytical biochemistry* **400**(1), 78–88 (2010).

[195] Yan, J., Liu, S., Zhang, Z., He, G., Zhou, P., Liang, H., Tian, L., Zhou, X., and Jiang, H. *Colloids and Surfaces B: Biointerfaces* **111**, 392–397 (2013).

[196] Skriver, H. L. and Rosengaard, N. *Physical Review B* **46**(11), 7157 (1992).

[197] Tran, R., Xu, Z., Radhakrishnan, B., Winston, D., Sun, W., Persson, K. A., and Ong, S. P. *Scientific data* **3**, 160080 (2016).

[198] Fang, Y., Guo, S., Zhu, C., Dong, S., and Wang, E. *Langmuir* **26**(23), 17816–17820 (2010).

[199] Song, Y.-J., Kim, J.-Y., and Park, K.-W. *Crystal Growth and Design* **9**(1), 505–507 (2008).

[200] Yae, S., Nasu, N., Matsumoto, K., Hagihara, T., Fukumuro, N., and Matsuda, H. *Electrochimica Acta* **53**(1), 35–41 (2007).

[201] Conrad, R. and Harsdorff, M. *International Journal of Electronics Theoretical and Experimental* **69**(1), 153–167 (1990).

[202] Wang, A.-J., Li, F.-F., Bai, Z., and Feng, J.-J. *Electrochimica Acta* **85**, 685–692 (2012).

[203] Burke, L. and Casey, J. *Journal of the Electrochemical Society* **140**(5), 1284–1291 (1993).

[204] Majumder, S., Satpati, B., Kumar, S., and Banerjee, S. *ACS Applied Nano Materials* **1**(8), 3945–3955 (2018).

[205] Park, S., Chung, T. D., and Kim, H. C. *Analytical chemistry* **75**(13), 3046–3049 (2003).

Thesis Highlight

Name of the Student: ABHIJIT ROY

Name of the CI/OCC: Saha Institute of Nuclear Physics Enrolment No.: PHYS05201504002

Thesis Title: Structural Study of Metal Nanostructure Deposited on Semiconductor Surface and Their Multifunctional Applications

Discipline: Physical Sciences Sub-Area of Discipline: Nanomaterials for Plasmonics

Date of viva voce: 09/09/2020

Surface-enhanced Raman scattering (SERS) is a very powerful novel analytical tool that provides a very high level of detection sensitivity with molecular precision and has excellent potential to be used as a tool for chemical and biological sensing. The base of SERS is the Raman scattering which has a very low cross-section. In the SERS process, the scattering cross-section can be increased up to 10^{14} times using metal nanoparticles by "localized surface plasmon resonance (LSPR)". It is the dominant reason behind such a huge enhancement observed in SERS. It occurs when the incident light interacts with rough metal surfaces (apex, edges) and produces a sub nano-meter region of immensely concentrated EM field called "hot spots". Gold (Au) and silver (Ag) are the two most used metal for this purpose as they possess superior optical properties compared to others in the UV-Vis region.

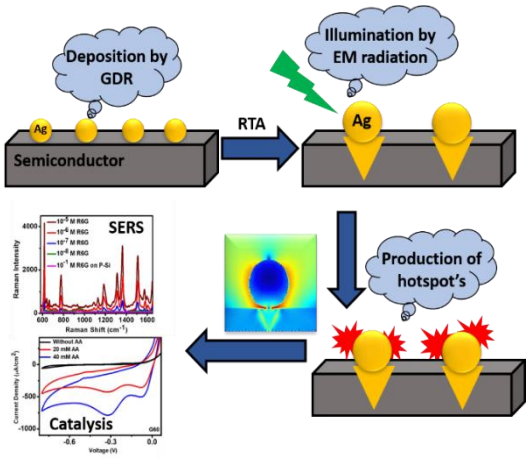

Figure 1. Schematic of formation of complex shaped metal nanoparticle due to RTA process and their applicability as multifunctional substrate

Here, we have shown that rapid thermal annealing of Ag-based SERS substrate (2D and 3D) actually enhances its performance. This is contributed by the formation of a composite nanostructure consisting of endotaxial Ag with Ag sphere on planar Si substrate and triangular Ag with spherical Ag on pyramidal Si substrate in O_2 atmosphere. The morphology, interface was studied extensively using different complementary techniques. The substrates produced in this process are very much low-cost, reproducible, efficient, and showed very efficient detection of rhodamine 6g (R6g) dye even after keeping them in an ambient atmosphere for one month. The extensive use of Ag and Au in SERS restricts the use of other metals, especially Pt group metals for SERS related applications because of their relatively poor optical properties. To overcome this limit, we also tried to produce SERS active substrate based on Pd nanoparticles which have a very good catalytic efficiency. We have observed that different nanostructure of Pd can be grown on different semiconductor substrates by keeping the other parameters the same (solvent concentration, temperature, deposition time, etc.) during deposition. This process does not involve any surfactants to control the morphology and we observed enhancement factor ~ 10^6 using this process. The substrates were also able to detect glucose and ascorbic acid (AA) qualitative as well as quantitatively with very good sensitivity and detection limits. This opens up the possibility of using these substrates in various important applications like diagnostic detection, illicitly sold narcotics detection, and civil defense applications in forensic laboratories.